

Temporal distribution and frequency of explosive volcanism in the Kermadec Arc, SW Pacific: Insights from marine cores

Kirsty Rose Herbert

A thesis submitted in fulfilment for the degree of Masters of Science in Geology,
Victoria University of Wellington, January 2013

Abstract

Studies along the Kermadec arc, SW Pacific, over the past two decades have shown the presence of numerous volcanoes with histories of caldera collapse, and abundant evidence of explosive eruptions involving evolved magmas (dacite to rhyodacite). However, as there are only two substantially emergent volcanoes in the arc, Raoul and Macauley, the history of this explosive volcanism is difficult to constrain from subaerial exposures. In contrast, the marine record offers the opportunity to document activity from these volcanoes over a longer time period. This thesis presents stratigraphic and chemical data from sediment cores collected along offshore transects west and east of Raoul and Macauley islands. Individual grain analysis of glass shards from the tephra layers was conducted using electron microprobe and laser ablation inductively coupled plasma mass spectrometry to analyse each shard for major and trace element compositions. These geochemical data allowed for discrimination between successive tephra deposits, and identification of 51 tephra layers in the cores, each of which is interpreted to represent a single eruptive event. The data also addressed the diversity or uniformity of individual eruptions and traced changes in the geochemistry of the eruption units through time. Oxygen isotope analyses of foraminifera were used to construct an age model for the cores, allowing model age estimates of individual tephra units and proving the marine core record extends back to *ca.* 170 ka. Silicic volcanism from these two volcanoes dates back to at least *ca.* 166 ka, indicating that it is not a recent development as the onshore record would suggest. Onshore exposures on Macauley Island record only one silicic eruption, the 6.3 ka Sandy Bay Tephra; however, the offshore cores show that Macauley has erupted silicic magmas since 166 ka, and is the dominant source for tephtras recorded in the cores.

Construction of a tephrochronology of the cores provides a context as to the eruptive frequency of volcanoes along the arc, indicates apparent fluctuations in the magma supply rate, and also indicates that fractionation is the dominant process by which silicic magmas are generated in the arc. The average eruptive frequency of Raoul and Macauley volcanoes is 1 eruption/kyr. If extrapolated to the other volcanoes along the arc, there are *ca.* 40 eruptions/kyr of significant size that could be preserved in the marine record. The presence of periods of quiescence in the eruptive history implies that magma supply rates may have a primary control on the frequency of eruptions linked to compositions, such that when supply rates slow, the magmas stall in the crust and fractionate to form silicic magmas.

Table of Contents

Abstract	i
Table of Contents	ii
List of Figures	viii
List of Tables	xii
List of Equations	xiv
Acknowledgements	xv

Chapter 1: Introduction

1.1 Introduction	2
1.1.1 Research objectives	3
1.1.2 Thesis structure	3
1.2 Oceanic arc volcanism and the generation of silicic magmas	4
1.3 Kermadec arc marine core samples	5
1.4 Tephrochronology	7
1.4.1 Stratigraphy	7
1.4.2 Dating techniques	8
1.4.3 Tephrochronology in the Kermadec arc	11

Chapter 2: Setting

2.1 Regional overview	15
2.1.1 The Kermadec arc	15
2.1.2 Raoul Island	17
2.1.3 Macauley Island	20
2.1.4 Raoul SW	23
2.2 Site setting and influences on tephra dispersion	25
2.2.1 Currents and water masses	25

2.2.1.1 Present day settings	25
2.2.1.2 Glacial/interglacial cycles	26
2.2.2 Wind dynamics	27
2.2.2.1 Present day settings	27
2.2.2.2 Climate variability	27
Chapter 3: Methods	
3.1 Sample Collection	33
3.2 Non-invasive methods	34
3.2.1 Photography	34
3.2.2 Core descriptions	34
3.2.3 Magnetic susceptibility	34
3.2.4 Spectrophotometer	34
3.2.5 X-ray imaging	34
3.3 Invasive methods – sediment and foraminifera	36
3.3.1 Sample collection	36
3.3.2 Grain size sieving preparation and analysis	36
3.3.3 Laser grain size analysis	36
3.3.4 Calcium carbonate analysis	36
3.3.5 Foraminifera	37
3.3.6 Oxygen isotope analysis	37
3.4 Invasive methods – tephra	39
3.4.1 Tephra sample preparation	39
3.4.2 Electron Probe Microanalyser	40
3.4.2.1 EPMA glass shard major and minor element analytical precision and accuracy	41
3.4.3 Laser Ablation Inductively Coupled Mass Spectrometry	45
3.4.3.1 LA ICP-MS data acquisition and processing	47

Chapter 4: Geochemical Results

4.1 Geochemistry of Kermadec arc tephra layers	57
4.1.1 Classification of Kermadec arc tephra layers	57
4.1.2 Major element chemistry	60
4.1.2.1 Raoul cores	60
4.1.2.2 Macauley cores	70
4.1.3 Trace element chemistry	75
4.1.3.1 Raoul cores	75
4.1.3.2 Macauley cores	84
4.2 Overall geochemical trends	88
4.3 Geochemical correlations of tephra layers between cores	96
4.4 Summary of geochemical findings	104

Chapter 5: Stratigraphy Results

5.1 Introduction	113
5.2 Lithostratigraphy	113
5.3 Non-invasive properties	115
5.4 Calcium carbonate content	118
5.5 Sediment textures	120
5.5.1 Grain sizes from sieving	120
5.5.2 Grain sizes from laser diffraction analysis	120
5.6 Chronostratigraphy	124
5.6.1 Age models	124
5.6.2 Sedimentation rates	130
5.6.3 Accuracy of age model	130

Chapter 6: Discussion

6.1 Source volcanoes of marine core tephras	135
6.1.1 Potential source volcanoes	135
6.1.2. Volcanic source of tephra layers	138
6.1.3 Volcanic source of clasts	144
6.1.4. Sandy Bay Tephra	145
6.2. Modes of emplacement and preservation of tephra layers	149
6.2.1 Primary emplacement processes	149
6.2.1.1 Subaqueous eruptions	149
6.2.1.2 Subaerial eruptions	150
6.2.2. Secondary emplacement processes	151
6.2.2.1 Volcaniclastic turbidites	151
6.2.2.2 Settling and winnowing of tephra	151
6.2.3 Preservation of tephra layers in the marine environment	152
6.3 Homogeneous vs heterogeneous tephras and implications for magma genesis	153
6.3.1. Homogeneous tephras	153
6.3.2 Heterogeneous tephras	153
6.3.3 Bimodal tephras	154
6.3.4 Kermadec arc magmatic processes and the generation of silicic magmas	154
6.4 A tephrochronological model for Raoul and Macauley marine cores	156
6.6 Frequency and magnitude of Kermadec arc eruptions	160

Chapter 7: Conclusions

7.1 Key findings of this study	164
7.2 Key questions addressed	164
7.3 Future work	165

References	167
Appendix A: Core descriptions	disc
Appendix B: Properties of marine cores	disc
Appendix C: Major element data	disc
Appendix D: Trace element data	disc

List of Figures

Chapter One: Introduction

Figure 1.1: Overview of the regional setting for this study	2
Figure 1.2: Bathymetry surrounding Raoul, Raoul SW and Macauley Islands	6
Figure 1.3: Tephrochronology constructed by Shane and Wright (2011)	13

Chapter Two: Setting

Figure 2.1: Regional setting of the Tonga-Kermadec-TVZ subduction system	16
Figure 2.2: Map of Raoul Island showing the main caldera locations	18
Figure 2.3: Bathymetry of the Macauley massif and its immediate surrounds	21
Figure 2.4: Map showing the bathymetry surrounding Raoul Island and the newly discovered Raoul SW edifice	24
Figure 2.5: Oceanography of the southwest Pacific Ocean around New Zealand and the Kermadec Ridge	28
Figure 2.6: Diagram illustrating the circulation dynamics of the Southern Hemisphere	29

Chapter Three: Methods

Figure 3.1: Flow chart showing the different methods used to create a detailed core stratigraphy	33
Figure 3.2: Image showing the non-invasive methods used in determining core stratigraphy	35
Figure 3.3: Carbon coated epoxy resin mount	40
Figure 3.4: Back scattered electron image (BSE) highlighting the differences in tephra shard size between samples	42
Figure 3.5: Image illustrating Iolite data display	48
Figure 3.6: Images highlighting issues with trace element data analyses	49

Chapter Four: Geochemistry results

Figure 4.1: Dominant bulk compositions of the samples analysed in this study	58
--	----

Figure 4.2: Total Alkalis – Silica (TAS) diggram for individual glass shards in each core	58
Figure 4.3: Diagram showing the range in SiO ₂ vs. K ₂ O contents from individual glass shards from each of the cores	59
Figure 4.4: Diagram displaying the SiO ₂ vs. FeOt/MgO (wt %) for individual glass shards in each core	59
Figure 4.5: Variation diagrams for samples in core TAN0706-1	61
Figure 4.6: Variation diagrams for samples in core TAN0706-2	62
Figure 4.7: Variation diagrams for samples in TAN0706-3	64
Figure 4.8: Variation diagrams for samples in TAN0706-4	65
Figure 4.9: Variation diagrams for samples in TAN0706-5	67
Figure 4.10: Variation diagrams for samples in TAN0706-7 & 8	68
Figure 4.11: Variation diagrams for samples in TAN0706-9 & 10	69
Figure 4.12: Variation diagrams for samples in TAN0706-12	71
Figure 4.13: Variation diagrams for samples in TAN0706-13	72
Figure 4.14: Variation diagrams for samples in TAN0706-15	73
Figure 4.15: Variation diagrams for samples in TAN0706-16	74
Figure 4.16: Variation diagrams of selected major and trace elements, including trace element ratio plots for samples from core TAN0706-1	77
Figure 4.17: Variation diagrams of selected major and trace elements, including trace element ratio plots for samples from core TAN0706-2	78
Figure 4.18: Variation diagrams of selected major and trace elements, including trace element ratio plots for samples from core TAN0706-3	79
Figure 4.19: Variation diagrams of selected major and trace elements, including trace element ratio plots for samples from core TAN0706-4	80
Figure 4.20: Variation diagrams of selected major and trace elements, including trace element ratio plots for samples from core TAN0706-5	81
Figure 4.21: Variation diagrams of selected major and trace elements, including trace element ratio plots for samples from core TAN0706-7 & 8	82
Figure 4.22: Variation diagrams of selected major and trace elements, including trace element ratio plots for samples from core TAN0706-9 & TAN0706-10	83
Figure 4.23: Variation diagrams of selected major and trace elements, including trace element ratio plots for samples from core TAN0706-13	85

Figure 4.24: Variation diagrams of selected major and trace elements, including trace element ratio plots for samples from core TAN0706-15	86
Figure 4.25: Variation diagrams of selected major and trace elements, including trace element ratio plots for samples from core TAN0706-16	87
Figure 4.26: Variation of diagrams of SiO ₂ vs. K ₂ O and CaO for homogeneous tephtras showing the range of data obtained in this study	89
Figure 4.27: Variation of diagrams of SiO ₂ vs. K ₂ O and CaO for heterogeneous tephtras showing the range of data obtained in this study	90
Figure 4.28: Variation of diagrams of SiO ₂ vs. K ₂ O and CaO for bimodal tephtras showing the range of data obtained in this study	91
Figure 4.29: Variation diagrams of selected major oxides against SiO ₂ for selected samples which are representative of the dataset as a whole	93
Figure 4.30: Variation diagrams of selected major and trace elements and trace element ratio plots for selected samples which are representative of the dataset as a whole	94
Figure 4.31: Multi-element plot and REE plot for samples representative of the overall dataset	95
Figure 4.32: Multi-element plot and REE plot for potential correlatives	98
Figure 4.33: Variation diagrams of selected major oxides against SiO ₂ for potential Sandy Bay Tephra (SBT) correlative tephra layers	99
Figure 4.34: Variation diagrams of selected major and trace elements and trace element ratio plots for potential Sandy Bay Tephra (SBT) correlatives	100
Figure 4.35: Multi-element diagram and REE plot showing the mean of each of the potential Sandy Bay Tephra (SBT) correlative samples	101
Figure 4.36: Multi-element plot and REE plot for shards from samples 4-161 and 16-187 to show that the two tephtras are distinct	102
Figure 4.37: Variation diagrams for SiO ₂ vs. Major oxides for tephra layers 13-51 and 16-71, identified as correlatives by Shane and Wright (2011)	103

Chapter Five: Stratigraphy Results

Figure 5.1: Lithology and stratigraphy of cores at locations offshore of Rauol Island	116
Figure 5.2: Lithology and stratigraphy of cores at locations offshore of Macauley Island	117
Figure 5.3: Box and whisker plots for the calcium carbonate content of each facies	118
Figure 5.4: CaCO ₃ contents of samples in each core, showing downcore variations	119

Figure 5.5: Grain size fractions that make up a cumulative % of the samples	121
Figure 5.6: Sand:Silt:Clay (>63/63 – 2/<2 µm) diagram showing the composition of samples for each of the facies determined by laser grain size analysis	122
Figure 5.7: Cumulative plot displaying the composition of each facies between gravel/sand/mud (>2 mm/2 mm – 63 µm/<63 µm) as determined in GradiStat	123
Figure 5.8: Cumulative plot displaying the composition of each facies in finer detail, with grain sizes ranging between very coarse sand (1 mm) to clay (<2 µm)	123
Figure 5.9: Oxygen isotope values presented from this study alongside the reference values from Lisiecke and Raymo (2005)	126
Figure 5.10: Age model for Core 4 presented as age downcore	127
Figure 5.11: Age model for Core 13 presented as age downcore	128
Figure 5.12: Age model for Core 16 presented as age downcore	129
Figure 5.13: Stratigraphic framework of TAN0706-16	132

Chapter Six: Discussion

Figure 6.1: K content from volcanic materials produced from volcanoes along the Kermadec arc	135
Figure 6.2: Location of submarine and subaerial volcanoes along the Kermadec arc	136
Figure 6.3: Tephra layers in this study compared to published data on volcanic materials from the region	138
Figure 6.4: Satellite image showing the recent eruption of Havre Volcano in the Kermadec Arc	142
Figure 6.5: Tephrochronology for the cores analysed in this study	143
Figure 6.6 Image of TAN0706-13	145
Figure 6.7 Variation diagrams between silicic lithic blocks and C16 206-207	147
Figure 6.8 Submarine pumice clast comparisons to silicic lithics	148
Figure 6.9 Satellite image showing July 2012 Havre eruption	150
Figure 6.10 SEM of sample 13-75	153
Figure 6.11 Preliminary Brophy model plot	155
Figure 6.12 Final tephrochronology for the marine cores	158
Figure 6.13 Erupted compositions of materials over past <i>ca.</i> 170 ka	159
Figure 6.14 Eruptive frequency of the volcanic centres over the past <i>ca.</i> 170 ka	161

List of Tables

Chapter One: Introduction

Table 1.1: Location and water depth for each of the marine cores collected on the R.V. <i>Tangaroa</i> TAN0706 voyage	6
---	---

Chapter Two: Settings

Table 2.1: Summary of eruptions from Raoul and Denham calderas	19
Table 2.2: Table of eruptive formations preserved on Macauley Island	22
Table 2.3: Table displaying mean wind speeds at various pressure levels above Raoul Island	29
Table 2.4: Table summarising the measured heights of differing pressure levels recorded at Raoul Island	29

Chapter Three: Methods

Table 3.1: Key information on the appearance and habitat of each of the foraminifera used in this study	38
Table 3.2: EPMA precision and accuracy for the international glass standard ATHO measured in this study	43
Table 3.3: EPMA precision and accuracy for the international glass standard VG568 measured in this study	43
Table 3.4: EPMA precision and accuracy for the international glass standard T1-G measured in this study	44
Table 3.5: EPMA precision and accuracy for the international glass standard VG-A99 measured in this study.	44
Table 3.6: Correction factors calculated for individual analysis to correct for machine drift	45
Table 3.7: LA ICP-MS instrumental and analytical operating parameters	46
Table 3.8: LA ICP-MS precision and accuracy for international glass standard ATHO-G measured in this study	50
Table 3.9: LA ICP-MS precision and accuracy for international glass standard BCR-2G measured in this study	52
Table 3.10: LA ICP-MS precision and accuracy for international glass standard NIST612 measured in this study	54

Chapter Four: Geochemical Results

Table 4.1: Summary table of results from this study	104
---	-----

Table 4.2: Major element results for samples analysed by Shane and Wright (2011) and reanalysed in this study	105
---	-----

Chapter Five: Stratigraphic Results

Table 5.1: Grain size table adopted in GradiStat program	122
--	-----

Table 5.2: Sediment properties for each facies	123
--	-----

Table 5.3: Oxygen isotope data collected in this study and used to create an age model for the cores	125
--	-----

Table 5.4: Calculated ages for Core 4 using the reference curve from Lisiecke and Raymo (2005)	127
--	-----

Table 5.5: Calculated ages for Core 13 using the reference curve from Lisiecke and Raymo (2005)	128
---	-----

Table 5.6: Calculated ages for Core 16 using the reference curve from Lisiecke and Raymo (2005)	129
---	-----

Table 5.7: Recalculated sedimentation rates for cores investigated in this study	130
--	-----

Chapter 6: Discussion

Table 6.1 Assigned volcanic source and age of all samples analysed in this study	139
--	-----

Table 6.2 Assigned volcanic source and age of clasts	144
--	-----

List of Equations

Chapter One: Introduction

Equation 1.1 Equation detailing the components used to calculate Stokes Law 10

Chapter Three: Methods

Equation 3.1 Equation used to determine the oxygen isotope ratio 37

Acknowledgements

I would like to thank first and foremost my supervisors, Colin Wilson, Richard Wysoczanski and Helen Neil for all of their educational support throughout the duration of my thesis. Your discussions have proved invaluable. Colin, while you may have failed to make me cry you have been an excellent supervisor, always providing constructive feedback, motivation and caffeine when I needed it the most! You have kept me motivated over the years with your quirky science anecdotes and enthusiasm for volcanological research. Richard, thank you for your help making sense of all of the geochemical data, turning squiggles into meaningful (and in some cases exciting) geochemical trends. Your help with this has been invaluable, and without it I would still be glaring at Excel.

Thank you to the EQC and NIWA for providing financial and laboratory support allowing this thesis to proceed. Also to Marsden Fund of the Royal Society of New Zealand Grant VUW 0613 for providing a stipend which has been most appreciated.

Thanks must also go to Lisa Northcote for all of her help with the sediment cores, forams and lab work was much appreciated, as were the cooking tips! Alan Orpin – thank you for your help with the X-ray machine and photography out at NIWA. Helen Bostock-thank you for your excellent editing services.

To those at VUW – Ashley Pocock, George Cooper, Aidan Allan, Katy Chamberlain - thank you for your help with lab work and analysis of samples. Apologies to anyone forced to listen to me singing along to the radio during long days in the lab. Thanks must go to Gavin Dunbar for this help with constructing the age model. Thanks to Simon Barker and Melissa Rotella, for their support on the Kermadecs project and help with pulling the thesis together, and printing. Thanks also to Katie Collins for her excellent editing services. To my office mates over the years: Melissa, Chelsea, Sophie, Sarah, John and Ben – for putting up with the girly chatter, frantic editing and ‘stressed Kirsty’ you have my eternal thanks. You all made this so much more enjoyable, and provided great feedback on ideas and frustrations. To Ben thanks for your patience whilst I verbally assaulted my laptop!

To all of my friends, especially those at Mount St Flat – thank you for all of the productive study groups, dinners and most importantly motivation with which you provided me. You listened to all of my geological mutterings and bore it with fortitude – so thank you! To Sarah – I’m so lucky to have you as a friend. Knowing I had our Friday nights to look forward to always made the weeks pass much quicker. Thanks for believing in me, supporting me and for generally being amazing.

To my two families – the Cooke’s (Janelle, Gary, Tracy, Megs, Colin and Kels), thank you for keeping me laughing and introducing me to family Christmas; and the Herbert-Daniels’ (Dad, Grandad and Auntie Debs) - for all of your love and support, both financial and emotional over the past few years, it has been greatly appreciated. To my Mum, who has listened to endless conversations of unintelligible ramblings about geological processes – you are my rock. For all of the care packages, phone hugs and wise advice – thank you and I love you.

Chapter 1

Introduction

1.1 Introduction

Intra-oceanic arcs are less well documented than continental arcs, yet are important in the generation of continental crust and may present a hazard in the form of explosive eruptions. An increasing number of studies are drawing attention to the frequency and significance of silicic volcanic events and associated caldera-bearing edifices in intra-oceanic arcs, the process through which silicic magmas are generated, and the risk they present to communities. Onshore information on past eruptions is limited, however, examination of marine core material, in addition to the more common use of dredge sampling, can be used to establish the frequency and magnitude of past eruptions in oceanic arcs. In this thesis I use a case study of marine cores collected from the Kermadec arc, SW Pacific (Figure 1.1), to illustrate the value of core materials by establishing the number and compositional characteristics of tephra from silicic explosive eruptions, and to address how silicic magmas are generated in such a setting.

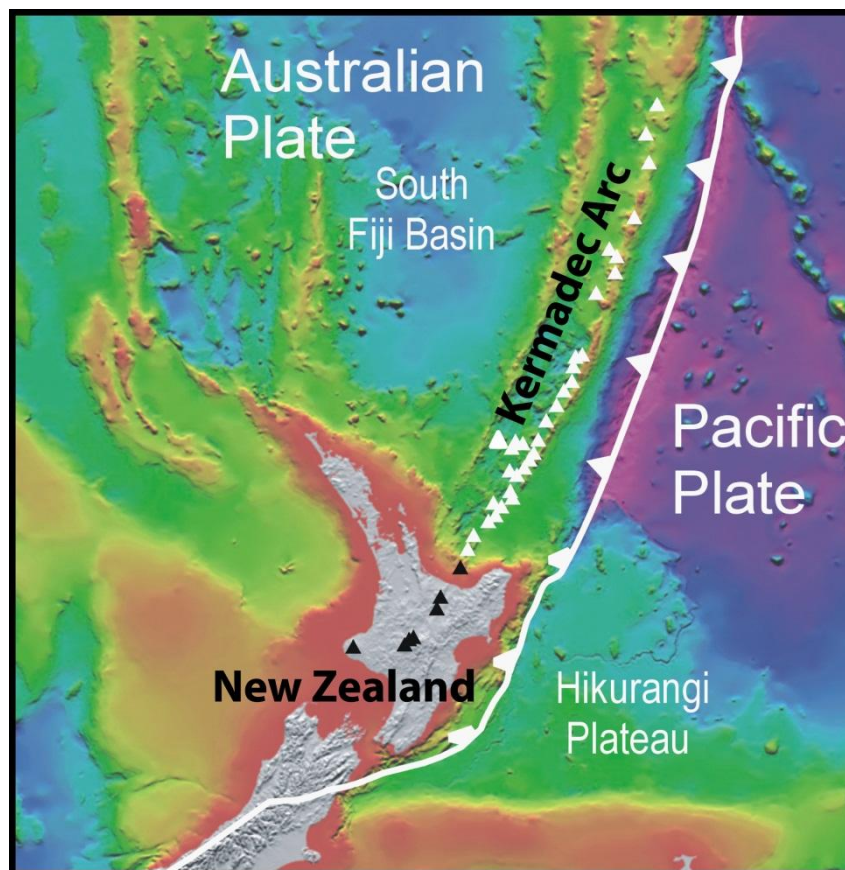


Figure 1.1 Overview of the regional setting for this study. White triangles are volcanoes of the Kermadec arc and black triangles represent volcanoes of continental New Zealand (Image courtesy of NIWA).

1.1.1 Research objectives

The aim of this study is to provide a detailed picture of Quaternary explosive volcanism in the northern Kermadec arc utilising tephrochronological methods on marine cores. These data are then used to assess eruption size and frequency and present preliminary estimations of the hazards posed by large silicic eruptions in the region.

Key research techniques include:

- Major element chemical analysis of tephra glass shards using Electron Probe MicroAnalysis (EPMA)
- Trace elements chemical analysis of glass shards using Laser Ablation Inductively Coupled Plasma – Mass Spectrometry (LA ICP-MS)
- Development of an age model for the whole depth of the marine cores using $\delta^{18}\text{O}$ analyses of foraminifera
- Development of a tephrochronology for the cores

These techniques will be used to answer the following key questions:

- A. Is silicic volcanism in the Kermadec arc a recent development, or does it pre-date records preserved onshore?
- B. Is there any cyclicity to the eruption of silicic magmas? If yes, what processes can explain this?
- C. How frequent are eruptions of a sufficient size to be preserved in the cores?

1.1.2 Thesis structure

This thesis is presented in seven chapters with additional information provided in appendices:

Chapter 1) *Introduction:* An overview of tephrochronology techniques and the research aims of this thesis.

Chapter 2) *Setting:* A background to the geological settings and location of the study area. The geological setting provides a background to the Kermadec arc and an overview of the volcanoes investigated here whilst site settings discusses the ocean current and wind characteristics of the study area.

Chapter 3) *Methods:* A description of the stratigraphic and analytical tools used to obtain stratigraphic and geochemical data. Included in this chapter are the results from secondary standards used to measure the precision and accuracy of the major and trace element data.

Chapter 4) *Geochemistry results:* Presents key geochemical results. The chapter is divided into major and trace element data, concluding with correlations between cores.

Chapter 5) *Stratigraphy results:* Presents key results pertaining to the stratigraphy of the cores including identification of facies, presentation of isotopic data, and fitting of these data to established oxygen isotope curves to provide a chronology, especially beyond the limits of radiocarbon dating.

Chapter 6) *Discussion:* An interpretation of the results is presented, focusing on a complete tephrochronology including the identification of the source volcano for each tephra and the calculation of the eruptive frequency for Raoul and Macauley volcanoes.

Chapter 7) *Conclusions:* A summary of the key findings of this study, along with proposed avenues for future work.

Appendices: A series of appendices (A-D) containing core descriptions, non – invasive properties of the marine cores, and major and trace element data collected.

1.2 Oceanic arc volcanism and the generation of silicic magmas

Intra-oceanic arcs provide a reasonably simple setting in which to study subduction zones. As there is little silicic crustal input in these areas, it is easier to understand magma-generation processes in the mantle and how continental crust is generated (Leat and Larter, 2003). Magmas of mafic and felsic compositions dominate the erupted compositions of oceanic arcs, with a distinct lack of intermediate compositions being recorded (Leat *et al.* 2003; Leat and Larter, 2003, Tamura and Wysoczanski, 2006). The eruption of silicic material in subduction settings was previously thought to be a minor phase of intra-oceanic arc volcanism, however more recent work shows that silicic volcanism can be abundant in intra-oceanic settings (Leat and Larter, 2003), and at water depths >1000 m, which was previously thought to inhibit explosive silicic eruptions (Busby, 2005).

Models for the generation of silicic magmas in this intra-oceanic arc setting have fuelled longstanding and continued debate with competing models of crustal anatexis versus crystal fractionation being proposed. For the Kermadec arc in particular, arguments for both crustal anatexis by melting of amphibolite crustal material (e.g. Smith *et al.* 2003a; 2006; 2009) and fractional crystallisation (e.g. Haase *et al.* 2006; Saunders *et al.* 2010; Barker *et al.* 2012; 2013) have been put forward to explain the presence of silicic magmas. A potentially valuable contribution to the debate on silicic magma generation in intra-oceanic arcs where there are limited subaerial exposures is to identify and analyse tephra layers preserved in marine cores. Such cores can provide a high resolution record of significant volcanic events in the region and provide an overview of the evolution of the magma system over time.

Silicic magmas in intra-oceanic arc settings are reasonably voluminous in surficial deposits and have been documented in the Izu-Bonin arc (e.g. Tamura and Tatsumi, 2002), the South Sandwich arc (e.g. Leat and Larter, 2003; Leat *et al.* 2003) and the Kermadec arc (e.g. Brothers and Martin, 1970; Brothers and Searle,

1970; Ewart *et al.* 1977; Lloyd and Nathan, 1981; Worthington *et al.* 1999; Smith *et al.* 2003a; 2006; 2009, Barker *et al.* 2012; 2013). However, because most of these records are surficial with samples collected from marine dredging, there is no stratigraphic context for the samples, unless correlations can be made to onshore dated deposits. This is one of the major strengths of using marine cores to look at eruptive material in a submarine setting as correlations can be made in tephra layers between cores to generate a detailed tephrochronology.

1.3 Kermadec arc marine core samples

Volcanism from the Kermadec arc system has been well studied with numerous expeditions undertaken in the region since the 1960's, focusing on identifying the petrological, tectonic and geophysical characteristics of the arc (see Smith and Price (2006) for a comprehensive review). In particular, with the emergence of multibeam mapping, numerous submarine volcanic cones have been discovered since the 1990's (Wright *et al.* 2006; Graham *et al.* 2008; Wysoczanski *et al.* 2010; Barker *et al.* 2012) and the focus was again drawn to the system as a whole as a type-example of intra-oceanic tectonic subduction.

There are two significant subaerial outcrops along the length of the arc: Raoul and Macauley Islands. These islands are the emergent parts of large strato-cone volcanoes that record volcanism in the arc dating back to *ca.* 1.5 Ma (Lloyd and Nathan, 1981). There are other subaerial exposures along the length of the arc (Smith *et al.*, 1988), but these are much small in size and will not be addressed in this study. On the R.V *Tangaroa* TAN0706 voyage (May 2007), sediment core retrieval for 19 sites was attempted, with 10 sediment cores successfully collected from both the forearc and back-arc regions surrounding Raoul and Macauley Islands (Figure 1.2) (Table 1.1). Retrieval of some material from sites C7, C9 and C12 (Figure 1.2) was analysed and data is presented in Chapter 4. Multibeam mapping using the Kronsberg EM300 echosounder and multi-channel seismic reflection mapping undertaken on the same and earlier voyages shows that the bathymetry to the west of the islands slopes down from the Kermadec Ridge to the Havre Trough, and on the east slopes down to the Kermadec Trench (Figure 1.2). Piston and gravity coring methods were used, with penetration limited by the presence of resistant layers of coarse volcanic ash and lapilli material. As such the longest records are more distal to the islands, with the longest core collected measuring 309.5 cm in length. A preliminary study of these cores by Shane and Wright (2011) found evidence for 27 discrete macroscopic tephra layers as well as numerous heterogeneous tephra layers with records extending back beyond 50 ka. This study reanalyses these cores and presents a more detailed tephrostratigraphy, which is then used to determine the frequency and size of eruptions in the region, as well as to provide first order insights into silicic magma generation.

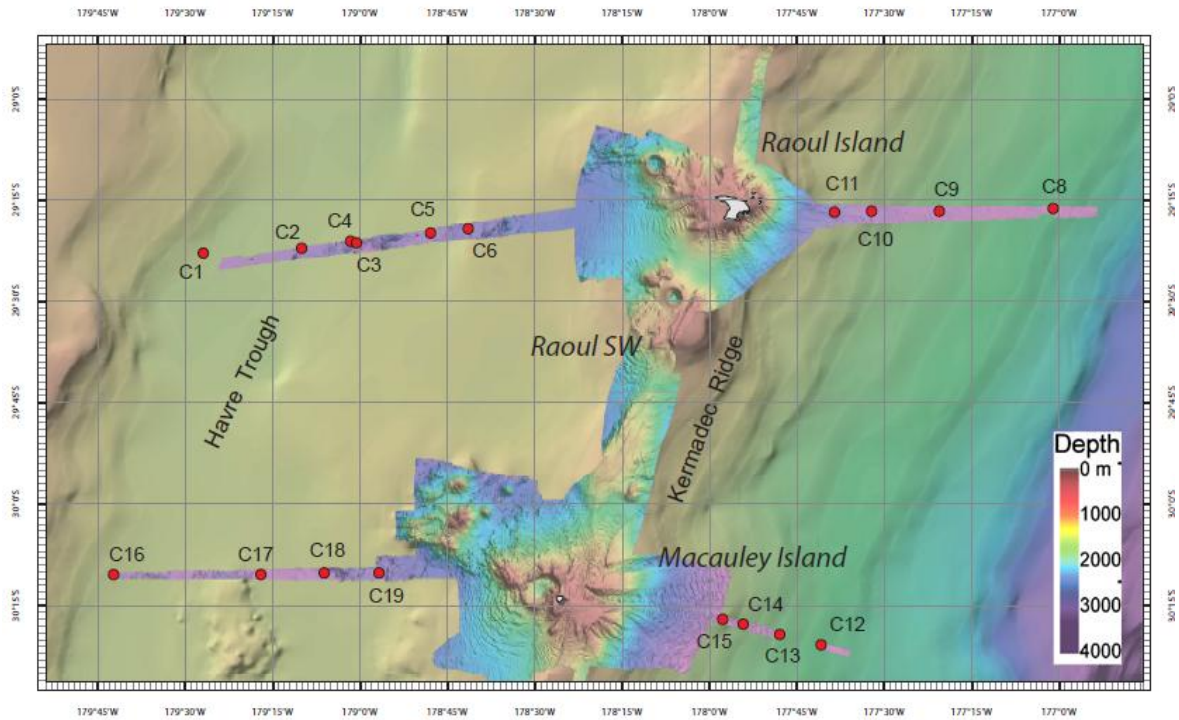


Figure 1.2. Bathymetry surrounding Raoul Island, Raoul SW and Macauley Island in the Kermadec arc as well as the location of core sites examined in this study (see Table 1.1 below). EM300 multibeam mapping extends west and east of the island illustrating the complex bathymetry in greater detail. (Image courtesy of NIWA). Note that material retrieved for C7 is located in the same position as C8.

Table 1.1 Location and water depth for each of the marine cores successfully retrieved on the R.V *Tangaroa* TAN0706 voyage and studied in this thesis.

TAN0706 Station Data				
Station	Gear	Water depth (m)	Latitude	Longitude
TAN0706 - 1	Piston	2550	29 22.917 S	179 27.044 W
TAN0706 - 2	Piston	2430	29 22.247 S	179 10.195 W
TAN0706 - 3	Piston	2144	29 21.326 S	179 00.818 W
TAN0706 - 4	Gravity	2258	29 21.190 S	179 01.699 W
TAN0706 - 5	Gravity	2424	29 19.897 S	178 47.999 W
TAN0706 - 8	Piston	3350	29 16.260 S	177 00.971 W
TAN0706 - 9	Gravity	3065	29 16.726 S	177 20.571 W
TAN0706 - 10	Gravity	2654	29 16.719 S	177 32.170 W
TAN0706 - 12	Gravity	3721	30 20.768 S	177 40.877 W
TAN0706 - 13	Gravity	3288	30 19.235 S	177 48.057 W
TAN0706 - 15	Gravity	2574	30 17.066 S	177 57.738 W
TAN0706 - 16	Piston	2353	30 10.404 S	179 42.534 W

1.4 Tephrochronology

The definition of tephra encompasses all explosively generated, unconsolidated pyroclastic materials up to a size of 64 mm, and includes both fall and flow deposits (Shane, 2000; Lowe, 2011). The definition of tephrochronology *sensu stricto* refers to using tephra layers as isochronous layers to connect together sequences, allowing for the transferral of determined ages (relative or numerical) between cores (Westgate and Briggs, 1980; Shane, 2000; Pearce *et al.*, 2004; Lowe, 2011). Tephrostratigraphy is the study of the distribution and stratigraphic relationships of tephra layers and associated materials within a single core, including their relative and numerical ages (Lowe, 2011). Once the tephrostratigraphy for each core has been determined, a tephrochronology can be constructed using methods to determine the physical, geochemical and mineralogical properties of tephra layers, as well as determining an age for each layer where possible. Stratigraphic relationships, major and trace element geochemistry, glass morphology and mineral assemblages can be used to establish correlations (Kennett and Huddleston, 1972; Lowe, 2011).

In general, the principles of constructing a tephrochronology have been well studied and documented. Major element concentrations of glass shards have primarily been the method used to geochemically correlate tephra layers. While trace elements have been used for decades when analysing deep-sea tephra layers (e.g., Bowles *et al.*, 1973) it has only recently been more widely recognised that trace elements are often crucial in distinguishing between tephra layers with nearly identical major elements. Trace element concentrations may show variations of orders of magnitude in tephra layers with similar major element compositions, making correlations much easier and more accurate (Bowles *et al.*, 1973; Allan *et al.*, 2008). They can also provide insights into chamber dynamics and magma evolution over time. This study utilises stratigraphic position and both major and trace element geochemistry to correlate tephra layers.

Tephra layers are erupted and deposited almost instantaneously in terms of the geological time scale. Layers deposited in the deep-sea tend to be a few to tens of centimetres thick and are predominantly composed of glass shards up to a few hundred microns in diameter with scattered crystals and lithic fragments interspersed throughout (Manville and Wilson, 2004). These tephra layers often display sharp basal contacts and gradational or bioturbated upper contacts (Fisher and Schmincke, 1984). Previously only macroscopic tephra layers (visible to the naked eye) could be identified and studied, but as new methods of non-invasive analysis have developed, microscopic tephra layers (cannot be seen with the naked eye) can now be identified which allows for much more detailed and well-constrained volcanic histories to be constructed. In this study many macro and microscopic tephra layers were identified using techniques outlined below.

1.4.1 Stratigraphy

The stratigraphy of marine cores can be established using some or all of the following methods:

- a) Core descriptions
- b) Magnetic Susceptibility
- c) Spectrophotometer readings
- d) Grain Size analysis
- e) Carbonate Content
- f) Laser Grain Size analysis
- g) X-ray Imagery
- h) Photography
- i) Oxygen Isotope analysis
- j) Radiocarbon dating
- k) Tephra correlations
- l) Paleomagnetism

This study uses the methods a to k listed above to construct a detailed stratigraphy for each of the cores.

Much of the material in marine tephra layers is juvenile volcanic material, which over time, and exposure to processes such as sediment reworking or bioturbation, may become contaminated with other material such as detrital sediment (Westgate and Briggs, 1980; Froggatt, 1983; Westgate *et al.*, 1994; Pearce *et al.*, 1996). For this reason bulk analysis methods such as X-Ray Fluorescence are unsuitable, as any contaminants will lead to inaccuracies. Analysis using grain specific methods such as EPMA and LA ICP-MS allows individual glass shards to be examined, with the shards representing the pure glass phase of the melt (Pearce *et al.*, 2004). A benefit of this method is that single glass shards are analysed, so the amount of sample required is very small when compared to bulk analysis methods (Westgate *et al.*, 1994). It also allows the identification of compositional heterogeneities in the melt, which may indicate that complex processes contributed to the chemical variations in the parental magma chamber.

1.4.2 Dating techniques

Different dating methods can be used to establish stratigraphic relationships in cores, those used in this study being radiocarbon dating, oxygen isotope analysis and sedimentation rates. Radiocarbon dating is useful for dating material preserved in marine cores from the past 50,000 years. Most of the material that is used for dating tephra in marine cores is organic detritus which must be carefully selected (Calderoni and Turi, 1998). The ideal material for the ¹⁴C dating is material such as charcoal or organic detritus preserved within the tephra layer itself. However the most common source of material for carbon dating in marine cores is microfossils preserved in the bracketing sediments. The carbon dates used in this study were obtained by processing selected species of planktic foraminifera at the Rafter Laboratories at GNS Science, New Zealand and were published by Shane and Wright (2011).

The abundance of foraminifera tests in marine sediments makes them an ideal material for analysis for several parameters that can act as proxies for age determinations. Since the oxygen isotope ratios of

foraminifera tests were discovered to be of use in constructing marine core stratigraphies, this tool has become standard when correlating and dating deep sea sediments (Emiliani, 1955; Shackleton and Opdyke, 1973; Jansen, 1989). The oxygen isotope values of the tests can be used to construct an oxygen isotope curve which can be correlated with existing global oxygen isotope curves exhibiting globally synchronous events (Jansen, 1989). As the oxygen isotope content of foraminifera tests varies between glacial and interglacial cycles (in response to oxygen isotopic changes in the sea water), age-depth models can be created where isotope stage boundaries can be distinguished and ages established in tandem with other absolute dating techniques (Jansen, 1989; Weaver *et al.* 1998). In deep sea cores, however, the preservation potential of foraminifera tests is an issue as tests recovered often show signs of breakage and dissolution as a result of predation and the effects of mildly acidic water (Hayward *et al.*, 2010). There are two ecological 'types' of foraminifera; planktics which live in the water column and infaunal benthics which burrow into bottom sediments. Benthic tests are more resistant to dissolution than those of their planktic counterparts, which is reflected in the degree of preservation of tests. This is more marked below the lysocline, which in the Pacific Ocean lies at *ca.* 3500 m water depth (Douglas and Woodruff, 1981). Different benthic foraminifera are associated with different water bodies and depths. In the Pacific Ocean the two benthic foraminifera used in this study, *Cibicides mullerstorfi* and *Uvigerina peregrina* are associated with bottom waters and can be found at differing depths (Douglas and Woodruff, 1981; McCave *et al.*, 2008). Bottom waters in the study area are a mix of upper Circumpolar Deep water and North Pacific Deep water (Bostock *et al.*, 2011).

An important indirect method of establishing age estimates in core stratigraphy and for tephras is through inferring the rates of sedimentation for the non-tephra material. This can be subject to significant errors due to fluctuating sedimentation rates between glacial and interglacial cycles and mass wasting events which deposit significant amounts of material in relatively short timeframes. Sedimentation rates in the southern Kermadec arc region show large fluctuations between glacial/interglacial cycles, with much more sediment, derived from the New Zealand landmass, being deposited during glacial cycles (Pillans and Wright, 1992). Sediment input in the study area for this thesis is, however, more limited due to its greater distance from substantial landmass. However during glacial periods when sea level falls the sedimentation rate could still increase, resulting in problems for the approximate tephra ages published by Shane and Wright (2011), which were dependent on estimated sedimentation rates.

Sedimentation rates are also important in the preservation and recognition of individual tephra layers as these are easier to distinguish as a discrete event when separated by a thickness of sediment. Tephra fallout from the atmosphere can occur within days if the material remains in the troposphere and is washed out (Oberhuber *et al.*, 1998). An issue with this pertains to the settling rates of different volcanic material through the water column. Stokes Law allows the settling velocity of particles to be calculated based on Equation 1.1. Using this equation in experiments led to the discovery that generally the fastest settling particles are large, heavy and spherical and the slowest settling particles are irregularly shaped and

***Stokes' law is given by :**

$$v = \frac{2}{9} r^2 \frac{(\sigma_1 - \sigma_2)}{n} g$$

v = settling velocity of particle
 r = radius of particle
 σ_1 = density of particle
 σ_2 = density of fluid
 n = viscosity of fluid
 g = acceleration due to gravity

small. The general principle is that in water where currents are faster than the settling velocity you would expect the particle to be transported further laterally than vertically over time. Experiments by Fisher (1965) indicate that layers may become mixed due to differential settling rates of various volcanic products and that only very fine grained particles follows the settling velocity outlined by Stokes Law (Fisher, 1965). This is an important consideration when interpreting any heterogeneous tephra layers.

Normally graded tephra layers may represent a near-instantaneous eruption, as the water column works to separate particles based on their settling velocity. In longer or intermittent eruptions complex grading is often observed as delivery of particles is more continuous (Ledbetter and Sparks, 1979). However this does not take into account particle aggregation as discussed below. The grain size of a deposit is a complex function of the distance from source, explosivity of the eruption and atmospheric conditions (Carey, 1997).

Settling time through the ocean plays an important role in the location and thickness of tephra deposits. While it was initially thought that ocean currents would disperse tephra delivered from above, research has found that particle aggregation often occurs readily, and the tephra shards join together to form particulate aggregates which settle out to the ocean floor more rapidly than individual shards (Shaw *et al.*, 1974; Carey, 1997). Accretionary lapilli associated with phreatomagmatic eruptions would settle through the ocean more rapidly, before breaking up upon reaching the sea floor (Fisher and Schminke, 1984). Another process affecting tephra deposition is that of vertical gravity currents. When tephra reaches the air-water interface the settling velocity decreases dramatically and the surface layer of water becomes loaded with tephra. This creates a diffuse vertical gravity current which transports the tephra particles rapidly down towards the sea-floor at velocities that are one to three orders of magnitude faster than that observed by Stokes-law settling (Fisher, 1965; Carey, 1997; Manville and Wilson, 2004). The rapidity of this process minimises the effects of currents on tephra dispersal and highlights the dominance of wind directions in determining the distribution of tephra (Carey and Sigurdsson, 1980; Carey, 1997).

The dispersal of volcanic material from a plume is strongly controlled by prevailing winds, the height to which the plume ascends (Wilson and Walker, 1987; Sparks *et al.*, 1997), and other factors such as ocean currents and bathymetry must be considered when looking at tephra deposition (Shane, 2000); these factors will be discussed further in Chapter 2. Important factors which need to be considered are bioturbation, turbidity flows, remobilisation of sediments and preferential deposition of tephra due to wind and current controls.

1.4.3 Tephrochronology in the Kermadec arc

The only significant subaerial exposures in the Kermadec arc are on Raoul and Macauley islands, the emergent portions of volcanoes which have produced large silicic eruptions. Raoul Island and Macauley Island have been widely studied, with the onshore exposures yielding some of the only information we have on the history of the arc. Outcrop exposures on Raoul Island display the oldest volcanic eruptive units, which were erupted >1 Ma (Lloyd and Nathan, 1981). Macauley Island hosts much younger units, and the island is dominated by the deposits of a single eruption, the Sandy Bay Tephra (SBT), which erupted approximately 6.3 ka ago (Lloyd *et al.*, 1996). The petrology of the arc is generally considered to be relatively simple for a volcanic arc; however an interesting shift from predominantly basalt-basalt andesite volcanism to more silicic dacite and rhyolitic eruptions occurs on Raoul Island at 3.7 ka (Lloyd and Nathan, 1981; Smith *et al.*, 2006). As the eruptive record is relatively young, we cannot see if this is a unique change in the history of Raoul volcano, or if it is part of a cyclical evolution of magma compositions. One way to address this is to construct a tephrochronology from marine cores collected offshore from Raoul and Macauley islands, which provide a more detailed volcanic history and allow us to look at the composition and frequency of eruptions as recorded in the cores over a longer time period than that available from the terrestrial record.

Two studies have been conducted on sediment cores from the Kermadec arc. The first was conducted on cores from around the Kermadec islands by Ninkovich (1968) as part of a broad exploration of tephra in the SW Pacific. Unfortunately there is no geochemical data from these layers and the youngest macroscopic tephra layers were dated to *ca.* 0.31 Ma, which is older than the cores examined for this thesis. The second tephrochronology study in the Kermadec arc used the same cores that are studied in this thesis and has been published by Shane and Wright (2011). They found that the core record extended beyond 50 ka, including 27 macroscopic tephra layers ranging in thickness from <1 cm to *ca.* 50 cm. Major elements of glass from samples were determined and it was found that samples displayed either distinctly medium-K (labelled as high-K in their study) or low-K trends. Compositional bimodality was identified for many samples and was attributed to incomplete magma mixing. Heterogeneous tephra layers were also identified and attributed to one or more of: (a) the slow sedimentation rates which would not allow for separation of separate events by a sediment horizon, (b) bioturbation, or (c) vertical mixing of tephra after deposition (Shane and Wright, 2011). The most heterogeneous tephra layers were explained as near-contemporaneous eruptions from two or more volcanoes. Three discrete tephra layers were proposed to have correlatives in numerous cores; a layer identified as the SBT was found in five cores, and two other correlative tephra layers were found in two cores (see Figure 1.3). After identifying these correlatives, they conclude that there are a total of 11 low-K affinity and 12 high-K affinity tephra layers, each of which are considered to represent an individual event. From examination of rocks in the subaerial records of Raoul and Macauley islands, Shane and Wright (2011) observed that the volcanic eruptives of Raoul show low-K trends and those of Macauley Volcano display a high-K trend. Based on this observed trend, tephra layers were assigned a source volcano based on K₂O content.

The source of the tephra layers identified in the study conducted by Shane and Wright (2011) were attributed to Raoul and Macauley islands almost exclusively. They examined the potential of other submarine volcanoes in the region to be the source of tephra layers and found a more distant source to be “less likely” due to the water depth above the volcanoes requiring an “exceptionally large eruption” to produce a plume of a sufficient size to deposit tephra (Shane and Wright, 2011). Wind and current directions in the region would also inhibit the preservation and dispersal of tephra to the core sites from these submarine volcanoes. Tephra layers in the cores to the west of the islands were the result of ash cloud dispersal and subsequent water column fallout while some of those to the east of the islands could have been sourced from turbidites and represent the fine-grained distal deposits from a turbidite or from turbidite suspension clouds (Shane and Wright, 2011).

The SBT received much attention in their study, as it was the only tephra layer which could be confidently correlated between cores and correlated to onshore deposits. The tephra was traced in cores one, three, five and thirteen with the deposit being classed as thickest in Core 13 where it was identified as being 13 cm thick as illustrated in Figure 1.3. They also revised the age of the eruption from 6310 ka as published by Lloyd *et al.* (1996) from onshore organic matter to 5.7 ka based on radiocarbon ages obtained from the cores, stratigraphic positioning of tephra layers in the cores and sedimentation rates. This age revision will be addressed in Chapter 5.

This study re-examines the cores initially examined by Shane and Wright (2011) in greater detail and presents new findings, using a wider range of analytical techniques.

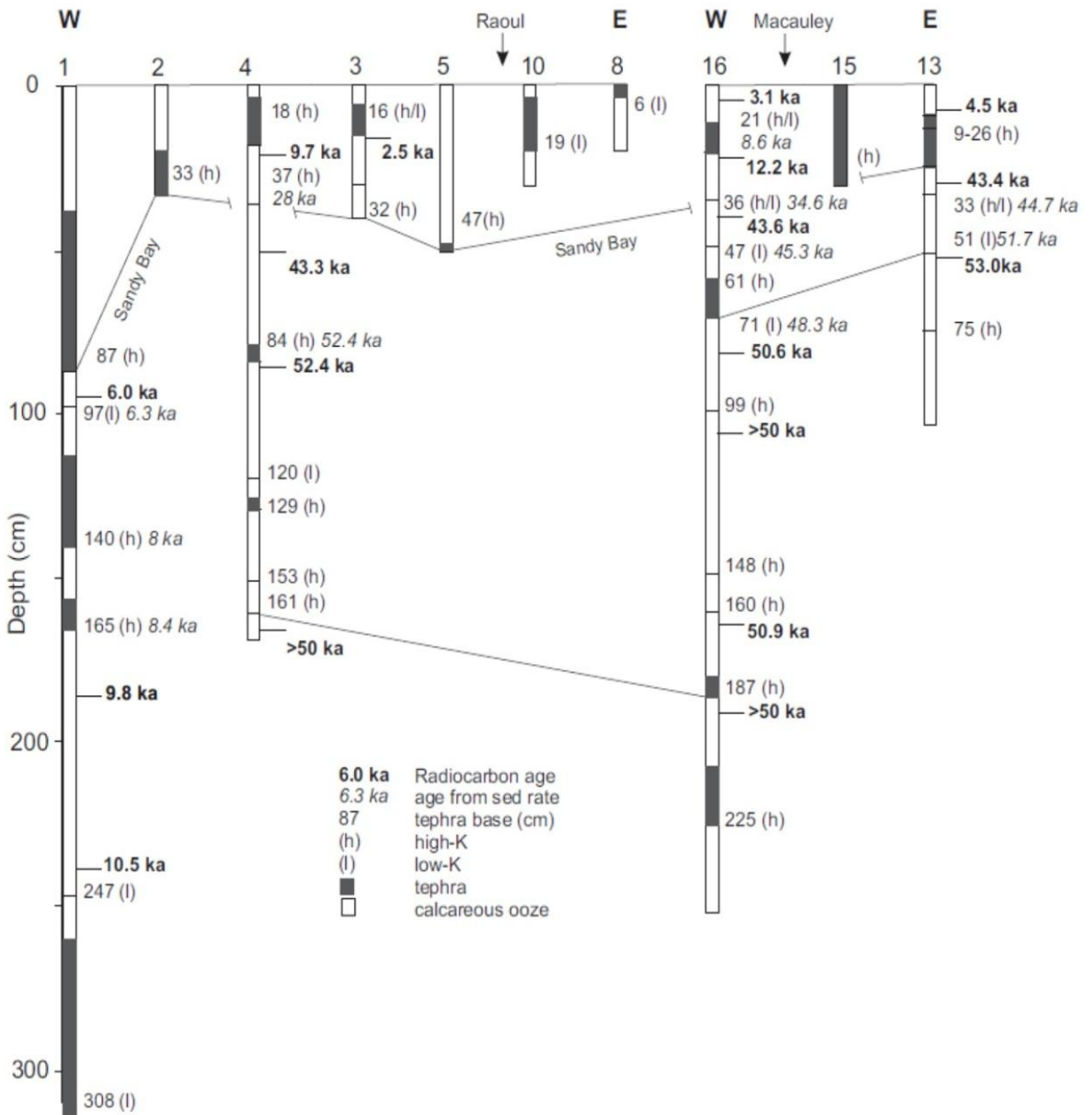


Figure 1.3 Tephrochronology published by Shane and Wright (2011) showing correlations between cores and also the SBT. The radiocarbon ages are presented in bold and have been calibrated using the CalPal_2007_HULU curve and have the marine reservoir age subtracted, with the calculated sedimentation rate ages in italics.

Chapter 2

Setting

2.1 Regional overview

2.1.1 The Kermadec arc

The Tonga-Kermadec-New Zealand island arc volcanic system extends some 2800 km from the continental volcanic province of the Taupo Volcanic Zone (TVZ) in New Zealand to the intra-oceanic island arc volcanic province of Tonga (Ewart *et al.*, 1977). The Kermadec arc stretches nearly 1500 km offshore from the TVZ to 25.6°S, where the Louisville Ridge intersects the Pacific–Australian plate subduction zone at the Kermadec Trench. The volcanoes of the active Kermadec arc are spaced at intervals of 30–50 km along the Kermadec Ridge, with a total of 40 known volcanic edifices along the length of the arc (Graham *et al.*, 2008). Raoul, Macauley, Curtis and L'Esperance islands between *ca.* 29°S and 31°S are the only partially emergent volcanoes along the arc. Many of the volcanoes fall along ESE trending ridges, normal to the NNE trend of the Kermadec Ridge, interpreted to reflect a structural control over the location of the volcanoes along the arc (Lloyd *et al.*, 1996; Worthington *et al.*, 1999; Campbell *et al.*, 2007). The distance from the subduction zone to the associated volcanic front is controlled by the angle of the subducting slab, which steepens northwards (Graham *et al.*, 2008). The arc front is *ca.* 300 km from the trench at 37°S and *ca.* 185 km at 32°S. Parallel to the Kermadec arc is the remnant Colville arc; both were contiguous until back arc spreading, as a result of slab rollback, began at approximately 4 Ma to develop the Havre Trough (Wright, 1993; Wright *et al.*, 1996; Graham *et al.*, 2008). The Colville and Kermadec ridges are now separated by some 130 km at the 2000 m isobath (Wright, 1993).

The onset of arc activity in the SW Pacific has been attributed to changes in plate motion which led to an increase in plate convergence at around 25 Ma (Ballance *et al.*, 1999). Convergence rates increase northwards along the ridge away from the Pacific-Australian pole of rotation with rates of convergence of 53 ± 1 mm yr⁻¹ at 35°S, 58 mm yr⁻¹ at 32°S and 66 mm yr⁻¹ at 28°S (DeMets *et al.*, 1990; Wallace *et al.*, 2009). The differences between the rates are accommodated by back-arc extension in the Lau-Havre-Taupo rift systems (Smith and Price, 2006).

Volcanism in the southern Kermadec arc is dominated by basaltic to basaltic-andesitic volcanism, whereas north of 32°S, volcanism is dominated by more silicic (SiO₂ >63%), explosive, caldera forming eruptions, recorded especially in younger deposits (Ewart *et al.*, 1977; Brothers and Martin, 1980; Lloyd and Nathan, 1981; Graham *et al.*, 2008). The petrology of the Kermadec arc displays wider geochemical variability than the Tonga arc to the North (Ewart *et al.*, 1977). Overall, sampled eruptive units of the Kermadec arc display bimodal compositions with basaltic-andesites and dacites dominating the petrology of the arc (Tamura and Wysoczanski, 2006; Graham *et al.*, 2008). Magmatism in the northern Kermadec arc is recognised as being relatively hybrid in nature, with short residence times in the crust illustrated by the presence of numerous xenoliths, xenocrysts and also disequilibrium textures (Graham *et al.*, 2008). Trace element data show that the Kermadec arc volcanic rocks have a determinable sediment subduction signature which decreases northwards with distance from the New Zealand landmass (Gamble *et al.*, 1996; Ewart *et al.*, 1998). The most complete record available of Kermadec arc eruptive units is on Raoul and Macauley islands, which have been extensively studied (Brothers and Martin, 1970; Brothers and Searle, 1970; Ewart *et al.*, 1977; Lloyd and Nathan, 1981; Worthington *et al.*, 1999; Smith *et al.*, 2003a,b; 2006; 2009, Barker *et al.*, 2012; 2013). Much work has been conducted on subaerial deposits, but little on those from the seafloor.

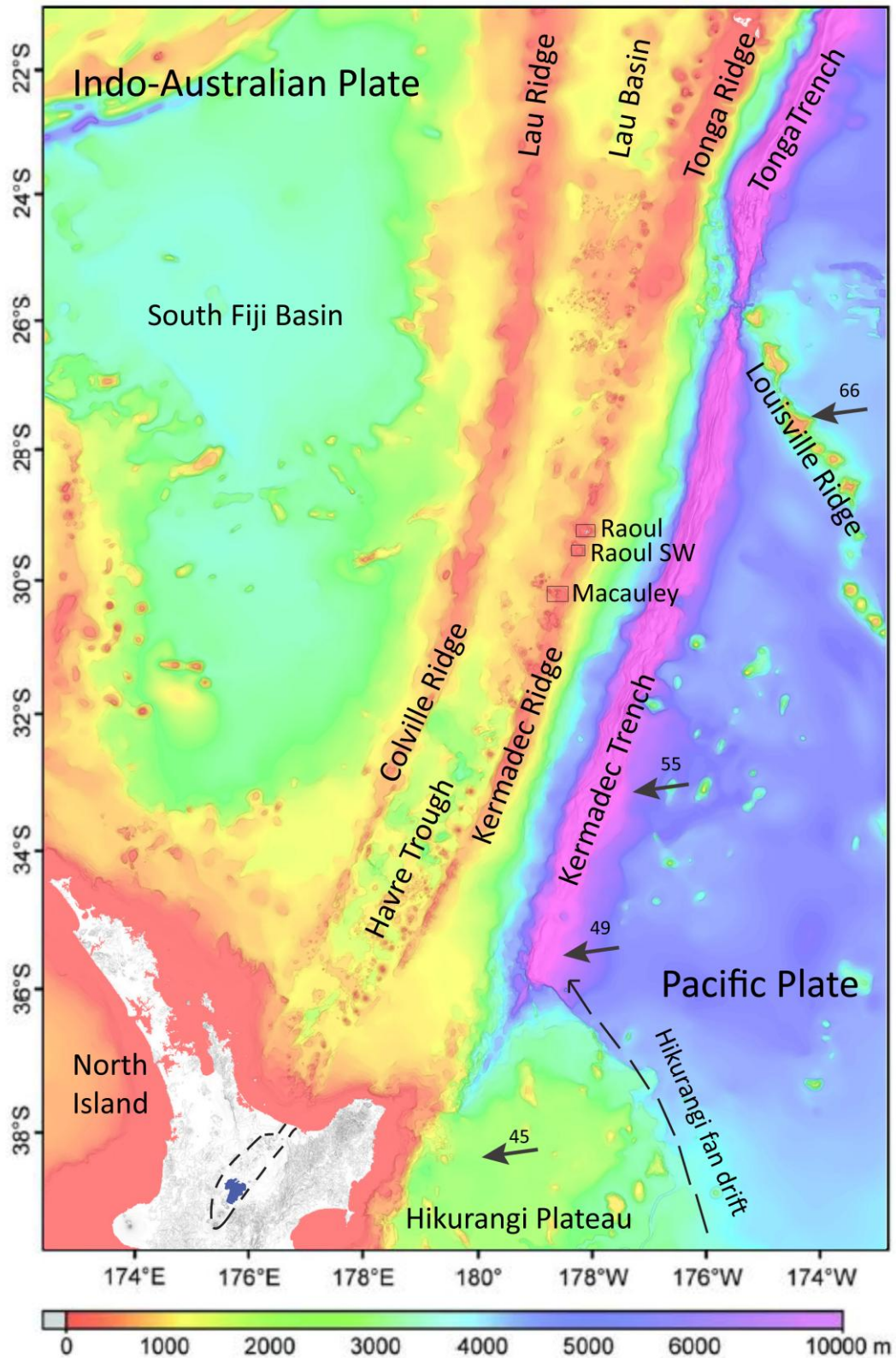


Figure 2.1. Regional setting of the Tonga-Kermadec-TVZ subduction system. Relative plate motions (mm/yr) are represented by arrows, taken from Wallace *et al.*, (2009) following from DeMets *et al.* (1994). The modern TVZ outline is taken from Wilson *et al.*, (1995). The direction of sediment drift (Hikurangi fan drift) is adapted from Carter and McCave (1994) and Carter *et al.* (1996). The volcanoes in this study are outlined in squares.

The 2007 voyage of the RV *Tangaroa* collected both dredge samples from the seafloor surrounding Raoul and Macauley islands, as well as from a newly discovered volcanic edifice referred to as Raoul SW in this study (following Barker *et al.*, 2012). Both of these volcanoes have produced large silicic eruptions during the Holocene, associated with caldera formation (Lloyd and Nathan, 1981; Lloyd *et al.*, 1996). The tephra layers preserved in these cores will allow us to produce a more detailed picture of silicic volcanism in the region extending back to >50 ka, giving a detailed history of silicic volcanism in the region to be pieced together. Descriptions of the volcanoes are as follows.

2.1.2 Raoul Volcano

Raoul Island is located 1155 km north of Auckland (Worthington *et al.*, 1999) and is the northernmost and largest subaerial exposure in the Kermadec arc. The island rises to 520 m above sea level and is the 29.4 km² subaerial exposure of the larger Raoul stratovolcano, which has a volume of 214 km³ and dimensions of 28 by 20 km at the 900 m isobath (Brothers and Searle, 1970; Ewart *et al.*, 1977; Worthington *et al.*, 1999; Smith *et al.*, 2006). The island provides relatively detailed exposures of 8 eruptive groups (Lloyd and Nathan, 1981) dating back to *ca.* 1 Ma, ranging from the Boat Cove Formation (earliest) to more recent deposits (Table 2.1).

Early development of the stratocone was founded atop submarine volcanic and calcareous sediments, dated to *ca.* 1 Ma, with the early formations consisting of basalt to basaltic-andesite successions. The early stages of volcanism on Raoul are tholeiitic basalts and basaltic-andesites, which dominated until 3.7 ka when silicic, caldera forming volcanism became more predominant (Brothers and Searle, 1970).

The largest calderas, Denham and Raoul, are slightly elongated in the NE-SW direction, perpendicular to the principle extension axis of the Kermadec arc. Raoul Caldera has dimensions of 3 x 2 km² and formed as a result of the Matatirohia and Oneraki eruptions; other formations erupted from this caldera are the Green Lake, Blue Lake and Tui Lake as listed in Table 2.1. Denham Caldera has dimensions of 6.5 x 4 km and >300 m depth and formed as a result of the voluminous Fleetwood eruption at 2.2 ka of *ca.* >8 km³ of dacitic material (Lloyd and Nathan, 1981; Worthington *et al.*, 1999; Smith *et al.*, 2006).

Volcanism from Raoul Volcano is relatively frequent, with numerous eruptions observed since the 1800s (Healy *et al.*, 1965; Lloyd and Nathan, 1981). The onshore exposure records only the most recent subaerial eruptions, and only those which are large enough or erupted in favourable conditions to be preserved. To date *ca.* 15 km³ of dacitic material has been erupted since 3.7 ka (Worthington *et al.*, 1999; Smith *et al.*, 2006).

EM300 mapping on the flanks around Raoul Island found evidence for mass wasting events with submarine landslides from large volume failures. Many of the flows observed were up to 1.5 km in width and had run-outs of up to 12 km (NIWA, 2007). Most of these flows originated from the shelf break at around 120 m water depth. Two new caldera volcanoes were discovered through the EM300 mapping, one to the NW and the other to the SW of Raoul Island. The north-western caldera has a diameter of 4 km, with caldera walls up to 1000 m high and displays evidence of hydrothermal venting (NIWA, 2007). The south-western caldera, Raoul SW, is outlined in section 2.1.4.

Figure 2.2 Map of Raoul Island showing the main caldera locations. Contours are at 40m intervals. The outline for Denham Bay is taken from Worthington *et al.* (1999). Adapted from Lloyd and Nathan (1981).

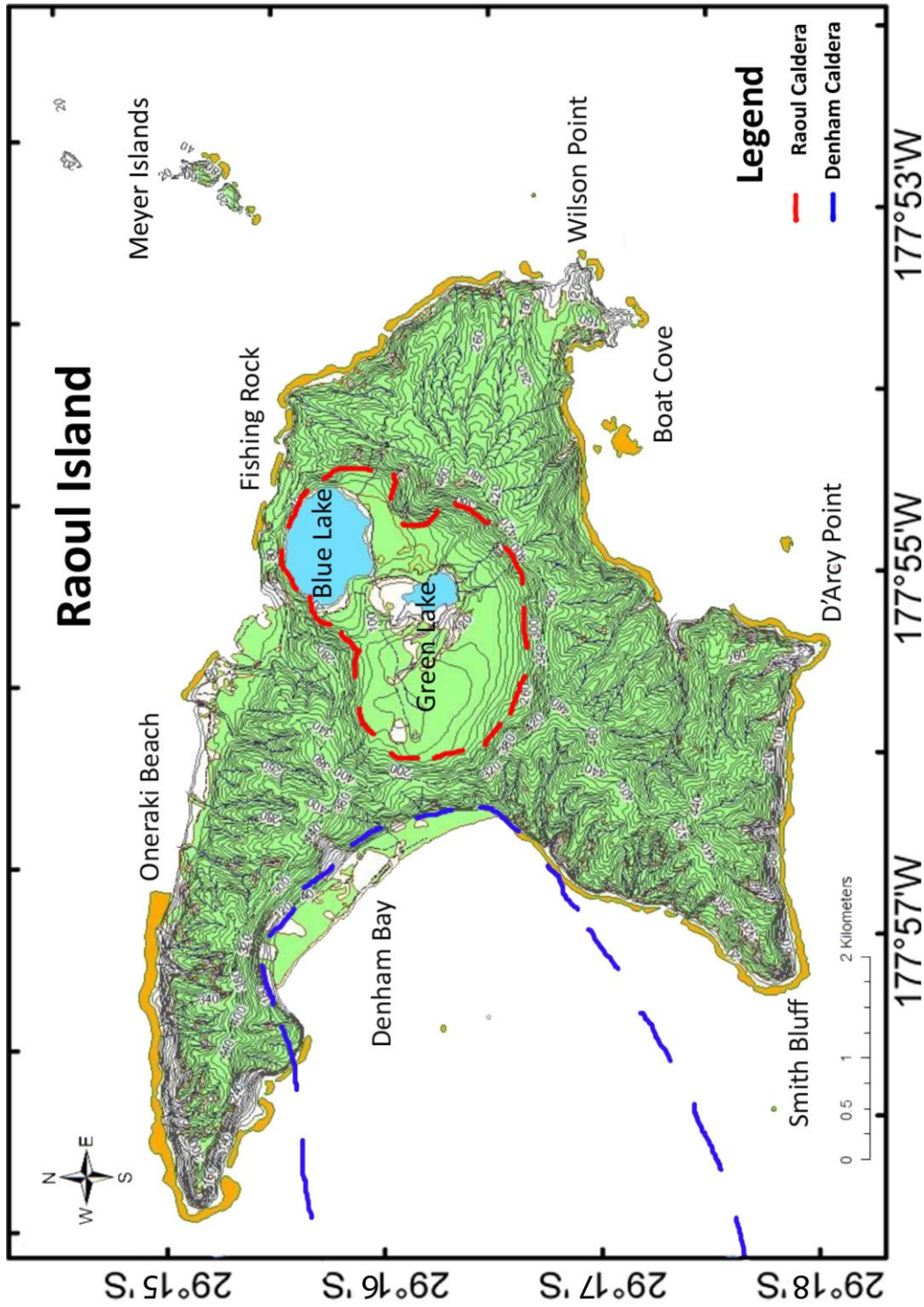


Table 2.1 Summary of eruptions from Raoul and Denham calderas. Adapted from Brothers and Searle, 1970; Lloyd and Nathan, 1981; Worthington *et al.*, 1999; Barker *et al.*, 2012.

Formation	Age (ka)	Vent location	Eruption description
<i>Ngaio Group</i>			
[2006 breccia]		Raoul Caldera	
1964 breccia		Green Lake (Raoul caldera)	Phreatic
1872 (observed)		Green Lake (Raoul caldera) and Denham Caldera	Phreatomagmatic
1814 (observed)		Denham Caldera	Phreatomagmatic
Smith Breccia	0.18	Raoul Caldera	Phreatic
Tui breccia	(0.28)	Raoul Caldera	Phreatic
Sentinel	0.28	Denham caldera?	Small pumiceous dacite
Rangitahua	0.37	Raoul Caldera	Small; pumiceous dacite, pyroclastic cone
Meyer	(0.5)	Meyer Islands	Small, scoriaceous basaltic andesite
Expedition breccia	1.1	Raoul Caldera	Phreatic
Pukekohu breccia	(1.25)	Raoul Caldera	Phreatic
Green Lake pumice	1.4	Raoul Caldera	Medium, pumiceous dacite
Floated pumice		Raoul caldera	Dacite pumice, floated from crater lake dome
Rayner	(1.55)	Raoul Caldera	Small, pumiceous dacite
Judith	(1.85)	Raoul Caldera	Medium, scoriaceous basaltic andesite
Bell	(2.05)	Denham Caldera?	Small pumiceous dacite
Fleetwood	2.2	Denham Caldera	Voluminous pumiceous dacite, pyroclastic flows
Oneraki	3.15	Raoul Caldera	Large, pumiceous dacite, pyroclastic flows
Matatirohia	3.7	Raoul Caldera	Large, pumiceous dacite, pyroclastic flows
Older Formations		Description	
Moumoukai	(4 - 10)	Basaltic andesite flows and pyroclastic deposits, stratocone formed, now cut by Raoul caldera	
Hutchison	(50 - 100)	Basaltic andesite flows, debris flows, fall and pyroclastic flow deposits. Stratocone built near current day Denham caldera	
D'Arcy	(100 - 200)	Basalt and basaltic andesite flows with interbedded pyroclastic deposits	
Boat Cove	600 - 1400	Pillow basalt, hyaloclastite and calcareous sediments outcropping, possibly formed stratocones	

The age of the Boat Cove volcanics was determined using K-Ar dating. The ages for the Ngaio group were determined using ¹⁴C dating. Those eruptives of the Ngaio group with ages in brackets were determined taking into account paleosol thicknesses (Lloyd and Nathan, 1981).

2.1.3 Macauley Volcano

Macauley Island is situated approximately 100 km south of Raoul Island and represents the tip of an otherwise submerged caldera volcano. The island itself is relatively small (3 km²) when compared to the submarine edifice which occupies 380 km² at the 900 m isobath (Figure 2.3: Lloyd *et al.*, 1996). The highest part of the island is Mount Haszard at *ca.* 238 m above sea level. Macauley Island is situated on the southeast rim of the submarine Macauley Caldera, which has a *ca.* 12 km diameter and reaches depths of *ca.* 1.1 km (Lloyd *et al.*, 1996). Access to the island is limited, as most of the shoreline consists of steep cliff sections. These preserve a partial record of the erupted units, described by Brothers and Martin (1970) and summarised in Table 2.2. These cliff sections reveal that the pre-caldera volcanic centre was subaerial and has erupted a variety of volcanic material (Brothers and Martin, 1970). North Cliff Aa lava flows are interpreted as forming an early stage of subaerial shield growth from a vent location just to the north of the island. The unit reaches up to 15 m above sea level, with much of the unit extending below sea level. Shortly after the effusive North Cliff Formation ceased, the Boulder Beach Formation was erupted as sequences of basaltic fall, surge and ballistic deposits (Lloyd *et al.*, 1996). This phreatomagmatic style of eruption was succeeded by the Annexation Formation, which was a return to an effusive style of volcanism. Lavas of the Annexation Formation were erupted from just north of the island, and built the volcano to *ca.* 150 m height and 4 km in diameter. Explosive episodes are represented by thin tephra units between lava flows. An abrupt switch in volcanism followed with the eruption of the dacitic Sandy Bay Tephra (SBT), represented by multiple ignimbrite flow units resting on lithic and ash beds (Smith *et al.*, 2003a). The roughly bedded nature of the flow deposits indicates discontinuous eruption of the pyroclastic flows due to either multiple individual eruptions or episodic collapse of a continuous high eruptive column. Onshore distribution of the tephra deposits indicates a source to the north of the island, and the submarine caldera is thought to have been formed as a result of this eruption (Brothers and Martin, 1970; Lloyd *et al.*, 1996; Smith *et al.*, 2003b). The Haszard Formation followed, producing mainly lava flows and a scoria cone in the early phase of the eruptives. Flank fissuring and effusive flows were succeeded by the strombolian eruptions of the Haszard scoria member, which escalated into perhaps a sub-plinian eruption, forming thick massive scoria deposits (Lloyd *et al.*, 1996). The end of the Haszard Formation sequence was phreatomagmatic accompanied by partial sector collapse in the northern section of the crater.

Onshore exposures show that the majority of the eruptives preserved are lava flows and tuff units which are relatively uniform high-alumina basalts or basaltic-andesite, with the exception of the SBT (Brothers and Martin, 1970; Lloyd *et al.*, 1996; Smith *et al.*, 2003b). The SBT is a pumiceous, light grey vitric tuff that is the only silicic deposit recorded on the island. Composed predominantly of juvenile dacitic poorly sorted material, it is also inclusion rich, containing materials such as gabbros and glass cumulates thought to be from older units (Brothers and Martin, 1970; Lloyd *et al.*, 1996). Up to 100 m thick at the southern end of the volcano, the unit thins to 15 m in the north, due mainly to erosional processes (Lloyd *et al.*, 1996). The eruption has been dated (using fossil carbon from vegetation in the lower units of the tephra) to 6.31 yr BP (Lloyd *et al.*, 1996), an age which has been revised to *ca.* 5.7 ka by Shane and Wright (2011). The carbon age obtained by Lloyd *et al.* (1996) is a conventional radiocarbon age, whereas Shane and Wright (2011) used planktic foraminifera in sediment cores to date the eruption. The accuracy of this will be addressed further in Chapter 5.

Figure 2.3 Bathymetry of the Macauley massif and its immediate surrounds. Image courtesy of NIWA

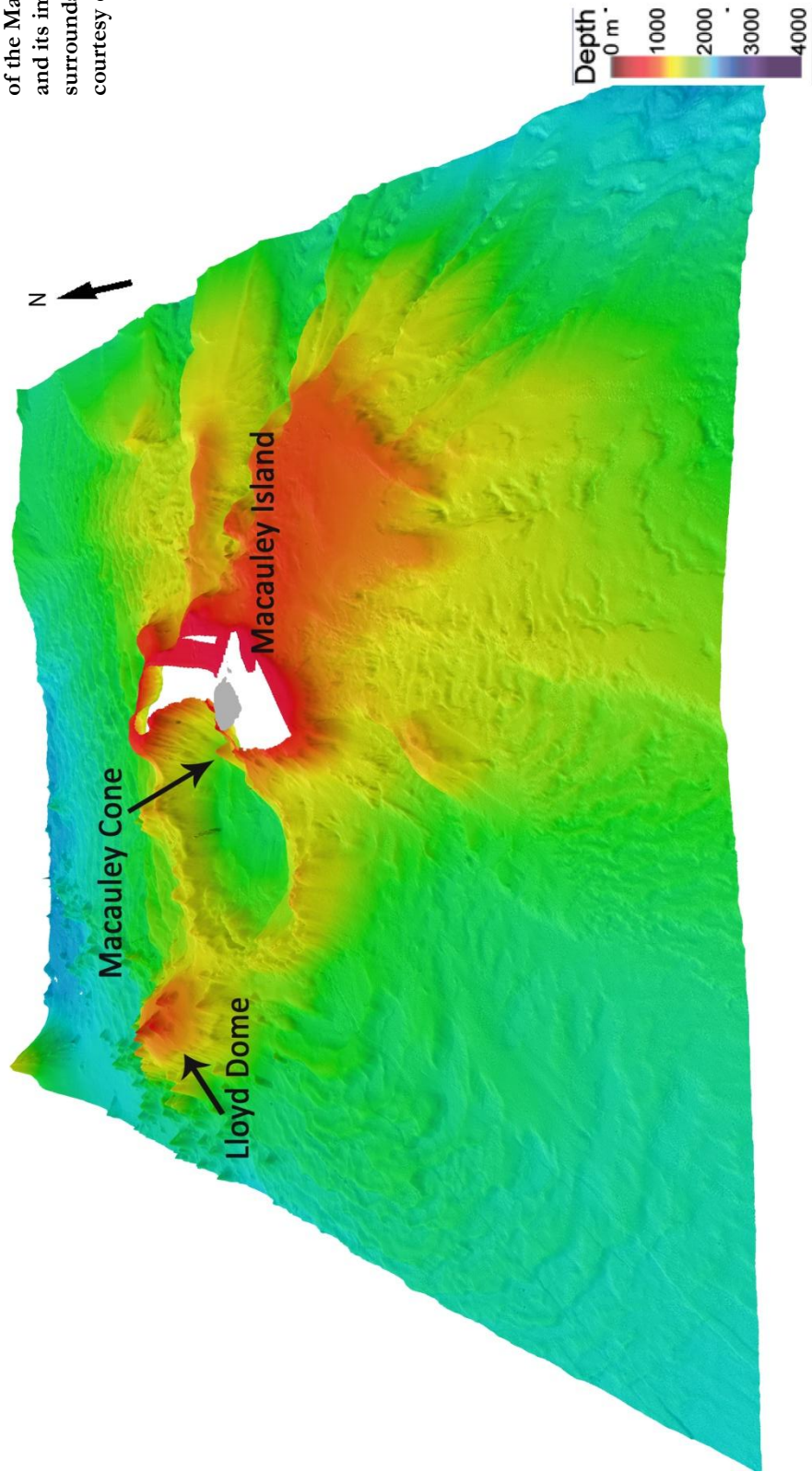


Table 2.2. Table of eruptive formations preserved on Macauley Island. Adapted from Brothers and Martin (1970) and Lloyd *et al.* (1996).

Formation	Eruption description
Grand Canyon	Thin sequence of sedimentary rocks deposited in Grand Canyon, consists of
Formation	interbedded tuffs, sandstones, mudstones and volcanic sands.
Haszard Formation	i. Thin, well bedded, partially welded tuffs, thickest surrounding Mt
i. Parakeet Tuff member	Haszard,
ii. Haszard scoria member	ii. Single massive bed of scoriaceous basalt, deposited as a coarse volcanic ash (?), thickest surrounding Mt Haszard,
iii. Cascade Lavas	iii. Overlies notable erosional unconformity, series of olivine basalt flows, plagioclase rich, flowed from vent source/s near Mt Cascade.
Sandy Bay Tuff	Highly pumiceous grey vitric tuff, irregular bedding structures (subaerially erupted), inclusion rich (crystalline gabbros, glassy fragments, abraded boulders, fragments of older eruptives), overlies slight erosional unconformity, 60 m thickness at Sandy Bay, thinning to the northwest.
Perpendicular Cliff intrusion	Internally irregular igneous intrusion (olivine basalts on eastern edge); could contain fragments of older eruptives.
Annexation Lavas	Gently dipping porphyritic vesicular olivine basalt flows, thin continuous flows separated by scoriaceous layers.
Boulder Beach Formation	Atop angular unconformity, interbedded coarse sandstone grits, conglomerates, breccias of volcanic debris. Interbedded, dyke fed lava flow.
North Cliff Lavas	Subaerially deposited, highly vesicular olivine basalt aa flows, horizontally deposited.

Eruption size estimates range from a minimum of 1-5 km³ (Lloyd *et al.*, 1996) to a maximum of 100 km³ (Latter *et al.*, 1992) the latter of which, if correct, would make the Sandy Bay eruption one of the largest globally during the Holocene (Latter *et al.* 2012). The accurate correlation of tephtras in the marine cores studied here may offer additional constraints on the volume of the eruption, and also identify the distribution of material erupted.

Previous EM300 mapping (TAN0205), combined with data collected on the TAN0706 voyage, reveal the complex bathymetry surrounding Macauley Island. Macauley Island itself represents less than *ca.* 5% of the volcanic edifice as illustrated in Figure 2.3. To the west of the island, the outer flanks of the edifice structure reveal sea-floor morphologies including mega-ripple bedforms up to 110 m in height which are concentrically orientated proximal to the caldera rim (NIWA, 2007). These bedforms are inferred to be associated with large-scale sector collapse and associated density flows. To the east, the sea-floor morphology indicates that the bathymetry of the pre-caldera edifice channelled pumice-laden density flows to the north, east and south (NIWA, 2007).

2.1.4 Raoul SW

Discovered via EM3000 multibeam mapping on the TAN0706 RV *Tangaroa* voyage in 2007, this unofficially named volcanic edifice is located to the southwest of Raoul Island (Figure 2.4). It forms a caldera structure *ca.* 4 km in diameter, with the caldera floor at water depths of *ca.* 1200 m and walls *ca.* 500 m high. Dredge samples recovered were fresh in appearance and the pristine morphology of the edifice suggests that it has been a site of recent explosive volcanism (Barker *et al.*, 2012;2013).

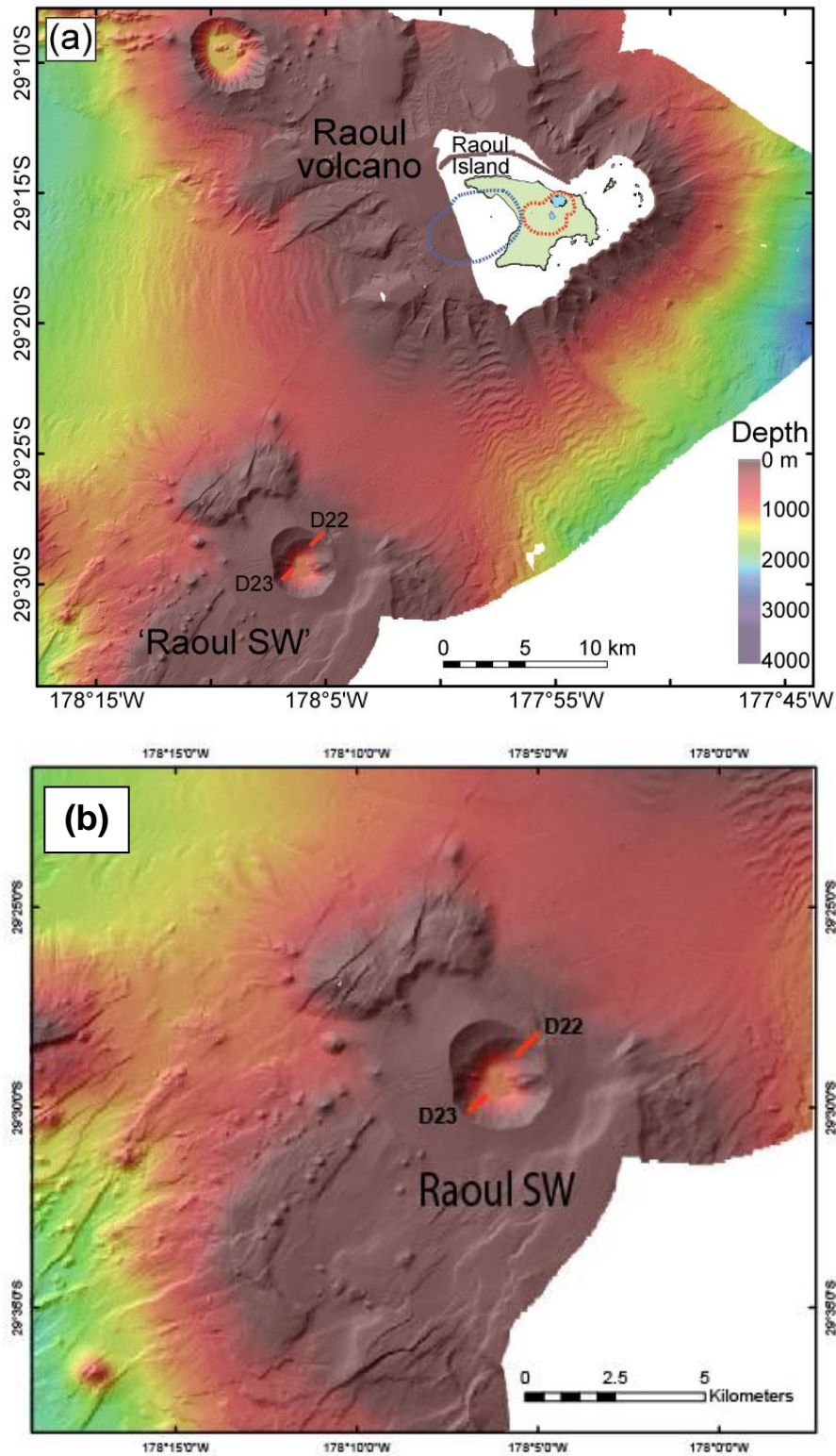


Figure 2.4 Map showing the bathymetry surrounding Raoul Island and the newly discovered Raoul SW volcanic edifice. a). Location of Raoul SW in relation to Raoul volcano. b). Bathymetric map of Raoul SW, with the locations of the dredge hauls from the RV *Tangaroa* TAN0706 voyage indicated by red lines and labelled by dredge number. Adapted from Barker *et al.* (2012)

2.2 Site setting and influences on tephra dispersion

As the Kermadec arc is relatively isolated, few studies have investigated the oceanographic or atmospheric conditions in any detail. As such, much of what we know of those conditions in the region is inferred from more detailed studies conducted closer to the New Zealand continent. The SW Pacific Ocean is heavily influenced both by Antarctica and the equatorial Pacific regions, resulting in dynamic atmospheric and oceanic conditions. Ocean currents from Antarctica bring cool water into the region, where it mixes with warm water transported from equatorial regions (Figure 2.5). At depth currents are reasonably weak, but can be locally intensified due to bathymetric controls. Atmospheric conditions are controlled by Hadley Cell circulation, with the prevailing winds in the region being easterlies. The region is also strongly affected by the El Niño Southern Oscillation (ENSO) climate modes, the strength of which varies on 3 – 7 year timescales and is controlled over a longer timescale by the Interdecadal Pacific Oscillation and potentially the present warming phase (Ummenhofer and England, 2007; Carter *et al.*, 2008; Gomez *et al.*, 2012). Understanding winds and ocean currents in the region is important to understand when interpreting the tephrochronology and for identifying preferential transport directions of tephra dispersal.

2.2.1 Currents and water masses

From examining studies conducted in the southern Kermadec arc we can reasonably assume that localised currents around the seamounts affect the distribution of sediments in the region, which may have important ramifications for tephra deposition and dispersal. Images published by Wright (1996; 2001) show that around the southern Kermadec arc seamounts localised bottom-currents form winnows and ripple structures down to water depths of *ca.* 2200 m. However as all of the cores in this study, with the exception of Core 3, are collected from > 2200 m, I conclude that the cores are unaffected by this process.

2.2.1.1 Present day settings

Past studies in the region have shown that there is at present no dominant current in the areas surrounding Raoul and Macauley islands. The influence of the Deep Western Boundary Current (DWBC) is largely restricted to the Kermadec Trench in water depths >2000 m (Whitworth *et al.*, 1999). The Tasman Front flows into the southern end of the Havre Trough–Kermadec arc system and the East Auckland Current eddy does not extend that far north (Wright *et al.*, 1995; Tilburg *et al.*, 2001; Wright, 2001). In the southern Havre Trough – Kermadec arc system differing water bodies dominate at depth: between 2200 – 2500 m depth upper circumpolar deep water (UCDW) entrained within the DWBC is evident, and interfingers in sills with the North Pacific deep water (NPDW) at depths of 1200 – 1400 m and 2200 – 2500 m depth (Wright *et al.*, 1995). The generalised trend of the low velocity currents in the area are to the north, meaning that if currents do play a role in tephra dispersal in the region one would expect a small north trending pattern to emerge from marine core records. Data presented by Thiede *et al.* (1997) contradict this, however, and they conclude that the surface currents in the study area flow southwards. The recent pumice raft erupted from Havre has been observed hundreds of km's from source. Much of the material has floated in a NW direction, towards Tonga; however some material has been observed well to the south of Havre (Richard Wysoczanski, pers comm.). Currents in the region can therefore disperse material from an eruption in variable directions. The lack of high velocity currents in the region indicates that the main control on the directional

dispersal of subaerially transported tephra is wind direction aided by rapid settling as discussed in Chapter 1 (Carter *et al.*, 2003).

A comprehensive study by Wright (2001) on the submarine volcanoes of the Kermadec arc from 34° 50' S to 36° 50' S found that currents in the region were controlled mainly by the East Cape eddy, an offshoot of the Tasman Front. The East Cape eddy has surface speeds varying from ca. 30-40 cm/s, dropping to ca. 10 cm/s at 1000 m water depth (Wright, 2001). The influence of this eddy decreases at ca. 2000 m water depth, where limited amounts of water from the DWBC spill into the southern Kermadec arc (Warren *et al.*, 1994; Wright, 2001). At depths of up to ca. 1800 m Wright (1996; 2001) observed bedforms associated with current flow, such as sediment winnowing, ripples and scour textures. It is possible that some of these processes may act in the region that the cores in this study were sourced from, however, all of the cores were collected from water depths of >2100 m, at which current velocities are low, so it is unlikely that any major bedform development or sediment transport processes have taken place.

Sediment deposition occurs as the (DWBC) flows around the Chatham Rise, turning North into the Hikurangi Trough through Valerie Passage and subsequently flowing into the Kermadec Trench (Carter and Mitchell, 1987; Carter and McCave, 1994; Hall *et al.*, 2001). The DWBC changes flow paths and depositional and erosional zones during glacial/interglacial cycles, the current itself intensifying in both inflow and ventilation into the Pacific region during glacial cycles (Hall *et al.*, 2001). The current entrains large amounts of sediment, and large depositional sediment drifts are located along the fringes of the flow in many areas. Before passing into the Kermadec Trench the DWBC entrains sediment flowing through the Hikurangi Trough and mobilises it northwards, but thickened sediment only occurs as far North as 35° S (Carter and McCave, 1994; Carter *et al.*, 1996). The majority of the Kermadec Trench sea floor shows minimal evidence of sediment, and what sediment is present there is likely to be subducted rather than forming an accretionary prism. Channels feeding sediment into the DWBC increase their input during glacial cycles due to increasing terrigenous erosion.

Volcanic material erupted from the Taupo Volcanic Zone is incorporated into the DWBC as it rounds the northern tip of the Chatham Rise (Carter *et al.*, 1996). As noted earlier the main depositional centre for this airborne material is to the East of the North Island, but it is possible that some material is transported further North. Material from an eruption of significant magnitude and duration could potentially be preserved as a distinct layer in these cores, but it is unlikely that material from smaller eruptions would be preserved as a distinct layer; it is possible that there will be numerous shards from these smaller TVZ eruptives preserved in the cores.

2.2.1.2 Glacial/interglacial cycles

During the glacial periods, deep sea records indicate that sea surface temperatures (SST) in the region 30° – 45° S in the Tasman Sea were 2°C colder when compared to present-day temperatures (Wright *et al.*, 1995; Weaver *et al.*, 1998), and were 4°C colder in the southern Havre Trough (Weaver *et al.*, 1998). These temperature decreases reflect the colder glacial climate but may be enhanced locally by increased upwelling of cool bottom waters in response to increased glacial wind speeds (Schulmeister *et al.*, 2004). Current systems changed positions also at 13.5 ka, with the Tasman Front entering into the Pacific at 32°S, 6° North of its current position (Carter *et al.*, 2008). Cooling occurred in the southern Havre Trough at ca. 11 ka, followed by warming at ca. 8 ka before the waters again cooled to present day temperatures (Weaver *et al.*, 1998). From this we can extrapolate similar timings and events further

North in the cores studied here, but the intensity of the fluctuation may vary in light of the stronger subtropical influence in the study area. As Carter *et al.* (2008) noted, the impact of the Antarctic Cold Reversal (14.5 to 12.5 ka) was ameliorated at 40°S by the subtropical inflow. Hence such Antarctic forcing of the ocean/climate in the study area is likely to be even more subdued. Changes in currents during glacial cycles is important to note, as it may affect tephra dispersal to the cores, as well as the sedimentation rate (as alluded to above) which will affect the accuracy of tephra ages calculated using sedimentation rates.

2.2.2 Wind dynamics

The Kermadec arc straddles the transition zone between Hadley Cell circulation north of 30°S and Ferrel Cell circulation south of 30°S (Sturman and Tapper, 2005) (Figure 2.6).

2.2.2.1 Present day settings

Dominant westerly trade winds to the south are associated with Ferrel Cell circulation and South East trending trade winds to the north are part of the Hadley cell circulation (Figure 2.6). Within the study area complex wind patterns are evident, controlled by seasonal wind patterns and ENSO. At latitudes of *ca.* 30°S westerly winds are dominant as cooled tropical air descends towards the surface in this subtropical high pressure belt. The winds at the top of the Hadley cell can reach up to 200 km hr⁻¹ in the subtropical jet streams before descending to the surface (Sturman and Tapper, 2005). The mean maximum velocity of 60 m/sec in the jet stream occurs in winter at around 13.7 km height and slows to 23 m/sec in February (Maunder, 1971) due to increases in the temperature gradient (Schulmeister *et al.*, 2004). This region is an area of high air pressure due to the descending air, so often the winds are variable and light. On Raoul Island the average yearly wind speed is *ca.* 12 km hr⁻¹ (weather2, 2012). In summer months, the study area is an area of high pressure with south-easterly trade winds while in winter it is an area of low pressure with southwesterlies (Rasmussen and Carpenter, 1982; Salinger *et al.*, 1995; Thiede *et al.*, 1997).

Some direct measurements of the wind speed and atmospheric structure above Raoul Island are presented in Tables 2.3 and 2.4, which were collected during the period from November 1973 – September 1979 (Reid and Penney, 1982). The upper level atmospheric measurements were collected using either a theodolite or laser tracking of a hydrogen filled balloon.

2.2.2.2 Climate variability

Wind intensity fluctuates between glacial/interglacial cycles, with more intense winds inferred to occur during glacial periods due to increasing temperature gradients between the poles and the equators. During glacial periods the winds north of the Chatham Rise are thought to reduce in intensity and the prevailing westerly winds shift northwards by 7-10° in response to changing circulation patterns (Toggweiler *et al.*, 2006). Over the Kermadec islands the prevailing winds swing around to prevailing north to northwest winds (Weaver *et al.*, 1998).

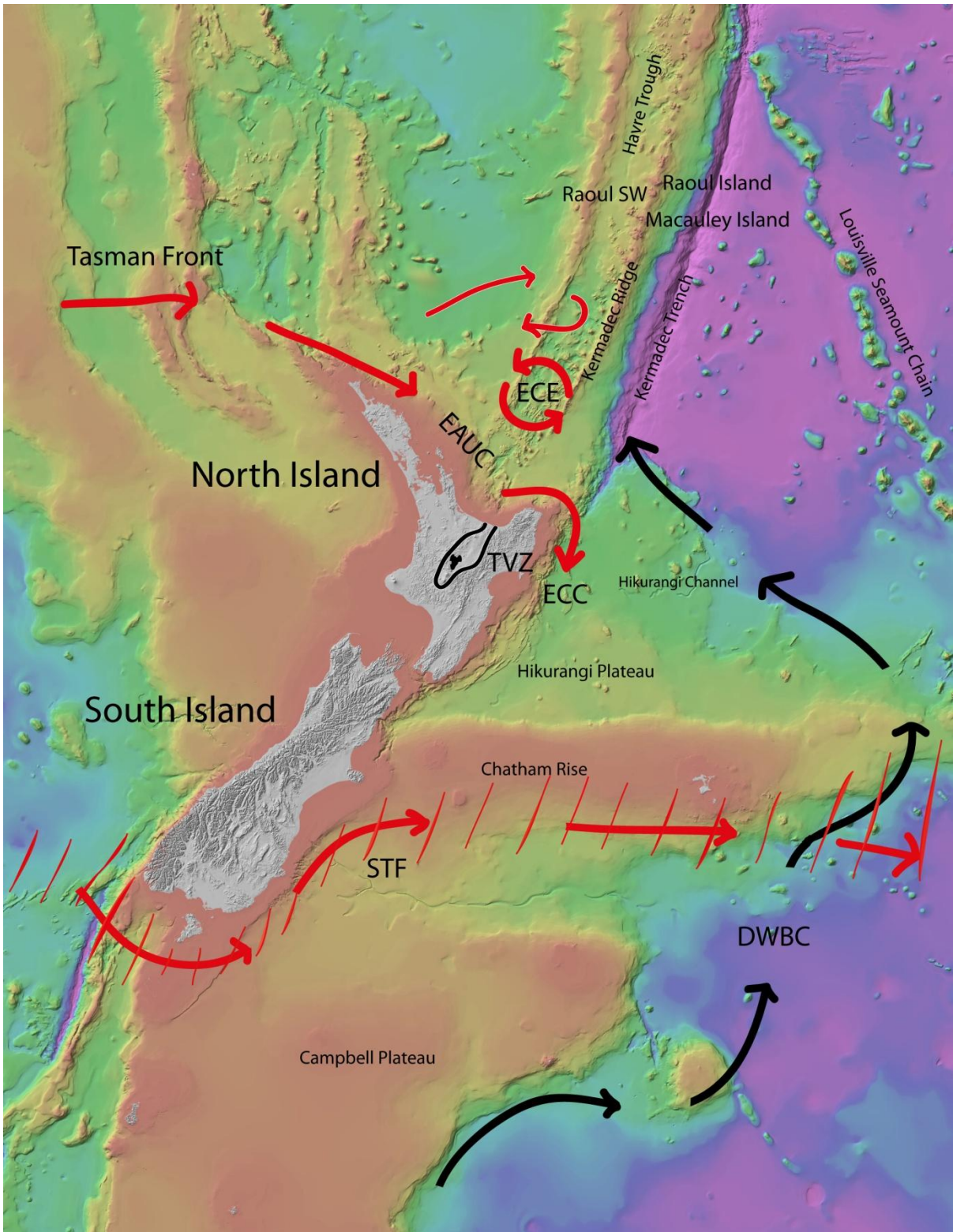


Figure 2.5. Oceanography of the southwest Pacific Ocean around New Zealand and the Kermadec Ridge. The elements shown are the Tasman Front, East Auckland Current (EAUC), East Cape Eddy (ECE), East Cape Current (ECC), the Deep Western Boundary Current (DWBC) and the Sub-Tropical Front (STF) along with known surface water currents (Carter *et al.*, 1995; Tilburg *et al.*, 2001; Carter *et al.*, 2003; Carter *et al.*, 2008). Outline of the Taupo Volcanic Zone taken from Wilson *et al.*, 1995. Image courtesy of NIWA.

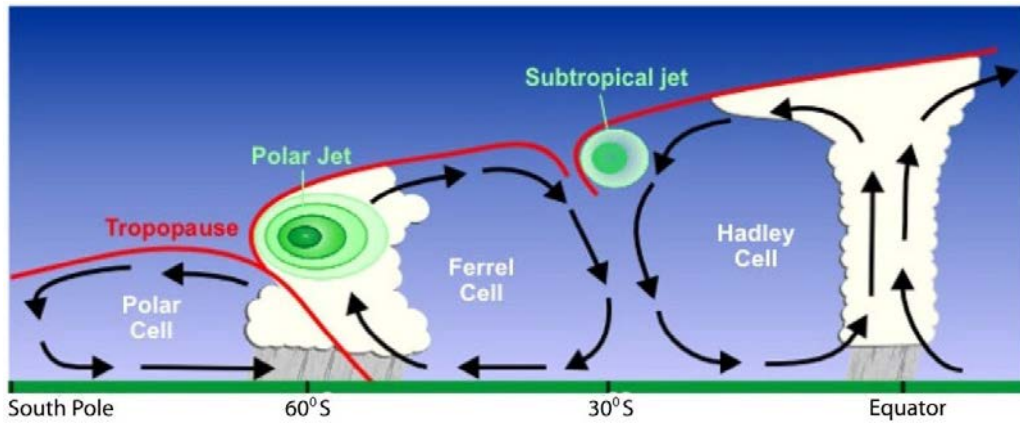


Figure 2.6 Diagram illustrating the circulation dynamics of the Southern Hemisphere (Sturman and Tapper, 2006)

Table 2.3. Table displaying mean wind speeds at varying pressure levels above Raoul Island from the period November 1973 - September 1979. Taken from Reid and Penney (1982).

Mean wind speed (m/s) at varying pressures above Raoul Island													
LEVEL (mb)	Jan	Feb	Mar	Apr	May	Jun	Jul	Aug	Sept	Oct	Nov	Dec	Mean
900	7.9	9.3	9.0	9.4	8.6	10.1	9.1	9.8	8.6	7.6	7.3	7.1	8.7
800	7.0	6.5	6.7	8.0	8.5	10.6	11.2	11.0	9.5	8.6	6.6	6.8	8.3
700	7.4	6.9	6.6	8.5	9.9	12.3	13.9	13.6	11.5	10.7	7.5	7.6	9.6
600	8.7	7.9	7.6	10.5	13.2	16.9	19.0	18.9	16.0	14.3	9.5	9.5	12.5
500	10.9	10.0	10.3	14.0	19.1	24.5	26.3	26.8	22.4	18.9	13.4	12.7	17.1
400	14.9	13.3	14.2	19.3	25.4	33.5	36.3	37.6	31.0	24.9	18.3	16.6	23.2
300	19.0	19.1	19.6	25.6	35.3	44.1	48.8	47.6	40.8	33.2	25.9	22.5	30.4
200	22.7	24.4	23.5	29.3	42.3	46.4	48.3	45.3	41.7	36.6	31.2	26.8	32.2
100	9.4	9.7	10.1	11.0	18.0	17.7	19.2	17.5	11.5	12.1	12.3	11.7	11.6

Table 2.4. Table summarising the measured heights of differing pressure levels recorded at Raoul Island. Data from Reid and Penney (1982).

Measured Heights at differing pressure levels at Raoul Island						
Pressure (mb)	500	400	300	200	150	100
Height (km)	5.8	7.4	9.5	12.2	14.0	16.5

Interannual climate variability over the study area is dominated by the effects of ENSO which have direct and measurable impacts on climatic and oceanic conditions in the study area although the signal is much softer than areas closer to the equator (Karoly, 1989; Salinger *et al.*, 2001). During El Nino years there is increased precipitation in the study area, and prevailing north-easterly winds (Rasmussen and Carpenter, 1982; Ummenhofer and England, 2007). During the strong ENSO event of 1982-1983, winds fluctuated from south-easterlies in winter of 1982, to south-westerlies in the summer months then changed again to north-westerlies in autumn of 1983 at heights of *ca.* 1.5 km (Rasmussen and Wallace, 1983). Winds speeds associated with an ENSO event are up to *ca.* 50 m/s⁻¹ in the troposphere at heights of *ca.* 12 km (Karoly, 1989). During ENSO events the distribution of tephra is likely to be different to a normal year; however the resolution of this study is not high enough to distinguish these events.

Other climatic signals evident in the area are the effects of the Interdecadal Pacific Oscillation (IPO) and the Southern Oscillation (SO) which moderate the intensity of ENSO (Salinger *et al.*, 2001). ENSO is a complex two-way cycle between the atmosphere and ocean whereby weakening of the southeast trade winds causes a decrease in upwelling rates along the eastern Pacific, resulting in increased SST's which influences atmospheric conditions further (Cane, 1983).

Chapter 3

Methods

3.1 Sample Collection

On board the R.V. *Tangaroa* each core was split in two: the working split core and the reference core. Prior to and post analysis the reference split of the core is kept in cold storage to enhance preservation. Non-invasive (or non-destructive) analyses, which included visual logging, geophysical techniques and imaging, were carried out on the reference core. Following these analyses the reference core was sealed for future reference. Based on the results of non-invasive analyses, sampling of the working split core was conducted. Sediment, foraminifera and tephra samples were then processed and analysed as described below. An outline of the analytical methods used is summarised in Figure 3.1

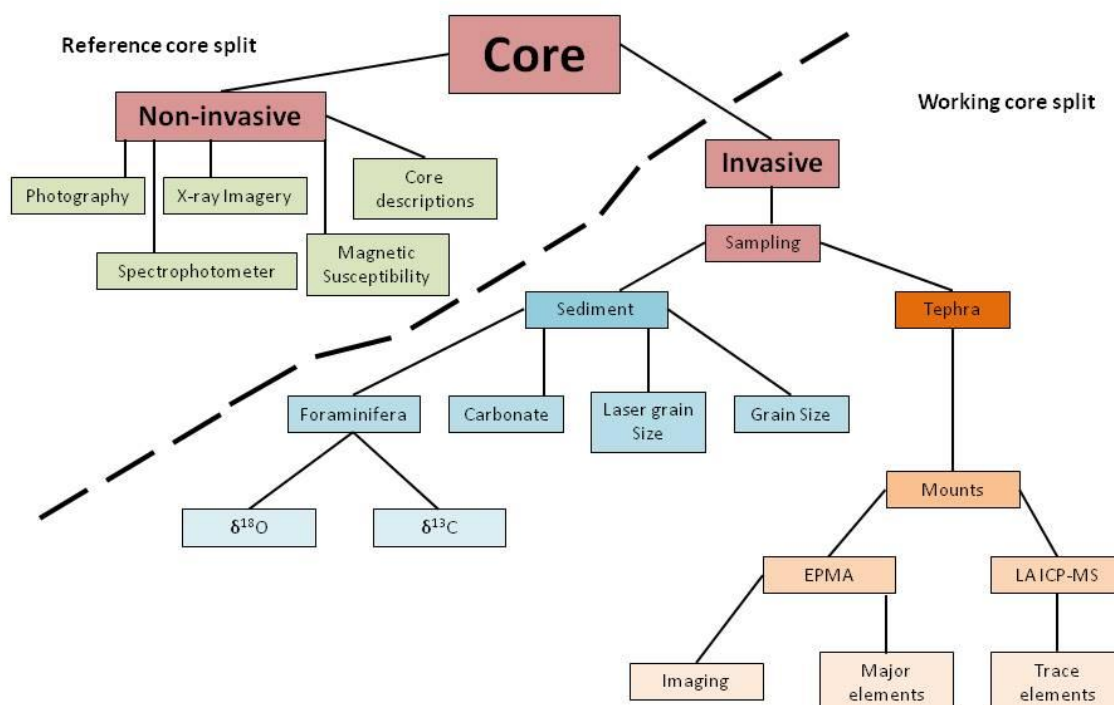


Figure 3.1 Flow chart illustrating the methods used to create a detailed core stratigraphy. Non invasive analyses were conducted on the reference split of the core and invasive analyses (sampling) were conducted on the working split of the core.

3.2 Non-invasive methods

All data collected using the methods below are illustrated in Appendix B and methods except for the core descriptions are represented in Figure 3.2.

3.2.1 Photography

Photographs of the cores were taken using a mounted SLR Olympus Camedia E-20 camera with an ED lens, 4.0 times zoom and 5.0 megapixels. The images were processed using Adobe Photoshop Elements 2.0.

3.2.2 Core descriptions

Detailed descriptions were conducted on each core, identifying different units within each core and noting any interesting structures. Colour was identified using the Munsell colour chart. All core descriptions can be found in Appendix B.

3.2.3 Magnetic susceptibility

Magnetic susceptibility measurements were collected using a Magnetic Susceptibility Meter (model MS2), produced by Bartington instruments of Oxford, England. Measurements were collected every 2 cm to avoid overlapping data, and processed on an Excel spreadsheet provided by NIWA.

3.2.4 Spectrophotometer

Measurements were collected using a Minolta Spectrophotometer CM-508D (Version 2.05) in Munsell mode with the white calibration set to 90.00 (L*). Measurements were collected at 2 cm intervals along the core to avoid overlapping data. The raw data was processed using an excel spreadsheet developed by staff at NIWA.

3.2.5 X-Ray

The reference split from the cores was X-rayed using the facilities at NIWA. The core splits which are approximately 5 cm in thickness were X-rayed in 30 cm lengths using a Varian PaxScan 4030E flat panel imaging system and an Ecotron EPX-F2800 portable veterinary X-ray generator. Typical energy settings for this study were 100 kVp and 6.4 mA. Exposure and grey-level mapping were controlled using proprietary Varian software (ViVA 2.0, Revision L.04) to produce images similar to the one shown in Figure 3.2.

Physical properties from non-invasive analysis (TAN0706 - 13)

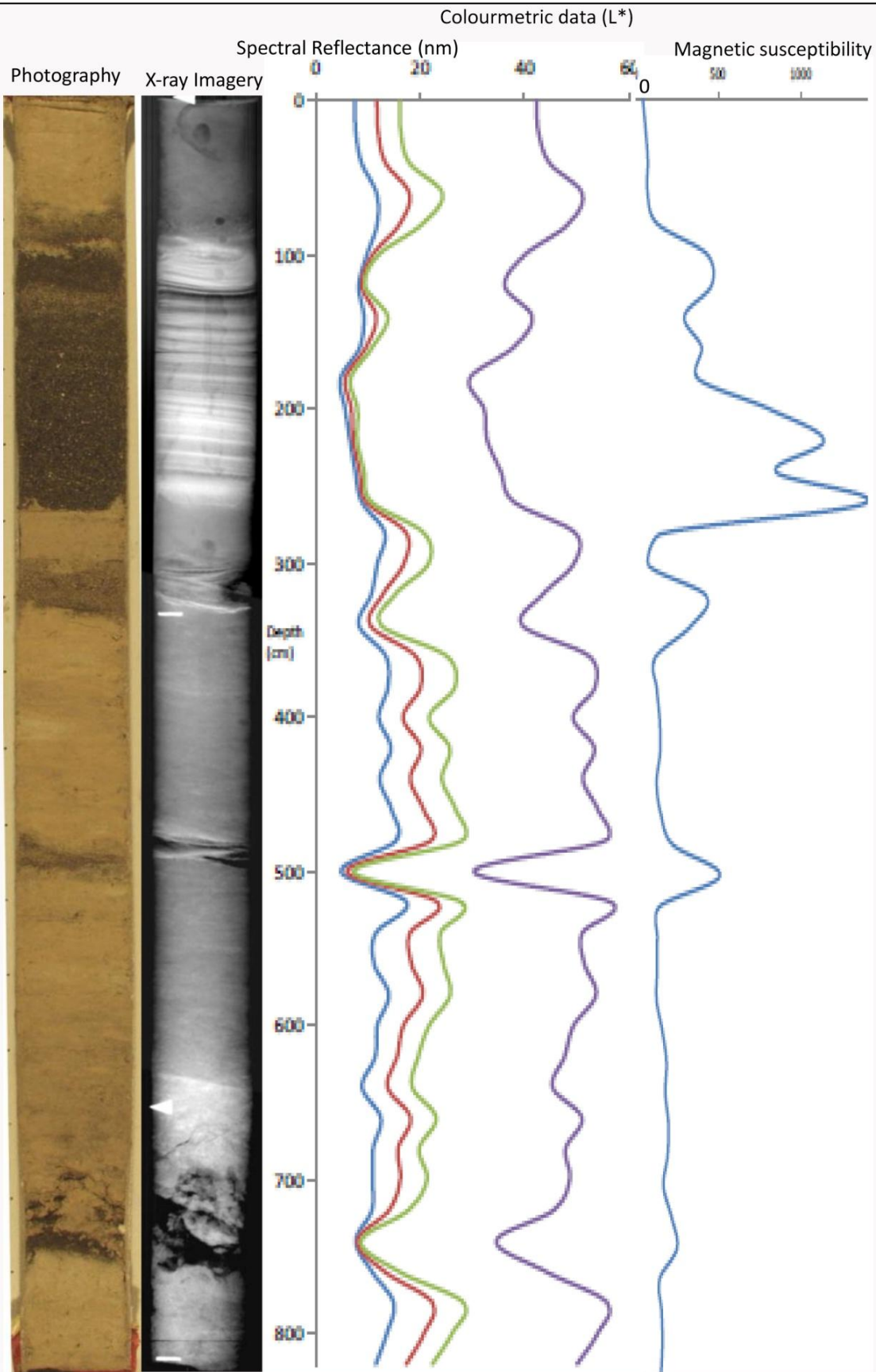


Figure 3.2 Example of an image displaying the non-invasive method results used in determining core stratigraphy

3.3 Invasive methods – sediment and foraminifera

Physical sampling of the cores was undertaken to prepare samples for analysis by several analytical methods (Figure 3.1). Samples consisted of sediment, foraminifera and tephra.

3.3.1 Sample collection

Sediment samples were collected from hemipelagic zones identified by core descriptions at 3, 4 or 5 cm intervals depending on the published sedimentation rate of the core (Shane and Wright, 2011).

3.3.2 Grain size sieving preparation and analysis

The hemipelagic sediment samples were weighed into beakers, and the dry weight recorded. They were then filled with distilled water, shaken, and left to soak overnight. They were then ultrasonicated for a few minutes, before being emptied into a sieve set (140 μm and 60 μm mesh sizes) and rinsed using distilled water. When the water ran clear, the samples (in their sieve fractions) were swilled into folded filter paper, and the water drained off. The <60 μm fraction was rinsed further, with the mud being decanted. The leftover material was then swilled into filter paper. The samples were put into an oven at 40°C and left to dry overnight. They were then emptied into labelled acid washed plastic bottles. Each fraction was weighed once in the bottle, and the weights corrected using an Excel spreadsheet.

3.3.3 Laser grain size analysis

Approximately 6 g of sample was inserted into a beaker filled to $\frac{3}{4}$ full with washing solution. The beaker was shaken then ultrasonicated for *ca.* 15 seconds. The sample was then washed into the machine using distilled water. The machine used was a LS 13 320 Laser Diffraction Particle Size Analyser with an Aqueous Liquid Module attached. An auto rinse with an average time of 152 seconds was conducted between samples and if the obscuration value was still high another rinse was conducted. Run settings were set to 90 seconds.

3.3.4 Calcium carbonate analysis

Using small foil dishes (tared) and the Mettler PC 200 balance, 0.333 g of dried sediment was weighed out. The sediment was then ground, using a mortar and pestle until the grain size was homogenized. The sample was then redried and reweighed.

Using small foil dishes (tared) and the Mettler PC 200 balance, 0.333 g of dried sample sediment was weighed out and inserted into the carbonate test tube. The same was done for two CaCO_3 standards for each run, the standard used being AnalaR from BDH chemicals which is pure, minimum assay 99.5%. The rim of the tube was wiped with paper tissues and 5 drops of distilled water added to prevent puffing when the acid was introduced. Using a syringe, approximately 3 ml of 70% orthophosphoric acid was inserted into the side arm of the tube, taking care not to drip any acid on the sediment below. O rings coated in silicone grease were put on the bomb, followed by the bomb lid. A clamp was applied to ensure

a vacuum could form, and all bomb lids were closed. Measurements were conducted using a standard method summarised in Muller and Gastner (1971) and Dunn (1980). The results were entered into an Excel spreadsheet supplied by NIWA and the percentage carbonate calculated.

3.3.5 Foraminifera

A variety of foraminifera species were present in the marine cores. A brief description of characteristic habitats of the species used for oxygen isotope analysis is given in Table 3.1.

Foraminifera samples were washed using a 60 µm nylon sieve and distilled water until the water ran clear. They were washed into filter paper and dried overnight at 40°C. After washing, the >60 µm fraction of each mixed hemipelagic and tephra sample was examined for foraminifera. If present, the planktic species of *Globigerina bulloides*, *Globorotalia inflata* and *Globigerinoides ruber*, along with the benthic species of *Uvigerina peregrina* and *Cibicides muellerstorfi* were hand-picked under a binocular microscope (see Table 3.1). For the planktic species which were more abundant, > 10 specimens were picked. Benthic species were present in lesser abundances and those present were picked.

Individual species from each sample were then washed and separated by picking individual species with a fine artist's brush and placing them into a 10 mL Teflon tube containing MilliQ water. A 10 mL Teflon pipette was used to remove all water, and the tube was filled again with MilliQ. This was repeated once more before the tube was semi-immersed in a sonic bath for up to 3 seconds. The water was again pipetted out and the sample flushed with MilliQ. Each individual foraminifera was then picked and placed back into the sample holder.

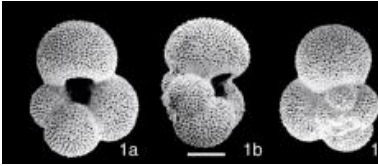
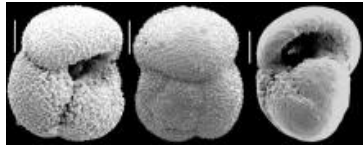

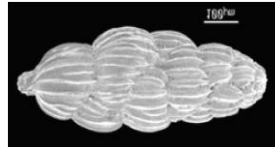

3.3.6 Oxygen isotope analysis

The use of oxygen isotopes in stratigraphic studies was pioneered by Urey (1947) and continued by Emiliani (1955). The general principle upon which this stratigraphic tool is based is that oxygen isotopic fractionation between water and calcite during carbonate formation is temperature dependent. Positive values indicate enrichment in the heavier isotope ($\delta^{18}\text{O}$) and negative values indicate enrichment in the lighter isotope ($\delta^{16}\text{O}$) relative to Vienna Pee Dee Belemnite (vPDB). Isotope values are presented in delta notation (δ) using Equation 3.1. It then follows that the oxygen isotopic value of measured foraminiferal calcite depends on the formation temperature and the isotopic composition of the water in which calcite precipitation occurred (Jansen, 1989). The isotopic composition of the formation waters varies between glacial and interglacial cycles, and this allows the correlation of measured isotopic compositions and variations to that of global and locally recorded isotopic variations therefore giving us an approximate age. More than one species was used in this study order to construct a complete history, following Jansen (1989).

Equation 3.1 Equation used to determined the oxygen isotope ratio (Emiliani, 1955)

$$\delta = 1,000 \frac{\text{O}^{18}/\text{O}^{16} (\text{sample}) - \text{O}^{18}/\text{O}^{16} (\text{standard})}{\text{O}^{18}/\text{O}^{16} (\text{standard})} .$$

Table 3.1 Table displaying information on the appearance and habitat of each of the foraminifera used in this study. Note the distinction between the epifaunal planktic foraminifera and the infaunal benthic foraminifera.

				
Planktic			Benthic	
<i>Globigerina bulloides</i>	<i>Globorotalia inflata</i>	<i>Globigerinoides ruber</i>	<i>Uvigerina peregrina</i>	<i>Cibicides wuellerstorfi</i>
Characterises upwelling conditions; found above 400 m water depth, but mainly above the thermocline; borderline between spinose and non-spinose species, calcifies during spring.	Transitional to subpolar species; encrusted by smooth calcite deposit; reflect temperatures at 100–400 m depth.	Shallow water dweller; tropical to sub-tropical species, calcifies in summer.	Dwells at depths from 50-5000 m, infaunal species dwelling in bottom sediments at ca. 150 mm depth	Dwells at depths of 400-3000 m.; epifaunal species living in bottom sediments at ca. 10 mm depth or attached to substrates above the sediment surface
Hemleben <i>et al.</i> , 1989; Ganssen and Kroon, 2000	Hemleben <i>et al.</i> , 1989; Ganssen and Kroon, 2000	Hemleben <i>et al.</i> , 1989; Ganssen and Kroon, 2000; Thiede <i>et al.</i> , 1997	Hayward <i>et al.</i> , 2001; Hayward <i>et al.</i> , 2010	Hayward <i>et al.</i> , 2001 ; Hayward <i>et al.</i> , 2010

Foraminifera samples were analysed at NIWA Greta Point, Wellington using an automated individual-carbonate reaction (Kiel III) device coupled with a Finnigan MAT252 mass spectrometer. The samples were first reacted with 3 drops of H_3PO_4 at 75°C before being analysed. The internal precision of measurements is 0.02-0.08‰ for $\delta^{18}\text{O}$ and 0.01-0.06‰ for $\delta^{13}\text{C}$, external precision is 0.03‰ for $\delta^{18}\text{O}$ and 0.02‰ for $\delta^{13}\text{C}$ relative to vPDB. All values reported are relative to vPDB where $\delta^{13}\text{C}$ has a value of +1.95‰ and $\delta^{18}\text{O}$ has a value of -2.20‰ for NBS19 calcite.

3.4 Invasive methods – tephra

Tephra samples were collected based on information gained from the non-invasive methods described above, the most important being the X-ray imaging and magnetic susceptibility measurements which most clearly identified areas of potential tephra. Samples which were tephra rich were collected from a *ca.* 1 cm x 1 cm area. Those which were less tephra rich were collected from a *ca.* 2 cm x 1 cm area.

3.4.1 Tephra sample preparation

Tephra samples were prepared for analysis following the methods used by Allan *et al.* (2008) adapted from Froggatt (1983). The samples were rinsed into beakers using deionised water and placed into an ultrasonic bath for >30 seconds. The muddy water was then decanted off and the process repeated until the water was mostly clear. The samples were then wet sieved through nylon mesh sieves of 140 μm and 60 μm using distilled water. The size fractions were washed from the sieves onto filter paper and dried overnight at 40°C . Between each sample the mesh was rinsed and placed in the ultrasonic bath for >3 minutes to remove any particles. The cleaned samples consisted of mainly glass shards, with minor amounts of crystals, foraminifera and diatoms in varying proportions.

Epoxy mounts were made by mixing epoxy resin and hardener at a ratio of 3:1 and then poured into standard plastic moulds and left to cure overnight. Six holes were drilled into each epoxy resin mount and the tephra samples were subsequently mounted, taking care to avoid any cross-contamination. The mounts were then polished using 250-4000 grit silicon carbide paper and 3 μm and 1 μm liquid diamond suspensions on a polishing lap. Finally a 25 μm carbon coating was applied before EPMA analysis to ensure the surface was conductive.

For LA-ICP-MS analysis the epoxy mounts were polished using 1 μm liquid diamond suspension to remove the carbon coating and cut into halves. The mounting process is illustrated in Lowe (2011).

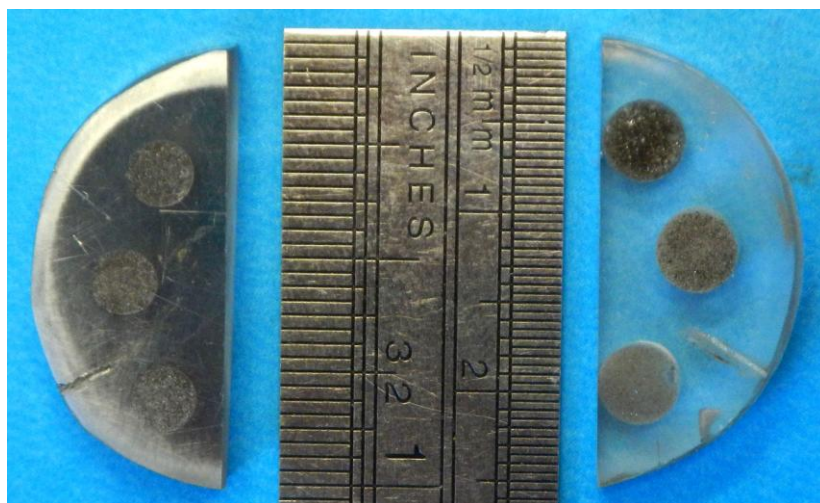


Figure 3.3 Carbon coated epoxy mount (left) ready for analysis using EPMA, and an epoxy mount ready for LA ICP-MS analysis (right).

3.4.2 Electron Probe Microanalyser

Major and minor element analysis was conducted on a JEOL JXA 8320 Superprobe electron probe microanalyser (EPMA) at Victoria University of Wellington (VUW). The EPMA is equipped with an energy dispersive X-ray spectrometer (EDS), 5 wavelength dispersive X-ray spectrometers (WDS), and detectors able to image in backscattered electron (BSE) and secondary (SEI) mode.

EPMA analyses were undertaken on 32 mm epoxy discs each containing six samples, or 3 samples if they were cut to a half moon shape illustrated in Figure 3.3. All analyses were conducted using WDS. International standards of similar composition to the material being analysed were used to calibrate the EPMA for quantitative analyses and to measure any machine drift. The standards used were Smithsonian standards VGA99 and VG-568 (Jarosewich *et al.*, 1980), and the MPI-DING standards T1-G and ATHO (Jochum *et al.*, 2006) for SiO₂, Al₂O₃, TiO₂, FeO, MnO, MgO, CaO, Na₂O, and K₂O. The Smithsonian standard Scapolite R6600-1 (Jarosewich *et al.*, 1980) was used to calibrate for Cl. Analysis of glass shards used an electron beam defocused to 10 µm, a beam current of 8 nA to reduce the effects of alkali-migration during irradiation and an accelerating voltage of 15 kV. Major element oxide concentrations were calculated using the ZAF method, where Z is the mass number, A is the absorption and F the fluorescence and are used to correct for matrix effects which report incorrect major element concentrations. A minimum of 12 shards were analysed per tephra sample to accommodate bimodality, heterogeneity or inherited glass shards. In some samples the shard sizes were not large enough to accommodate the spot size, resulting in less shards being analysed. A minimum of 5 shards per sample were analysed. A BSE (Figure 3.4) was taken of each sample so that each glass shard analysed for major elements could also be analysed for trace elements using the LA ICP-MS as an internal standard (i.e. a measured amount of an element) must be used to correct the data (Allan *et al.*, 2008)

Secondary standards were analysed together with sample glass shards (approximately one standard to ten sample shards) to monitor for machine drift and test for precision and accuracy. The results of standard analyses are given in Table 3.2. Note that the 2σ precision values decrease for those elements which have lower concentrations (e.g. Cl is only just above detection limit in most standard glasses analysed, so the mineral scapolite was used as a standard). In general the results show high levels of precision and accuracy.

3.4.2.1 EPMA glass shard major and minor element analytical precision and accuracy

Calibrated standards (Tables 3.2-3.5) were run as unknowns every *ca.* 20 analyses to measure instrumental drift (if any present) and to monitor the accuracy and precision of the measurements. The results of these analyses show that the machine was stable, and the results are plotted in Tables 3.2 - 3.5. These tables display the 2σ analytical precision calculated from numerous analyses of the calibrated standards. Note that the 2σ precision values decrease for those elements which have lower concentrations. As the glass standards all yielded low precision values for Cl, an additional standard, Scapolite was analysed which has higher concentrations of chlorine and all Cl values presented here have been corrected using this standard. Analytical totals for individual glass shards ranged from 85% to 105%, but only glass shards with totals between 93-103% have been included in the dataset. Samples with low totals are unrealistic and most likely result from hitting epoxy during analysis. A correction factor was applied to the major element data in order to correct for instrument drift within the EPMA.

A correction factor was calculated for each individual analysis session and applied to the data collected during that session only (Table 3.6). The average major element compositions and the precision of individual glass shards from each tephra layer are presented in Appendix C. For samples in which there was bimodality in the glass shard population, a separate average has been calculated and attributed to the population.

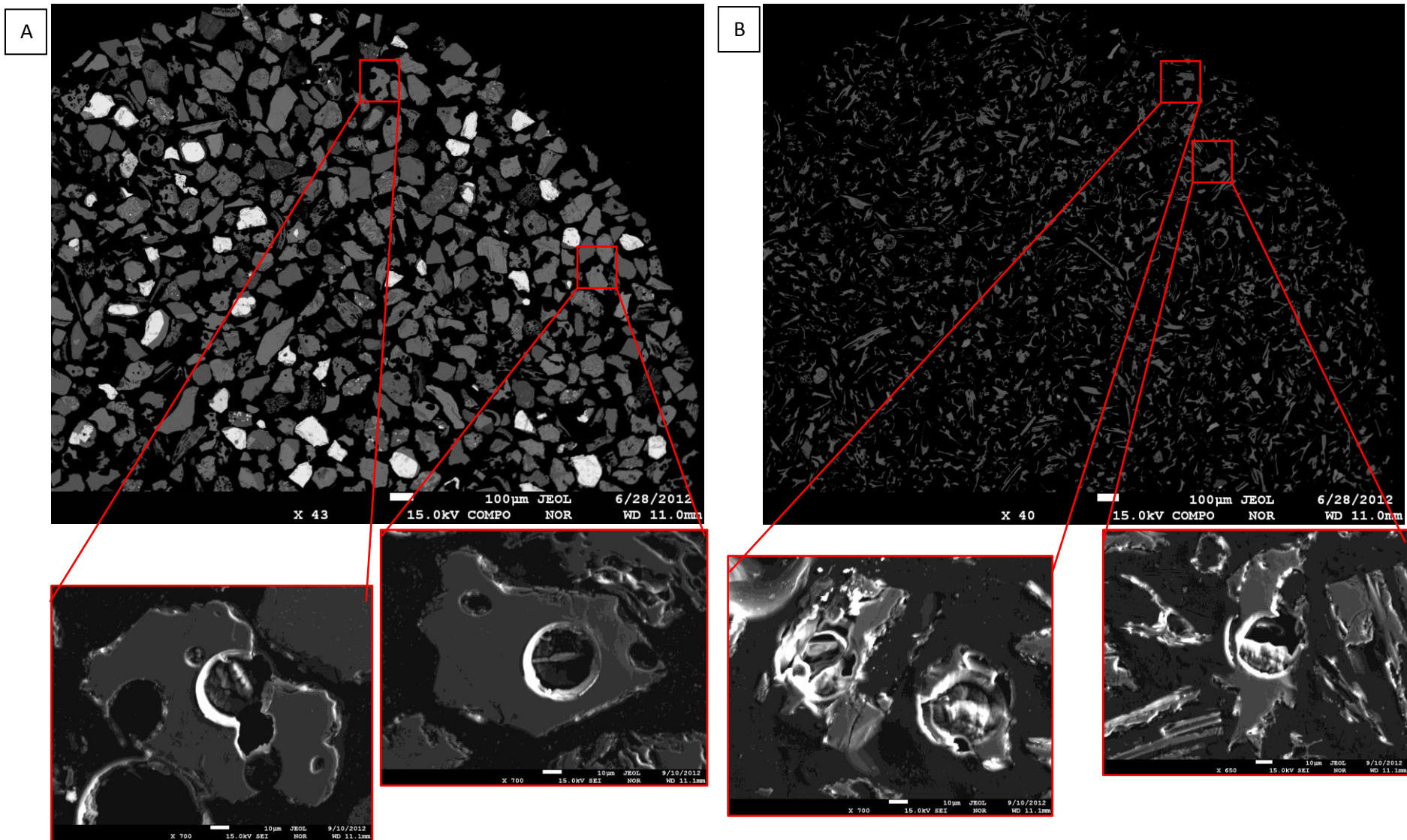


Figure 3.4 Images showing two tephra samples taken in BSE mode, highlighting the differences in tephra shard size between samples. The image on the left is sample 13-26 which has larger glass shards than sample 1-87 on the right. The smaller images show laser pits generated by the LA ICP-MS. Glass shards in sample 1-87 are much smaller than in 13-26, and the pit has ablated most of the shard, and potentially ablated through the shard to the material underneath.

Table 3.2 EPMA precision and accuracy for the international glass standard ATHO measured in this study. The reference value is taken from Jochum *et al.* (2006) and these values as well as the mean and the 2σ values are reported in wt.%. Standard values are averaged across all analyses.

ATHO standard (n = 167)										
	SiO ₂	Al ₂ O ₃	TiO ₂	FeO	MnO	MgO	CaO	Na ₂ O	K ₂ O	Cl
Average	75.95	12.24	0.23	3.22	0.07	0.08	1.77	3.33	2.67	0.04
Maximum	78.93	12.72	0.26	3.54	0.13	0.15	1.83	4.05	2.81	0.06
Minimum	74.33	11.84	0.20	2.90	0.00	0.06	1.66	3.02	2.44	0.00
2σ	2.18	0.41	0.03	0.26	0.04	0.04	0.10	0.83	0.13	0.02
% 2σ	2.89	3.70	27.72	9.90	83.27	66.49	6.26	31.09	5.02	81.15
Reference value	75.60	12.20	0.25	3.27	0.10	0.10	1.70	3.75	2.64	0.04
% offset	0.46	0.39	-9.80	-1.46	-30.18	-13.59	4.11	-11.04	1.40	-6.97

Table 3.3 EPMA precision and accuracy for the international glass standard VG568 measured in this study. The reference value is taken from Jarosewich *et al.* (1980) and these values as well as the mean and the 2σ values are reported in wt.%. Standard values are averaged across all analyses.

VG568 standard (n = 162)										
	SiO ₂	Al ₂ O ₃	TiO ₂	FeO	MnO	MgO	CaO	Na ₂ O	K ₂ O	Cl
Average	76.98	12.05	0.05	1.04	0.02	0.02	0.49	3.48	4.83	0.10
Maximum	79.77	12.59	0.09	1.52	0.07	0.08	0.64	3.93	5.06	0.14
Minimum	73.54	11.81	0.00	0.31	0.0	0.00	0.36	2.28	4.07	0.00
2σ	1.45	0.31	0.05	0.29	0.03	0.03	0.12	0.55	0.36	0.04
% 2σ	1.89	2.60	105.84	26.00	184.75	149.67	18.85	15.85	7.63	45.37
Reference value	76.96	12.17	0.08	1.08	0.02	0.03	0.45	3.52	4.93	0.10
% offset	0.03	-0.96	-37.50	-3.51	0.00	-16.66	10.00	-0.99	-1.96	-0.29

Table 3.4 EPMA precision and accuracy for the international glass standard T1-G measured in this study. The reference value is taken from Jochum *et al.* (2006) and these values as well as the mean and the 2σ values are reported in wt.%. Standard values are averaged across all analyses.

T1-G standard (n = 166)										
	SiO ₂	Al ₂ O ₃	TiO ₂	FeO	MnO	MgO	CaO	Na ₂ O	K ₂ O	Cl
Average	59.27	17.05	0.72	6.35	0.10	4.12	7.04	3.20	2.00	0.01
Maximum	59.58	17.35	0.77	6.87	0.15	4.59	7.28	3.48	2.09	0.03
Minimum	57.85	16.71	0.68	5.95	0.00	3.49	6.79	2.28	1.82	0.00
2σ	2.13	0.49	0.04	0.37	0.04	0.64	0.22	0.35	0.11	0.01
% 2σ	3.59	2.89	5.60	5.92	49.82	16.59	3.23	11.12	5.68	119.02
Reference value	58.60	17.10	0.75	6.44	0.12	3.75	7.10	3.13	1.96	0.01
% offset	1.15	-0.26	-4.23	-1.28	-14.96	9.89	-0.83	2.42	2.50	-2.65

Table 3.5 EPMA precision and accuracy for the international glass standard VG-A99 measured in this study. The reference value is taken from Jarosewich *et al.* (1980) and these values as well as the mean and the 2σ values are reported in wt.%. Standard values are averaged across all analyses.

VGA99 standard (n = 60)										
	SiO ₂	Al ₂ O ₃	TiO ₂	FeO	MnO	MgO	CaO	Na ₂ O	K ₂ O	Cl
Average	51.74	12.58	4.12	13.26	0.17	5.39	9.24	2.79	0.85	0.02
Maximum	53.25	12.89	4.27	13.54	0.22	5.89	9.44	3.00	0.87	0.03
Minimum	50.11	12.10	3.97	13.07	0.14	4.78	9.04	2.46	0.79	0.01
2σ	2.14	0.51	0.16	0.32	0.04	1.56	2.41	0.2	0.04	0.01
% 2σ	4.15	4.08	3.91	3.82	23.70	12.78	2.34	8.34	4.69	61.57
Reference value	51.01	12.47	4.12	13.35	0.20	5.05	9.23	2.68	0.84	0.02
% offset	1.43	0.88	0.09	-0.66	-14.00	6.89	0.17	4.40	1.19	17.07

Table 3.6 Correction factors calculated for individual analysis sessions to correct for machine drift.

Correction Factor	SiO ₂	Al ₂ O ₃	TiO ₂	FeOt	MnO	MgO	CaO	Na ₂ O	K ₂ O	Cl
A	1.00	0.99	1.08	1.00	1.00	0.88	1.00	1.07	0.98	0.72
B	1.00	1.02	1.07	1.05	1.47	1.02	1.01	0.94	1.02	0.99
C	1.01	1.00	1.09	1.04	1.00	0.84	0.99	0.98	1.01	1.11
D	0.99	0.99	1.00	0.99	0.96	0.99	0.96	1.05	0.96	1.00
E	1.01	1.00	1.15	1.00	-	0.89	0.99	0.99	1.01	0.97
F	0.97	0.98	1.08	1.04	-	0.92	0.93	0.95	1.01	1.09

3.4.3 Laser Ablation Inductively Coupled Mass Spectrometry

Trace element compositions of individual glass shards were measured using an Agilent 7500CS octopole ICP-MS at Victoria University of Wellington. The minor and trace elements analysed are presented in Table 3.7 along with the analytical conditions. Internal standards used for this study were Si (²⁹Si) and Ca (⁴³Ca), which were determined from EPMA analysis. Due to conflicting results from mono-isotopic measurements of some elements, multiple isotopes for some elements (⁸⁶Sr, ⁸⁸Sr, ⁹⁰Zr, ⁹¹Zr, ¹⁵¹Eu, ¹⁵³Eu) were measured in later runs to provide confidence in trace element measurements. Standards were run in between each sample to measure for any machine drift.

Laser ablation analyses were generally attained using a 35 µm static spot in order to counterbalance low sensitivity at a repetition rate of 5 Hz and laser power at 85%. Further machine parameters are presented in Table 3.7. Three different calibration standards were used. ATHO was initially used for tephra layers with SiO₂ compositions > 63%. Many of these samples had to be reanalysed however due to machine fluctuation compromising the data. When these samples were re-run, NIST612 (Jochum *et al.*, 2011) was used as a calibration standard. For tephra layers with SiO₂ contents <63%, BCR-2G was used. Si was used as the internal standard for samples with SiO₂ contents > 63%, as Ca was low in abundance in the more evolved glasses. Ca was used as the internal standard for samples with SiO₂ contents <63%.

Table 3.7 LA ICP-MS instrumental and analytical operating parameters

ICP-MS	
System	Agilent 7500 octopole
Detection Mode	Pulse and analog
Ablation mode	Spot
Laser power	85%
Repetition rate	5Hz
Spot size	35 µm
Analysis	
Background acquisition	60s
Sample acquisition	60s
Washout times	70s
Measured isotopes	⁷ Li, ²³ Na, ²⁴ Mg, ²⁹ Si, ⁴³ Ca, ⁴⁴ Ca, ⁴⁵ Sc, ⁴⁷ Ti, ⁵¹ V, ⁵³ Cr, ⁵⁵ Mn, ⁵⁹ Co, ⁶⁰ Ni, ⁶³ Cu, ⁶⁶ Zn, ⁷¹ Ga ⁸⁵ Rb, ⁸⁶ Sr, ⁸⁸ Sr, ⁸⁹ Y, ⁹⁰ Zr, ⁹¹ Zr, ⁹³ Nb, ⁹⁵ Mo, ¹³³ Cs, ¹³⁸ Ba, ¹³⁹ La, ¹⁴⁰ Ce, ¹⁴¹ Pr, ¹⁴⁶ Nd, ¹⁴⁷ Sm, ¹⁵¹ Eu, ¹⁵³ Eu, ¹⁵⁷ Gd, ¹⁵⁹ Tb, ¹⁶³ Dy, ¹⁶⁵ Ho, ¹⁶⁶ Er, ¹⁶⁹ Tm, ¹⁷² Yb, ¹⁷⁵ Lu, ¹⁷⁸ Hf, ¹⁸¹ Ta, ¹⁸² W, ²⁰⁸ Pb, ²³² Th, ²³⁸ U
Tuning	
Tuning standards	ATHO, BCR-2G, NIST612
Monitored Isotopes during tuning	⁷ Li, ²⁴ Mg, ²⁹ Si, ⁴³ Ca, ⁸⁸ Sr, ¹³⁸ Ba, ²⁰⁸ Pb, ²³⁸ U
Calibration standards	ATHO, BCR-2G, NIST612
Oxide interference	248/232Th, typically <1.5%
Carrier gas (argon)	0.82-0.89 L/min
Ablation gas(helium)	80-91.5%
RF power	1500 W
Standards and calibration	
Calibration standards	ATHO, BCR-2G, NIST612
Internal standard	²⁹ Si or ⁴³ Ca
Precision/accuracy standard	ATHO, BCR-2G, NIST612
Standards and calibration	ATHO, BCR-2G, NIST612

3.4.3.1 LA ICP-MS data acquisition and processing

Abundances of individual trace elements were calculated relative to a bracketing standard (either ATHO-G, BCR-2G or NIST612), which was analysed under identical conditions. Trace element data collected from repeated analyses is presented in Tables 3.8, 3.9 and 3.10.

Data reduction was achieved using the software Iolite (version 2.15), which was developed at the University of Melbourne, Australia (Paton *et al.*, 2011). Iolite is a self-contained package for Igor Pro which was developed by Wavemetrics Incorporated. Iolite presents data collected from the LA ICP-MS (for this study) in graphical form versus time, and allows the user to view combinations of trace elements simultaneously as shown in Figure 3.5. This provides a unique framework to visually identify any potential problems with data points (Figure 3.6). Data integration periods are displayed visually as a box encompassing a selected time period of data and a 95% confidence window for the average value (Figure 3.6A). A more detailed discussion on the process and merits of using Iolite as a data reduction scheme is given in Paton *et al.* (2011).

In this study issues were encountered due to several factors as outlined below:

A. High Sr background levels

This is illustrated in Figure 3.6A. The Sr values even at background levels for analyses using the calibration standard NIST612, are orders of magnitude higher than is normal. This is an issue with the machine rather than standards, and for this study it is assumed that Iolite (using the background levels) corrects for this.

B. Small glass shards

Many of the glass shards analysed using LA ICP-MS were close to the 35 μm diameter of the laser beam. Small shards were found in this study to be thin, and often the laser beam would penetrate through the glass shard and into the underlying material (Figures 3.6B and 3.6C). Care was needed when processing the data to ensure that only the exposed glass shard was analysed, and that the underlying material was not included in the data processed.

In addition, often the diameter of the laser beam was the same size, or a little larger than the glass shard itself (Figure 3.4B). Data produced from these points was often questionable, as surrounding material (either glass shards or epoxy) was measured. If a clear peak was identifiable it was analysed, otherwise the glass shard data was discarded.

In some samples the shard size was not large enough to accommodate the laser spot size, which resulted in fewer shards being analysed. A minimum of 5 shards per sample were analysed, but often for the smaller samples the data was unusable, so only the useable data is presented in Appendix D. Some samples of interest were re-probed to gather more major element data, resulting in some samples having up to 29 analyses.

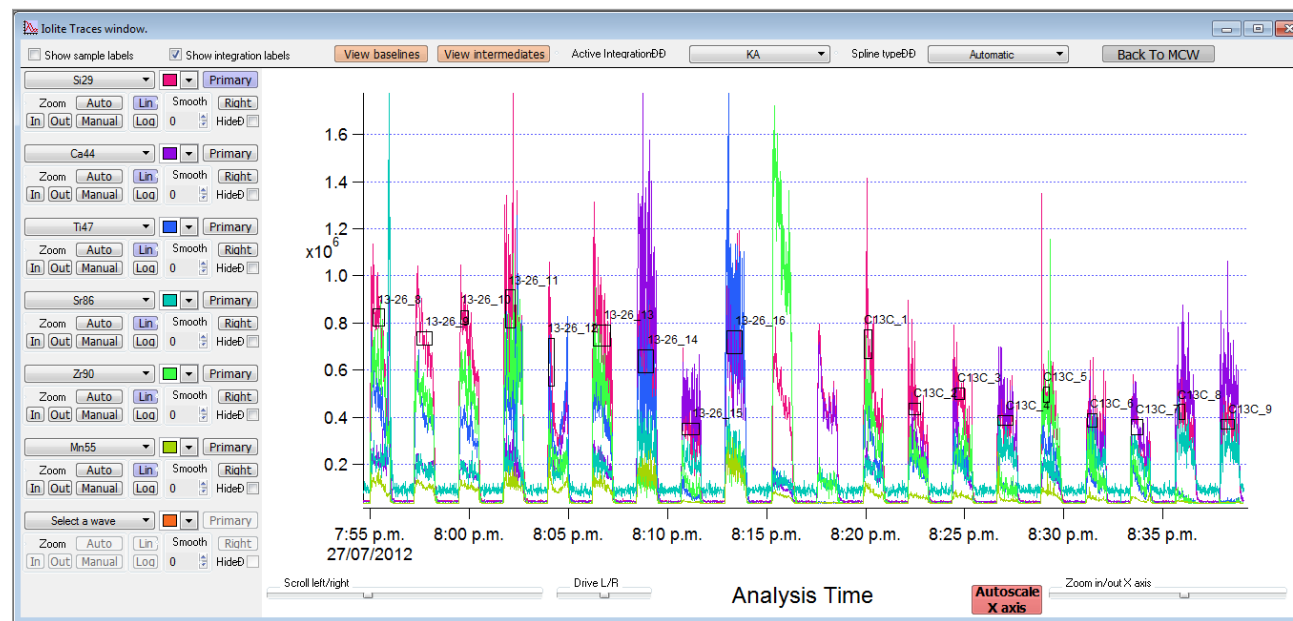
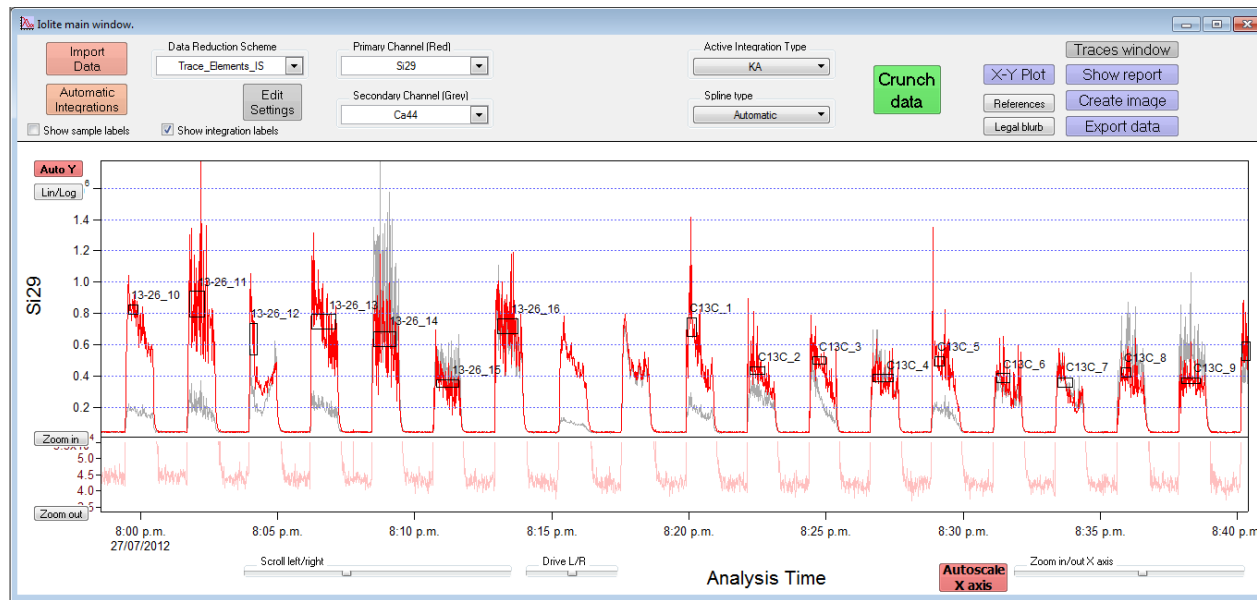


Figure 3.5 Image illustrating Iolite data display. The top image is of sample KA from the main screen while the bottom image is from the sample in the traces window screen. The traces window allows for more elements to be displayed, allowing for more accurate selection of data. Note the data is plotted versus time and the horizontal component of the data integration box represents the time period of data selected, and the vertical component represents the 95% confidence interval in the for the average value.

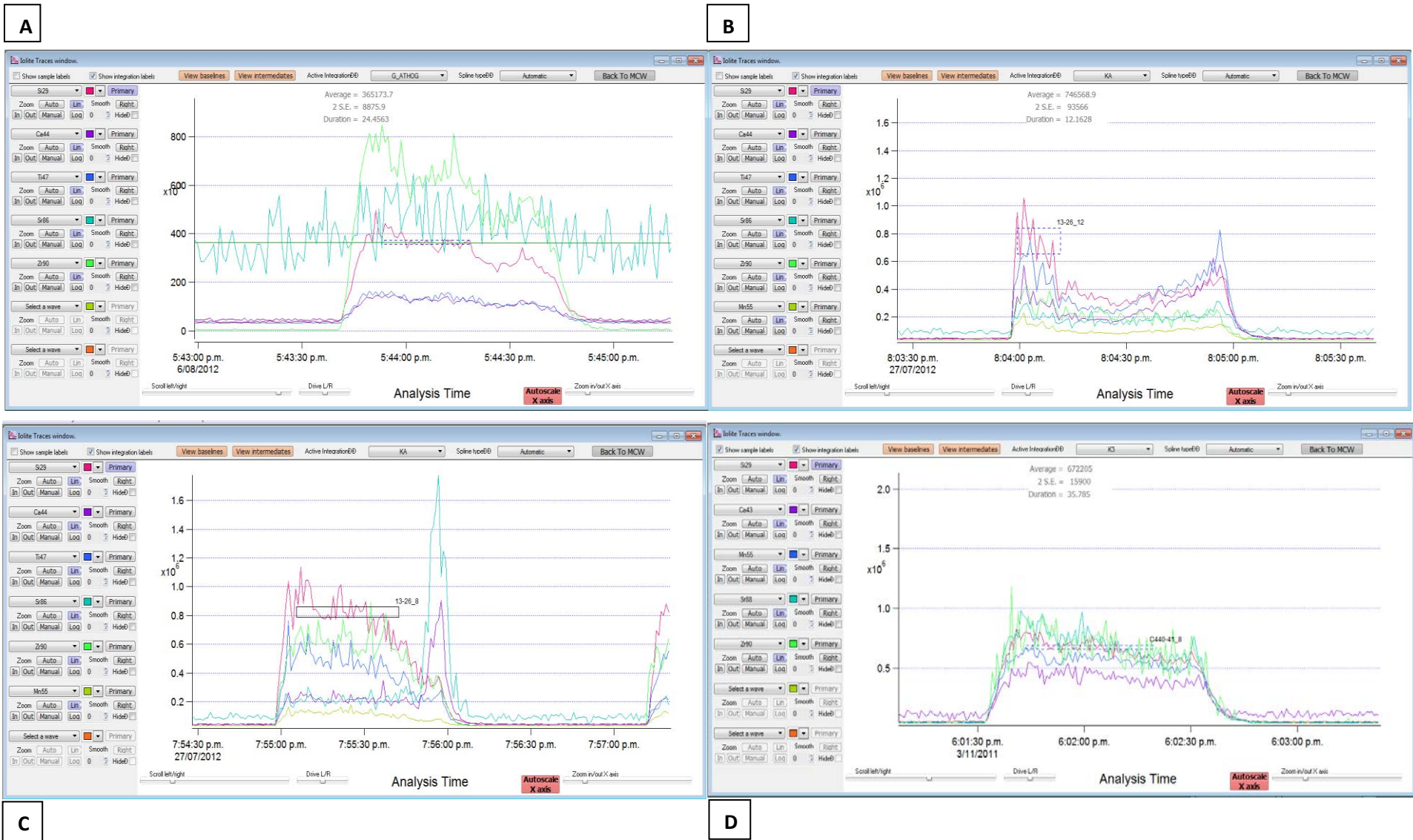


Figure 3.6 (A) Zoomed in image of an ATHO standard. Note the high ^{86}Sr background value. Above the selected time period of data the average, 2SE and duration of selection are displayed. (B) Image highlighting one of the strengths of visual processing of data. The peak of the trace element values declines rapidly then increases. The best explanation of this is that the laser beam has penetrated through the glass shard being analysed (the sharp drop of trace element values) and begins to analyse the underlying material (the trace element data begins to increase). (C) A similar process to (B), where the laser penetrates through the glass shard and begins to analyse the material beneath, here represented by a sharp peak in ^{44}Ca and ^{86}Sr values (has started to analyse an underlying feldspar). (D) Sample where all of the data represented is from a single glass shard, as the laser did not penetrate through the shard.

Table 3.8 LA ICP-MS precision and accuracy for international glass standard ATHO-G measured in this study. The reference value is taken from Jochum *et al.* (2006) and these values along with the mean and 2 standard errors are in parts per million

Rhyolitic glass ATHO-G (n = 84)							
	Mean	Maximum	Minimum	2 σ	Precision (% 2 σ)	Reference Value	Accuracy (% offset)
²⁹ Si	403885.9	633000.0	52700.0	254690.9	63.1		
⁷ Li	29.9	33.2	27.3	2.5	8.3	28.6	4.6
²³ Na	31737.9	33900.0	27470.0	3434.3	10.8		
²⁴ Mg	686.1	768.0	611.0	79.8	11.6		
⁴⁴ Ca	12219.3	12850.0	11540.0	513.5	4.2		
⁴⁵ Sc	8.9	11.6	6.8	2.3	25.9	7.0	26.5
⁴⁷ Ti	1673.4	2101.0	1317.0	259.3	15.5		
⁵¹ V	3.6	5.4	2.8	0.7	20.7	3.9	-7.9
⁵³ Cr	5.5	14.0	0.2	5.7	104.3	6.1	-9.7
⁵⁵ Mn	802.9	1015.0	576.0	123.7	15.4		
⁵⁹ Co	1.5	3.5	0.5	1.1	73.3	2.1	-30.4
⁶⁰ Ni	6.9	17.9	3.4	6.2	89.5	13.0	-46.7
⁶³ Cu	16.1	26.2	9.7	7.1	44.1	18.6	-13.2
⁶⁶ Zn	132.6	165.4	108.0	19.5	14.7	141.0	-6.0
⁷¹ Ga	21.4	26.3	18.2	3.7	17.4	25.3	-15.2
⁸⁵ Rb	63.4	70.9	54.6	8.5	13.4	65.3	-3.0
⁸⁶ Sr	92.0	115.0	69.0	18.9	20.5	94.1	-2.2
⁸⁸ Sr	182.0	248.0	109.0	71.4	39.2		
⁸⁹ Y	95.0	105.1	83.8	8.7	9.2	94.5	0.5
⁹⁰ Zr	530.7	631.0	466.0	60.0	11.3	512.0	3.6
⁹¹ Zr	522.1	638.0	457.0	82.3	15.8		
⁹³ Nb	65.5	85.4	56.5	8.1	12.4	62.4	5.0
⁹⁵ Mo	4.3	6.1	3.0	1.4	32.2	4.8	-10.1
¹³³ Cs	0.9	1.3	0.7	0.2	23.8	1.1	-14.2
¹³⁸ Ba	540.9	627.0	476.0	47.1	8.7	547.0	-1.1
¹³⁹ La	54.8	60.9	43.3	5.6	10.3	55.6	-1.5
¹⁴⁰ Ce	120.5	133.8	110.2	8.5	7.1	121.0	-0.4
¹⁴¹ Pr	14.2	15.8	12.4	1.2	8.3	14.7	-3.4
¹⁴⁶ Nd	60.6	69.9	50.1	7.6	12.5	60.9	-0.5
¹⁴⁷ Sm	14.8	18.1	11.6	2.7	18.3	14.2	3.9
¹⁵¹ Eu	2.7	3.3	2.2	0.4	14.2	2.8	-2.3

Table 3.8 continued.

Rhyolitic glass ATHO-G (n = 84)							
	Mean	Maximum	Minimum	2 σ	Precision (% 2 σ)	Reference Value	Accuracy (% offset)
¹⁵³ Eu	2.701429	3.15	2.04	0.404268	14.964975		
¹⁵⁷ Gd	14.94353	18.4	11.8	2.531224	16.938592	15.3	-2.329873
¹⁵⁹ Tb	2.489882	3.06	2.14	0.347816	13.969184	2.51	-0.8015
¹⁶³ Dy	17.12393	19.8	15.1	2.072275	12.101632	16.2	5.7032628
¹⁶⁵ Ho	3.598706	4.17	2.93	0.46679	12.971061	3.43	4.9185388
¹⁶⁶ Er	10.62988	12.84	9.1	1.373475	12.920895	10.3	3.2026995
¹⁶⁹ Tm	1.586118	1.85	1.31	0.258882	16.321747	1.52	4.3498452
¹⁷² Yb	10.65536	12.3	9	1.51924	14.257995	10.5	1.4795918
¹⁷⁵ Lu	1.535059	1.93	1.2	0.289542	18.861941	1.54	-0.320856
¹⁷⁸ Hf	13.82444	15.5	12.28	1.595299	11.539699	13.7	0.9083536
¹⁸¹ Ta	4.069176	4.65	3.44	0.548897	13.489138	3.9	4.3378582
¹⁸² W	8.74	10.7	7.21	1.367291	15.64406	9.3	-6.021505
²⁰⁸ Pb	5.261412	6	4.39	0.781349	14.850557	5.67	-7.206142
²³² Th	7.691176	8.43	6.98	0.62595	8.1385473	7.4	3.9348172
²³⁸ U	2.279036	2.62	2.03	0.273043	11.980623	2.37	-3.838137

Table 3.9 LA ICP-MS precision and accuracy for international glass standard BCR-2G measured in this study. The reference value is taken from Jacob (2006) and these values along with the mean and 2 standard errors are in parts per million

Basaltic glass BCR-2G (n = 201)							
	Mean	Maximum	Minimum	2 σ	Precision (% 2 σ)	Reference Value	Accuracy (% offset)
⁴³ Ca	27594.4	551000.0	6210.0	169284.4	628.5		
⁷ Li	9.0	10.2	8.2	0.7	7.3	9.5	-5.0
¹¹ B	228.0	437.0	50.0	180.1	79.0		
²⁴ Mg	21457.0	22680.0	20290.0	707.6	3.3	20980.0	2.3
²⁹ Si	248296.5	265900.0	49400.0	69925.0	28.2		
⁴⁵ Sc	33.0	35.5	30.9	1.6	4.8	33.2	-0.6
⁴⁷ Ti	14100.8	14950.0	13400.0	505.0	3.6	13667.0	3.2
⁵¹ V	425.1	448.0	408.0	15.7	3.7	421.0	1.0
⁵³ Cr	17.1	23.6	12.9	3.6	20.8	16.9	1.1
⁵⁵ Mn	1550.1	1648.0	1450.0	54.5	3.5	1526.0	1.6
⁶⁰ Ni	13.1	15.7	11.0	1.7	12.8	12.1	8.4
⁶³ Cu	21.1	24.5	18.2	2.2	10.3	21.8	-3.4
⁶⁶ Zn	125.0	137.1	116.0	7.4	5.9	147.0	-15.0
⁷¹ Ga	23.0	25.4	21.3	1.5	6.4		
⁸⁵ Rb	47.1	50.4	44.1	2.4	5.0	48.3	-2.6
⁸⁸ Sr	342.0	363.0	323.0	14.5	4.2	333.0	2.7
⁸⁹ Y	35.0	37.6	32.5	1.8	5.0	34.4	1.9
⁹⁰ Zr	183.8	193.8	170.0	8.4	4.6	184.0	-0.1
⁹³ Nb	12.5	13.8	11.1	0.9	7.6	13.1	-4.5
¹³³ Cs	1.2	1.4	1.0	0.1	11.0	1.2	0.3
¹³⁸ Ba	683.4	721.0	639.0	29.9	4.4	668.0	2.3
¹³⁹ La	24.7	26.6	23.2	1.3	5.1	24.3	1.8
¹⁴⁰ Ce	53.3	56.9	49.8	2.3	4.3	51.4	3.7
¹⁴¹ Pr	6.7	7.3	6.1	0.4	6.4	6.7	0.1
¹⁴⁶ Nd	28.9	31.5	26.3	1.8	6.4	28.2	2.6
¹⁴⁷ Sm	6.6	7.9	5.7	0.6	9.5	6.5	0.9
¹⁵³ Eu	2.0	2.2	1.7	0.2	9.2	2.0	1.2

Table 3.9 continued.

Basaltic glass BCR-2G (n = 201)							
	Mean	Maximum	Minimum	2 σ	Precision (% 2 σ)	Reference Value	Accuracy (% offset)
¹⁵⁷ Gd	6.7	7.7	5.9	0.7	10.7	6.6	1.2
¹⁵⁹ Tb	1.0	1.2	0.9	0.1	9.3	1.0	-1.6
¹⁶³ Dy	6.4	7.1	5.7	0.5	7.9	6.3	1.8
¹⁶⁵ Ho	1.3	1.4	1.1	0.1	9.7	1.3	-0.6
¹⁶⁶ Er	3.7	4.2	3.3	0.3	8.4	3.6	3.8
¹⁶⁹ Tm	0.5	0.6	0.4	0.1	14.7	0.5	2.7
¹⁷² Yb	3.4	4.0	3.0	0.4	11.7	3.3	2.1
¹⁷⁵ Lu	0.5	0.6	0.4	0.1	14.0	0.5	0.3
¹⁷⁸ Hf	4.8	5.5	4.3	0.5	9.5	4.8	0.3
¹⁸¹ Ta	0.8	0.9	0.6	0.1	12.4	0.8	2.4
¹⁸² W	0.5	0.8	0.3	0.1	28.7	0.6	-13.0
²⁰⁸ Pb	11.0	11.9	10.0	0.6	5.8	11.0	-0.1
²³² Th	5.9	6.4	5.6	0.3	5.4	5.9	-0.5
²³⁸ U	1.7	1.8	1.5	0.1	7.1	1.7	-2.2

Table 3.10 LA ICP-MS precision and accuracy for international glass standard NIST612 measured in this study. The reference value is taken from Jochum et al. (2011) and these values along with the mean and 2 standard errors are in parts per million (ppm)

Rhyolitic glass NIST612 (n = 78)							
	Mean	Maximum	Minimum	2 σ	Precision (% 2 σ)	Reference Value	Accuracy (% offset)
²⁹ Si	343717.1	666000.0	52100.0	324672.5	94.5		
⁷ Li	41.9	43.7	39.6	1.7	4.0	40.0	4.7
²³ Na	103003.8	107200.0	88100.0	6924.3	6.7		
²⁴ Mg	76.3	80.2	67.4	5.0	6.6	68.0	12.2
⁴⁴ Ca	84973.7	87000.0	82500.0	1849.4	2.2		
⁴⁵ Sc	40.5	43.0	32.3	4.1	10.2	39.9	1.5
⁴⁷ Ti	43.6	48.5	38.2	4.7	10.9	44.0	-0.9
⁵¹ V	39.1	42.9	36.7	2.1	5.4	38.8	0.9
⁵³ Cr	36.9	60.0	26.9	9.7	26.2	36.4	1.3
⁵⁵ Mn	38.0	43.4	32.2	3.8	9.9	38.7	-1.8
⁵⁹ Co	36.1	63.4	32.0	10.0	27.8	35.5	1.6
⁶⁰ Ni	41.3	97.5	34.5	19.0	58.5	38.8	6.4
⁶³ Cu	37.3	45.7	30.5	5.9	15.7	37.8	-1.4
⁶⁶ Zn	38.3	44.4	33.8	3.7	9.6	39.1	-2.0
⁷¹ Ga	36.4	44.0	34.2	3.7	10.1	36.9	-1.2
⁸⁵ Rb	31.5	35.2	29.2	2.2	6.8	31.4	0.3
⁸⁶ Sr	78.9	94.0	60.0	13.3	16.8	78.4	0.6
⁸⁸ Sr	75.8	84.4	36.9	19.5	25.7		
⁸⁹ Y	38.1	42.8	36.0	2.0	5.2	38.3	-0.5
⁹⁰ Zr	38.0	40.9	34.0	2.7	7.2	37.9	0.4
⁹¹ Zr	38.1	45.5	29.8	6.1	15.9		
⁹³ Nb	39.9	43.1	36.5	2.5	6.3	38.9	2.6
⁹⁵ Mo	38.1	45.7	32.3	4.3	11.3	37.4	1.9
¹³³ Cs	42.6	53.3	39.2	4.9	11.5	42.7	-0.3
¹³⁸ Ba	39.8	43.0	37.3	2.1	5.3	39.3	1.3
¹³⁹ La	35.9	39.5	33.3	2.2	6.1	36.0	-0.3
¹⁴⁰ Ce	38.7	41.2	35.5	2.0	5.1	38.4	0.8
¹⁴¹ Pr	37.3	40.4	33.7	1.9	5.1	37.9	-1.5
¹⁴⁶ Nd	35.9	40.3	33.0	2.1	5.8	35.5	1.1
¹⁴⁷ Sm	38.1	42.2	33.9	2.7	7.0	37.7	1.1
¹⁵¹ Eu	35.0	37.4	32.3	1.7	4.8	35.6	-1.8

Table 3.10 continued

Rhyolitic glass NIST612 (n = 78)							
	Mean	Maximum	Minimum	2 σ	Precision (% 2 σ)	Reference Value	Accuracy (% offset)
¹⁵³ Eu	34.9	37.0	30.6	2.0	5.7		
¹⁵⁷ Gd	36.9	41.9	31.4	3.2	8.7	37.3	-1.2
¹⁵⁹ Tb	36.1	38.4	31.9	1.8	5.1	37.6	-4.1
¹⁶³ Dy	35.9	38.2	32.6	1.9	5.2	35.5	1.1
¹⁶⁵ Ho	37.9	39.3	35.6	1.5	4.0	38.3	-1.1
¹⁶⁶ Er	38.0	40.9	35.3	2.0	5.2	38.0	0.0
¹⁶⁹ Tm	37.8	40.3	33.1	2.1	5.7	36.8	2.7
¹⁷² Yb	39.2	41.3	36.9	1.9	4.8	39.2	0.1
¹⁷⁵ Lu	37.0	39.4	35.1	1.7	4.5	37.0	0.0
¹⁷⁸ Hf	35.0	37.2	32.1	1.9	5.4	36.7	-4.6
¹⁸¹ Ta	40.0	42.3	37.8	1.6	3.9	37.6	6.4
¹⁸² W	40.2	43.5	37.6	2.2	5.5	38.0	5.7
²⁰⁸ Pb	38.8	43.0	36.1	2.3	6.0	38.6	0.5
²³² Th	37.7	39.5	36.2	1.4	3.8	37.8	-0.2
²³⁸ U	37.5	39.9	35.3	1.5	3.9	37.4	0.2

Chapter 4

Geochemistry results

4.1. Geochemistry of Kermadec arc tephra layers

In the collection of major-element analytical data, considerable care was taken in shard selection and culling of analyses that were considered suspect. The same approach was taken with the collection of trace element data. A description of the analytical methods used is given in Chapter 3. Major element data for each samples is given in Appendix C and trace element data for each shard analysed is given in Appendix D.

4.1.1. Classification of Kermadec arc tephra layers

Major element data reveal that the tephra layers in this study have a broad range of compositions, with the dominant bulk compositions of the tephra layers being basaltic-andesite and rhyolite (Figure 4.1). Individual shards show a wider range in composition, varying in SiO₂ content from basalt to rhyolite as defined on the total alkali-silica (TAS) diagram (Figure 4.2). Notably, while bulk tephra compositions display a strong bimodal composition, individual glass shard analyses show a more even distribution that includes andesitic and dacitic compositions.

For the most part, the glass shards display a positive correlation between K₂O and SiO₂ and a negative correlation between CaO and SiO₂ (Figure 4.3 and figures in section 4.1.2). Lower SiO₂ shards (basalt-andesite) show a range of K₂O values between 0.25–1.80 wt%, while higher SiO₂ shards (dacite-rhyolite) show a range in values from 0.45–2.75 wt%. The samples display a medium-K trend and a low-K trend as identified in Shane and Wright (2011) (classified in their study as high-K and low-K, respectively) and Barker *et al.* (2013), which becomes more evident with increasing SiO₂ contents. Most of the tephra layers analysed have chemistries that plot in the tholeiite field (Figure 4.4) and also fall in this field when plotted on an AFM diagram (after Irvine and Baragar, 1971), an alkali index vs. Al₂O₃ diagram (after Wilson, 1989), or K₂O – FeO*/MgO diagram (after Gill, 1981).

Samples examined in this study are taken to represent a single tephra unit and tephtras which are homogeneous (show < 8 wt% variation in the SiO₂ content) are inferred to represent a single eruptive event. Exceptions to this are tephtras which are found to be correlatives (tephtras from different cores erupted in the same event), which is discussed further below and heterogeneous or bimodal tephtras. These will be discussed further in Chapter 6.

Sample names for tephtras collected in this study are listed as the core number, followed by the depth location of collection (in cm's), e.g. C4 24.5-25.5. Samples reanalysed from Shane and Wright (2011) are notated as the core number and depth to the base of the tephra unit (in cm's), e.g. 2-33.

Glass shards from the collected clasts were analysed for this study, and the results are presented within the core the clast was preserved in.

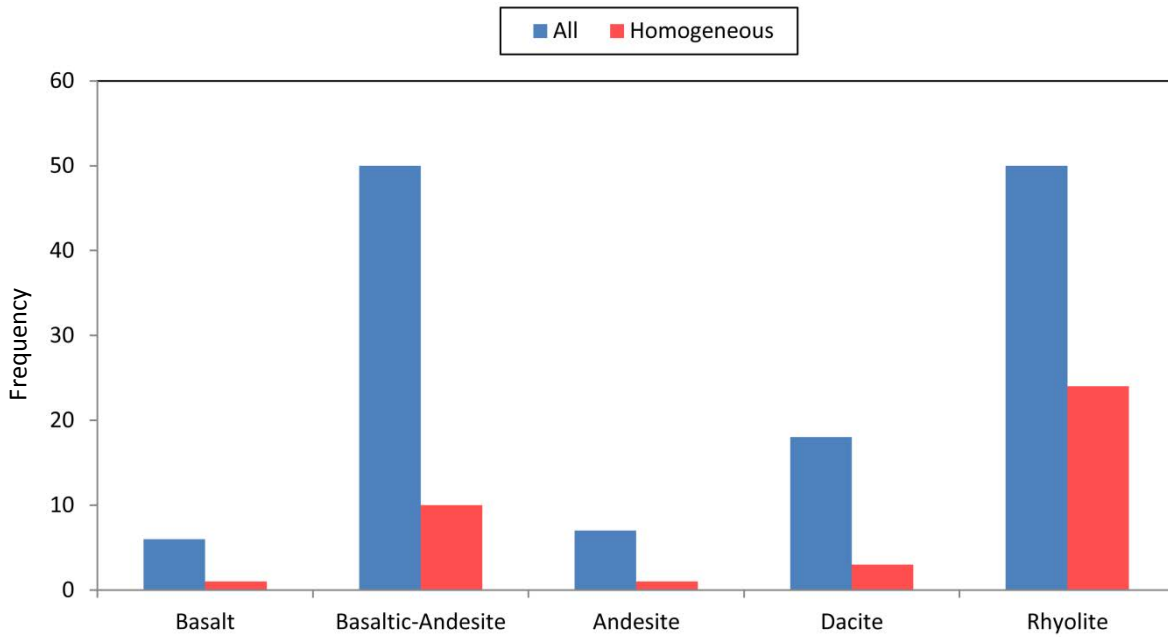


Figure 4.1 Diagram showing the dominant bulk compositions of the samples analysed in this study. Note that the blue data is for all samples; where a sample showed two distinct populations they were both plotted (data presented in Appendix B). The red plots are homogeneous samples only, which show that basaltic-andesite and rhyolite are the two dominant modes.

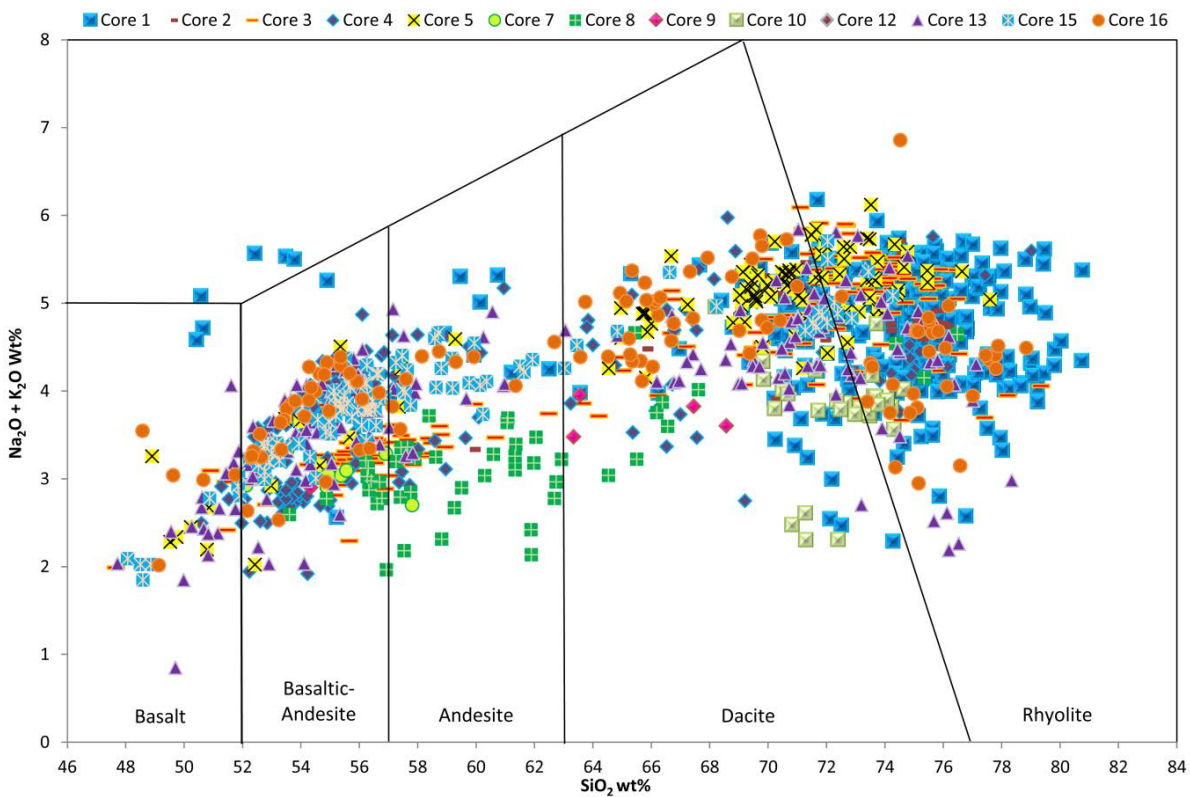


Figure 4.2 Total Alkalis – Silica (TAS) diagram displaying the values for individual glass shards in each core. Note the higher abundances of rhyolite and basaltic-andesite compositions, while noting that there is not a clear gap in the andesite compositional range. Compositional boundaries are from Le Maitre *et al.* (1989).

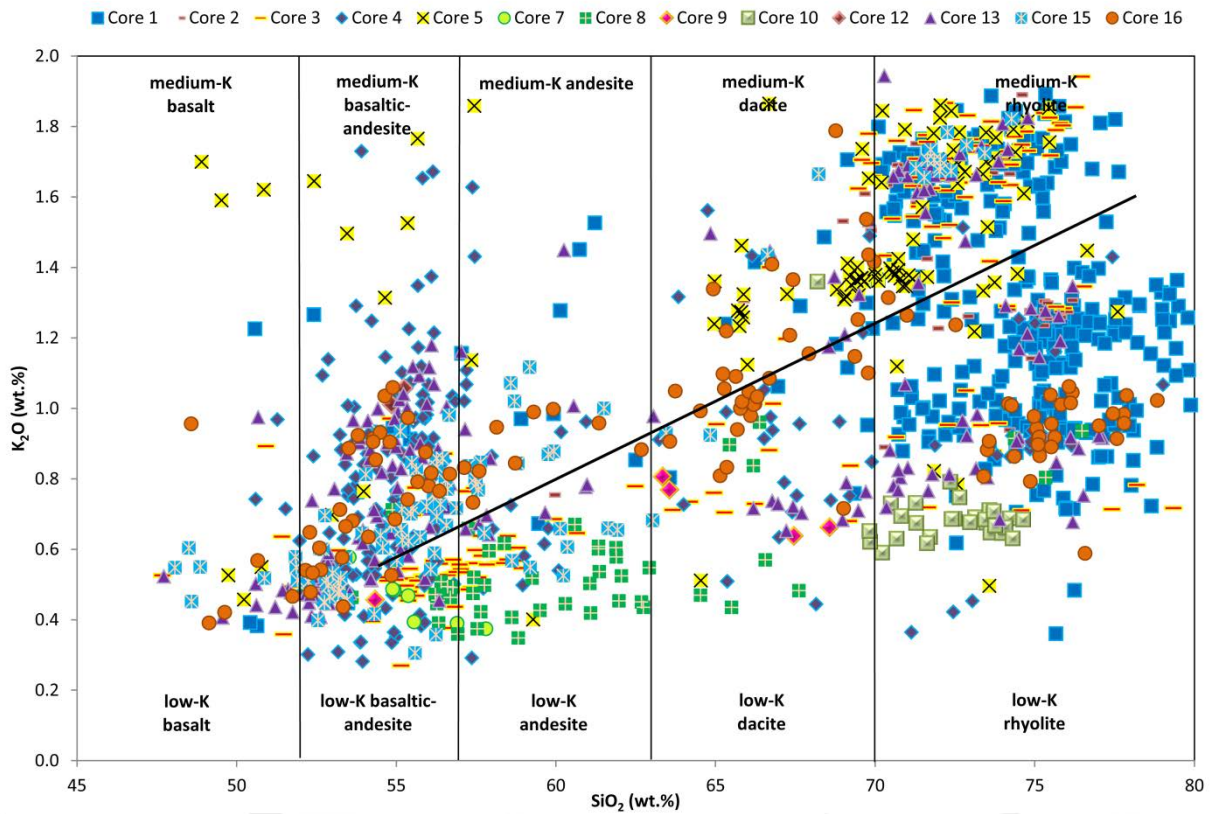


Figure 4.3 Diagram showing the range in SiO_2 vs. K_2O contents from individual glass shards from each of the cores. Compositional boundaries are taken from Miyashiro (1974).

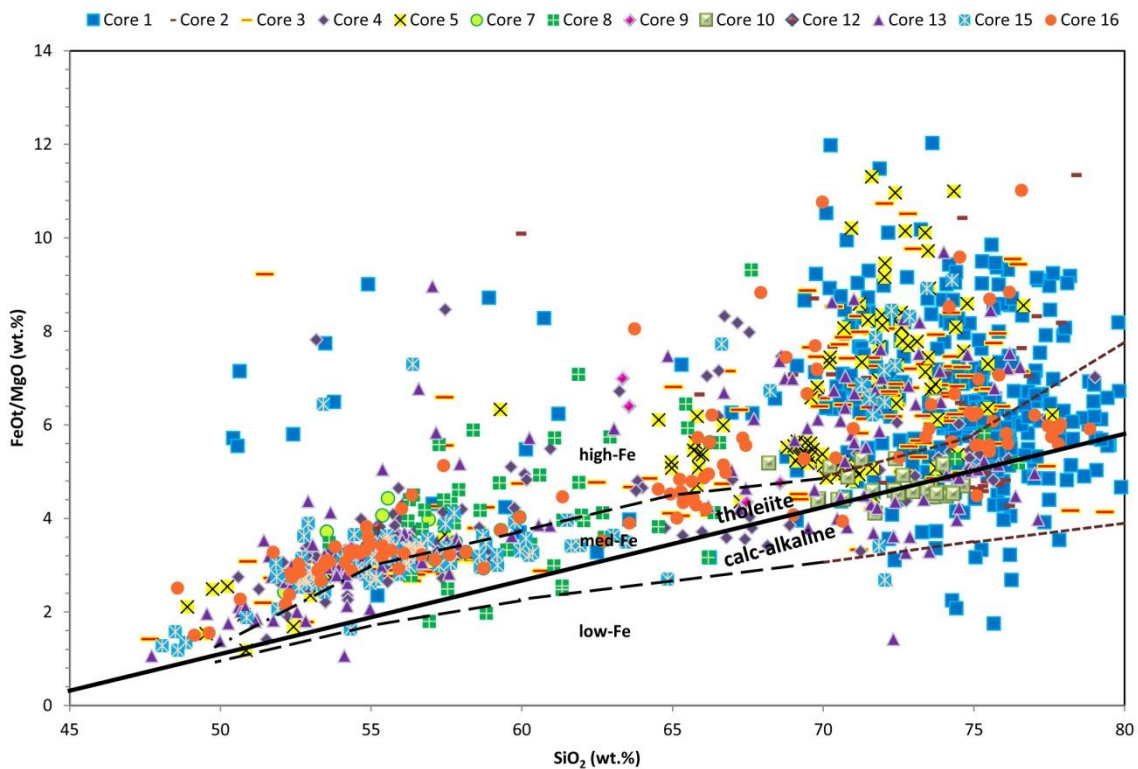


Figure 4.4 Diagram displaying SiO_2 vs. FeOt/MgO (wt %) for individual glass shards in each core. Dashed lines denote boundaries between low-Fe, medium-Fe and high-Fe groups. Boundaries between 50-70 wt % SiO_2 were taken from Arculus (2003) and between 70-80 wt % calculated using an equation from Arculus (2003). The dividing line between tholeiite and calc-alkaline compositions was calculated from Wilson (1989).

4.1.2 Major element chemistry

4.1.2.1. Raoul cores

Cores TAN0706-1 to TAN0706-10 were collected from transects west and east of Raoul Island (see Figure 1.2). In general, Raoul tephtras display K_2O contents between 0.2-1.95 wt %. The cores also show typical fractionation trends, with a distinct negative correlation between SiO_2 and CaO or MgO . A general overview of the geochemical trends for each of the cores is given below, with further information for any divergent samples.

Core 1 (80.1 km West) – Although TAN0706-1 is the most distal core, it contains the most tephtra layers. A total of 18 samples were analysed from this core, of which 14 were found to be homogeneous and thus likely to represent discrete events. The vast majority of the tephtra layers are rhyolitic.

Tephtras from Core 1 divide into two trends which correlate with stratigraphic position within the core. The younger samples (C1 39-40 to 1-97) are tholeiitic, high-Fe, medium-K, and have higher FeO/MgO contents relative to the stratigraphically older tephtras. Older tephtra layers (C1 158-159 to C1 302-303, but excluding C1 177-178) cluster on the boundary between tholeiite and calc-alkaline fields, are medium-Fe, low-K and have low FeO/MgO . Tephtra layers C1 269-270-C1 296-297 are potentially sourced from the same eruption, as they have identical major element concentrations. Trace elements may be able to distinguish between them, and this will be investigated below.

Shards from tephtra 1-97 shows two divergent parallel trends, one medium-K the other low-K. Variations in CaO show a tight cluster of rhyolitic, low- Ca shards with a distinct, near horizontal trend. The rest of the shards in this sample show a typical negative correlation between CaO and SiO_2 . The horizontal trending shards are slightly higher in CaO than the older tephtras in the core but follow an identical trend. Tephtra C1 114-115 has similar K_2O contents to the older tephtra layers, but CaO and FeO/MgO contents are similar to the younger tephtras, making this tephtra distinctive in its age group. Tephtra C1 177-178 is heterogeneous with SiO_2 contents between 57-79 wt %. With the exception of three shards (which are similar geochemically to the older tephtras), the compositions are medium-K, high-Fe and show a negative correlation between CaO or MgO against SiO_2 .

Core 2 (65.4 km West) – The single tephtra in Core 2 (2-33) contains predominantly medium-K, high-Fe shards, with the exception of two outliers. C2 10cm clast displays low-K, medium-Fe and straddles the boundary between tholeiitic and calc-alkaline. C2 19cm clast is a high-Fe tholeiitic and is low-K.

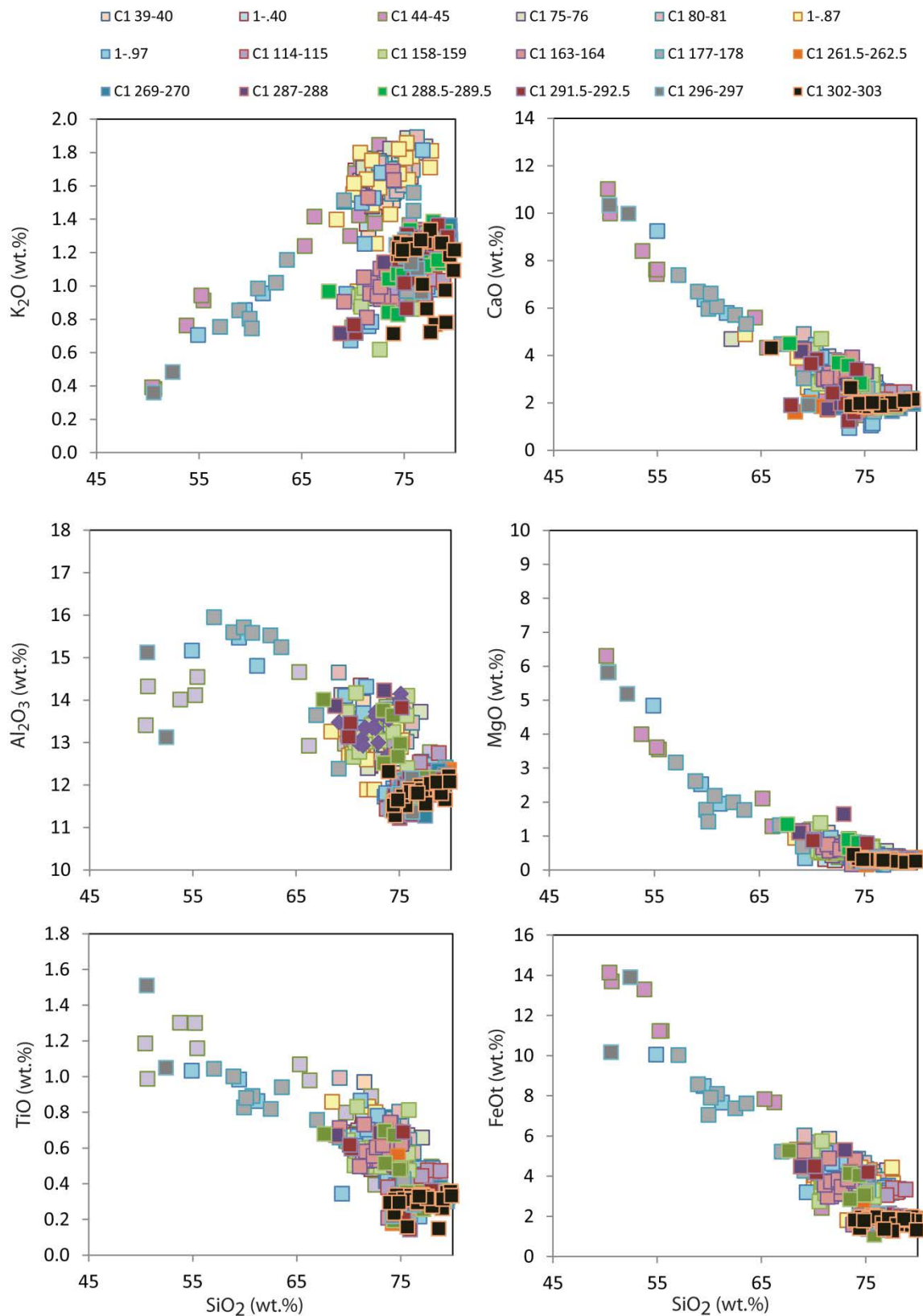


Figure 4.5 Variation diagrams of selected major oxides against SiO_2 for samples in core TAN0706-1. All analyses have been corrected for machine drift as outlined in Chapter 3. Raw data is presented in Appendix C. Lighter samples are stratigraphically younger, with symbol colours darkening down-core. Each point represents a single glass shard, and their depth is in cms.

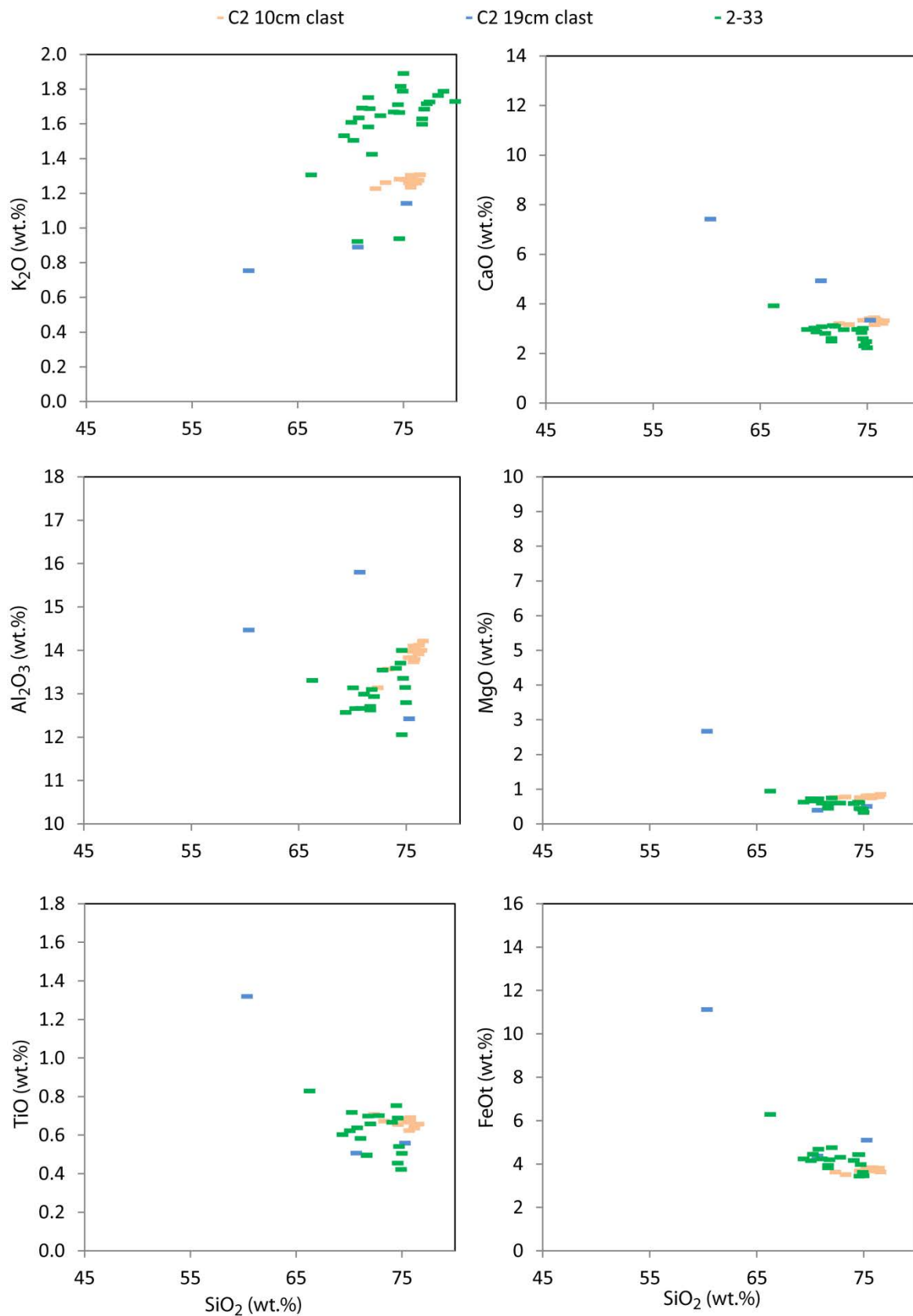


Figure 4.6 Variation diagrams of selected major oxides against SiO₂ for samples in core TAN0706-2. All analyses have been corrected for machine drift as outlined in Chapter 3. Raw data is presented in Appendix C. Lighter samples are stratigraphically younger, with symbol colours darkening downcore. Each point represents a single glass shard, and their depth is in cms.

Core 3 (57.2 km West) – A total of nine samples were analysed from Core 3, with seven of them showing a wide range in SiO₂ contents (Table 4.2). The majority of the shards analysed are tholeiitic, and the tephra divide into either a medium-K or low-K trend.

Shards from tephra 3-15 display a range in SiO₂ contents from 55-73 wt % and plot on the high-Fe and medium-Fe tholeiitic boundary. All of the shards in this tephra are low-K and there is a generally positive correlation between K₂O and SiO₂ contents, as well as a negative correlation between CaO, MgO and FeO_t and SiO₂. Tephra C3 24.5-25.5 is predominantly in the high-Fe tholeiitic range, but with a few shards in the calc-alkaline range. The tephra is homogeneous in terms of its SiO₂ content but shows a range in FeO_t and K₂O at similar silica contents. The majority of shards from this tephra are medium-K and show a general positive correlation between K₂O and SiO₂, but six shards are divergent from the bulk of the tephra, and plot in the low-K range and show a near horizontal positive correlation. These are the same shards which have lower Fe values than the rest of the sample. Most of the shards in tephra C3 27.5-28.5 are medium-K, with three outliers following the same trend as described above for shards from C3 24.5-25.5. Tephra C3 29-29.5 is a homogeneous tephra with medium-K and high-Fe values.

Core 4 (58 km West) – Tephra shards analysed from Core 4 show a range in SiO₂ contents from 50-79 wt % and are generally high-Fe, tholeiitic, medium-K basaltic-andesites, with the exceptions listed below.

Tephra C4 24-25 is low-K with shards ranging from 51-78 wt % SiO₂. Most of the shards form a positive correlation between SiO₂ and K₂O, with the exception of three mafic shards. Tephra C4 40-41 ranges in SiO₂ content from 53-71 wt % with the basaltic-andesite shards having low-K and the higher SiO₂ shards straddling the low-K/medium-K boundary. C4 51.5cm clast has a unique major element composition, distinguishing it from the other samples analysed in the core, as it is low-K, medium-Fe in composition, and straddles the boundary between the tholeiitic and calc-alkaline fields. Shards from tephra C4 62-63 are predominantly low-K basaltic-andesites, with the exception of one low-K rhyolite shard. Tephra 4-84 is a low-K, high-Fe sample, with the bulk of the sample having SiO₂ contents between 53-63 wt %. The exception to this is two high SiO₂ shards that plot in a different trend to the rest of the sample in terms of the major oxides. Tephra 4-120 displays bimodality in terms of SiO₂ content, K₂O content and FeO_t content. The lower silica shards plot in the tholeiitic high-Fe, medium-K range, and the higher silica shards plot in the calc-alkaline med-Fe, low-K range range. C4 144.5-145.5 shards vary in SiO₂ content from 52-71 wt %. With increasing SiO₂ content two distinct trends emerge, one low-K and high-Al, the other medium-K. The low-K shards straddle the boundary between tholeiitic and calc-alkaline.

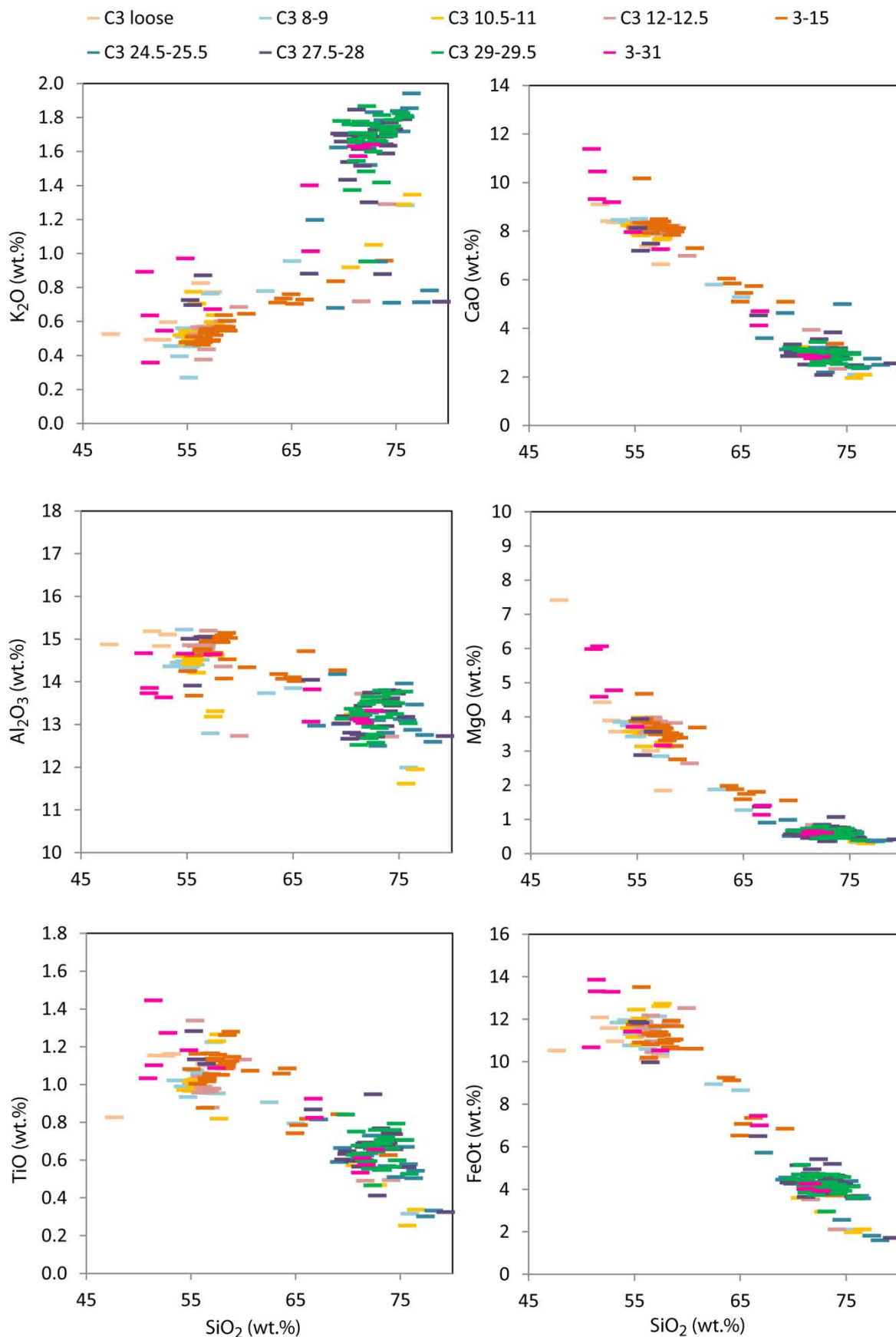


Figure 4.7 Variation diagrams of selected major oxides against SiO_2 for samples in TAN0706-3. All analyses have been corrected for machine drift as outlined in Chapter 3. Raw data is presented in Appendix C. Lighter samples are stratigraphically younger, with symbol colours darkening downcore. Each point represents a single glass shard, and their depth is in cms.

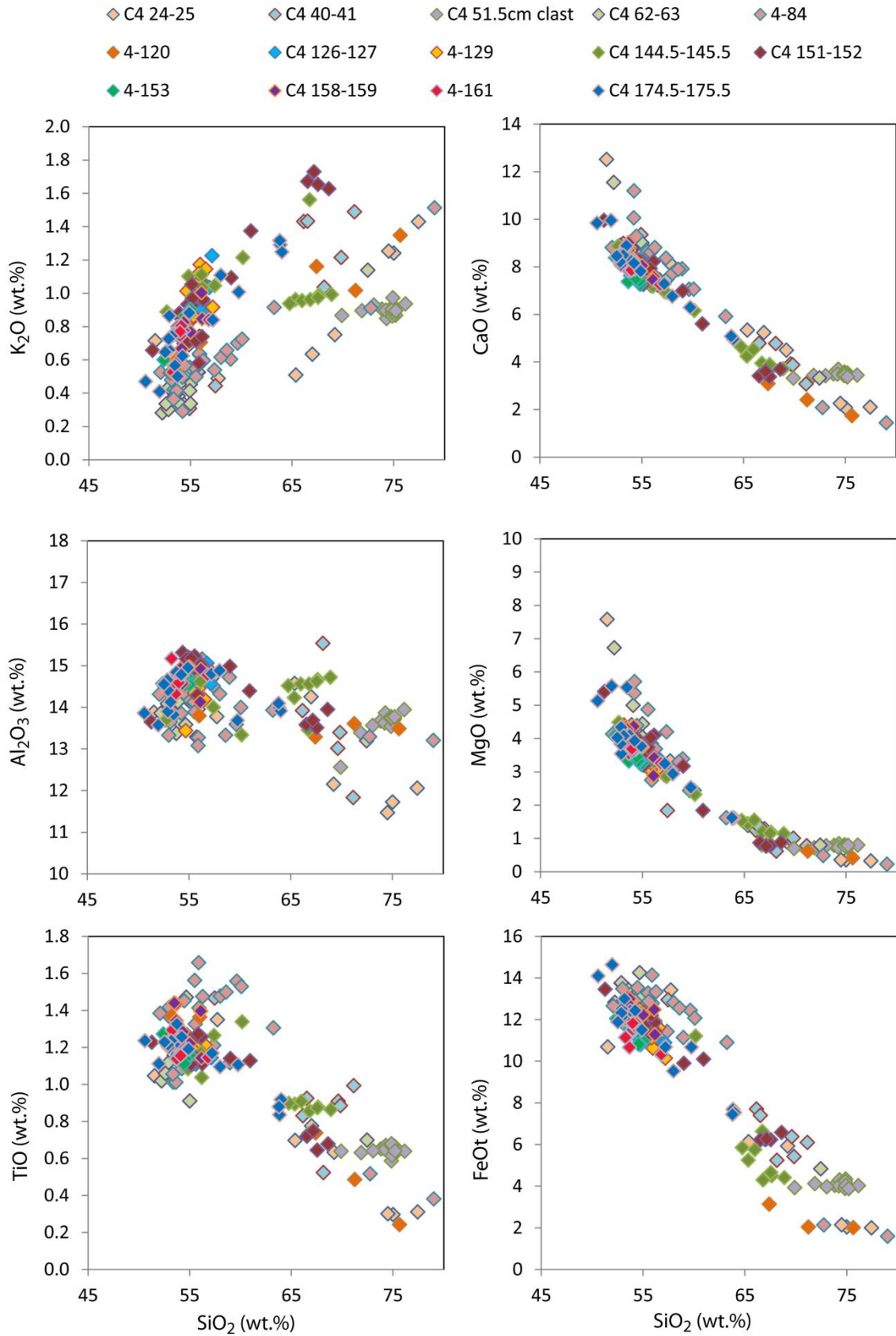


Figure 4.8 Variation diagrams of selected major oxides against SiO_2 for samples in TAN0706-4. All analyses have been corrected for machine drift as outlined in Chapter 3. Raw data is presented in Appendix C. Lighter samples are stratigraphically younger, with symbol colours darkening downcore. Each point represents a single glass shard, and their depth is in cms.

Core 5 (45.9 km West) – Tephra in Core 5 range in SiO₂ from 49-78 wt % and are predominantly medium-K, high-Fe. Sample 5-6 and the C5 4 cm clast are very similar in composition in all of the major oxide diagrams and form a trend distinct to the other tephra.

Cores 7 & 8 (47.6 km East) – Cores 7 and 8 were collected from the same location (Core 7 collection was unsuccessful so Core 8 was sampled in the same location) so the data are presented together. All of the shards analysed from cores 7 and 8 are low-K, with the one exception mentioned below. Samples range from 52-77 wt % SiO₂, with most of the shards being basaltic-andesitic or andesitic. Most of the samples are high-Fe tholeiitic, with the exception of C8 7-7.5 which plots along the high-Fe/medium-Fe boundary. A few outlier shards from other samples are also in the medium-Fe range. Tephra C8 1-2 has two outlier shards, which have higher silica content, are medium-K and calc-alkalic.

Cores 9 – Shards from Core 9 are all low-K, high-Fe tholeiitic. Two shards with SiO₂ values of 63 wt % have much higher Fe content than the other shards and form different major element trends to the other shards in the sample.

Core 10 (20.4 km East) - Both samples in Core 10 are predominantly medium-K, with C10 6-7 being medium-Fe calc-alkaline and C10 7-8 being tholeiitic. Tephra C10 7-8 straddles the boundary between medium and high-Fe.

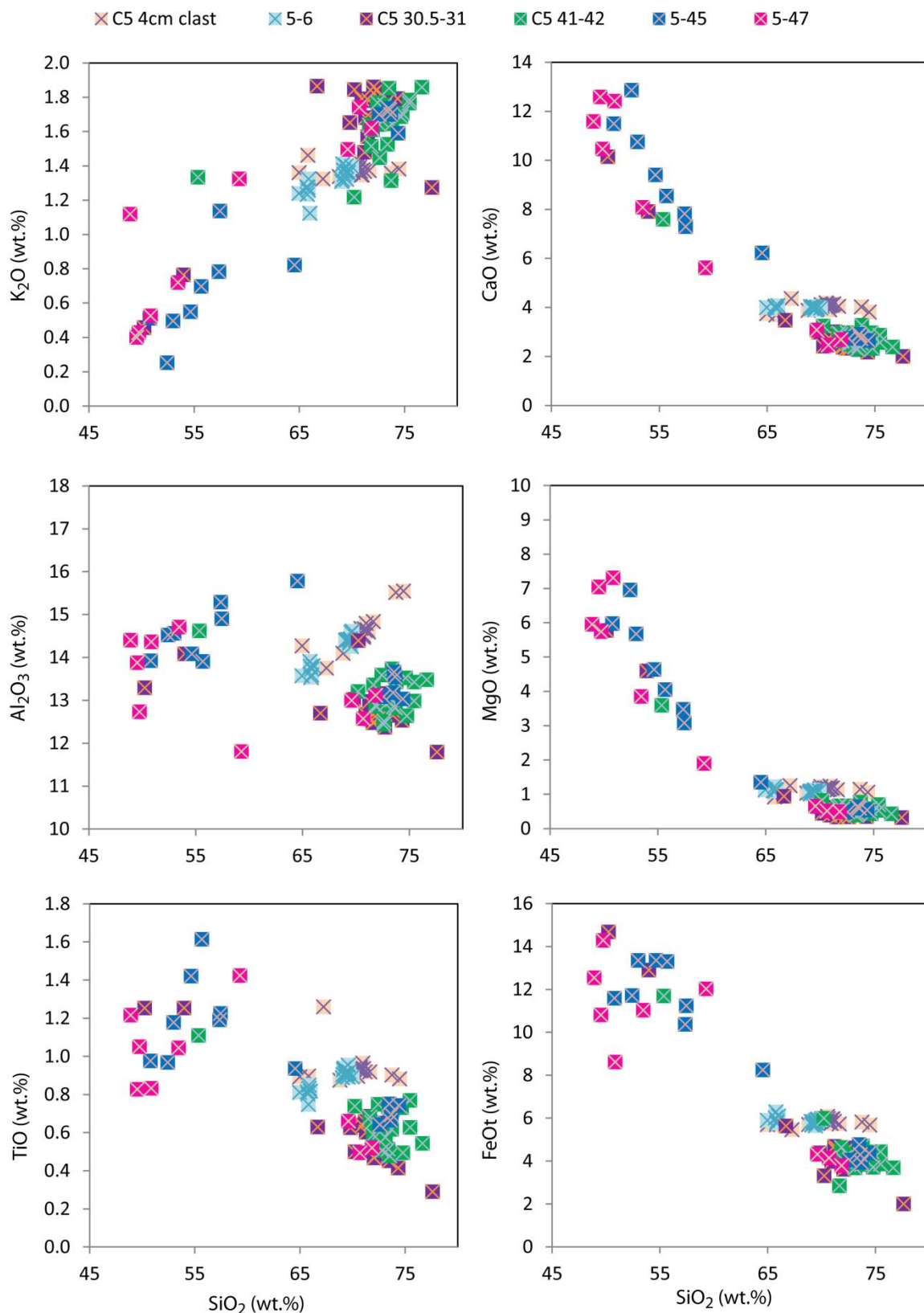


Figure 4.9 Variation diagrams of selected major oxides against SiO₂ for samples in TAN0706-5. All analyses have been corrected for machine drift as outlined in Chapter 3. Raw data is presented in Appendix C. Lighter samples are stratigraphically younger, with symbol colours darkening downcore. Each point represents a single glass shard, and their depth is in cms.

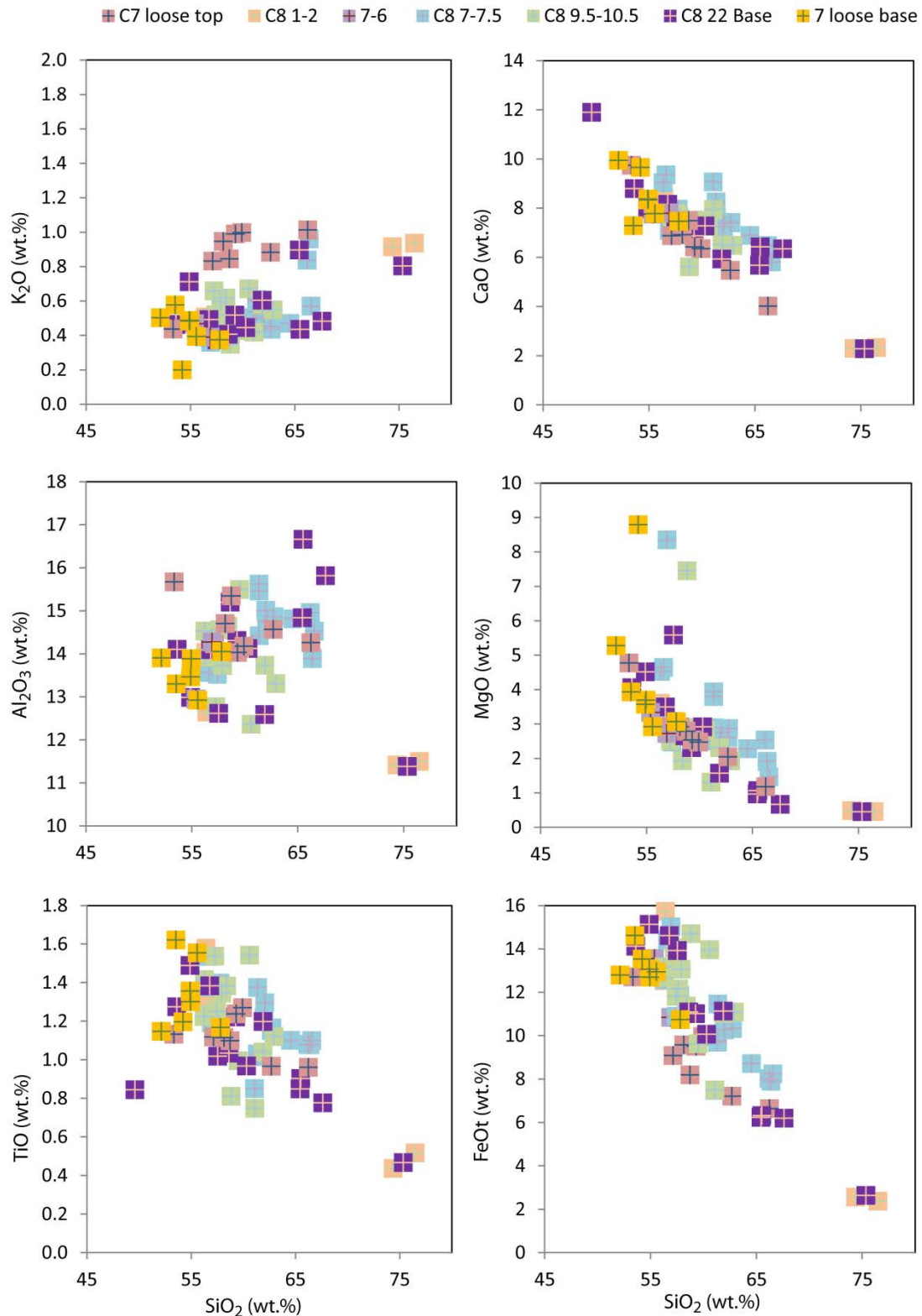


Figure 4.10 Variation diagrams of selected major oxides against SiO₂ for samples in TAN0706-7 & 8. All analyses have been corrected for machine drift as outlined in Chapter 3. Raw data is presented in Appendix C. Lighter samples are stratigraphically younger, with symbol colours darkening downcore. Each point represents a single glass shard, and their depth is in cms.

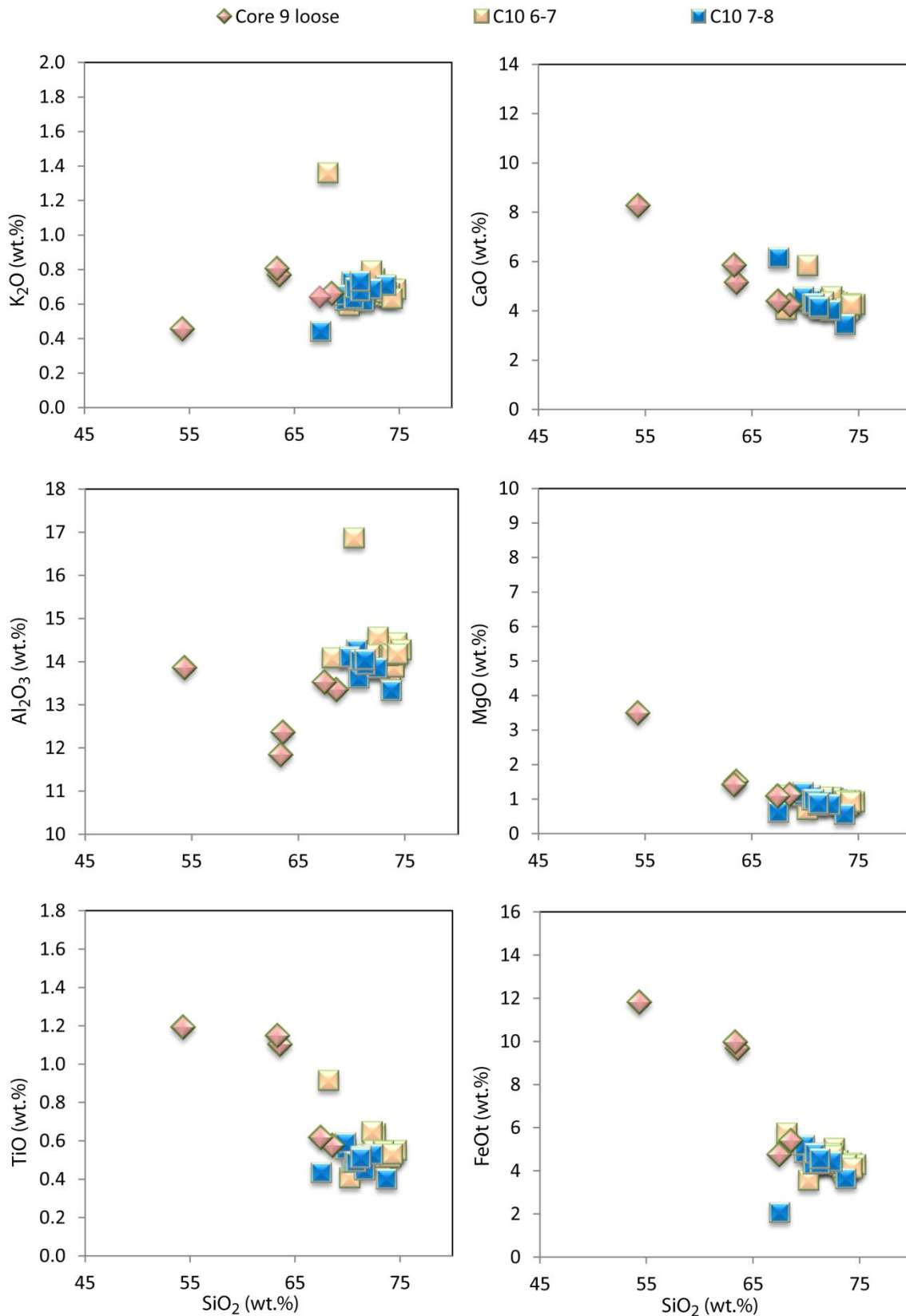


Figure 4.11 Variation diagrams of selected major oxides against SiO_2 for samples in TAN0706-9 & 10. All analyses have been corrected for machine drift as outlined in Chapter 3. Raw data is presented in Appendix C. Lighter samples are stratigraphically younger, with symbol colours darkening downcore. Each point represents a single glass shard, and their depth is in cms.

4.1.2.2. Macauley cores

Cores TAN0706-12 to TAN0706-16 were collected from transects west and east of Macauley Island (Figure 1.2). In general, Macauley cores show distinct medium-K and low-K trends at higher SiO₂ contents (>65 wt. %) which are less distinct at lower SiO₂ values. Like the samples from the Raoul cores, they also show typical fractionation trends with a positive correlation between K₂O and SiO₂ and negative correlations between CaO and MgO and SiO₂.

Core 12 - Only two shards from Core 12 were analysed. Both of the shards are low silica, high-K and high-Fe tholeiitic.

Core 13 (32.6 km East)- Tephra shards from Core 13 show a range in SiO₂ content from 47-78 wt %, and are predominantly medium-K, high-Fe tholeiitic, with the exceptions mentioned below.

Tephra 13-26 shows a range in SiO₂ content from 51-76 wt %, with lower silica shards displaying a large range in K₂O values from 0.2-1.2 wt %, whereas higher silica shards cluster together with K₂O values of 1.6-1.9 wt %. There are two anomalous shards, which have silica values around 70 wt % and K₂O values of 0.6 wt %. Tephra 13-33 ranges in silica content from 53-78 wt % and is predominantly low-K, with Fe contents ranging from high-Fe to medium-Fe. Most of the shards are tholeiitic, but those with medium-Fe contents straddle the tholeiite/calc-alkalic boundary. Two shards from 13-51 plot in the medium-Fe calc-alkalic range. The higher silica shards are low-K, with the lower silica shards having higher K values than the more evolved shards. C13 clast is medium-Fe calc-alkalic with K contents that straddle the low-K – medium-K boundary.

Core 15 (24.2 km East) –Tephra shards range in SiO₂ content from 48-75 wt % and are predominantly basaltic-andesitic, medium-K tholeiitic, with the higher silica shards being high-K, and the lower silica shards straddling the medium-Fe/high-Fe boundary. The tephtras in this core show a well defined fractionation trend, especially highlighted in the SiO₂ vs. CaO plot.

Tephtras C15 6-7 and C15 18-19 show shards ranging from low-Fe to high-Fe and from calc-alkaline to tholeiite. C15 0-1 and C15 3-4 have shards showing both medium-Fe and high-Fe; both are tholeiitic.

Core 16 (66.7 km West) - Tephra shards in Core 16 range from 48-79 wt % SiO₂ and are predominantly medium-K high-Fe tholeiites which display a well defined fractionation trend.

Tephra C16 48.5-49 is bimodal, and the higher silica shards are low-K, and range from medium-Fe calc-alkaline to high-Fe tholeiitic, while the lower silica shards are medium-K. Tephra C16 54-55 is a homogeneous rhyolitic layer with all shards having a low-K content. Tephra C16 206-207 crosses the boundary between low-K and medium-K and straddles the compositional gap between basaltic-andesitic and rhyodacitic.

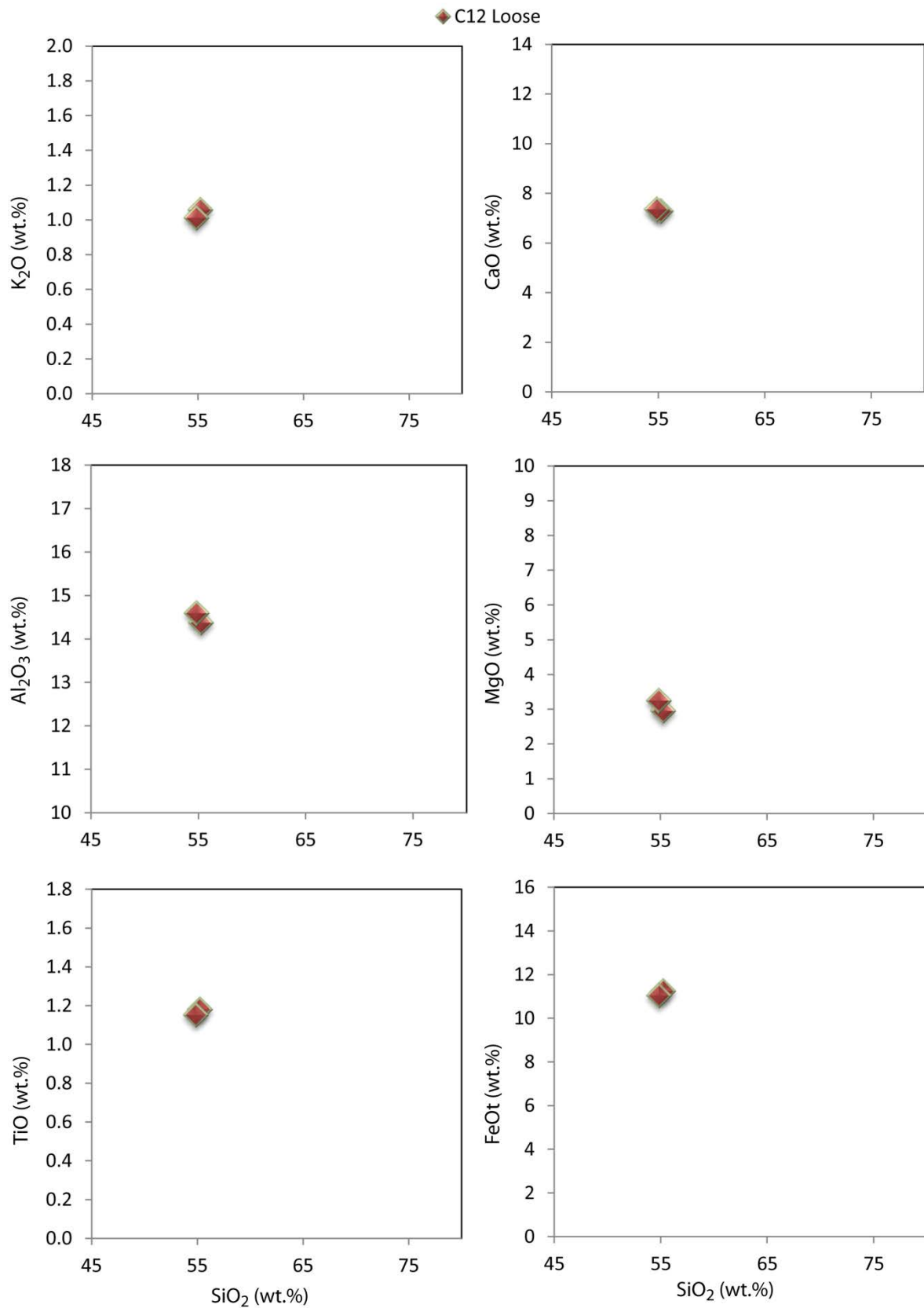


Figure 4.12 Variation diagrams of selected major oxides against SiO₂ for samples in TAN0706-12. All samples have been corrected for machine drift as outlined in Chapter 3. Raw data are presented in Appendix C. Each point represents a single glass shard, and their depth is in cms.

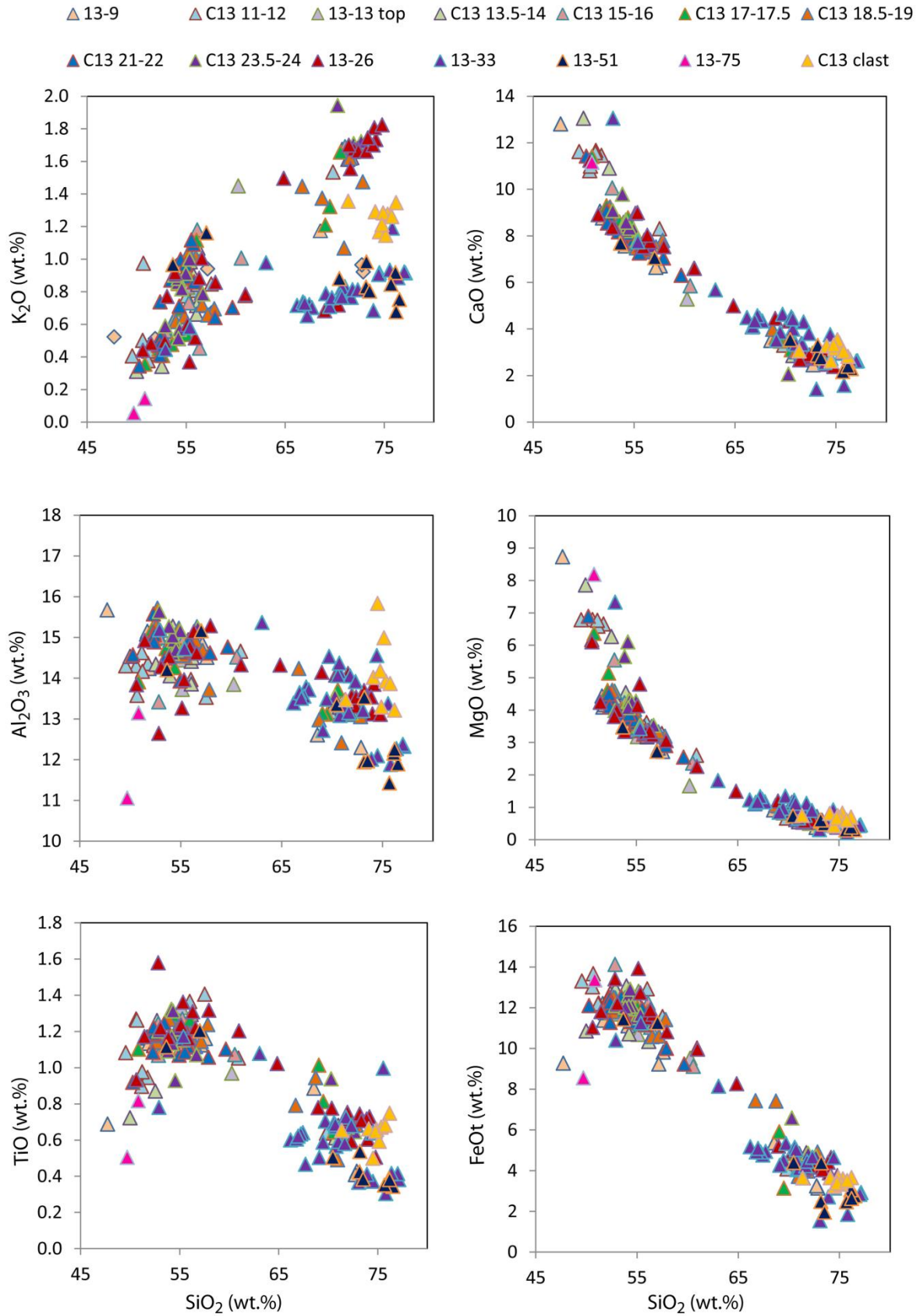


Figure 4.13 Variation diagrams of selected major oxides against SiO₂ for samples in TAN0706-13. All samples have been corrected for machine drift as outlined in Chapter 3. Raw data are presented in Appendix C. Lighter samples are stratigraphically younger, with symbol colours darkening downcore. Each point represents a single glass shard, and their depth is in cms.

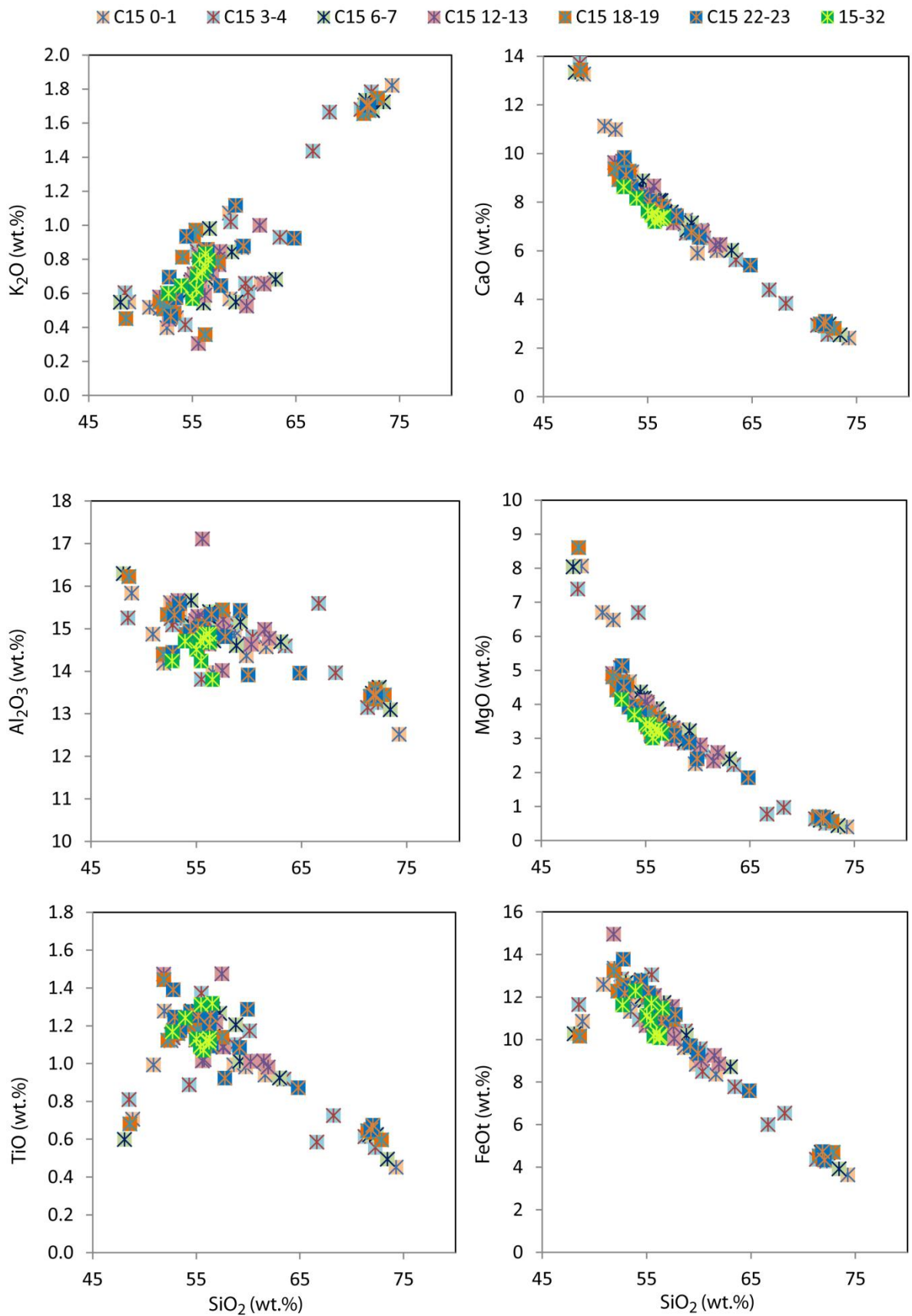


Figure 4.14 Variation diagrams of selected major oxides against SiO_2 for samples in TAN0706-15. All samples have been corrected for machine drift as outlined in Chapter 3. Raw data is presented in Appendix C. Lighter samples are stratigraphically younger, with symbol colours darkening downcore. Each point represents a single glass shard, and their depth is in cms.

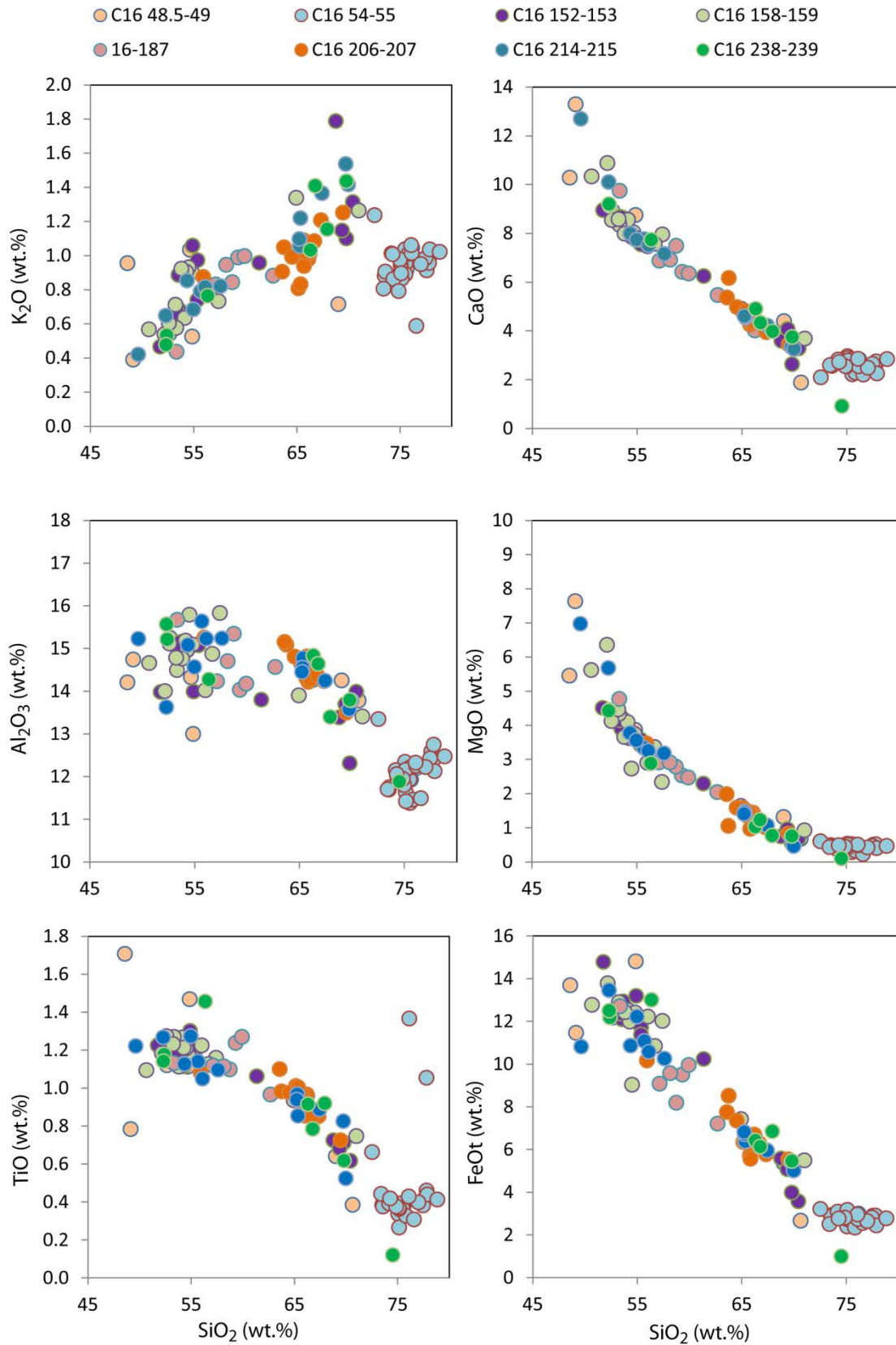


Figure 4.15 Variation diagrams of selected major oxides against SiO_2 for samples in TAN0706-16. All samples have been corrected for machine drift as outlined in Chapter 3. Raw data are presented in Appendix C. Lighter samples are stratigraphically younger, with symbol colours darkening downcore. Each point represents a single glass shard, and their depth is in cms.

4.1.3 Trace element chemistry

Geochemistry commonly acts as a fingerprint for each tephra, with each eruption in principle showing a unique chemical signature which allows us to identify it as a discrete event. As identified in section 4.1., tephra often show similar major element compositions that make identifying discrete events difficult. Trace elements are generally more sensitive to magmatic processes and show differences in magma composition on more precise scales than is possible with major elements alone.

In most cores a large range in trace element variations were observed (with the exception of the older samples in Core 1) allowing for identification of discrete tephra in each core. All tephra layers examined for trace elements show variations between individual shards, even where the tephra layer is homogeneous in terms of major element composition, possibly reflecting compositional variations in the magma chamber prior to eruption (see Chapter 6). An example of this is tephra 1-87, where Sr values range from 123-192 ppm. Tephra layers that are heterogeneous in major element composition also show the largest variations in trace element compositions, which is to be expected. An example of this is tephra C16 48.5-49 with SiO₂ values ranging from 48.58-76.18 wt % and Sr values ranging from 114-275 ppm.

A number of trace elements have been found to be particularly useful in identifying distinct tephra layers that correspond to individual eruptive events, and these are shown in the proceeding figures. SiO₂ (wt %) is plotted against La and Dy to highlight variations in light rare earth elements (LREE) and heavy rare earth element (HREE), respectively, with increasing silica content. Sr is plotted against Rb to distinguish variations in large ion lithophile (LIL) elements, and Nb (an incompatible high field strength element (HFSE) is plotted against Yb (HREE) to show variations in less mobile trace elements. Two trace element ratios are also plotted; Zr/Y vs. Ba/Sr and Zr/Nb vs. Y/Sc as they separated out the tephra and allowed for identification of discrete events and potential correlatives to be identified.

4.1.3.1 Raoul cores

Core 1 - Younger tephra layers are distinct from the older tephra (Figure 4.14) in that they are more enriched in REE and LIL elements. The older tephra have higher Ba/Sr ratios and a higher range in Zr/Nb and Y/Sc, with no discernible trend between the two. All of the older tephra show identical ranges in trace element variations with the exception of tephra C1 302-303 which shows less spread in trace element contents.

Identification of discrete tephra within the younger samples is more straightforward. Tephra C1 80-81 plots as a distinct cluster in Sr vs. Rb and Zr/Y vs. Ba/Sr plots. With the exception of two outlier shards, tephra 1-97 forms a distinguishable cluster in each trace element plot (Figure 4.16). Notably, this tephra plots within a similar range to the older tephra in the SiO₂ (wt %) vs. REE plots, Sr vs. Rb and Nb vs. Yb plots. In the Zr/Y vs. Ba/Sr trace element ratio plot tephra 1-97 forms a distinct cluster with low Zr/Y concentration. Tephra C1 114-115 directly overlies this cluster, as do two outlier shards from tephra 1-87.

Core 2 – With the exception of the single analysis from C2 19 cm clast, all of the shards analysed are high silica and both C2 10 cm clast and 2-33 samples follow the same geochemical trends, whilst being distinct from one another. Only one shard from the sample C2 19 cm clast was successfully analysed and this plots separately from other samples from core 2, with lower concentrations of all trace elements plotted (Figure 4.15). Tephra 2-33 shows an increase in Rb with no change in Sr compositions, with an identical trend in the Zr/Nb vs. Y/Sc plot.

Core 3 - Three of the stratigraphically older tephtras (C3 24.5-25.5 to C3 29-29.5) are distinct to the other tephtras (all of the younger tephtras and the oldest tephtra) in that they have significantly higher trace element concentrations (Figure 4.18). Notably, the oldest tephtra (tephtra 3-31) has trace element concentrations similar to the stratigraphically younger tephtras. All of the tephtra layers in this core are able to be distinguished as discrete events based on the trace element data, with the exceptions of C3 27.5-28.5 and C3 29-29.5, which are virtually indistinguishable.

Core 4 - The high silica sample, C4 51.5 cm clast, forms a distinct cluster in the trace element plots, with the exception of the Sr vs. Rb plot where it plots in a similar range to the lower silica samples. Tephtras C4 62-63 and C4 144.5-145.5 have lower La than the rest of the samples, with C4 144.5 145.5 also having lower Dy than other samples analysed. Tephtra 4-120 has two higher silica shards, with trace element concentrations distinct from the other tephtras in this core. Tephtra 4-129 has similar trace element concentrations to C4 126-127 but with slightly lower concentrations of La, Dy and Rb. Tephtra 4-153 is similar to the other low silica tephtras, but is distinct in terms of the SiO₂ vs. La and Zr/Y vs. Ba/Sr plots. Tephtra C4 174.5-175.5 forms a distinct cluster in the Sr vs. Rb plots and the two ratio plots, having higher Ba/Sr and Y/Sc ratios than the other samples in the core.

Core 5 – Core 5 samples show a wide range in trace element concentrations, with the REE abundances showing a positive correlation with increasing silica content, mirroring the major element trend. The samples in the core, with the following exceptions, are distinct. C5 4 cm clast and tephtra 5-6 overlap in all of the trace element plots. Tephtras 5-45 and 5-47 plot very similarly in terms of their trace elements with the exception of one shard from 5-47.

Cores 7 & 8 – All of the tephtra layers in these two cores are distinct in SiO₂ vs. REE plots. Shards from the same tephtra show tight clusters in trace element concentrations and ratios, with tephtras 7-6 and C8 7-7.5 showing the most variation.

Core 9 – Tephtra shards in Core 9 show a wide range in trace element composition.

Core 10 – The two tephtras in Core 10 have similar trace element compositions. However, in all of the trace element plots C10 6-7 is slightly more geochemically evolved, with C10 7-8 clustering in the lower range of C10 6-7 in the Nb vs. Yb plot and the Zr/Y vs. Ba/Sr plot.

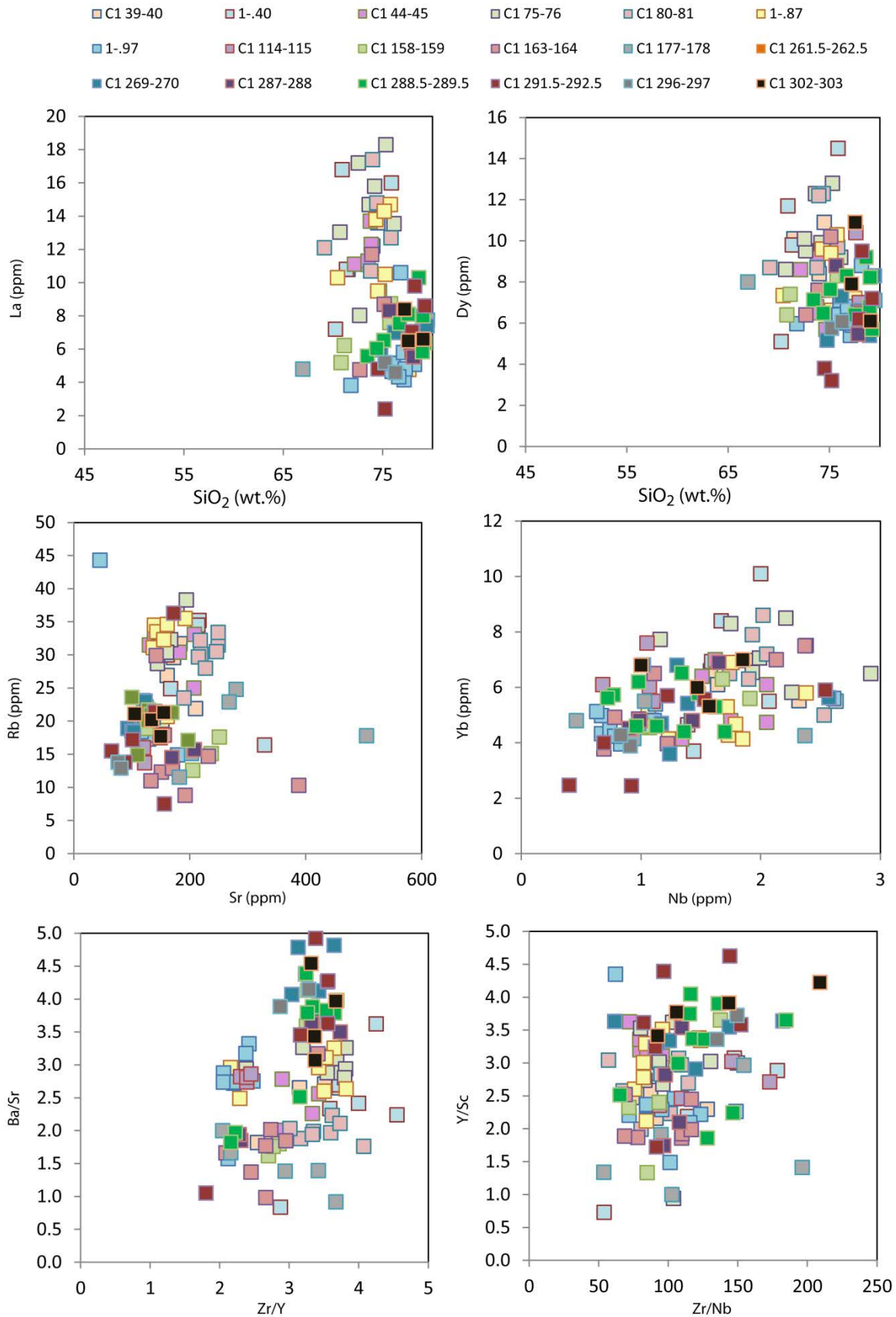


Figure 4.16 Variation diagrams of selected major and trace elements, including trace element ratio plots for samples from core TAN0706-1. Each symbol represents an individual analysis. Lighter coloured symbols represent stratigraphically younger samples, with colours darkening down core. Each point represents the analysis from a single glass shard, and their depth is in cms.

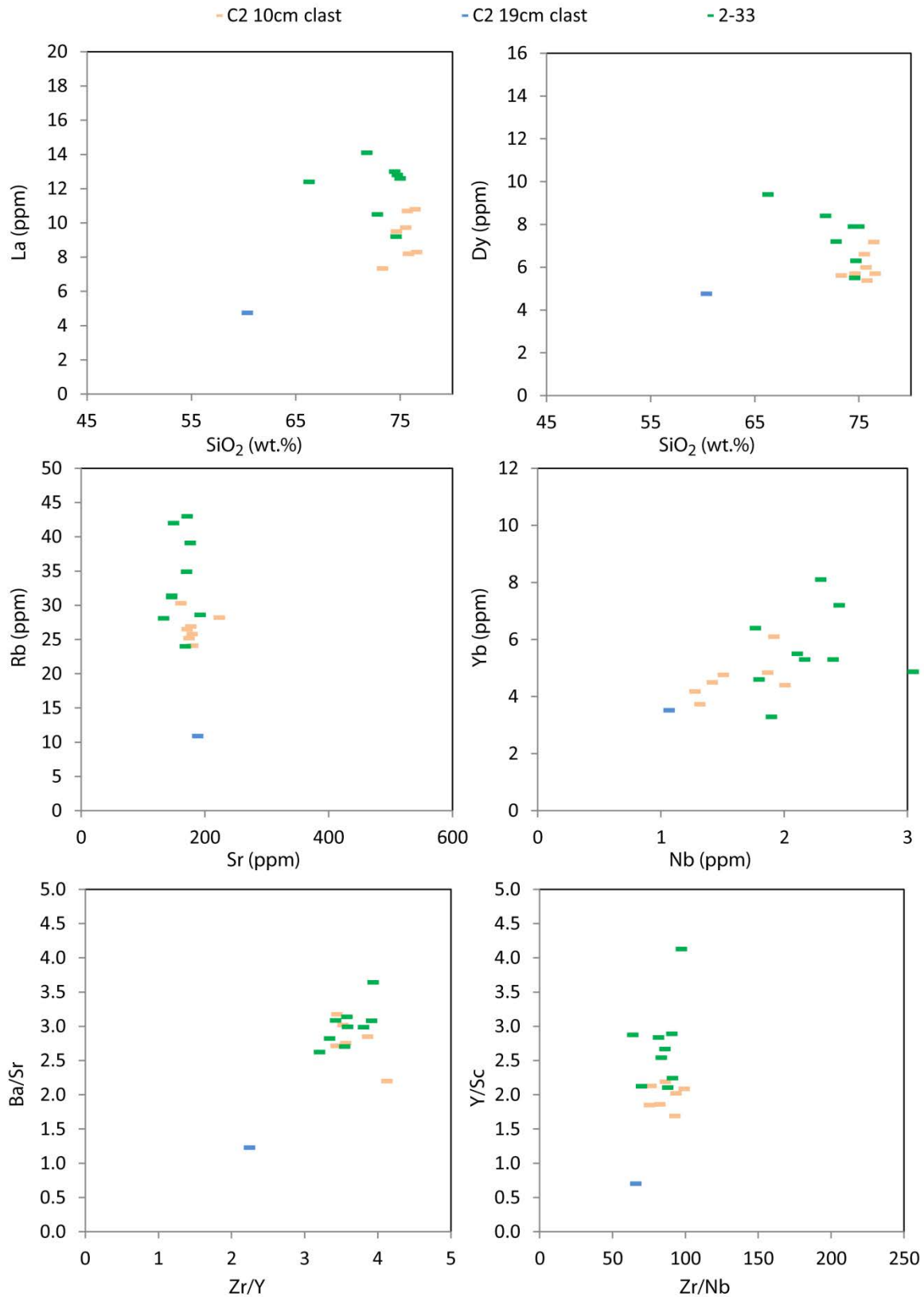


Figure 4.17 Variation diagrams of selected major and trace elements, including trace element ratio plots for samples from core TAN0706-2. Each symbol represents an individual analysis. Lighter coloured symbols represent stratigraphically younger samples, with colours darkening down core. Each point represents the analysis from a single glass shard, and their depth is in cms.

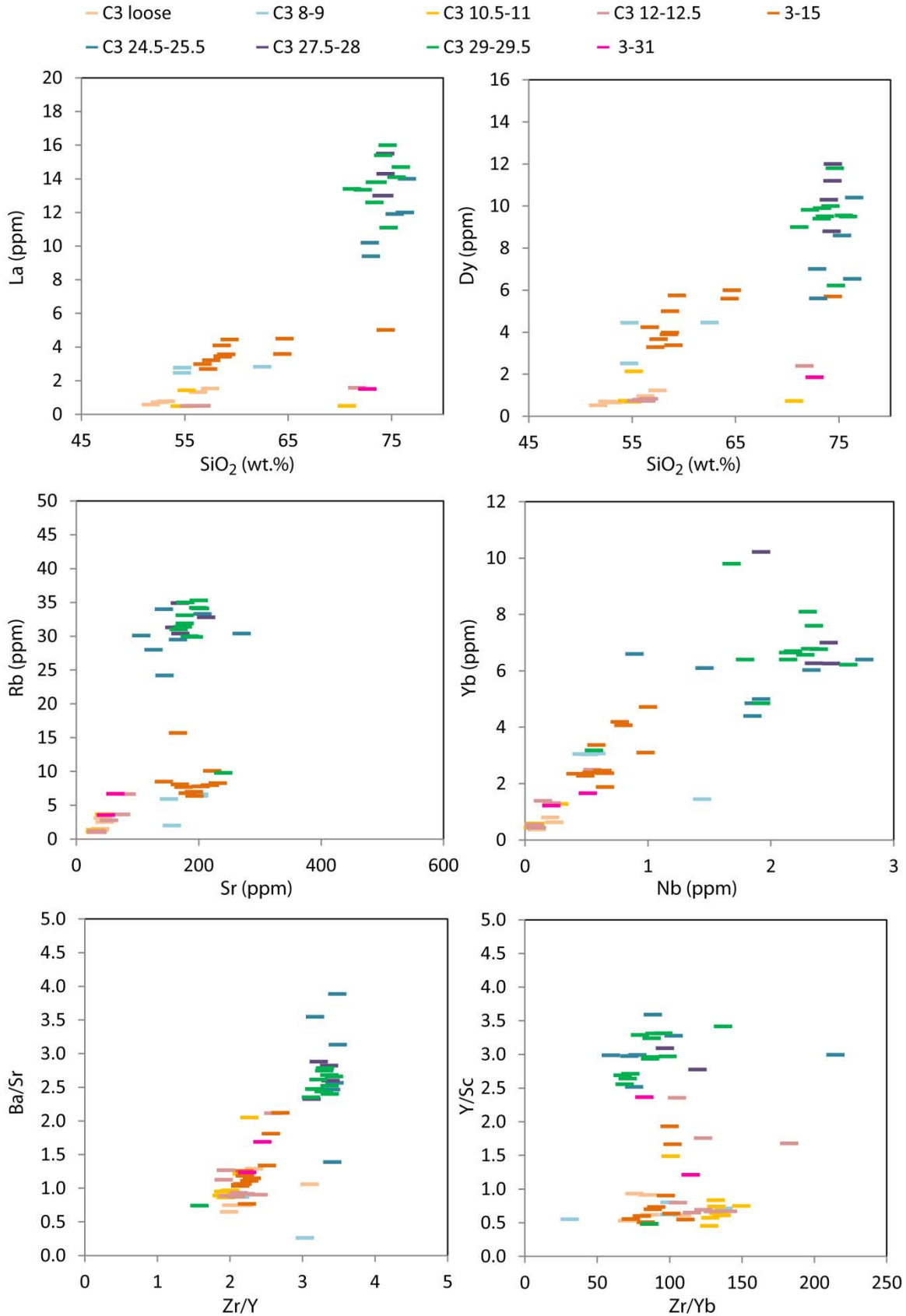


Figure 4.18 Variation diagrams of selected major and trace elements, including trace element ratio plots for samples from core TAN0706-3. Each symbol represents an individual analysis. Lighter coloured symbols represent stratigraphically younger samples, with colours darkening down core. Each point represents the analysis from a single glass shard, and their depth is in cms.

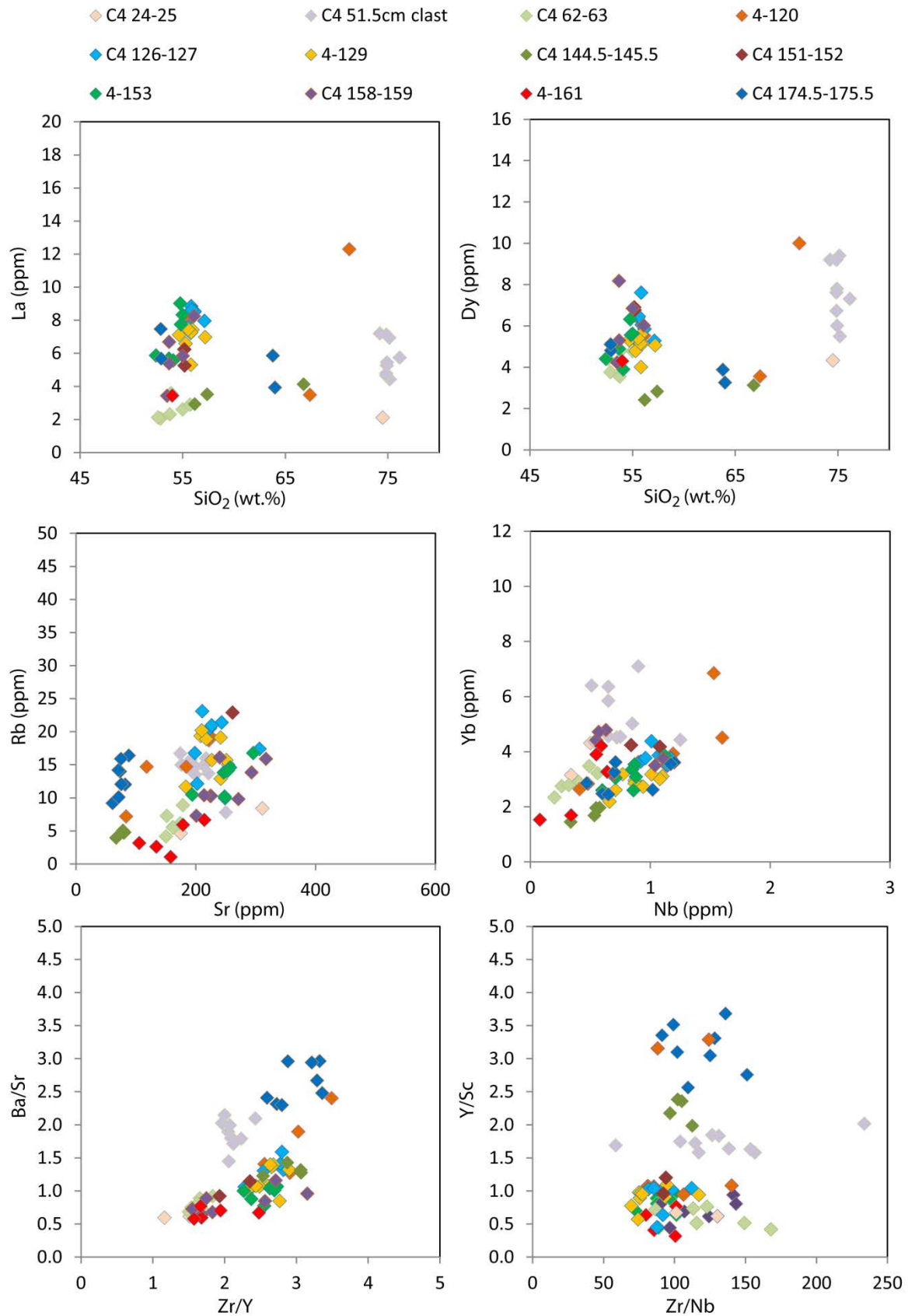


Figure 4.19 Variation diagrams of selected major and trace elements, including trace element ratio plots for samples from core TAN0706-4. Each symbol represents an individual analysis. Lighter coloured symbols represent stratigraphically younger samples, with colours darkening down core. Each point represents the analysis from a single glass shard, and their depth is in cms.

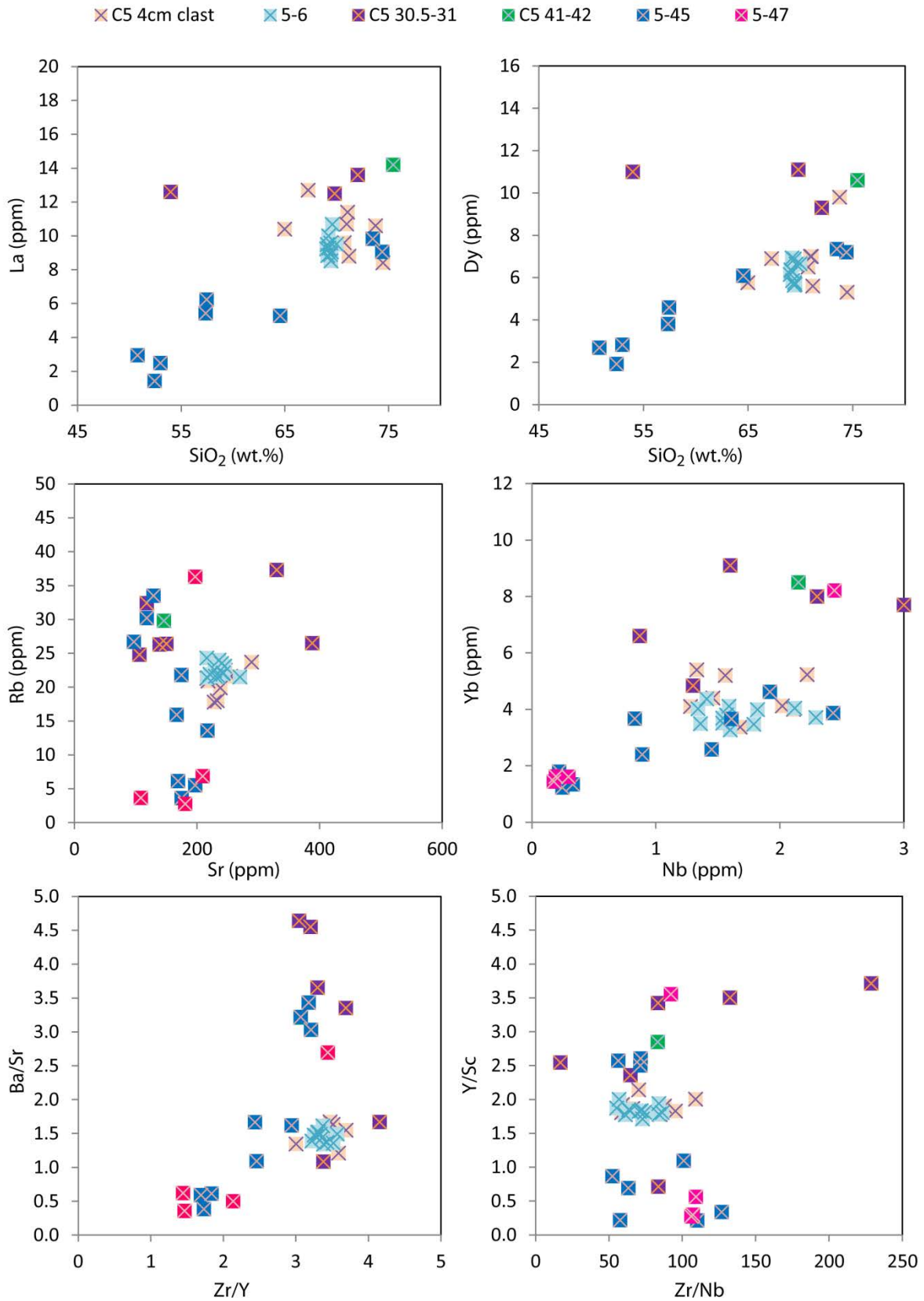


Figure 4.20 Variation diagrams of selected major and trace elements, including trace element ratio plots for samples from core TAN0706-5. Each symbol represents an individual analysis. Lighter coloured symbols represent stratigraphically younger samples, with colours darkening down core. Each point represents the analysis from a single glass shard, and their depth is in cms.

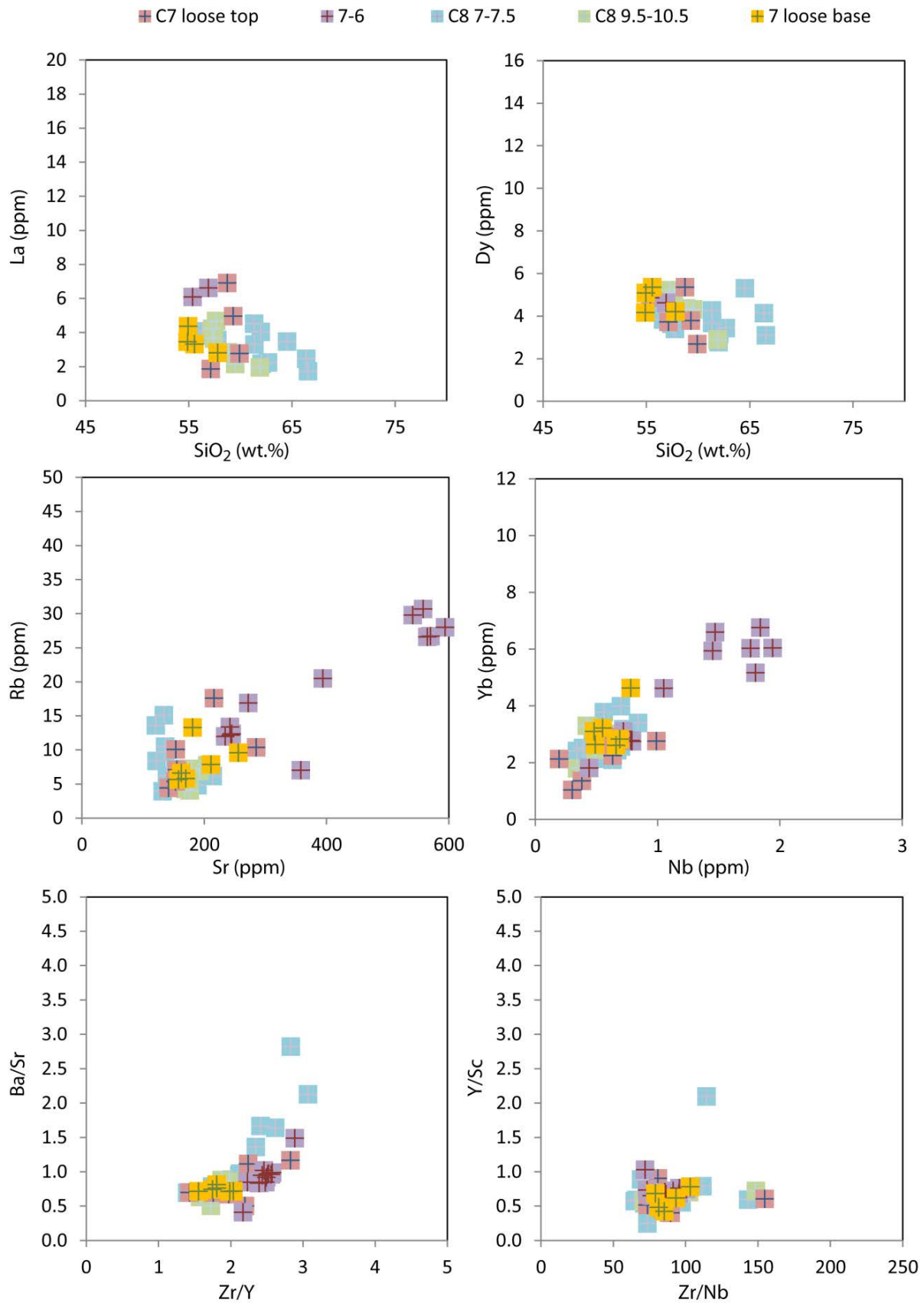


Figure 4.21 Variation diagrams of selected major and trace elements, including trace element ratio plots for samples from core TAN0706-7 & 8. Each symbol represents an individual analysis. Lighter coloured symbols represent stratigraphically younger samples, with colours darkening down core. Each point represents the analysis from a single glass shard, and their depth is in cms.

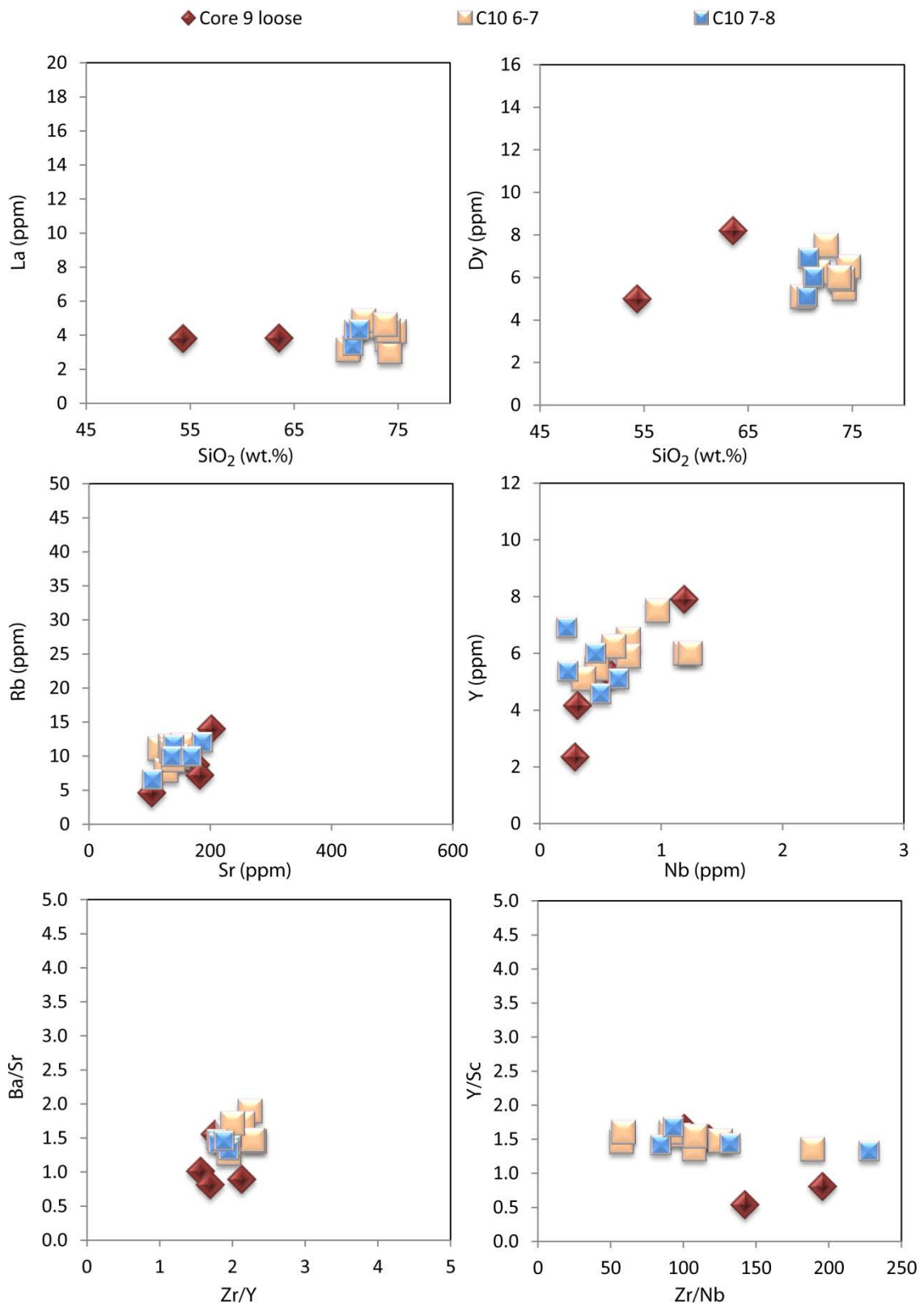


Figure 4.22 Variation diagrams of selected major and trace elements, including trace element ratio plots for samples from core TAN0706-9 & TAN0706-10. Each symbol represents an individual analysis. Lighter coloured symbols represent stratigraphically younger samples, with colours darkening down core. Each point represents the analysis from a single glass shard, and their depth is in cms.

4.1.3.2 Macauley cores

Core 12 – The trace element concentrations of the shards analysed for Core 12 have very low concentrations, which are most likely a function of analytical issues so the data has been discarded.

Core 13 – Samples show wide variations in terms of the silica and trace element concentrations, with no distinctive trends.

The five youngest tephtras (Tephtras 13-9 to C13 17.5-18) show a range in trace element concentrations at similar and low silica content. They are virtually indistinguishable, except for 13-13 top which has a slightly lower Zr/Y ratio and has slightly lower Sr values. C13 15-16 also has slightly lower Sr values, along with a two shards from C13 11-12 and three shards from C13 17-17.5.

Tephtra 13-26 forms a distinct cluster in terms of its SiO₂ vs. La, Nb vs. Yb and trace element ratios. While the sample has both low and high silica shards, the majority of the sample is high silica and is reasonably enriched in the trace elements shown in the plots. It forms a separate but co-linear trend to all but one (C13 clast) of the samples on the Zr/Y vs. Ba/Sr plot, having a higher Zr/Y ratio. Tephtra 13-33 is high silica, but generally has lower trace element concentrations compared to tephtra 13-26. They cluster together in the SiO₂ vs. Dy plot, but are distinct in the other trace element plots. Tephtra 13-51 is distinctive in terms of its lower Sr and La concentrations than the other higher silica shards. It also has the highest Ba/Sr ratio, and follows the same trend as sample 13-33 in this.

Core 15 – All of the tephtras analysed are low silica (due to poor data from the higher silica shards examined), and have very similar trace element concentrations with generally positive correlations on bivariate plots. The only sample which shows any measurable difference from the rest of the shards is C15 3-4 which has four shards with higher trace element concentrations, although the rest of the sample plots with the other tephtras in the core.

Core 16 - Tephtras show a range in trace element concentrations with no correlation to silica. With the Sr vs. Rb and Nb vs. Yb plots there is a general positive correlation present. C16 206-207 is homogeneous in silica content (averaging 65 wt % SiO₂), however it shows the greatest range in Nb vs. Yb, forming a distinct cluster in the trace element ratio plots, with the exception of one outlier shard. Tephtras C16 214-215 and C16 238-239 also have low trace element concentrations, similar to that of tephtra C16 158-159; unlike C16 158-159 they do follow the positive correlation mentioned above. C16 214-215 plots with C16 206-207 in the Zr/Y vs. Ba/Sr plot.

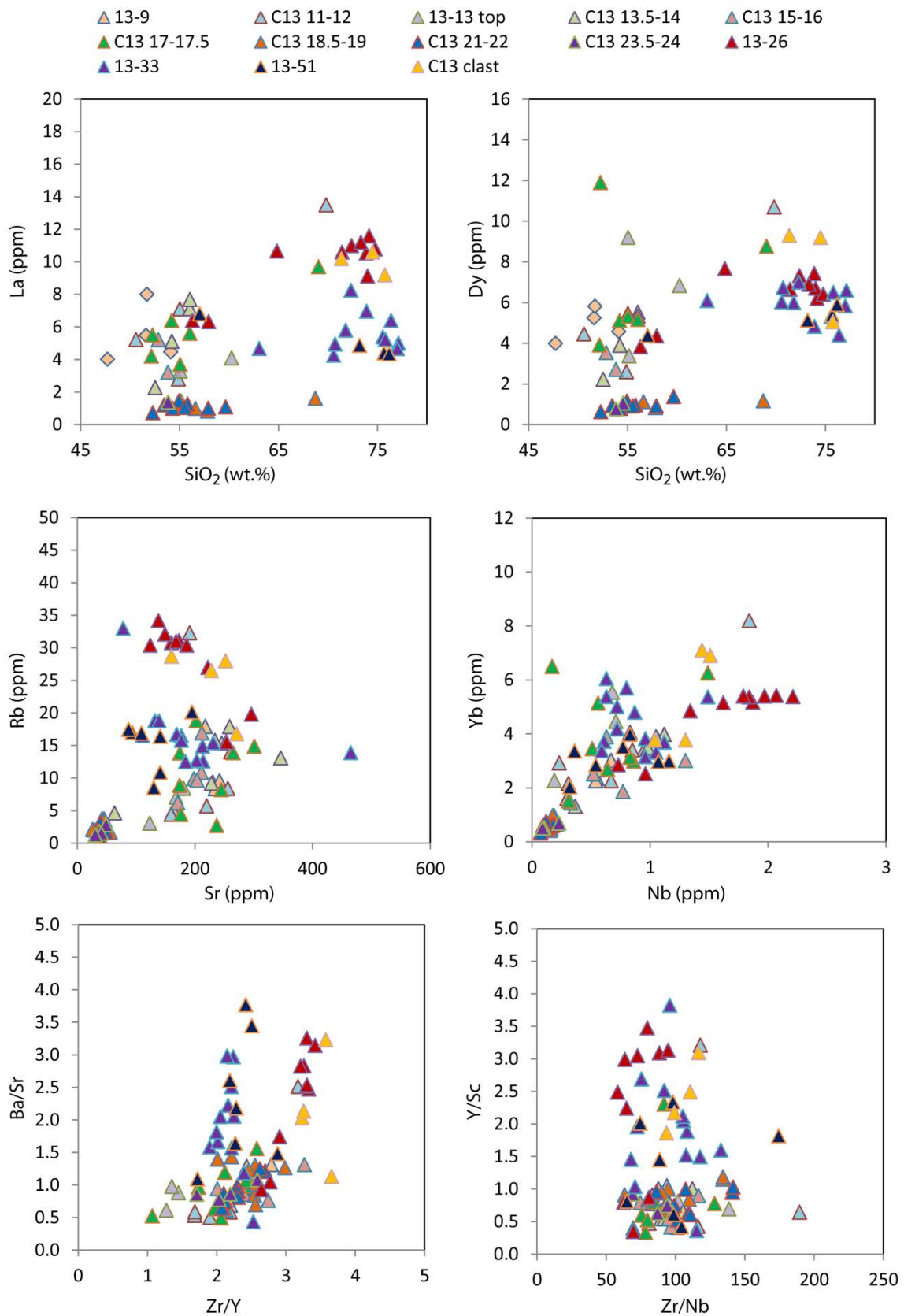


Figure 4.23 Variation diagrams of selected major and trace elements, including trace element ratio plots for samples from core TAN0706-13. Each symbol represents an individual analysis. Lighter coloured symbols represent stratigraphically younger samples, with colours darkening down core. Each point represents the analysis from a single glass shard, and their depth is in cms.

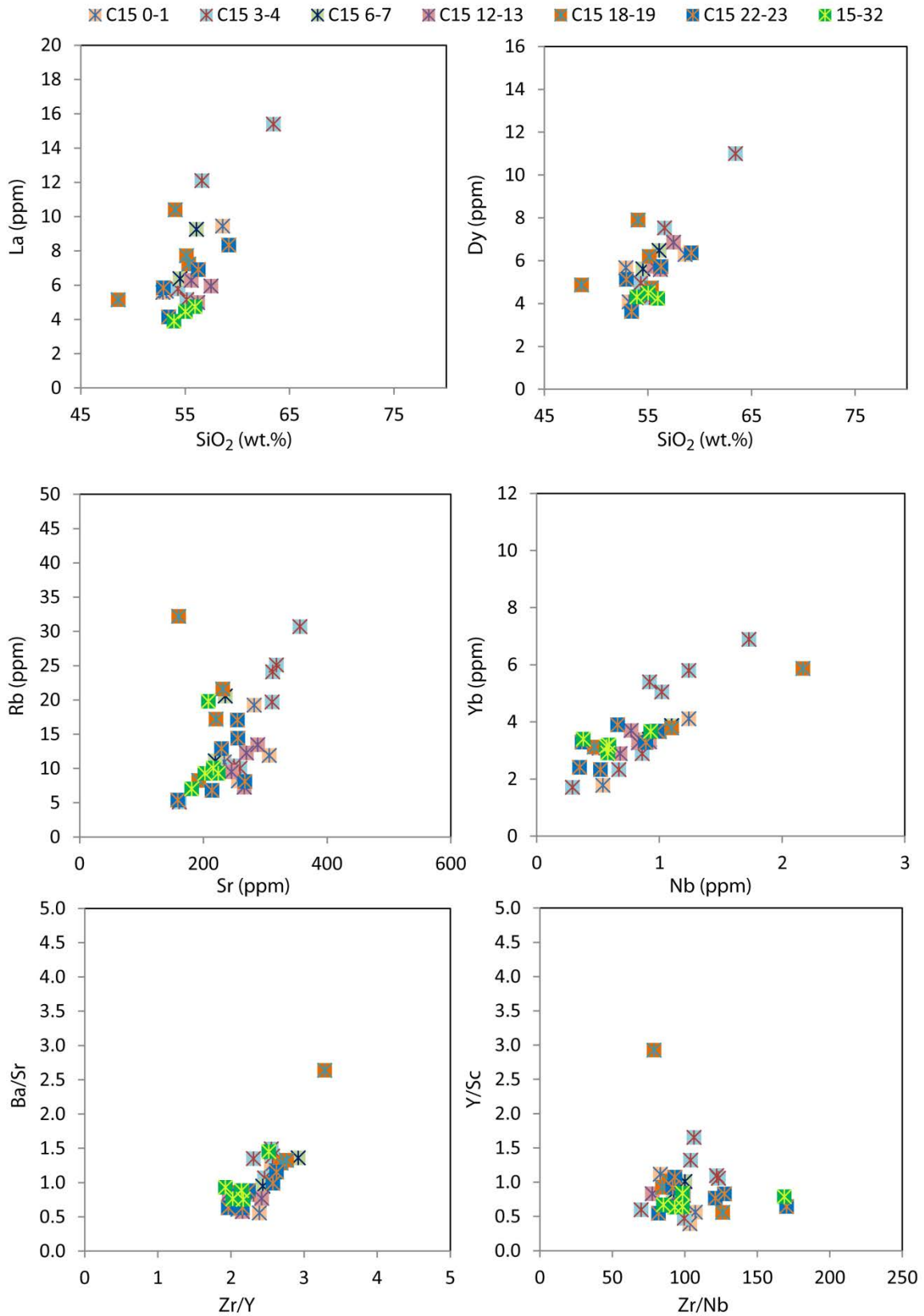


Figure 4.24 Variation diagrams of selected major and trace elements, including trace element ratio plots for samples from core TAN0706-15. Each symbol represents an individual analysis. Lighter coloured symbols represent stratigraphically younger samples, with colours darkening down core. Each point represents the analysis from a single glass shard, and their depth is in cms.

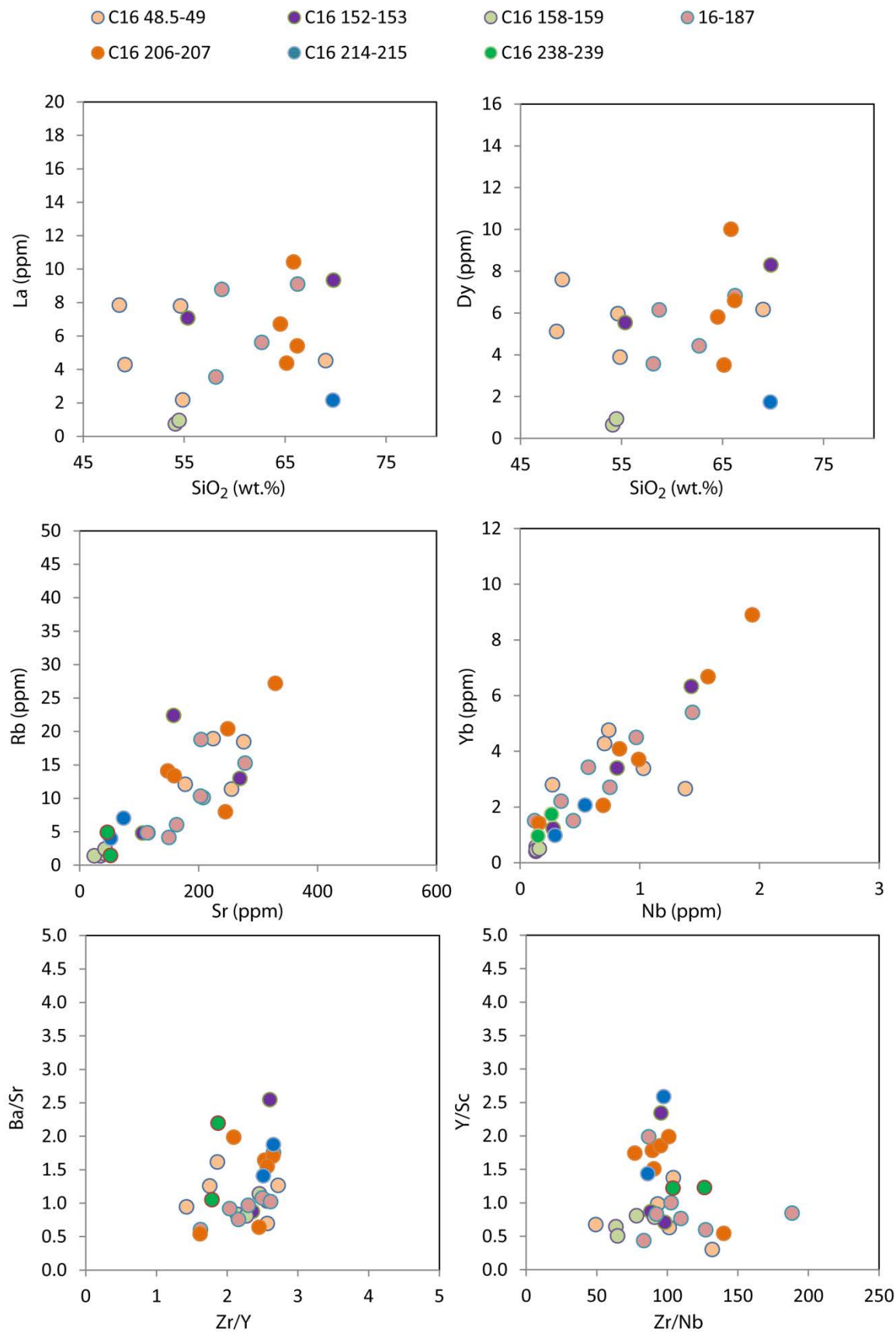


Figure 4.25 Variation diagrams of selected major and trace elements, including trace element ratio plots for samples from core TAN0706-16. Each symbol represents an individual analysis. Lighter coloured symbols represent stratigraphically younger samples, with colours darkening down core. Each point represents the analysis from a single glass shard, and their depth is in cms.

4.2 Overall geochemical trends

In general, the higher silica samples are more enriched in incompatible trace elements relative to lower silica samples. With the exception of the samples analysed in Core 1, there is no obvious trend showing increasing enrichment in incompatible elements with decreasing stratigraphic age of tephtras. In Core 1 the younger tephtras are noticeably enriched in all major and trace elements relative to the older tephtras.

Figures 4.5-4.15 illustrate the range of SiO₂ compositions of all the glass shards analysed for each core. The data all clearly indicate that fractionation and/or mixing trends are present in most of the cores. There is a positive relation between SiO₂ and K₂O, and a negative trend between SiO₂ and CaO which is characteristic of fractional crystallisation (Figures 4.26-4.28). Trace element analyses also indicate that fractionation is prevalent amongst the samples as illustrated, for example, by a positive trend between SiO₂ and La (Brophy, 2008).

Forty of the tephtra layers analysed were homogeneous in major elements, displaying narrow SiO₂ compositional ranges (<8% 2σ variation), 17 of the tephtra layers showed pronounced compositional bimodality, and 32 samples were heterogeneous in SiO₂ composition (>8% 2σ variation).

Homogeneous tephtras show a divergent pattern in SiO₂ vs. K₂O, with distinct low-K and medium-K trends evident (Figure 4.26). Two tephtras span the compositional gap, one being andesitic, the other dacitic. With the exception of these two, homogeneous tephtras are either basaltic-andesite or rhyolite.

Many of the heterogeneous layers show distinct fractionation trends as, although there is variation in SiO₂ content, the shards are clearly compositionally related (Figure 4.27). A distinct low-K and medium-K trend is evident and, unlike in the homogenous tephtras, there is no evident composition gap between basaltic-andesites and rhyolites.

Bimodal tephtra layers are predominantly basaltic-andesite and rhyodacite glass shards, with only one tephtra spanning the compositional gap between the two (Figure 4.28). A low-K and medium-K trend can be distinguished, but this is not as distinct as with the homogeneous tephtras.

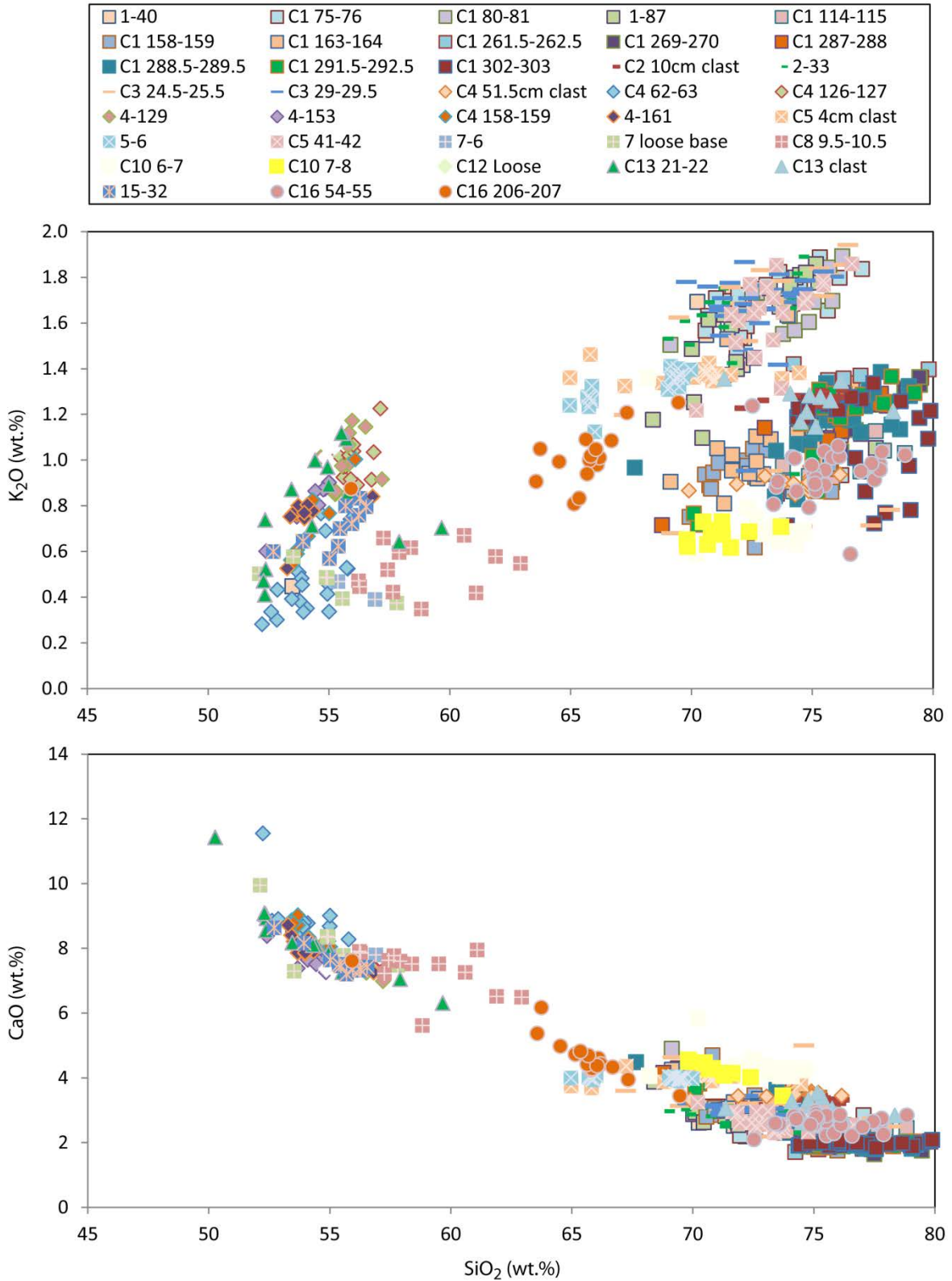


Figure 4.26 Variation diagrams of SiO₂ vs. K₂O and CaO for homogeneous tephras showing the range of data obtained in this study. Each point represents a single glass shard.

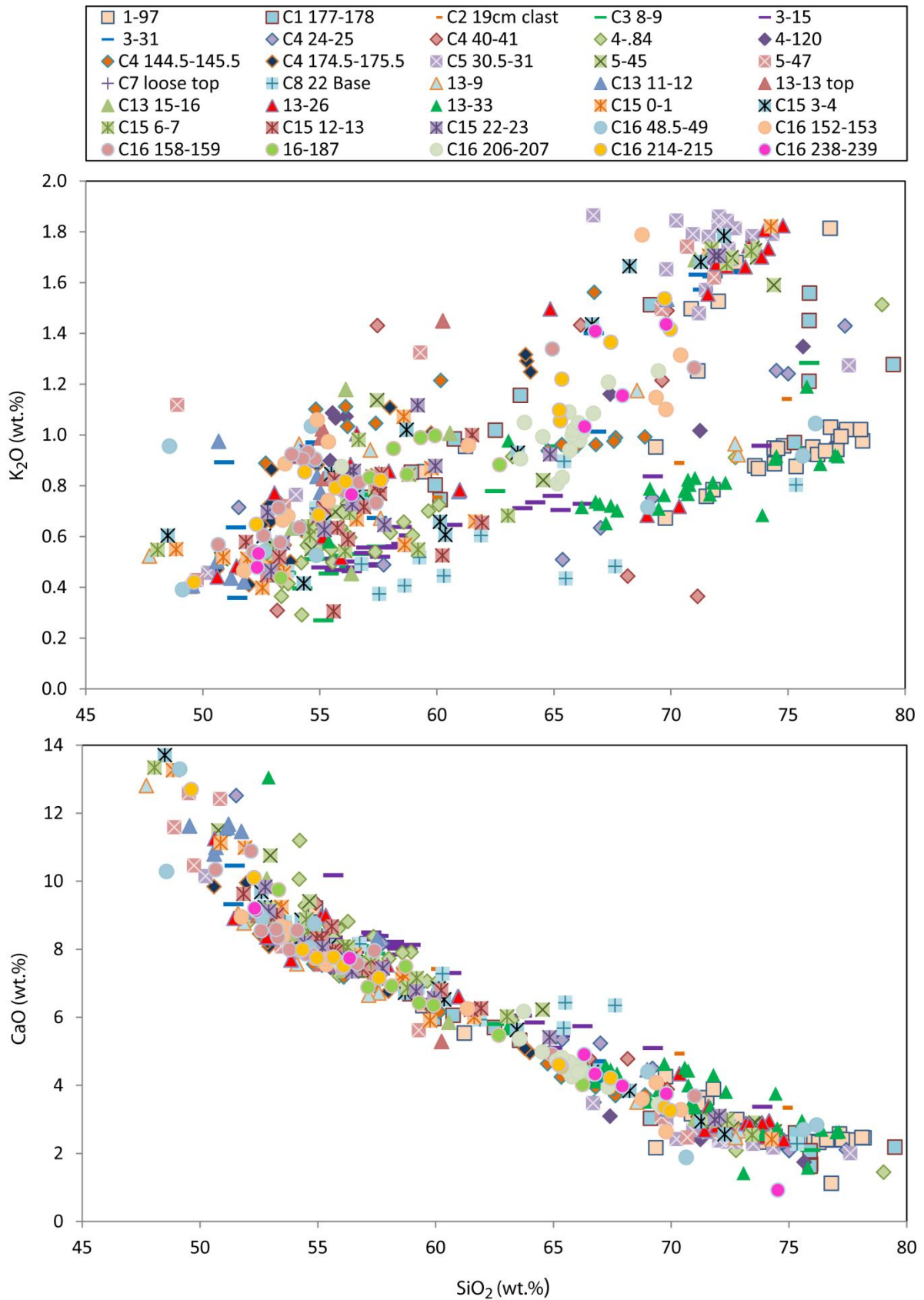


Figure 4.27 Variation diagrams of SiO₂ vs. K₂O and CaO for heterogeneous tephras showing the range of data obtained in this study. Each point represents a single glass shard.

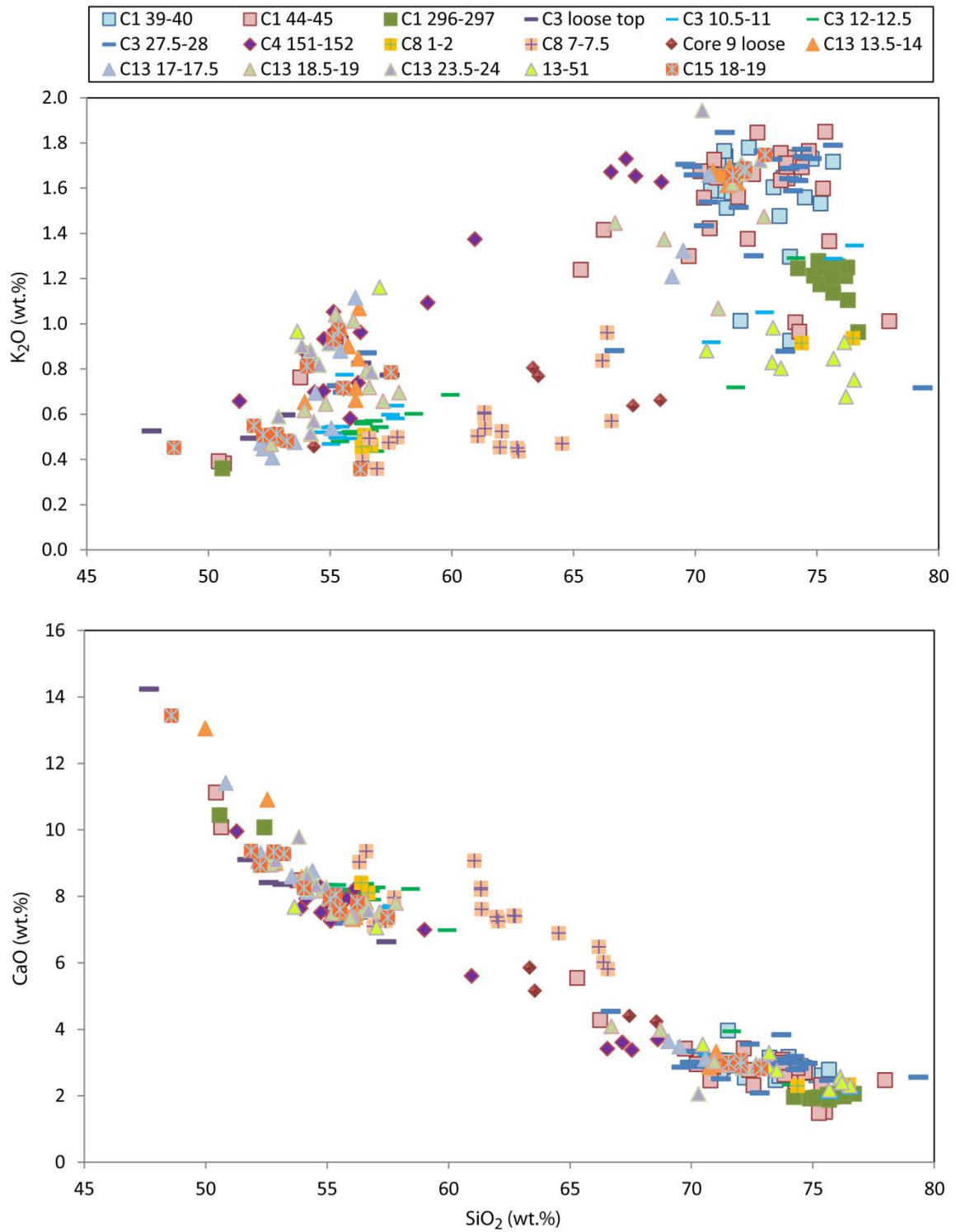


Figure 4.28 Variation diagrams of SiO₂ vs. K₂O and CaO for bimodal tephras analysed in this study. Each point represents a single glass shard.

Samples that are representative of the entire dataset are presented in Figures 4.29-4.31. Figure 4.29 shows the overall major element trends, with the distinctive fractionation trends evident in all plots. The distinction between low-K and medium-K tephtras is also clear. The trace element plots (Figure 4.30) show the range in trace element concentrations relative to silica, other trace elements and also trace element ratios. These plots show that the trace elements allow us to distinguish individual eruptive events, and highlight eruptions that are geochemically related both within and between cores.

Multi-element and REE plots show that the tephtras in this study have high concentrations of fluid-mobile, large ion lithophile (LIL) elements (K, Rb, Cs, Ba, Pb, Sr,) and relatively low concentrations of high field strength (HFS) elements (Ti, Ta, Nb) relative to mid-ocean ridge basalt (MORB). This is characteristic of arc magmas and similar to previously derived values from Kermadec arc samples (Figure 4.31). Three samples in the REE plot shown little to no depletion in Eu and two of these samples have lower concentrations in the multi-element plot relative to the other samples. These samples have lower silica and display lower trace element ratio values as shown in Figure 4.30.

The multi-element and REE plots again show the distinction between individual events, and these graphs have been used to correlate tephtras as presented below.

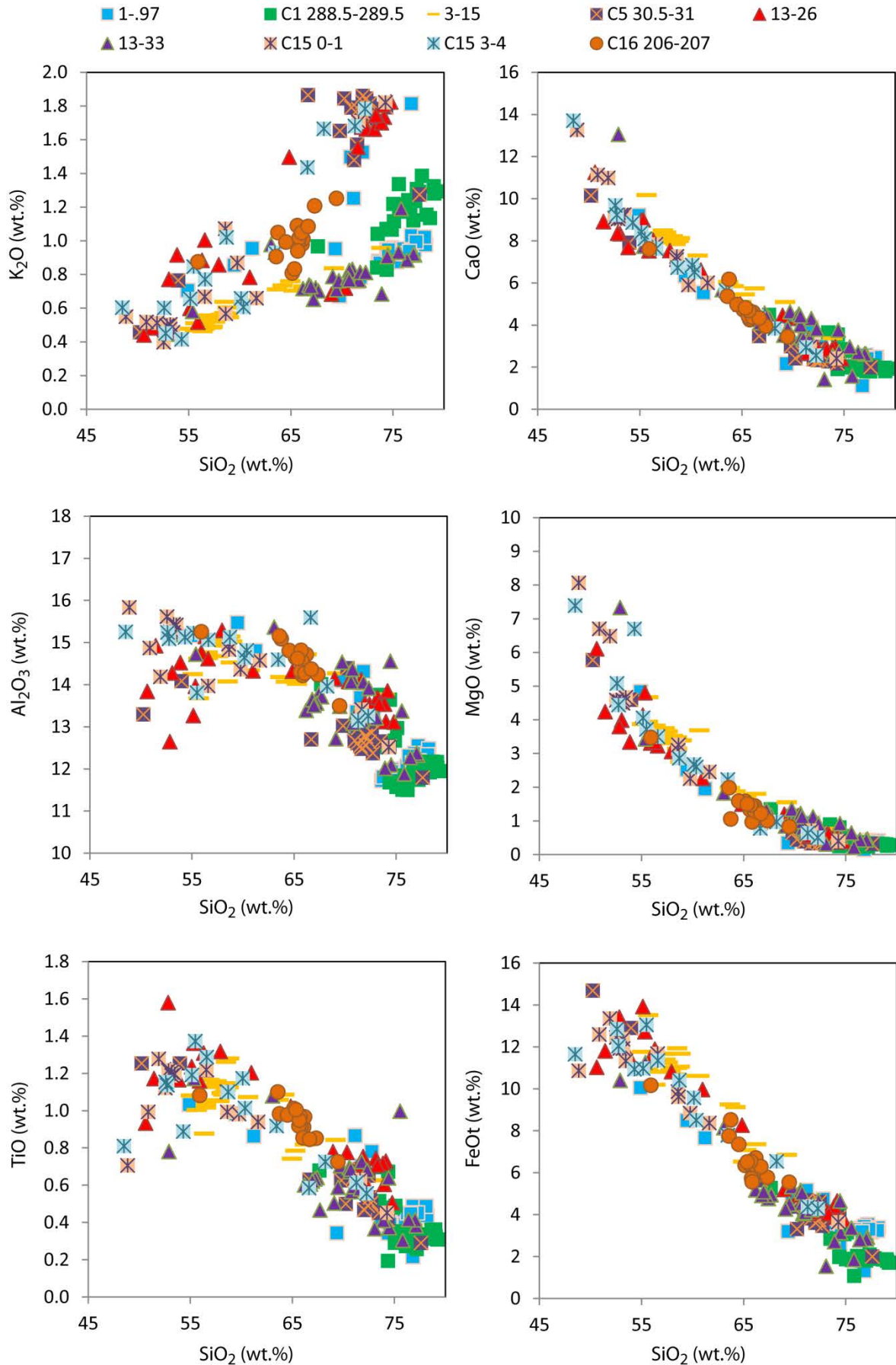


Figure 4.29 Variation diagrams of SiO₂ vs. major oxides for selected samples which are representative of the dataset as a whole. Each point represents a single glass shard, and their depth is in cms.

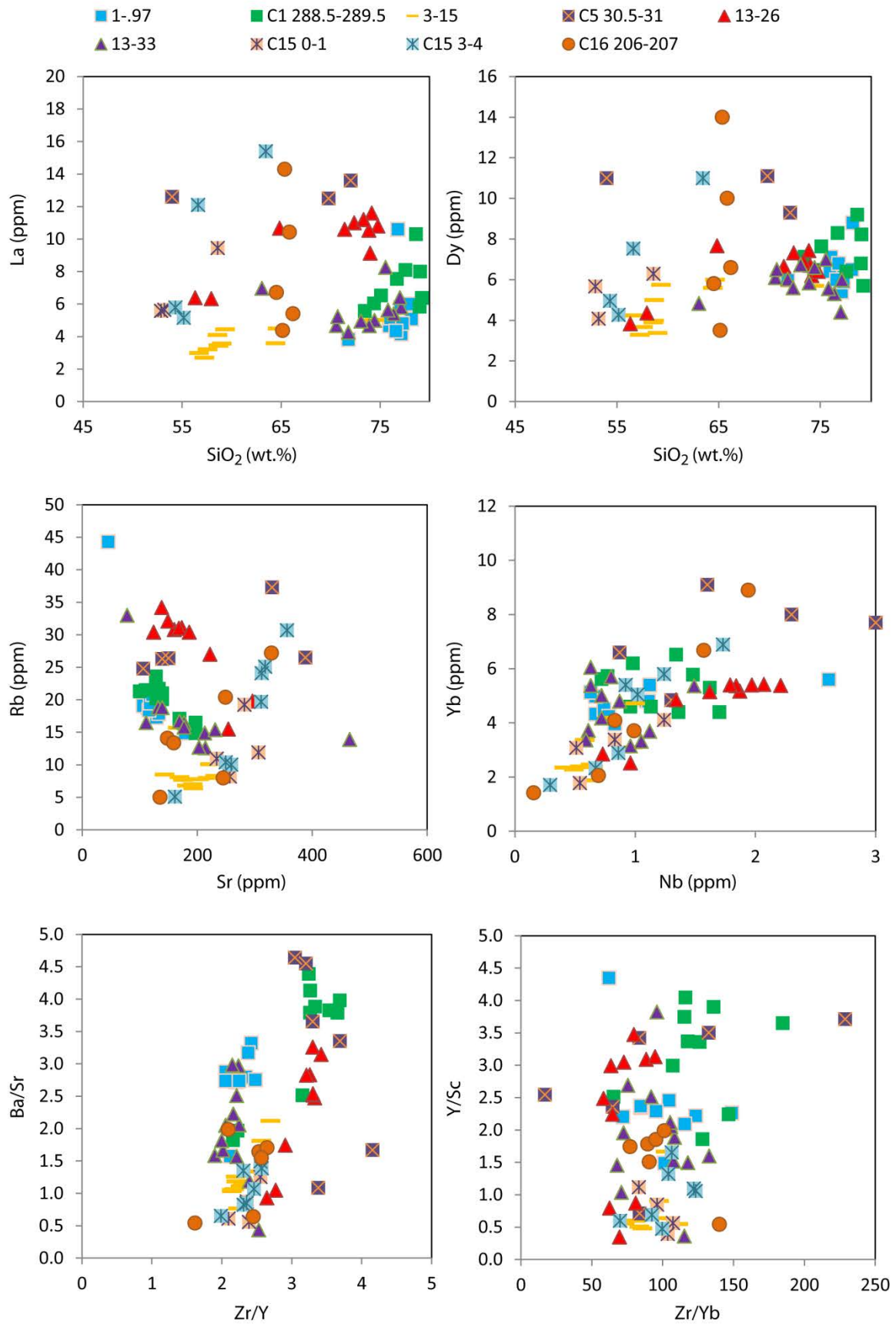


Figure 4.30 Variations diagrams of various major and trace elements and trace element ratios for selected samples which are representative of the dataset as a whole. Each point represents a single glass shard, and their depth is in cms.

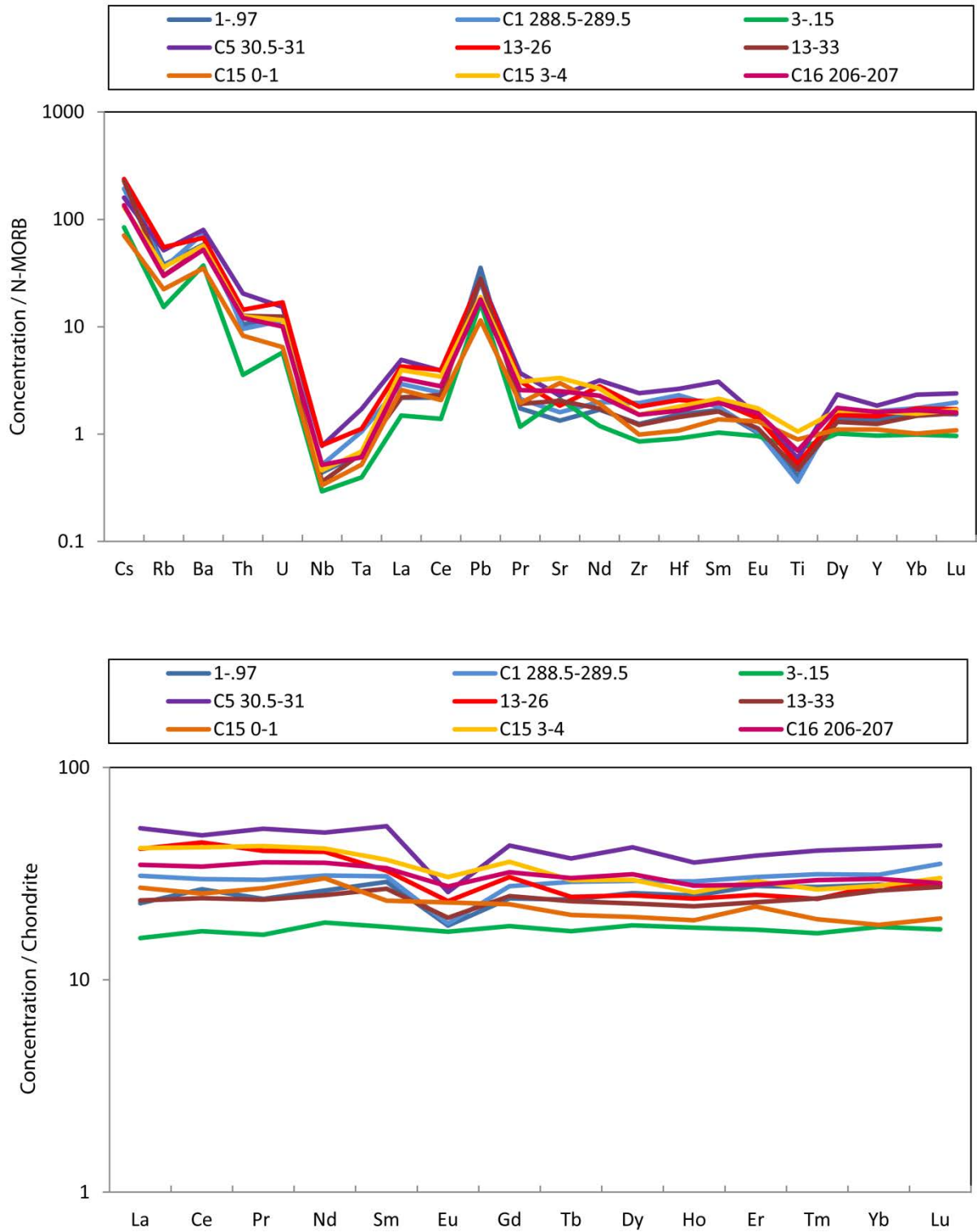


Figure 4.31 Multi-element plot and REE plot for selected samples representative of the overall dataset. Multi-element plot normalised to N-MORB values of Sun and McDonough (1989) and REE plot normalised to chondrite values from Sun and McDonough (1989).

4.3 Geochemical correlations of tephra layers between cores

Where tephra layers had similar elemental concentrations, they were plotted separately in order to see if they were correlatives and sourced from the same event. Major elements were used in the first instance and, if tephra layers had identical major element compositions, then trace elements were plotted in order to confirm whether they were from the same event, or from geochemically related magmas. Multi-element and REE plots were also used to confirm any correlations. Tephra layers examined which were potential correlatives are indicated below. Here we also re-examine correlations identified by Shane and Wright (2011) using their data and new data collected in this study on the same samples.

Tephra layers C15 0-1 – C15 22-23 share very similar elemental concentrations to samples examined from the banded tephra unit in Core 13 (Tephra layers C13 11-12, C13 13.5-14 – C13 21-22). The multi-element plot and REE plot clearly show that all of these tephra layers correlate, as there is no distinction between them (Figure 4.32). Trace elements from C13 18.5-19 and C13 21-22 have anomalously low trace element concentrations due to issues with the analysis. The multi-element and REE plots show that these two samples, whilst having low trace element concentrations, follow the same geochemical trend, and are assumed to correlate to the other tephra layers here examined. It may pay to note here that the SBT is present at the base of the banded tephra layer in Core 13; however it does not correlate to the tephra layers examined above as determined by examining the trace element concentrations.

Shane and Wright (2011) correlated tephra layers between cores 1, 2, 3, 5 and 13 that they inferred were part of the Sandy Bay Tephra (SBT). Tephra layers 3-31 and 5-47 correlated by Shane and Wright (2011) appear to be the geochemically related, lower silica relative to the SBT based upon major element analysis (Figure 4.33). When the trace elements are analysed however, it becomes evident that 3-31 is not the SBT as it plots separately to published data presented by Smith *et al.* (2003b) and Barker *et al.* (2013). Tephra layers 1-87, 2-33, 5-47 and 13-26 do correlate with the SBT in all major and trace element concentrations. Several tephra layers from Core 1 (1-87 and C1 75-76), however, also had similar composition to the SBT eruption (Figures 4.33 and 4.34). When plotted against values published by Smith *et al.* (2003b) and Barker *et al.* (2013) it can be confirmed that 1-87 is the SBT. Tephra layers C1 75-76 and C3 29-29.5 are very similar geochemically, but are slightly more enriched in REEs (Figure 4.35). They could be from a very geochemically similar magma source or could be the more evolved end-member of the SBT.

Two other tephra correlations presented by Shane and Wright (2011) are tested here: tephra layers 4-161 and 16-187, and tephra layers 13-51 and 16-71. Tephra layers 4-161 and 16-187 were reanalysed for both major and trace element data. The data published by Shane and Wright (2011) for these samples show that they have very similar major element compositions, with silica compositions ranging from 50-66 wt %. Data collected in this study shows that while the major elements are similar, 4-161 has lower silica values than that of 16-

187. The REE and multi-element plots also show that generally tephra 4-161 is distinctly less evolved than 16-187 (Figure 4.36). So while they are very similar in major elements, they do not correlate.

Tephra PS 13-51 and PS 16-71 are also very similar in major elements as shown in Figure 4.37. Only tephra 13-51 was reanalysed in this study, so there are no trace element concentrations for tephra 16-71. Based on the major elements alone, the two tephra are very similar, and could well be correlatives.

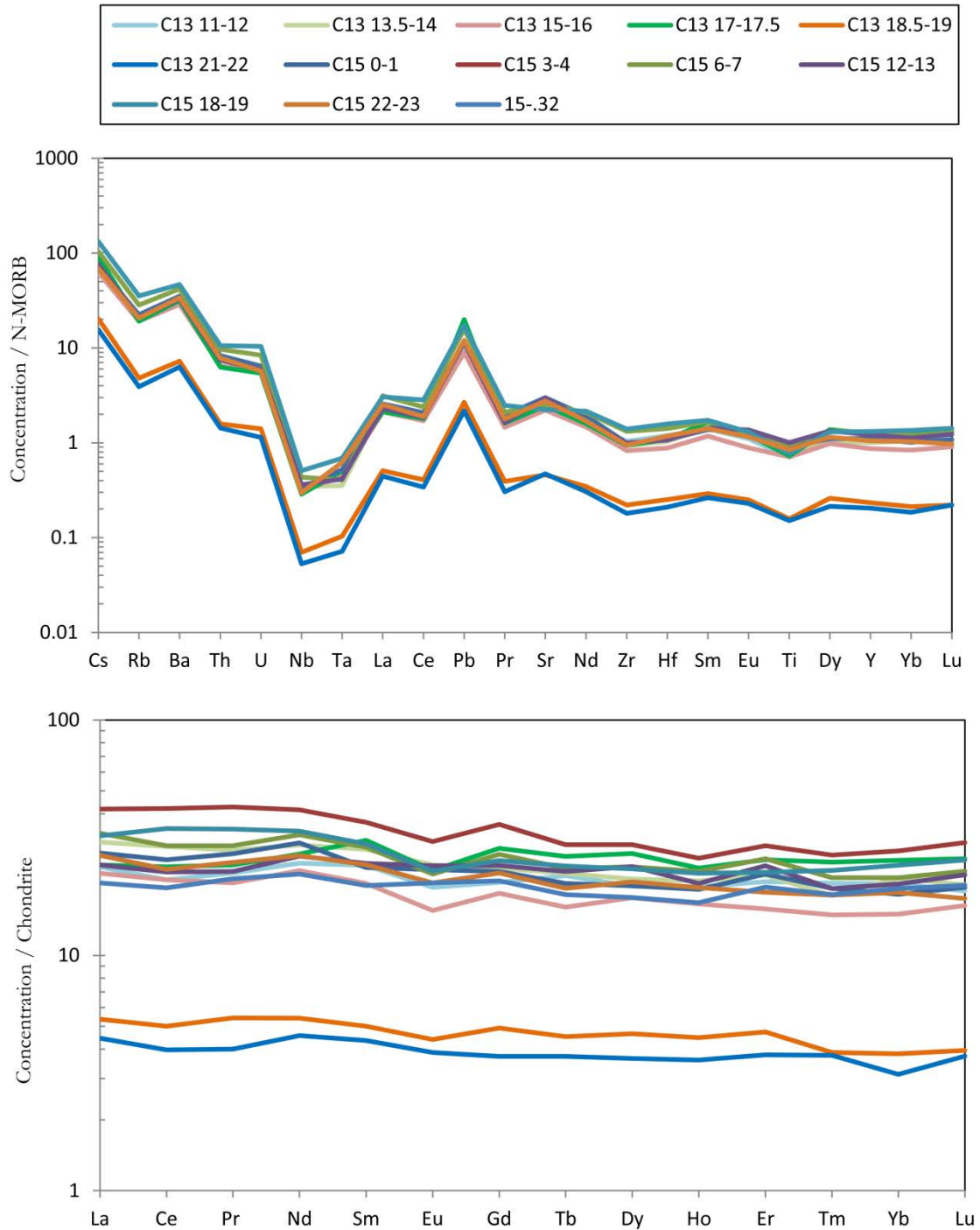


Figure 4.32 Multi-element plot and REE plot for potential correlatives. C13 18.5-19 and C13 21-22 have appear less enriched, but this is due to issues with the analysis. These two samples follow the same geochemical trends as the other potential correlatives. Multi-element plot normalised to N-MORB values of Sun and McDonough (1989) and REE plot normalised to chondrite values from Sun and McDonough (1989).

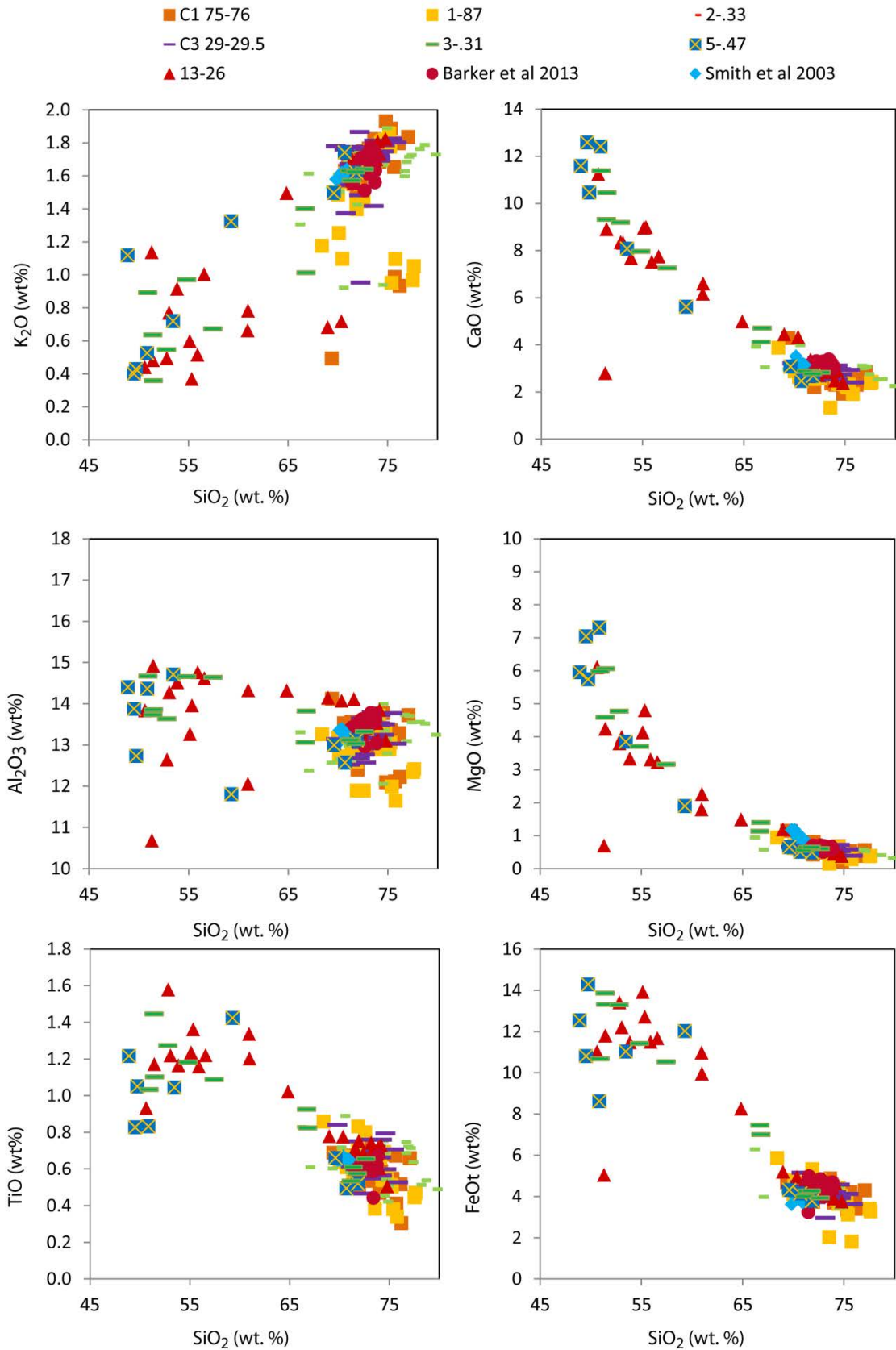


Figure 4.33 Variation diagrams of selected major oxides vs. SiO_2 for potential SBT correlative tephra layers. All analyses have been corrected for machine drift as outlined in Chapter 3. Each point represents a single glass shard, and their depth is in cms. Previously derived SBT values have been plotted from Barker *et al.* (2013) and Smith *et al.* (2003b).

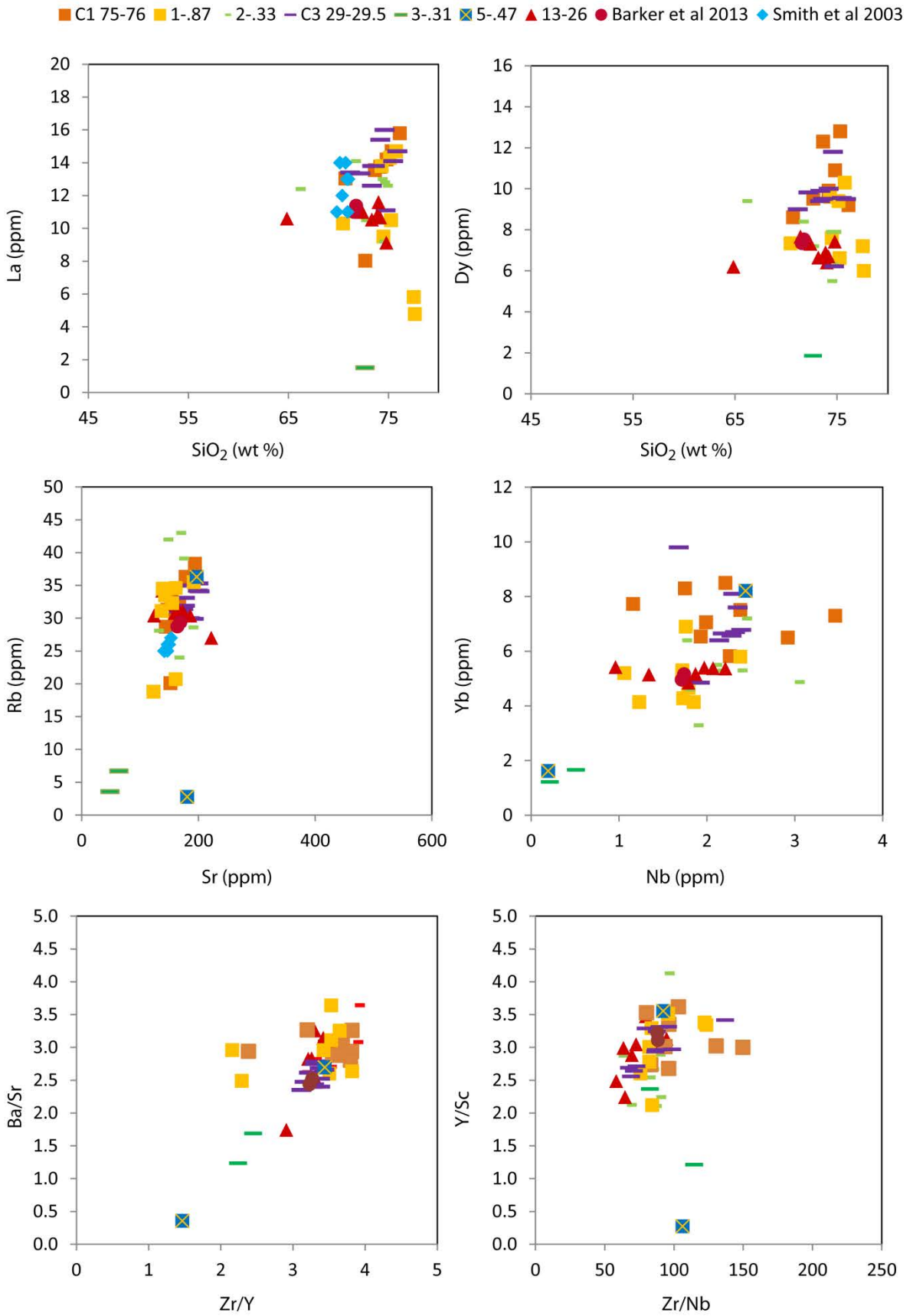


Figure 4.34 Variation diagrams of selected major and trace elements, including trace element ratio plots for potential SBT correlates. Each point represents a single glass shard, and their depth is in cms. Previously derived SBT values from Barker *et al.* (2013) and Smith *et al.* (2003b) have been plotted.

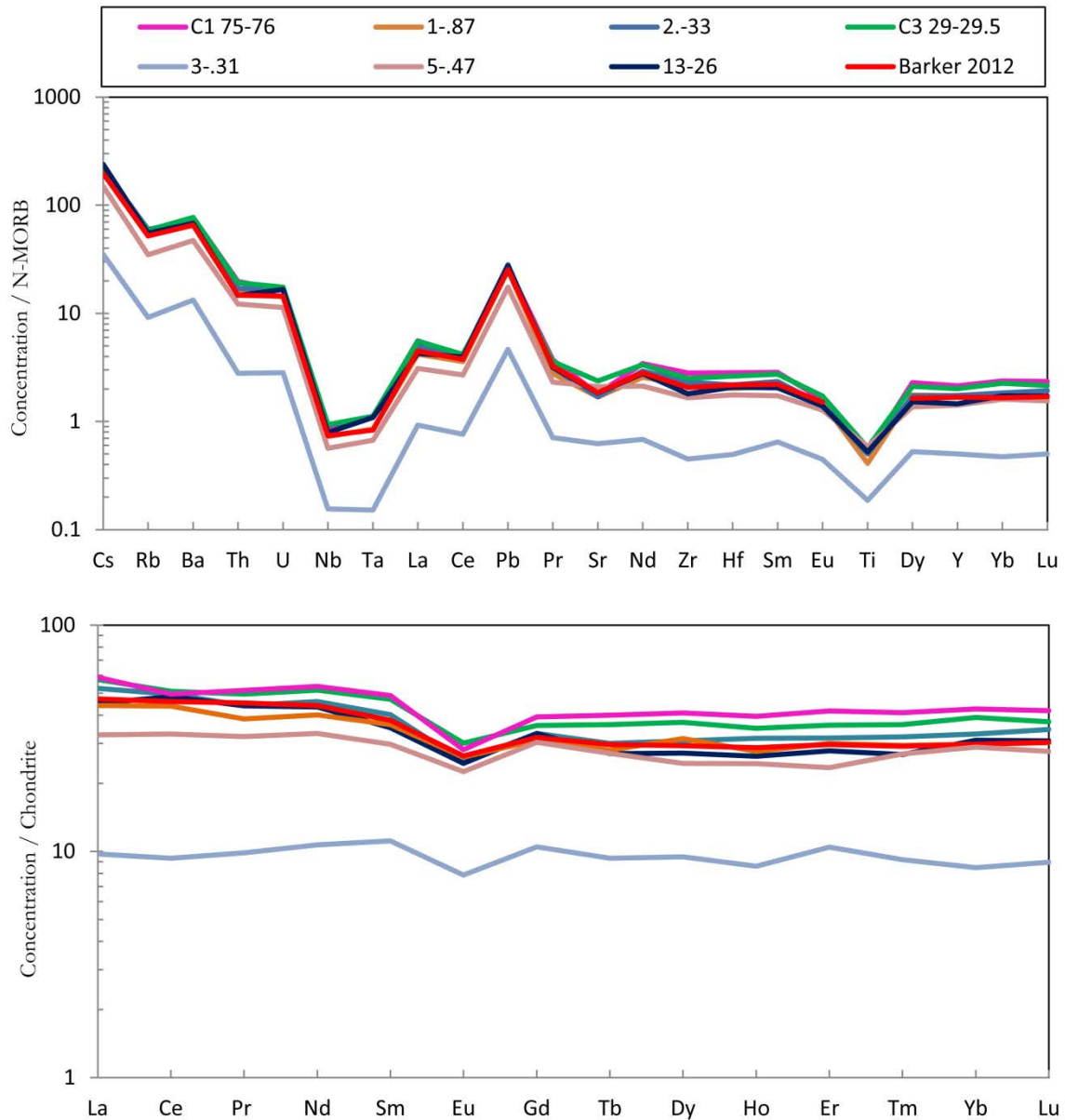


Figure 4.35 Multi-element diagram and REE plot showing the mean of each of the potential SBT correlative samples. Multi-element plot normalised to N-MORB values of Sun and McDonough (1989) and REE plot normalised to chondrite values from Sun and McDonough (1989). Note that although very similar geochemically, tephros C1 75-76 and C3 29-29.5 are slightly enriched in REEs compared to the other samples and SBT values published in Barker *et al.* (2013).

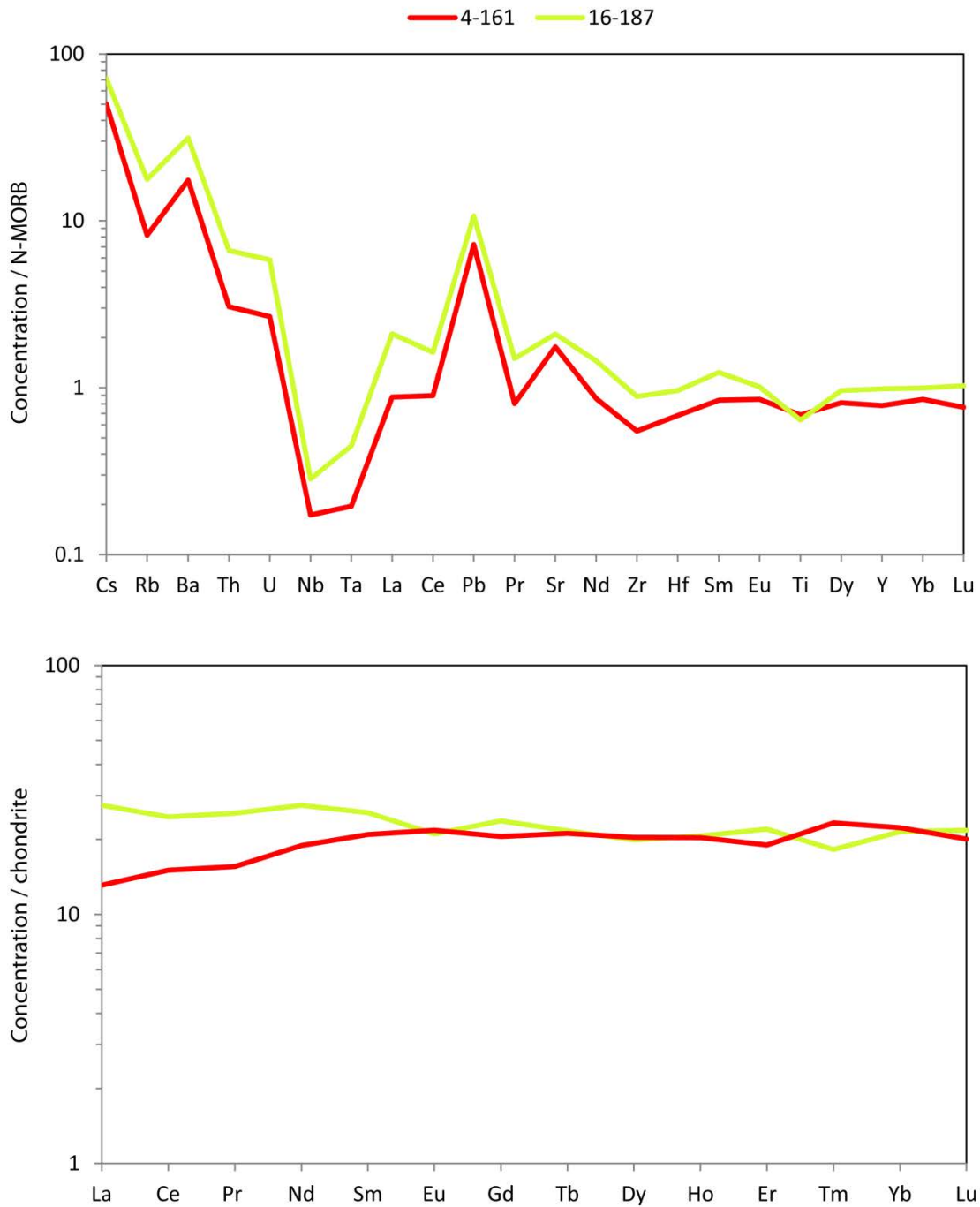


Figure 4.36 Multi-element plot and REE plot for shards from samples 4-161 and 16-187 to show that the two tephtras are distinct. Multi-element plot normalised to N-MORB values of Sun and McDonough (1989) and REE plot normalised to chondrite values from Sun and McDonough (1989).

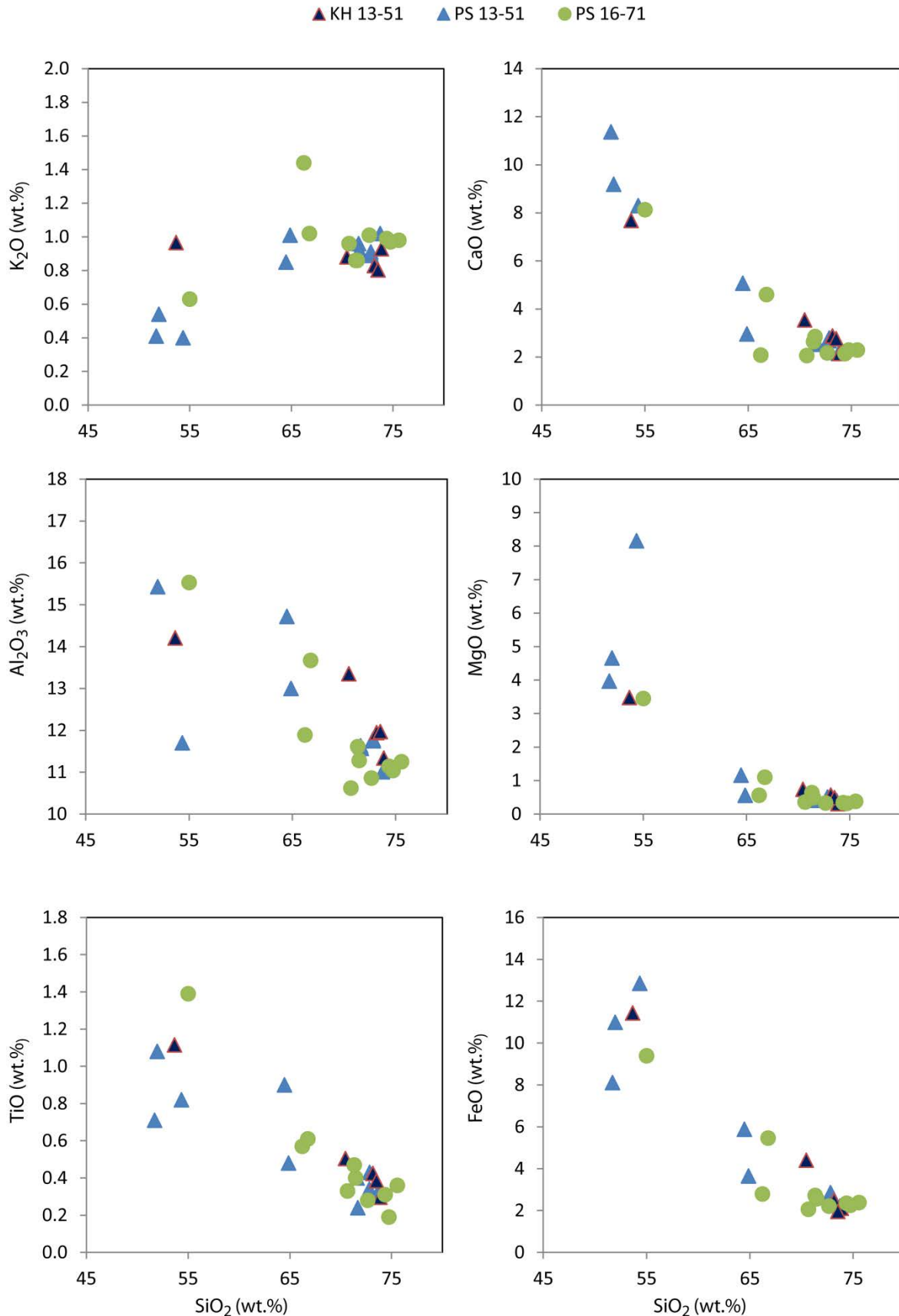


Figure 4.37 Variation diagrams for SiO₂ vs. major oxides for tephra layers 13-51 and 16-71, identified as correlatives by Shane and Wright (2011). KH 13-51 was analysed in this study and this data has been corrected for machine drift as outlined in Chapter 3. Each point represents a single glass shard, and their depth is in cms. PS 13-51 and 16-71 have been adapted from the published values by Shane and Wright (2011) in order to be comparable with the data from this study. KH = this study, PS = Shane and Wright.

4.4 Summary of geochemical findings

Of the 89 samples analysed in this study, 40 were homogenous (<8 % 2 sd SiO₂ variation). A summary of the results of geochemical analysis determining homogeneous, heterogeneous and bimodal tephra are presented in Table 4.1, which also shows the number of tephra samples analysed for each core. Three of the homogeneous samples were individual pyroclasts found in the cores, and are not considered to represent a discrete event. Also two of the homogeneous samples were correlatives with the SBT, and represent a single event; this has been taken into account when reporting the number of events recorded in the cores. Twenty seven of the samples presented in Shane and Wright (2011) were reanalysed and the combined results are presented in Table 4.2, showing the offset between the two datasets. After taking discrepancies between the datasets into account, this study presents 31 new tephra layers, each interpreted to represent a discrete eruptive event. Shane and Wright (2011) reported only 27 discrete tephra events, so with the results of this study a total number of discrete events recorded in the cores is 58. However, as shown in Table 4.2, two of the tephra samples presented as homogenous by Shane and Wright (2011) have in this study been found here to be heterogeneous. Therefore, there are a total of 56 homogeneous tephra events represented in the cores. As mentioned earlier in this chapter, many of the heterogeneous tephra layers show evidence of fractional crystallisation and may represent a discrete eruptive event. This will be discussed in more detail in Chapter 6.

Table 4.1 Summary table of results from this study outlining how many samples from each core were analysed and how many samples from each core were homogenous, heterogeneous or bimodal.

Core number	Number of samples analysed	Homogeneous samples	Bimodal samples	Heterogeneous samples	
TAN0706-1	18	14	4	-	Raoul
TAN0706-2	3	2	-	1	
TAN0706-3	9	2	3	4	
TAN0706-4	14	8	-	6	
TAN0706-5	6	3	1	2	
TAN0706-7	3	2	-	1	
TAN0706-8	4	1	2	1	
TAN0706-9	1	-	1	-	
TAN0706-10	2	2	-	-	
TAN0706-13	14	3	5	6	
TAN0706-15	7	1	1	5	
TAN0706-16	8	2	-	6	
Totals	89	40	17	32	

Table 4.2 Major element results for samples analysed by Shane and Wright (PS) (2011) and reanalysed in this study (KH). The data from Shane and Wright (2011) is italicised, and the offset between the data in each study presented. n represents the number of glass shards analysed in each sample. Data from Shane and Wright (2011) has been adapted from the published values in order to be comparable to the data from this study. Depth downcore is in cm (1-40 = Core 1, 40 cm depth)

sample number	1-.40 ^{KH}	<u>1-.40^{PS}</u>	% offset	1-.87 ^{KH}	<u>1-.87^{PS}</u>	% offset				
n	10	10		26	9					
EPMA	mean	2 sd								
SiO ₂ (wt %)	71.88	4.39	<i>72.37</i>	4.06	-0.49	73.15	6.37	<i>71.63</i>	1.05	1.52
Al ₂ O ₃	13.04	9.48	<i>12.78</i>	5.85	0.27	12.87	8.59	<i>13.04</i>	2.51	-0.17
TiO ₂	0.60	34.31	<i>0.59</i>	33.36	0.01	0.60	44.93	<i>0.59</i>	16.11	0.00
FeOt	4.12	37.63	<i>4.07</i>	21.92	0.05	4.00	42.99	<i>4.19</i>	10.50	-0.19
MnO	0.04	329.03	<i>0.15</i>	54.09	-0.11	0.13	65.55	<i>0.16</i>	51.06	-0.03
MgO	0.48	52.96	<i>0.57</i>	58.49	-0.09	0.53	61.71	<i>0.64</i>	28.20	-0.11
CaO	2.68	24.81	<i>2.74</i>	22.43	-0.06	2.60	34.70	<i>2.96</i>	9.92	-0.36
Na ₂ O	2.24	77.51	<i>4.64</i>	5.58	-2.40	3.48	23.72	<i>4.65</i>	4.78	-1.17
K ₂ O	1.54	24.48	<i>1.67</i>	30.01	-0.13	1.58	64.04	<i>1.71</i>	9.33	-0.14
Cl	0.35	54.82	<i>0.41</i>	36.70	-0.06	0.30	61.88	<i>0.42</i>	25.34	-0.12
Total	96.97	2.57				99.17	3.69			
sample number	1-.97 ^{KH}	<u>1-.97^{PS}</u>	% offset	2-.33 ^{KH}	<u>2-.33^{PS}</u>	% offset				
n	29	10		28	9					
EPMA										
SiO ₂ (wt %)	73.06	14.77	<i>75.40</i>	2.29	-2.34	73.78	8.50	<i>71.39</i>	3.16	2.39
Al ₂ O ₃	12.71	17.08	<i>12.14</i>	3.71	0.56	13.21	7.68	<i>13.02</i>	3.48	0.19
TiO ₂	0.52	79.13	<i>0.43</i>	32.21	0.09	0.62	35.92	<i>0.61</i>	53.17	0.01
FeOt	3.89	95.04	<i>3.19</i>	35.04	0.71	4.23	27.26	<i>4.46</i>	27.56	-0.23
MnO	0.06	226.94	<i>0.15</i>	84.57	-0.08	0.04	281.60	<i>0.19</i>	67.62	-0.15
MgO	0.72	251.39	<i>0.42</i>	45.28	0.30	0.54	53.36	<i>0.65</i>	43.90	-0.11
CaO	2.94	107.88	<i>2.49</i>	21.98	0.45	2.84	25.94	<i>3.08</i>	26.81	-0.23
Na ₂ O	3.41	17.73	<i>4.45</i>	6.18	-1.04	2.90	68.12	<i>4.47</i>	3.09	-1.57
K ₂ O	1.22	138.46	<i>1.08</i>	23.64	0.14	1.62	27.94	<i>1.73</i>	15.67	-0.12
Cl	0.21	61.10	<i>0.25</i>	48.99	-0.04	0.34	41.82	<i>0.40</i>	24.76	-0.06
Total	98.74	4.38				100.13	5.24			

Table 4.2 continued

sample										
number	3-.15 ^{KH}		<u>3-.15^{PS}</u>		% offset	3-.31 ^{KH}		<u>3-.31^{PS}</u>		% offset
n	30		10			13		10		
EPMA	mean	2sd								
SiO ₂ (wt %)	59.61	15.09	64.25	26.26	-4.63	62.21	29.09	66.60	20.92	-4.39
Al ₂ O ₃	14.71	9.57	13.95	17.07	0.76	13.62	10.51	13.70	18.45	-0.08
TiO ₂	1.04	29.69	0.80	66.11	0.24	0.91	66.85	0.83	69.66	0.08
FeOt	10.21	40.20	7.79	107.58	2.42	8.12	105.33	6.79	97.43	1.33
MnO	0.03	389.23	0.23	40.94	-0.20	0.13	88.90	0.19	77.09	-0.06
MgO	3.10	59.07	2.21	150.07	0.89	2.60	168.78	1.64	132.22	0.96
CaO	7.58	38.65	6.00	94.11	1.58	5.90	118.61	4.79	96.35	1.11
Na ₂ O	2.87	27.19	3.65	46.43	-0.79	3.19	59.54	3.98	30.25	-0.78
K ₂ O	0.59	41.79	0.88	100.72	-0.29	1.27	128.48	1.21	74.17	0.06
Cl	0.14	53.57	0.24	73.57	-0.10	0.20	130.18	0.28	32.78	-0.08
Total	99.88	2.47				98.14	4.93			
sample										
number	4-.84 ^{KH}		<u>4-.84^{PS}</u>		% offset	4-120 ^{KH}		<u>4-120^{PS}</u>		% offset
n	22		10			9		9		
EPMA										
SiO ₂ (wt %)	55.97	10.05	56.09	9.38	-0.12	60.70	27.51	72.22	16.36	-11.52
Al ₂ O ₃	14.08	7.66	14.21	16.36	-0.13	13.46	2.39	13.55	8.83	-0.09
TiO ₂	1.34	28.73	1.21	36.41	0.12	0.49	101.40	0.56	106.49	-0.07
FeOt	12.46	14.02	12.53	27.75	-0.07	2.39	53.71	3.13	192.70	-0.73
MnO	0.06	288.19	0.24	79.29	-0.18	0.12	118.52	0.17	91.66	-0.05
MgO	3.78	50.98	3.73	68.76	0.05	0.64	73.04	0.86	222.12	-0.22
CaO	8.37	25.84	8.43	30.28	-0.06	2.42	55.84	2.85	128.26	-0.44
Na ₂ O	2.48	22.95	2.75	44.70	-0.27	4.07	19.01	5.13	26.34	-1.06
K ₂ O	0.56	47.30	0.62	53.44	-0.06	1.18	28.25	1.23	24.02	-0.05
Cl	0.12	73.28	0.18	57.03	-0.06	0.16	34.74	0.29	29.44	-0.14
Total	99.22	4.24				96.35	6.11			

Table 4.2 continued

sample number	4-129 ^{KH}		<u>4-129^{PS}</u>		% offset	4-153 ^{KH}		<u>4-153^{PS}</u>		% offset
n	11		9			9		10		
EPMA	mean	2 sd								
SiO ₂ (wt %)	55.79	2.38	56.00	7.08	-0.22	53.98	3.95	63.91	18.80	-9.92
Al ₂ O ₃	14.42	5.25	14.40	7.27	0.02	14.27	14.54	14.08	8.92	0.19
TiO ₂	1.20	6.29	1.16	14.42	0.03	1.17	8.16	0.87	47.96	0.30
FeOt	11.41	11.30	11.92	18.24	-0.51	11.40	11.79	7.96	67.37	3.44
MnO	0.16	53.21	0.22	57.47	-0.07	0.15	103.58	0.26	63.19	-0.11
MgO	3.28	15.16	3.78	52.59	-0.50	3.91	74.07	1.88	144.21	2.04
CaO	7.42	8.02	8.15	29.38	-0.73	7.71	12.68	5.18	84.57	2.53
Na ₂ O	3.02	9.69	3.06	34.97	-0.04	3.03	22.15	4.04	28.70	-1.02
K ₂ O	1.02	21.66	1.02	46.86	0.00	0.78	29.18	1.46	56.05	-0.67
Cl	0.16	31.53	0.28	58.03	-0.13	0.13	32.42	0.37	55.79	-0.24
Total	97.86	0.88				96.54	0.91			
sample number	4-161 ^{KH}		<u>4-161^{PS}</u>		% offset	5-.47 ^{KH}		<u>5-.47^{PS}</u>		% offset
n	10					9		10		
EPMA										
SiO ₂ (wt %)	54.08	3.76	57.50	15.63	-3.42	58.21	33.99	66.83	19.92	-8.62
Al ₂ O ₃	14.68	3.07	14.87	11.20	-0.19	12.90	4.45	13.54	27.77	-0.64
TiO ₂	1.21	8.88	1.09	29.23	0.12	0.56	32.05	0.77	60.95	-0.21
FeOt	11.55	7.71	10.57	43.83	0.99	4.08	13.10	6.83	104.11	-2.75
MnO	0.17	69.77	0.22	73.67	-0.05	0.12	27.35	0.20	119.40	-0.08
MgO	3.80	9.38	3.45	70.15	0.35	0.55	31.88	1.68	215.73	-1.13
CaO	8.14	7.43	7.79	45.63	0.35	2.75	22.51	4.56	96.77	-1.82
Na ₂ O	3.01	7.47	3.34	38.99	-0.33	3.55	5.79	4.00	40.71	-0.45
K ₂ O	0.74	22.65	0.93	56.02	-0.19	1.62	15.17	1.27	76.58	0.35
Cl	0.12	20.79	0.24	75.49	-0.12	0.28	46.22	0.32	75.30	-0.04
Total	97.21	1.80				97.12	1.78	2.59	231.81	

Table 4.2 continued

sample number	7-.6 ^{KH}		<u>7-.6^{PS}</u>		% offset	13-.9 ^{KH}		<u>13-.9^{PS}</u>		% offset
n	2		10			10		10		
EPMA	mean	2 sd								
SiO ₂ (wt %)	56.14	3.86	68.21	28.61	-12.07	58.59	31.90	71.92	5.93	-13.33
Al ₂ O ₃	13.61	13.76	13.13	26.55	0.49	14.05	19.08	12.90	8.82	1.15
TiO ₂	1.28	17.21	0.76	79.76	0.53	0.93	67.23	0.60	49.31	0.33
FeOt	12.20	31.48	6.55	137.00	5.65	8.66	80.11	4.19	27.82	4.47
MnO	0.16	19.45	0.15	142.61	0.01	0.14	86.57	0.16	73.20	-0.02
MgO	3.03	28.49	1.68	172.33	1.35	3.22	153.78	0.75	128.10	2.47
CaO	7.78	0.71	5.09	114.78	2.69	6.91	94.91	3.04	30.65	3.88
Na ₂ O	2.73	17.01	3.59	42.87	-0.86	3.03	42.14	4.54	7.25	-1.51
K ₂ O	0.43	25.83	0.68	58.58	-0.25	0.76	67.27	1.54	38.62	-0.77
Cl	0.09	28.28	0.18	60.90	-0.08	0.12	89.45	0.36	36.84	-0.24
Total	97.46	0.48				96.42	1.26	4.36	60.49	
sample number	13-13 ^{KH}		<u>13-13^{PS}</u>		% offset	13-26 ^{KH}		<u>13-26^{PS}</u>		% offset
n	6		10			27		9		
EPMA										
SiO ₂ (wt %)	55.17	10.00	68.62	17.92	-13.45	64.00	27.69	57.26	17.93	6.74
Al ₂ O ₃	14.47	8.09	13.55	12.86	0.92	13.89	10.77	15.14	22.59	-1.25
TiO ₂	1.16	20.52	0.72	79.61	0.43	0.97	61.95	1.06	34.92	-0.09
FeOt	11.30	19.62	5.69	96.66	5.62	8.06	95.11	10.49	49.78	-2.43
MnO	0.13	73.08	0.20	75.52	-0.07	0.07	277.88	0.21	66.72	-0.14
MgO	3.46	58.46	1.19	209.30	2.27	2.13	158.09	3.62	73.33	-1.49
CaO	7.70	33.79	3.93	108.26	3.77	5.59	97.77	8.03	48.49	-2.44
Na ₂ O	2.88	13.86	4.23	25.21	-1.35	3.14	28.95	3.19	42.88	-0.05
K ₂ O	0.89	79.41	1.50	56.54	-0.61	1.13	94.55	0.82	53.62	0.31
Cl	0.15	80.97	0.38	42.36	-0.23	0.25	87.11	0.19	89.60	0.06
Total	97.30	1.56				99.22	3.48			

Table 4.2 continued

sample										
number	13-33 ^{KH}		<u>13-33^{PS}</u>		% offset	13-51 ^{KH}		<u>13-51^{PS}</u>		% offset
n	30		9			10		10		
EPMA	mean	2sd								
SiO ₂ (wt %)	69.71	16.46	68.70	15.36	1.01	70.56	23.45	67.82	30.37	2.73
Al ₂ O ₃	13.71	20.82	14.29	32.42	-0.58	12.79	18.96	13.67	35.56	-0.88
TiO ₂	0.61	69.18	0.60	80.35	0.01	0.56	113.94	0.59	96.58	-0.03
FeOt	4.61	91.91	5.06	108.87	-0.45	4.68	153.82	5.65	138.23	-0.96
MnO	0.07	237.40	0.14	113.56	-0.07	0.05	329.75	0.16	71.40	-0.11
MgO	1.18	220.40	1.15	162.23	0.04	1.00	225.14	2.13	252.80	-1.12
CaO	4.21	102.67	4.63	87.09	-0.41	3.67	109.37	5.12	133.59	-1.45
Na ₂ O	3.37	26.55	4.28	32.66	-0.90	2.39	73.00	3.82	44.66	-1.43
K ₂ O	0.84	77.27	0.94	60.41	-0.10	0.88	30.75	0.83	64.34	0.05
Cl	0.16	94.88	0.22	86.54	-0.06	0.19	58.09	0.22	58.97	-0.03
Total	98.48	4.47				96.77	2.47			
sample										
number	13-75 ^{KH}		<u>13-75^{PS}</u>		% offset	15-32 ^{KH}		<u>15-32^{PS}</u>		% offset
n	2		6			15		11		
EPMA										
SiO ₂ (wt %)	50.26	3.15	50.80	2.50	-0.54	55.32	4.29	58.08	22.50	-2.77
Al ₂ O ₃	12.10	24.44	15.51	12.13	-3.41	14.54	4.75	14.74	13.48	-0.20
TiO ₂	0.66	66.81	0.96	79.42	-0.30	1.17	15.31	1.07	49.36	0.10
FeOt	10.96	62.16	12.36	28.22	-1.39	10.99	14.25	10.56	53.32	0.43
MnO	0.24	45.62	0.23	95.94	0.00	0.16	56.37	0.17	69.53	-0.01
MgO	9.78	46.03	5.52	58.17	4.26	3.38	19.23	3.53	66.16	-0.15
CaO	13.89	55.56	12.52	28.19	1.36	7.60	11.77	7.69	49.28	-0.09
Na ₂ O	1.39	121.28	1.61	26.63	-0.22	3.03	12.19	3.22	28.23	-0.19
K ₂ O	0.10	127.07	0.37	129.39	-0.27	0.70	26.17	0.70	36.68	0.00
Cl	0.03	212.13	0.11	70.08	-0.08	0.14	28.53	0.22	52.70	-0.07
Total	99.41	1.57				97.05	1.10			

Table 4.2 continued

sample					
number	16-187 ^{KH}		<u>16-187^{PS}</u>		% offset
n	8		9		
EPMA	mean	2sd			
SiO ₂ (wt %)	59.43	<i>12.83</i>	60.88	<i>14.91</i>	-1.45
Al ₂ O ₃	14.63	<i>8.12</i>	14.47	<i>5.78</i>	0.16
TiO ₂	1.11	<i>19.87</i>	1.09	<i>20.74</i>	0.03
FeOt	9.11	<i>41.17</i>	9.03	<i>49.97</i>	0.08
MnO	0.14	<i>133.61</i>	0.18	<i>89.77</i>	-0.05
MgO	2.71	<i>75.09</i>	2.61	<i>82.77</i>	0.09
CaO	6.66	<i>49.26</i>	6.53	<i>48.55</i>	0.13
Na ₂ O	3.40	<i>19.24</i>	3.87	<i>27.92</i>	-0.47
K ₂ O	0.87	<i>43.25</i>	1.05	<i>58.48</i>	-0.18
Cl	0.13	<i>35.36</i>	0.29	<i>58.71</i>	-0.16
Total	98.19	<i>3.06</i>			

Chapter 5

Stratigraphy Results

5.1 Introduction

Ten piston cores collected on the TAN0706 voyage of the R.V. *Tangaroa* from offshore of Raoul and Macauley islands in the Kermadec arc form the stratigraphic database for this study. Non-invasive analyses were conducted on the cores, along with selected sediment and tephra sampling in order to construct a robust stratigraphy and associated tephrochronology for the dataset. The texture, laser grain size and calcium carbonate composition were analysed for 85 samples from the cores, oxygen isotope compositions were determined for 57 samples from three cores, and chemical analyses were conducted on 89 tephra samples as presented in Chapter 4. Data collected is presented in graphical format. Detailed core descriptions are presented in Appendix A.

5.2 Lithostratigraphy

Given the great variety of sediments (including volcanic ash layers) present in the cores, the most concise way of encapsulating their main characteristics is to group them into lithofacies. Lithofacies are distinctive bodies of sediment distinguished by characteristics such as colour, texture and sedimentary structures (Boggs, 1987). Eight lithofacies are used to describe the core materials in this study.

Facies A – Olive brown silt (bioturbated) typically occurring near the top of the cores collected. It is pale yellow - greyish brown clayey silt with signs of bioturbation and ranges in thickness from three to 37 cm. Facies A is generally (but not exclusively) underlain by an olive brown silt (Facies B, see below)

Facies B – Olive brown silt typically occurring below Facies A. It is light yellowish-olive brown, clayey coarse silt with no bioturbation and some faint laminations. The coarser grain size is associated with the presence of both foraminifera and fine ash. There are numerous tephra layers interspersed with this facies (Facies E, see below). The unit ranges in thickness from four to 103 cm and has a sharp basal contact.

Facies C – Grey fine sand is found exclusively in the lower section of Core 16 and is a light to dark grey silty fine sand, bioturbated unit with occasional laminations present throughout. Coarser grain sizes are associated with the tephra layers interspersed throughout this facies (Facies E, see below). The unit ranges in thickness from 19.5 to 22 cm.

Facies D – Light grey sand is found beneath Facies C in Core 16 and is light grey silty sand with no bioturbation. Laminations are present throughout as are tephra layers (Facies E, see below). Coarser grains are associated with tephra layers. Two small clasts (1 x 1 cm) were found embedded in this facies. The unit is 51 cm thick.

Facies E – Brown to grey ash occurring throughout the cores. They are divided into subfacies based on texture and colour.

E1 – Olive grey ash : fine-medium ash with coarse ash grains throughout. Slight bioturbation may be present in some layers. Thickness ranges from a few cm to 24 cm. Only present in cores collected from offshore of Macauley Island.

E2 – Black fine-medium ash : distinct colour and textural banding throughout. Thickness ranges from 3.7 to 16 cm. Only present in Core 13.

E3 – Greyish brown fine ash: small lapilli size at the top of the unit, slightly darker towards the base. The unit is 7.2 cm thick and is only present in Core 4.

E4 – Olive brown ash: medium-coarse ash. The unit is 12 cm thick and is only found in Core 4.

E5 – Dark grey coarse ash: coarse ash with some very coarse ash, slight colour banding. Thickness ranges from two to six cm. Only found in cores collected from offshore of Raoul Island.

E6 – Light grey ash: fine-medium ash which is a few cm in thickness

E7 – Light brown fine ash: fine-medium ash. Thickness from 3.5 to 15 cm. Only present in Core 16.

E8 – Black medium-coarse ash: coarse ash graded unit. Lower contact slightly bioturbated. Thickness ranges from 1-3.7 cm. Only present in Core 3.

E9 – Grey medium-coarse ash: graded unit, Lower contact bioturbated. Thickness ranges from 4 – 13 cm.

E10 - Dark grey to black fine-coarse ash: slight reverse grading. Thickness ranges from 2 to 5 cm.

E11 - Black ash with lapilli: graded unit, from fine –coarse ash near the top of the unit, grading to medium lapilli at the base. Thickness ranges from 2.7 to 6.5 cm and is present in Cores 7/8.

E12 – Olive ash to lapilli: graded unit, from medium lapilli at the base to fine-medium ash at the top of the unit. Lapilli covered in olive sandy material. Complex sloped boundary. Thickness of 6.5 cm. Only found in Core 10.

E13 – Dark grey lapilli: medium ash to medium lapilli . Faint normal grading evident. Sharp basal contact. Thickness of 9 cm. Only present in Core 10.

E14 – Grey fine-medium ash: slightly bioturbated lower contact. Thickness of 2cm. Only present in Core 15.

E15 – Dark grey ash: fine – very coarse ash with a few lapilli present. Normal colour gradation. Sharp basal contact. Thickness of 21 cm. Only found in Core 15.

E16 - Black coarse ash: coarse–very coarse ash, few fine lapilli. Thickness of 1.5 cm. Only present in core 15.

Facies F – Light brownish grey silty clay which shows no sign of bioturbation and has a sharp lower contact. It is present only in Core 1 and is 16 cm thick.

Facies G – Olive grey silty clay which varies from light olive grey to light brownish grey which varies from silty clay to clayey silt. The unit is bioturbated, and ranges in thickness from 6.5 to 7.5 cm and is present exclusively in Core 1.

Facies H – Greyish brown silty sand varies in colour from greyish brown to olive grey with some colour banding. The unit is bioturbated and only present in Core 1 and is 17 cm thick

5.3 Non-Invasive properties

Non-invasive analyses were conducted on the reference split of the cores in order to present a complete stratigraphy and also to select the best areas for sampling for both tephra and foraminifera. Results are summarised in Figure 3.11, with figures of each core displaying the non-invasive properties presented in Appendix B.

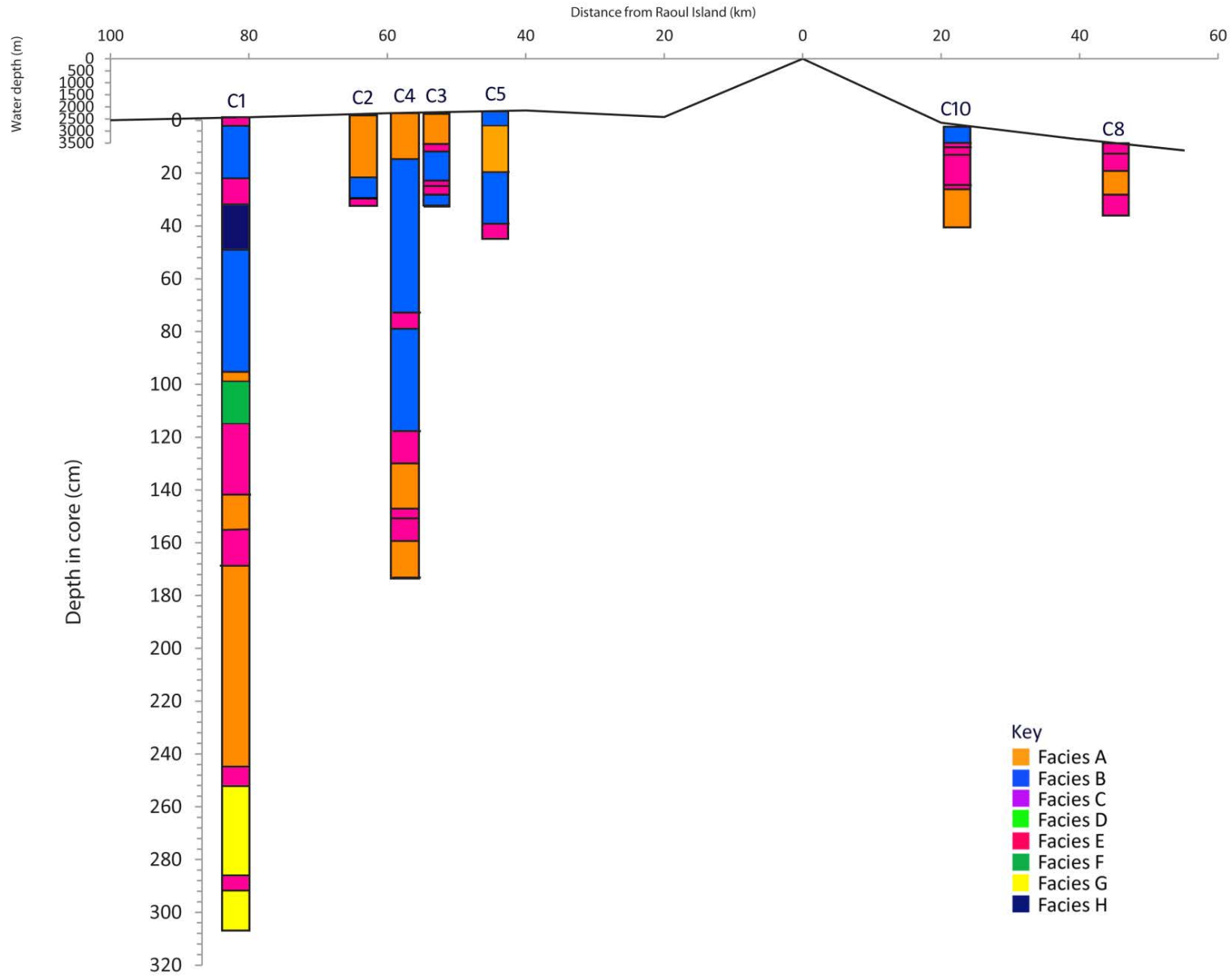


Figure 5.1 Lithology and stratigraphy of cores at locations offshore of Raoul Island showing the distance from Raoul Island and water depth at which the core was taken.

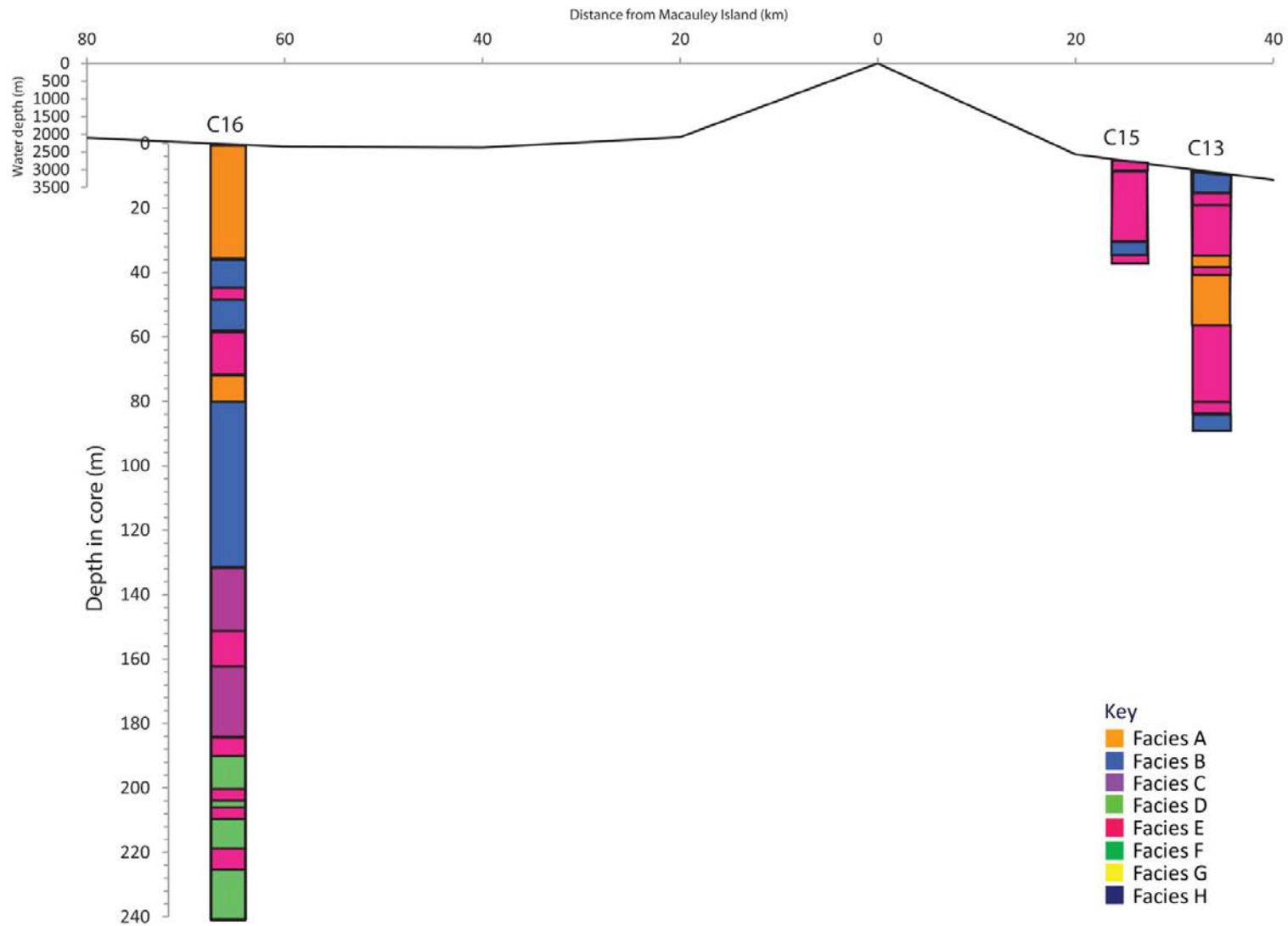


Figure 5.2 Lithology and stratigraphy at core locations from offshore of Macauley Island showing the distance of the core location from Macauley Island and water depth at which the core was extracted.

5.4 Calcium carbonate content

Calcium carbonate content was analysed for 87 samples. Calcium carbonate content of sediment samples varies throughout each core, and is generally lowest in tephra rich sections of the core. Samples from Core 1 are anomalous, in that they have much lower carbonate values than samples from any other core. During sampling there was noted a lack of foraminifera in the Core 1, so it follows that the carbonate content would be low. When presenting the mean carbonate content for each lithofacies the data from Core 1 has thus been omitted. The exception to this is Facies F, which is present only in Core 1. The carbonate properties for each facies are described below, and summarised in box and whisker diagram format in Figure 5.3. Carbonate curves for each of the major cores were generated to show variation downcore (Figure 5.4).

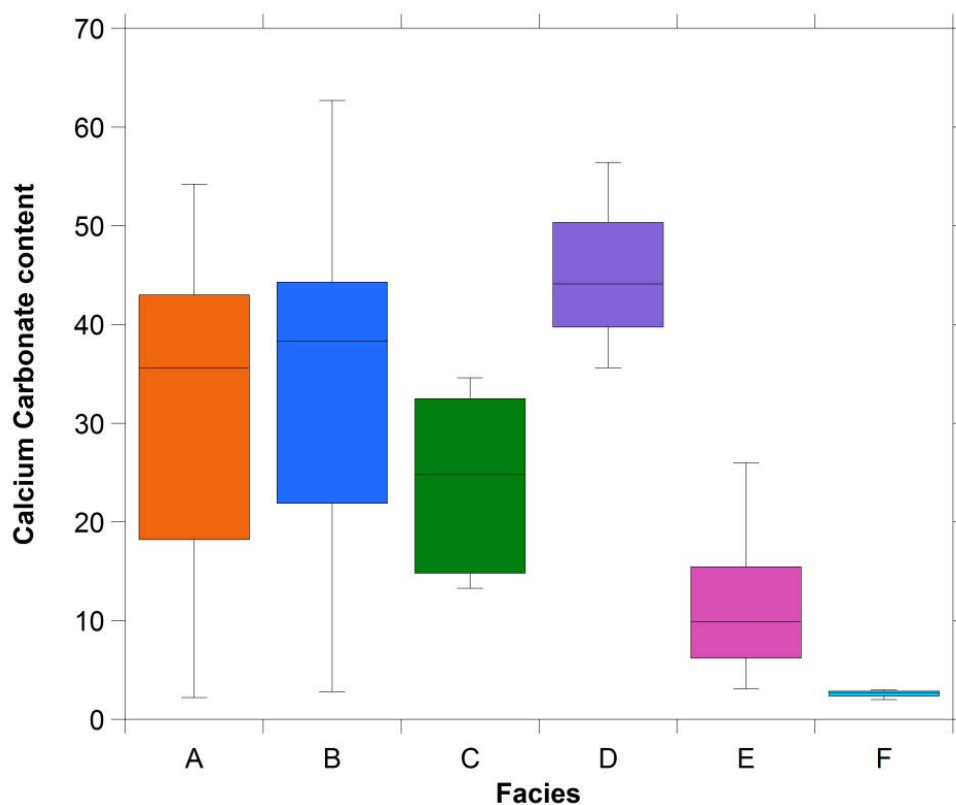


Figure 5.3 Box and whisker plots for the calcium carbonate content of each facies. Note that samples from Core 1 were omitted due to anomalously low CaCO_3 contents, with the exception of samples which make up Facies F.

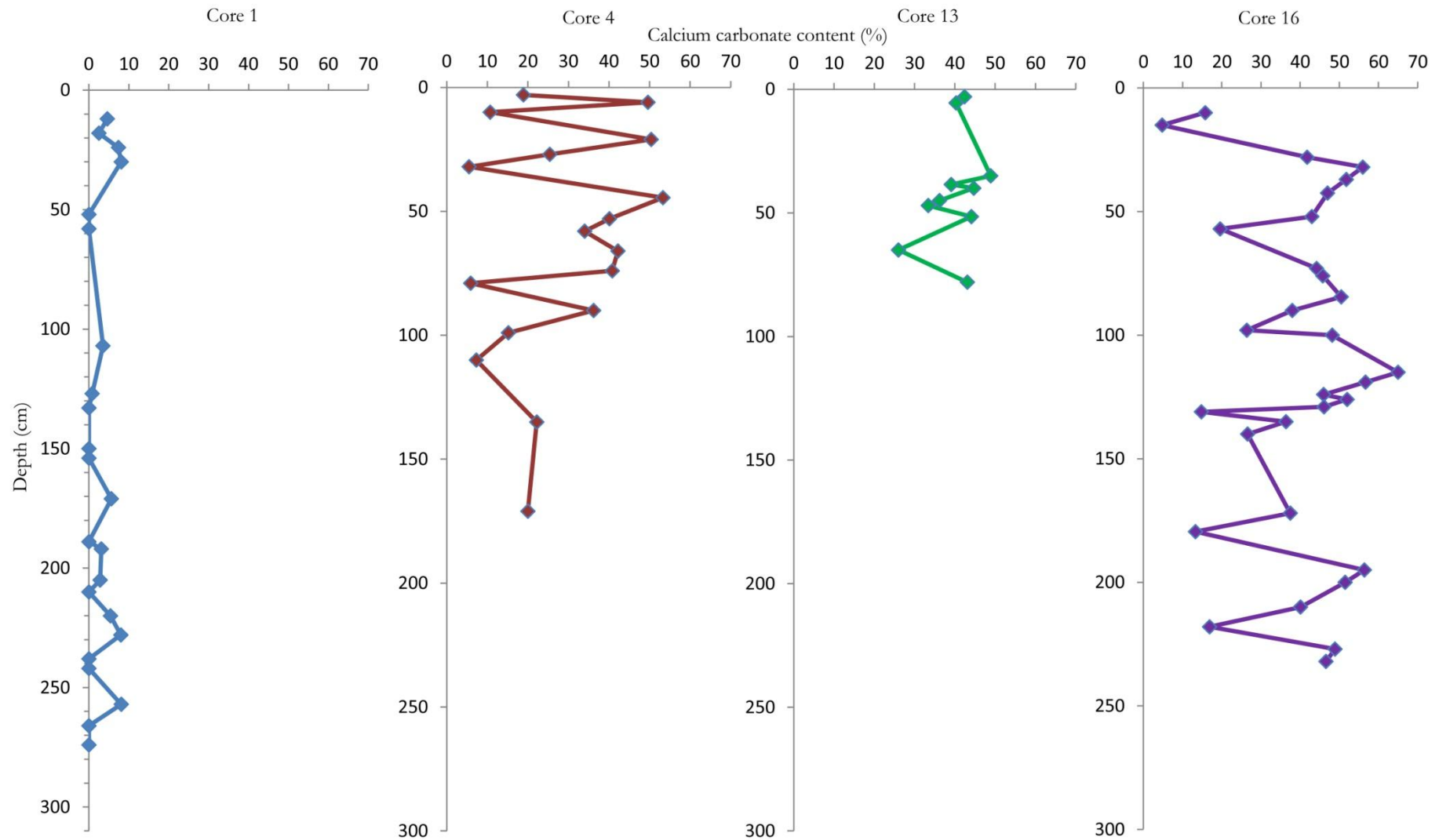


Figure 5.4 CaCO₃ contents of samples in each core, showing downcore variations. Note the anomalously low CaCO₃ content of samples in Core 1.

5.5 Sediment textures

Two methods were used to assess the grain size characteristics of sediment samples, as outlined in Chapter 3.

5.5.1 Grain sizes from sieving

Data collected from the sieving of samples at various size fractions ($>140\ \mu\text{m}$, $140\text{-}60\ \mu\text{m}$ and $<60\ \mu\text{m}$) were collated to find the cumulative percentage represented by each size fraction. Material $<60\ \mu\text{m}$ is silt or clay, material between $60\text{-}140\ \mu\text{m}$ is very fine-fine sand, and material $>140\ \mu\text{m}$ is any fraction coarser than fine sand (as defined by Udden, 1914; Wentworth, 1922). As illustrated in Figure 5.5 below, Core 1 is dominated by the $<60\ \mu\text{m}$ size fraction, with very little material $>140\ \mu\text{m}$. Cores 4 & 16 show more variation in grain size, as the middle sections of each core are dominated by the larger grain sizes. Core 13 is of lower resolution as less samples were collected from this core. In general, however, Core 13 displays the coarsest overall grain sizes, with the $<60\ \mu\text{m}$ size fraction having the lowest cumulative percent.

5.5.2 Grain sizes from laser diffraction analysis

Laser grain size descriptions are based on the Folk and Ward (1957) method and the distinction between grain sizes is presented in Table 5.1. Results were processed in GradiStat version 8.0 (developed by Blott, 2010). Results, divided up by lithofacies, are presented in Figure 5.6. With the exception of Facies E the majority of the facies are composed of material with silt or sandy silt grain sizes and all facies are poorly sorted. Facies A and B show the widest range of grain sizes. Figure 5.7 shows the total % of each facies which is gravel, sand or mud. We can see that no facies has any gravel component; all have some sand component which is a minor % of the total facies composition, with the exception of Facies E which is sand rich. Figure 5.8 shows the compositional breakdown of the grain sizes into smaller fractions. It shows that Facies E is noticeably coarser compared to the other facies, with the majority of the samples ranging from very coarse sand to very fine sand. All of the other facies are predominantly very coarse silt to very fine silt. Facies G seems to be slightly coarser than the other sedimentary facies, with 60% of the samples being coarser than coarse silt.

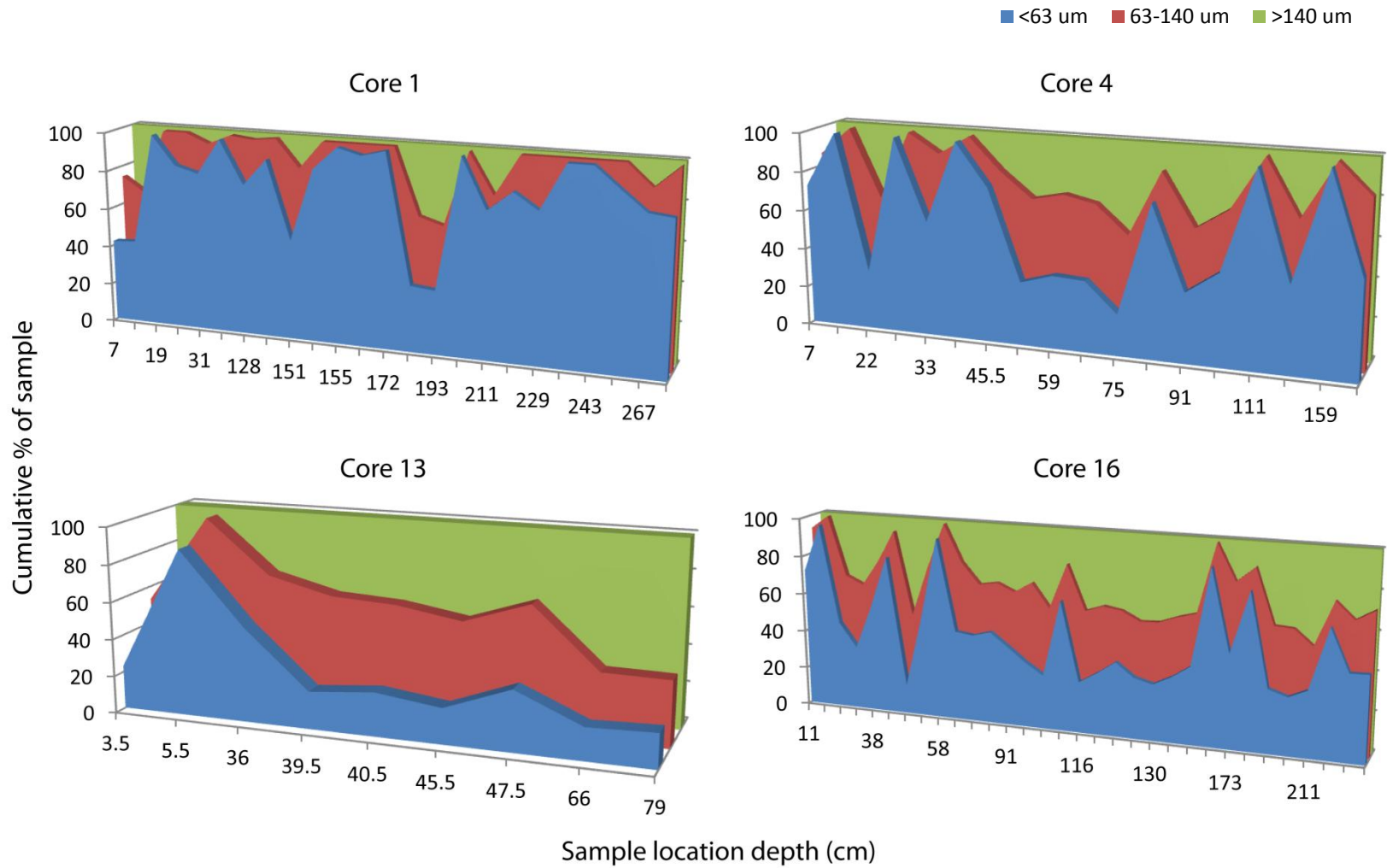


Figure 5.5 Grain size fractions that make up a cumulative % of the samples. Note that the x axis scale changes for each sample as the numbers displayed indicate the sample location.

Table 5.1 Grain size table adopted in GradiStat program, modified from Udden (1914) and Wentworth (1922).

phi	Grain Size		Descriptive term	
	mm			
-10	1024		Very Large	Boulder
-9	512		Large	
-8	256		Medium	
-7	128		Small	
-6	64		Very small	
-5	32		Very coarse	Gravel
-4	16		Coarse	
-3	8		Medium	
-2	4		Fine	
-1	2		Very fine	
0	1	microns	Very coarse	Sand
1	500		Coarse	
2	250	Medium		
3	125	Fine		
4	63	Very fine		
5	31		Very coarse	Silt
6	16		Coarse	
7	8		Medium	
8	4		Fine	
9	2		Very fine	
			Clay	

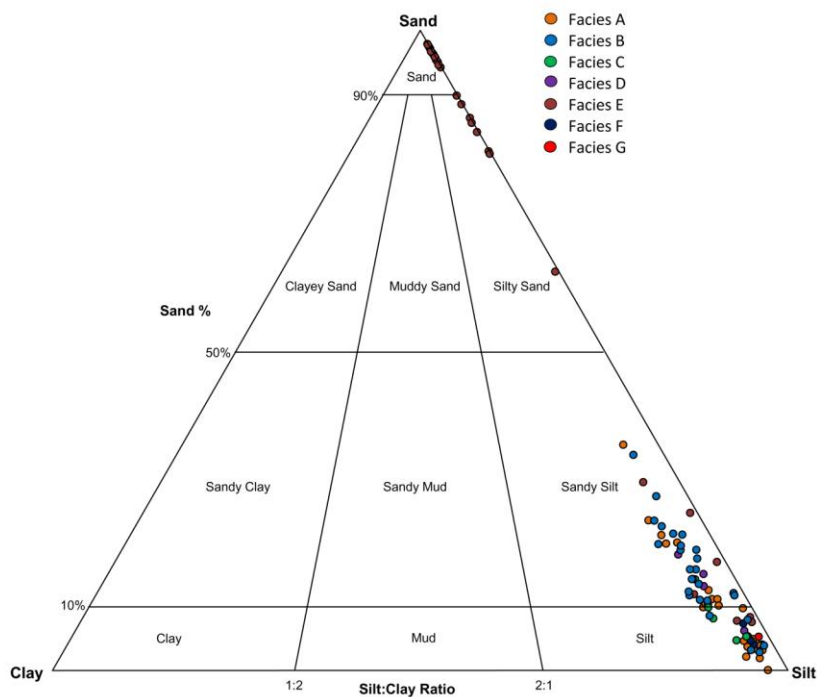


Figure 5.6 Sand:Silt:Clay (>63/63 - 2/<2 μm) diagram showing the composition of samples for each of the facies as determined by laser grain size analysis. Note that most of the facies display very similar textures, with the exception of Facies E.

Table 5.2 Sediment properties for each facies. Grain size properties were determined using GradiStat. The mean and range of CaCO₃ for each facies was calculated excluding data from Core 1, as it is anomalously low in CaCO₃ (with the exception of Facies F).

Facies	Sorting	Grain Size	Mean Grain size (μm)	Mean CaCO ₃ (%)	CaCO ₃ range (%)
A	Poorly sorted	Medium silt	16.2	31.4	2.2 - 54.2
B	Poorly sorted	Coarse silt	18.0	35.7	2.8 - 62.7
C	Poorly sorted	Medium silt	13.9	24.0	13.3 - 34.6
D	Poorly sorted	Medium silt	14.9	39.4	16.9 - 56.4
E	Poorly sorted	Fine-medium sand	233.4	12.6	3.1 - 51.5
F	Poorly sorted	Coarse silt	16.3	2.6	2.0 - 3.0
G	Poorly sorted	Coarse silt	19.0	3.8	3.8

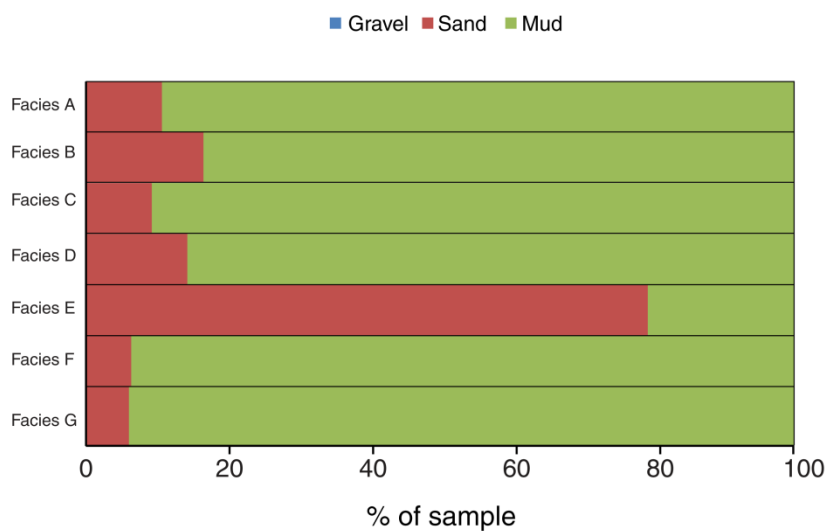


Figure 5.7 Cumulative plot displaying the composition of each facies between gravel/sand/mud (>2mm/2mm – 63 μm / <63 μm) as determined in GradiStat.

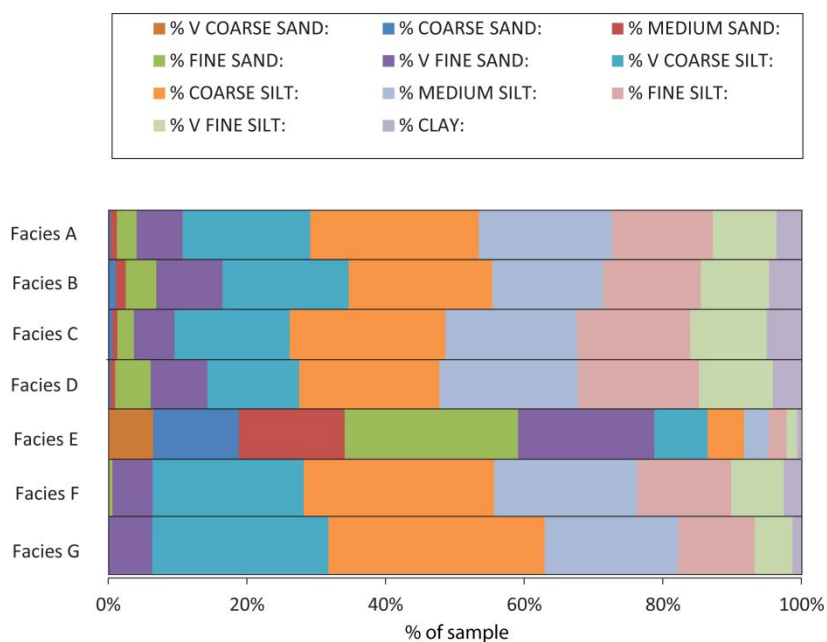


Figure 5.8 Cumulative plot displaying the composition of each facies in finer detail, with grain sizes ranging between very coarse sand (1 mm) to clay (<2 μm).

5.6 Chronostratigraphy

Foraminifera samples underwent oxygen isotope analysis at NIWA (Greta Point, Wellington) in order to construct a more robust age model for the cores and extend past the roughly 50 ka limit of radiocarbon dating (cf. Shane and Wright, 2011). The benefits of this method are manifold; the relative age of the entire core can be determined, all tephra layers can be assigned a relative age and more robust sedimentation rates can be calculated. Oxygen isotope analyses were undertaken on foraminifera from three cores (Cores 4, 13 and 16). An age model for Core 1 was originally planned, however when sampling the paucity of foraminifera in the core made this unfeasible and it was decided that the resolution would be too low to be of use in this study.

5.6.1 Age models

The oxygen isotope data from these cores were input into AnalySeries 1.2 (Paillard *et al.*, 1996), a program which uses a global reference oxygen isotope curve, LR04 (Lisiecki and Raymo, 2005) as a guide. Data from this study were then wiggle-matched or correlated to this reference curve. The data from each of the cores used to construct the age model are presented in Table 5.3 (note that benthic species were used). This correlation provided relative ages for the cores. This method does have inherent uncertainties, as discussed in Paillard *et al.* (1996), and there is also uncertainty in the correlation between data in this study and the reference curve; however this is very difficult to quantify. In order to minimise the uncertainty in the correlation, reliable 'tie points' are used, such as large transitions between glacial and interglacial cycles. In this study, oxygen isotope data from the benthic species *Uvigerina peregrina* for cores 13 and 16 and *Cibicides wuellerstorfi* for Core 4 were used to make correlations with the global reference curve.

Tephra layers complicate the age modelling process, as they are considered to be near instantaneous events and not part of background sedimentation. For this reason, the tephra layers are 'deleted' from the core, yielding the length of sedimentary material in the core and subsequently the actual depth that sediment samples were collected from. This actual depth is used as input into AnalySeries 1.2 along with the oxygen isotope data, and after correlating this data to the LR04 reference curve an age model is produced for each core. After correlation, a spreadsheet called 1AGECAL (part of the AnalySeries 1.2 program) is used to systematically re-add the tephra layers, without changing the overall age of the core based on the age model. This allows for tephra layers to be assigned ages based on the oxygen isotope curve.

Cores 4 and 13 were able to be correlated against the reference curve of Lisiecki and Raymo (2005); however, only two tie points were able to be used for both cores as shown in Figure 5.9. These two cores showed a glacial to modern sequence, which is reflected in the calculated ages which are presented in the Tables 5.4 and 5.5. The cores extend back to *ca.* 56 ka and *ca.* 33 ka, respectively. These age models could be improved with the collection and analysis of more samples from each core.

The presence of correlative tephra layers across cores provides an age tie point if the age of the tephra is known. For example, the Sandy Bay Tephra (SBT) from Macauley is present in three cores in this study: 1, 2 and 13. The SBT occurs at the base of Core 2, which means that this core extends to *ca.* 6.3 ka. It is also present as tephra 13-26 in Core 13; this conflicts, however, with the age model calculated here which dates the tephra layer at 12.5 ka. This contradiction again highlights the need to increase the resolution of the age model for this core.

Core 16 provided a robust correlation with the reference curve, as illustrated in Figure 5.9. Three tie points were used in the correlation with the reference curve, and other, tentative, tie points are also shown. The oxygen isotope curve for this core shows that the record extends back to the previous glacial, MIS6. The model ages calculated are presented in Table 5.6 and suggest that the Core 16 stratigraphic record extends back to *ca.* 170 ka.

Table 5.3 Oxygen isotope data collected in this study and used to create an age model for the cores. Note that Cores 13 and 16 used oxygen isotope data from *Uvigerina peregrina* whilst *Cibicoides wuellerstorfi* was used for Core 4 as more data was analysed for this sample. Precision data for the analyses is presented in Chapter 3.

Sample	$\delta^{13}\text{C}$	$\delta^{18}\text{O}$	Sample	$\delta^{13}\text{C}$	$\delta^{18}\text{O}$
Core TAN0706-13 <i>Uvigerina spp.</i>			Core TAN0706-16 <i>Uvigerina spp.</i>		
3	-0.28	3.37	10	0.85	2.79
35	-0.18	4.16	28	-0.58	4.75
38.5	-0.58	4.19	32	-0.39	4.59
40	-0.24	4.28	37	-0.44	4.29
45	-0.70	4.36	42.5	-0.25	4.18
47	-0.48	4.58	51.5	-0.07	4.15
65	-0.04	4.01	52	-0.42	4.22
78	-0.35	3.59	57	-0.05	4.31
Core TAN0706-4 <i>Cibicoides spp.</i>			76	-0.17	3.97
10	-0.58	3.12	84.5	-0.17	3.88
21	0.40	3.00	90	0.12	3.59
27	0.19	2.90	98	-0.08	3.94
40	0.24	3.89	100	-0.14	3.83
44.5	0.27	3.76	105	-0.32	4.05
58	0.21	3.26	115	0.01	3.66
66	0.06	3.71	119	0.15	3.67
74	0.09	3.69	124	-0.31	3.92
90	0.69	3.76	126	-0.06	3.82
99	0.28	3.27	129	-0.47	3.43
110	0.42	3.11	131	-0.22	3.87
126	0.22	3.08	135	0.10	3.67
135	0.51	2.88	140	0.38	3.27
171	0.31	2.94	172	-1.00	3.61
			195	-0.54	4.42
			200	-0.65	4.50
			210	-0.45	4.59
			227	-0.27	4.56
			232	-0.29	4.39

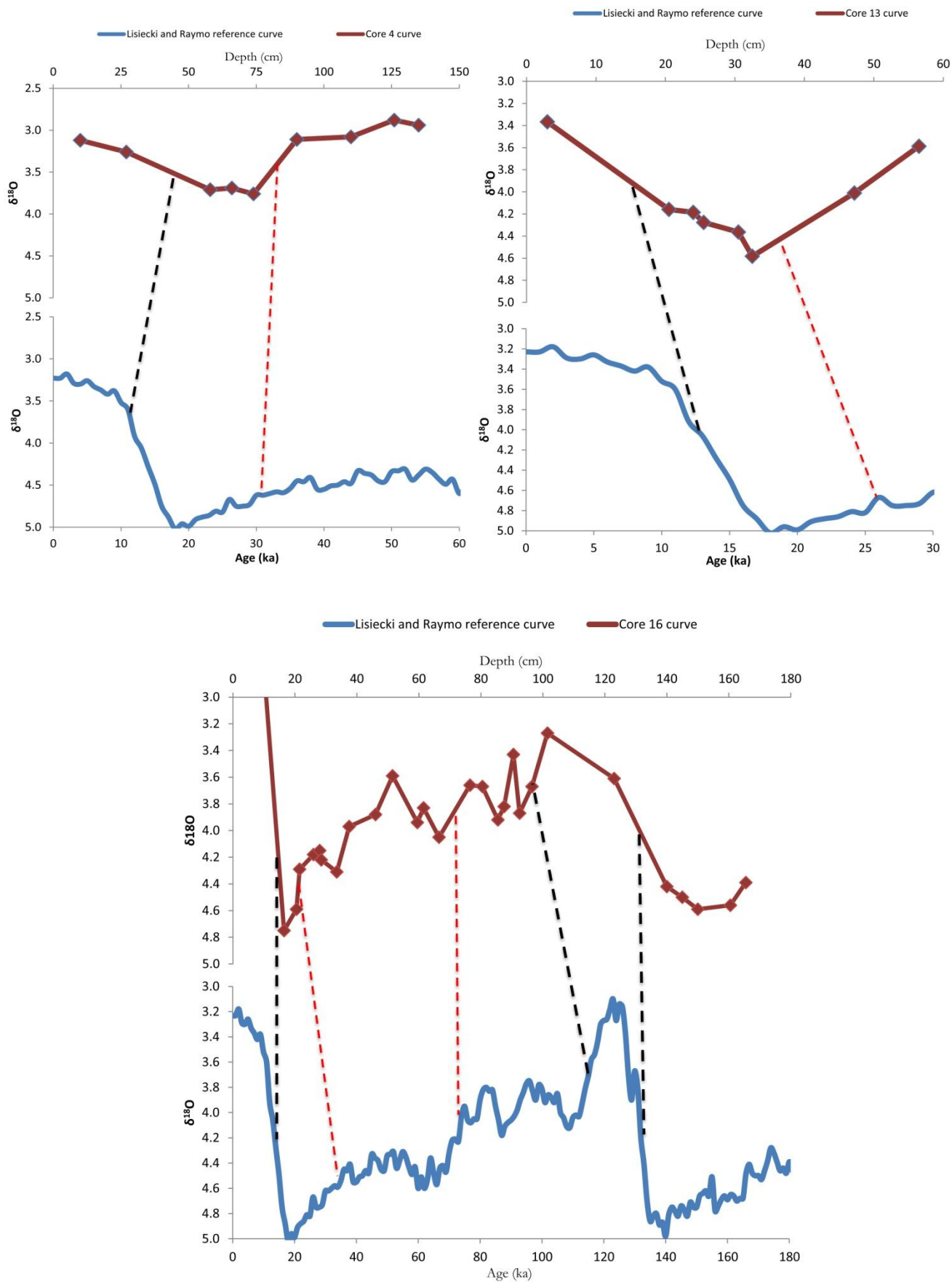


Figure 5.9 Oxygen isotope values presented from this study alongside the reference values from Lisiecki and Raymo (2005). The black dashed lines represent the tie points used to wiggle-match between the two curves, and the red lines are tentative tie points.

Table 5.4 Calculated ages for Core 4 using the reference curve from Lisiecke and Raymo (2005). Note that where there are two identical ages in the far right column this indicates the base and top of a tephra layer. As tephra deposits represent near-instantaneous events the top of the unit is considered to have the same age as the bottom.

Sample depth (cm) without tephra	Calculated Age (ka)	Sample depths (cm) including tephra	Calculated age (ka) including tephra
10.0	0.49	10.0	0.49
39.5	9.52	17.5	2.79
44.5	17.26	28.0	2.79
52.5	21.61	38.0	5.85
61.0	25.88	46.0	5.85
73.5	32.16	58.0	9.52
85.0	37.94	62.0	15.71
87.0	38.94	65.0	15.71
115.8	53.41	66.0	17.26
		74.0	21.61
		76.0	22.62
		83.5	22.62
		90.0	25.88
		95.0	28.40
		102.5	28.40
		110.0	32.16
		116.5	35.43
		121.0	35.43
		126.0	37.94
		133.0	37.94
		135.0	38.94
		149.0	46.28
		154.8	46.28
		160.0	48.88
		162.0	48.88
		171.0	53.41
		177.0	56.18

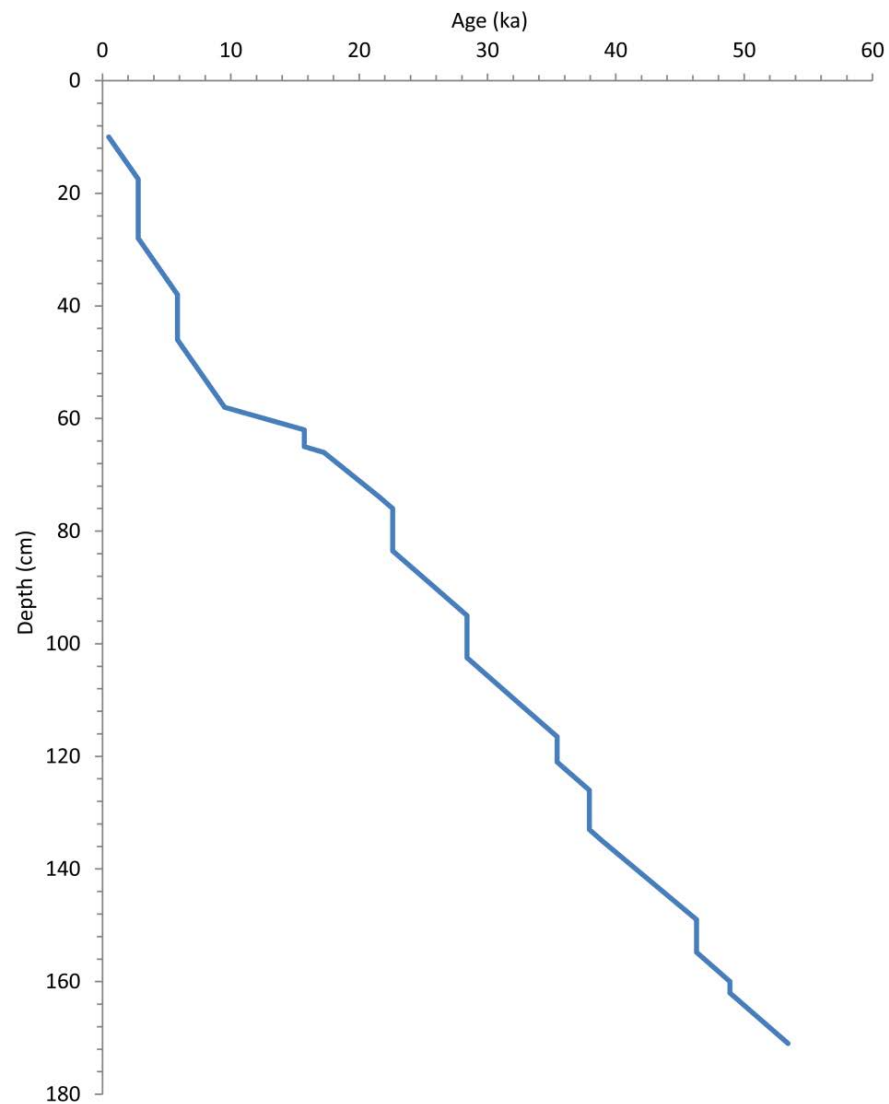


Figure 5.10 Age model for Core 4 presented as age downcore. Note that areas where the depth increases but the age does not include the presence of a tephra layer.

Table 5.5 Calculated ages for Core 13 using the reference curve from Lisiecke and Raymo (2005). Note that where there are two identical ages in the far right column this indicates the base and top of a tephra layer. As tephra deposits represent near-instantaneous events the top of the unit is considered to have the same age as the bottom.

Sample depth (cm) without tephra	Calculated Age (ka)	Sample depths (cm) including tephra	Calculated age (ka) including tephra
3.0	10.07	3.0	10.07
11.8	14.58	7.8	12.53
15.3	15.49	27.3	12.53
16.8	15.87	30.7	14.27
21.8	17.16	34.4	14.27
23.8	17.68	35.0	14.58
38.5	24.45	38.5	15.49
47.8	28.75	40.0	15.87
		45.0	17.16
		47.0	17.68
		48.0	18.14
		51.5	18.14
		65.0	24.45
		72.3	27.83
		76.0	27.82
		78.0	28.75
		85.0	32.98

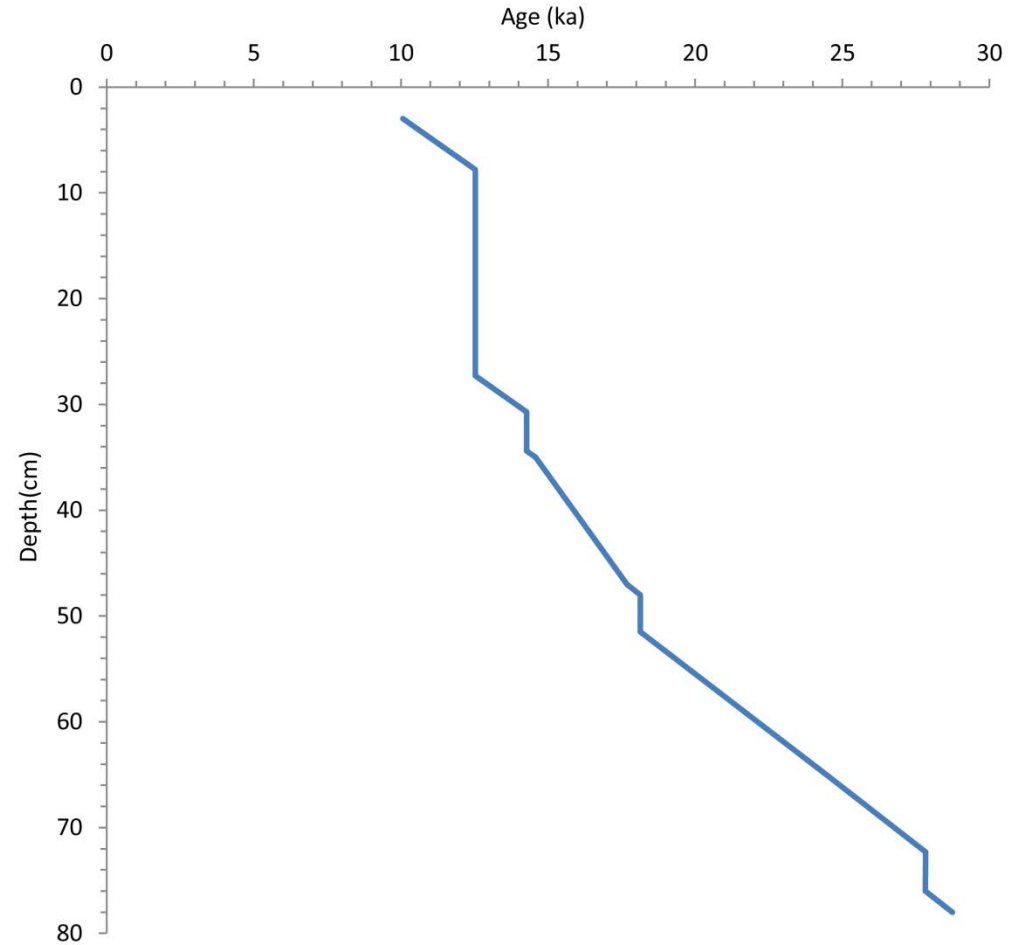


Figure 5.11 Age model for Core 13 presented as age downcore. Note that areas where the depth increases but the age does not include the presence of a tephra layer. The record for Core 13 starts at 10 ka, which could be the result of the core top being lost during recovery.

Table 5.6 Calculated ages for Core 16 using the reference curve from Lisiecke and Raymo (2005). Note that where there are two identical ages in the far right column this indicates the base and top of a tephra layer. As tephra deposits represent near-instantaneous events the top of the unit is considered to have the same age as the bottom.

Sample depth (cm) without tephra	Calculated Age (ka)	Sample depths (cm) including tephra	Calculated age (ka) including tephra
10.0	9.70	10.0	9.70
16.5	16.09	11.5	11.18
20.5	20.02	20.0	11.18
21.5	21.00	25.5	16.58
26.0	25.43	28.5	16.58
28.0	27.39	28.0	16.09
28.5	27.88	32.0	20.51
33.5	32.79	37.0	20.51
37.5	36.72	42.5	25.43
46.0	45.08	42.0	25.43
51.5	50.48	49.0	25.43
59.5	58.34	51.5	27.39
61.5	60.31	52.0	27.88
66.5	65.22	57.0	33.29
76.5	75.05	72.0	33.29
80.5	78.98	76.0	36.72
85.5	83.89	84.5	45.08
87.5	85.85	90.0	50.48
90.5	88.80	98.0	58.34
92.5	90.77	100.0	60.31
96.5	94.70	105.0	65.22
101.5	99.61	115.0	75.05
123.0	120.73	119.0	78.98
140.0	137.44	124.0	83.89
145.0	142.35	126.0	85.85
150.0	147.26	129.0	88.80
160.5	157.58	131.0	90.77
165.5	162.49	135.0	94.70
		140.0	99.61
		150.5	110.42
		161.0	110.42
		172.0	120.73
		183.0	132.03
		189.0	132.03
		195.0	137.44
		200.0	142.35
		201.0	143.83
		203.0	143.83
		205.5	146.28
		208.5	146.28
		210.0	147.26
		218.5	156.11
		225.0	156.11
		227.0	157.58
		232.0	162.49
		240.0	170.35

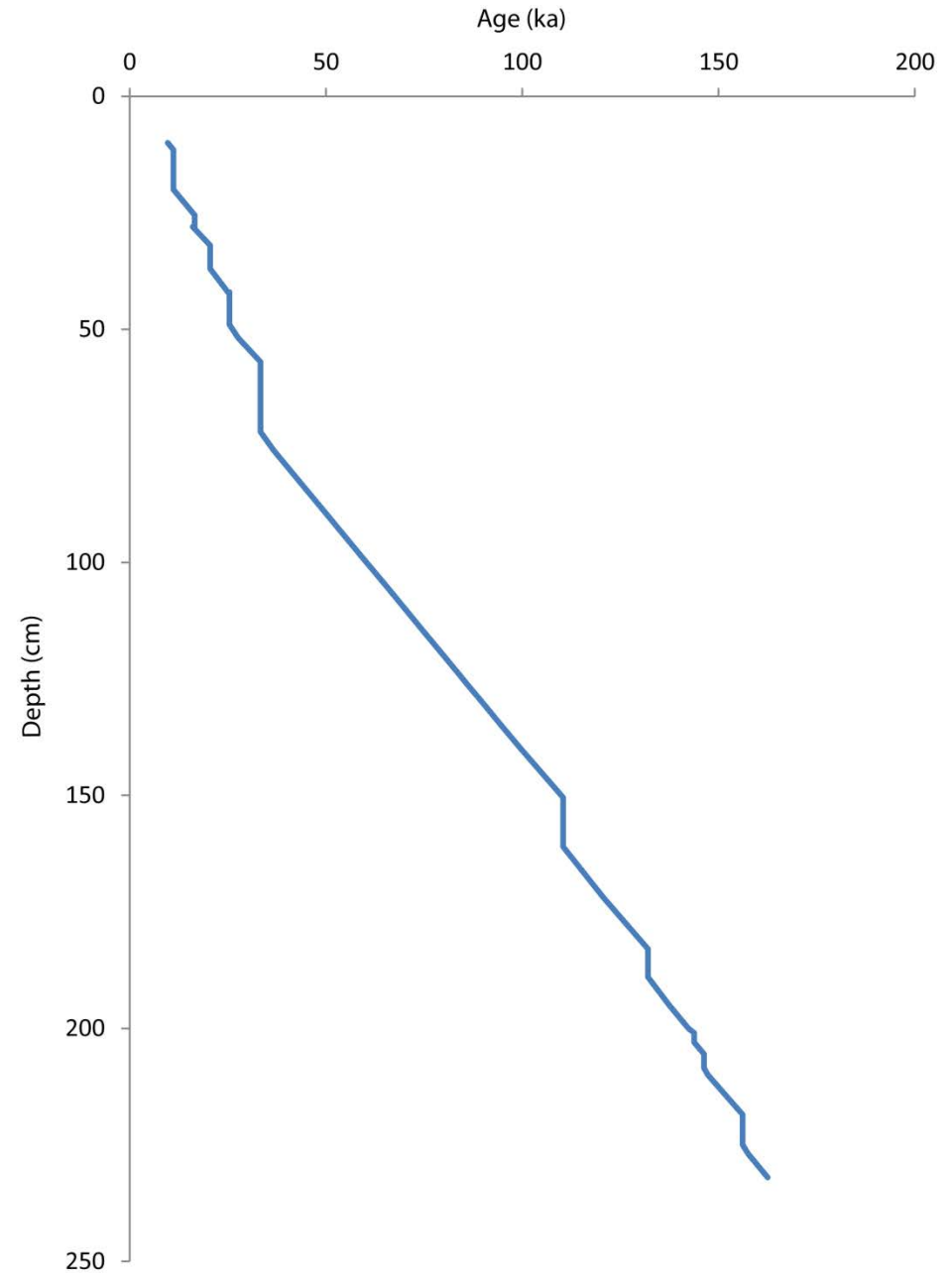


Figure 5.12 Age model for Core 16 presented as age downcore. Note that areas where the depth increases but the age does not include the presence of a tephra layer.

5.6.2 Sedimentation rates

Sedimentation rates for the cores were published by Shane and Wright (2011) using the carbon ages they obtained. They found that the sedimentation rate for Core 1 was 75-440 mm kyr⁻¹, and the rates for cores 4, 13 and 16 were in the range 1-35 mm kyr⁻¹. Here I recalculate these sedimentation rates based on my recognition of more tephra layers, re-estimation of their thicknesses and an improved age model. The age for each of the cores is presented in Table 5.7 below. The age for Core 1 is based on the radiocarbon age 10.5 ka at 235 cm depth published by Shane and Wright (2011) and also the identification of the SBT at 87 cm depth which is 6.3 ka. Both of these ages were taken into account when calculating the sedimentation rate. Here I use an age of 11.5 ka for the base of the core yielding a sedimentation rate of 210 mm kyr⁻¹. The sedimentation rate for Core 4 is based on the age model, and yields a rate of 26 mm kyr⁻¹. Cores 3 and 5 have a tephra layer at their base which Shane and Wright (2011) identified as the SBT, which date the base of the cores at 6.3 ka. However after reanalysis in this study, I have found that the tephra is Core 3 is not a correlative. Core 3 has a radiocarbon age of 2.5 ka collected from approximately half way down the core. Here I estimate that the age at the base of the core will be *ca.* 5 ka, and the sedimentation rate based upon this age is *ca.* 55 mm kyr⁻¹. Cores 8 and 10 have no correlative tephra layers and no radiocarbon ages with which to determine an approximate age of the core, and as such no sedimentation rate has been calculated for these cores. Tephra in Core 15, from 2 to 23 cm correlate to the SBT, indicating that the age at 23 cm depth is 6.3 ka. As the tephra above this was deposited in one event, no estimation can be made as to the age at the base of the core, here listed as >6.3 ka.

Table 5.7 Recalculated sedimentation rates for cores investigated in this study. Note that ages in bold are based upon ages determined in this study, whilst those in italics are based upon estimated ages following from the carbon ages published by Shane and Wright (2011).

	Core 1	Core 2	Core 3	Core 4	Core 5	Core 7 / 8	Core 10	Core 13	Core 15	Core 16
Length of core (cm)(sediment only)	242.2	30.0	27.3	147.0	43.0	10.8	12.5	35.5	6.5	208.0
Age at base of core (ka)	11.5	6.3	5.0	56.2	6.3			33.0	>6.3	170.4
Sedimentation rate (mm/ka)	210	48	54.6	26	70			11		12

5.6.3 Accuracy of age model

The age model for Core 13 begins at 10 ka. However the radiocarbon age from Shane and Wright (2011) date the sediment at 7 cm depth at 4.5 ka and the SBT which is 6.3 ka is present at 26 cm depth. This highlights some of the uncertainty with the age model for this core and indicates that the sediment has possibly been reworked, yielding an incorrect radiocarbon age.

Shane and Wright (2011) also correlated tephtras 16-71 and 13-51. If we rely on the age model, the two tephtras have an age difference of 15 ka, largely dependent on the accuracy of the Core 13 age model. This

would indicate that the correlation is dubious, but may possibly be within error of the Core 13 age model. Shane and Wright (2011) also correlated tephtras 4-161 and 16-187. In similar fashion, in the age models presented here, tephra 16-187 is *ca.* 83 ka older than 4-161, and the two, while having similar geochemistry, cannot be correlatives (see chapter 4).

In order to confirm the robustness of the age model developed from Core 16, the oxygen isotope curve was plotted alongside data collected from other stratigraphic analysis (Figure 5.13). As illustrated, changes in the oxygen isotope content are reflected in other proxies, and are especially distinguishable in the locations of the tie points for the age model. This again highlights the robustness of the age model for Core 16 and that the radiocarbon age of 43.5 ka published by Shane and Wright (2011) is unreliable.

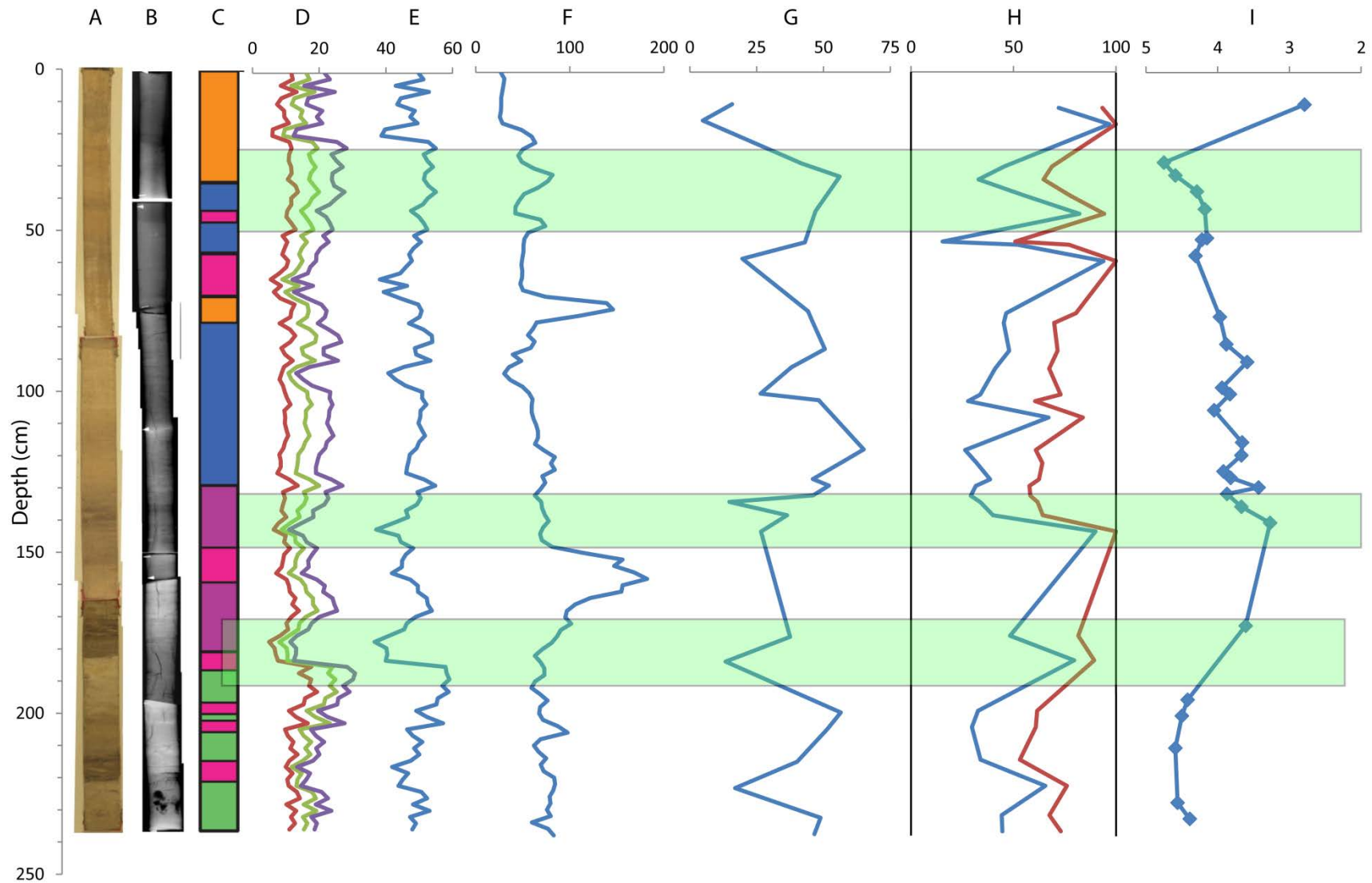


Figure 5.13 Graphical representation of data obtained from TAN0706-16 using non-invasive methods (A-F) and invasive methods (G-I). A) Photograph of core. B) X-ray image of core. C) Facies model for core. D) Spectral reflectance (nm). E) Colourmetric analysis (L^*). F) Magnetic susceptibility. G) CaCO_3 content (% of sample). H) Sieved cumulative grain size analysis (space between 0 and blue line represents $<60 \mu\text{m}$; space between blue and red lines represents $60\text{-}140 \mu\text{m}$; space between red line and 100 represents $>140 \mu\text{m}$). I) Oxygen isotope curve ($\delta^{18}\text{O}$). Green shaded boxes highlight areas where changes are evident in different proxies, and these correlate with the tie points used to construct the age model (as illustrated in Figure 5.9).

Chapter 6

Discussion

6.1 Source volcanoes of marine core tephras

Determining the source of tephras preserved in the core can tell us much about the frequency of eruptions from each volcanic centre, the temporal evolution of the magmatic system at each volcano, and also give indications as to the transport mechanisms for volcanic material in the Kermadec arc. Here I compare the geochemistry of tephras in this study to published data for a range of volcanic centres in the arc, and where possible determine the volcanic sources for the tephra layers.

6.1.1 Potential source volcanoes

Individual tephra layers can be assigned a volcanic source based on documented geochemical trends from each of the volcanic edifices in the area. The volcanic edifices along the arc show distinct trends in K content (Figure 6.1), and the K content is thus used here as a first order method to propose the volcanic source of tephras following Shane and Wright (2011). Published data show that Raoul volcano produces low-K material, whilst Macauley volcano produces predominantly medium-K material plus minor amounts of low-K material (Ewart *et al.*, 1977; Worthington *et al.*, 1999; Smith *et al.*, 2006; Barker *et al.*, 2012; 2013). Rather than just assigning the source of tephra to these two volcanoes, however, I also consider the possibility of inputs from more distant volcanoes. For example, the recent submarine eruption of Havre volcano produced a large pumice raft, which shows that volcanic material sourced from the arc can be transported hundreds of kilometres from source (Priestley, 2012).

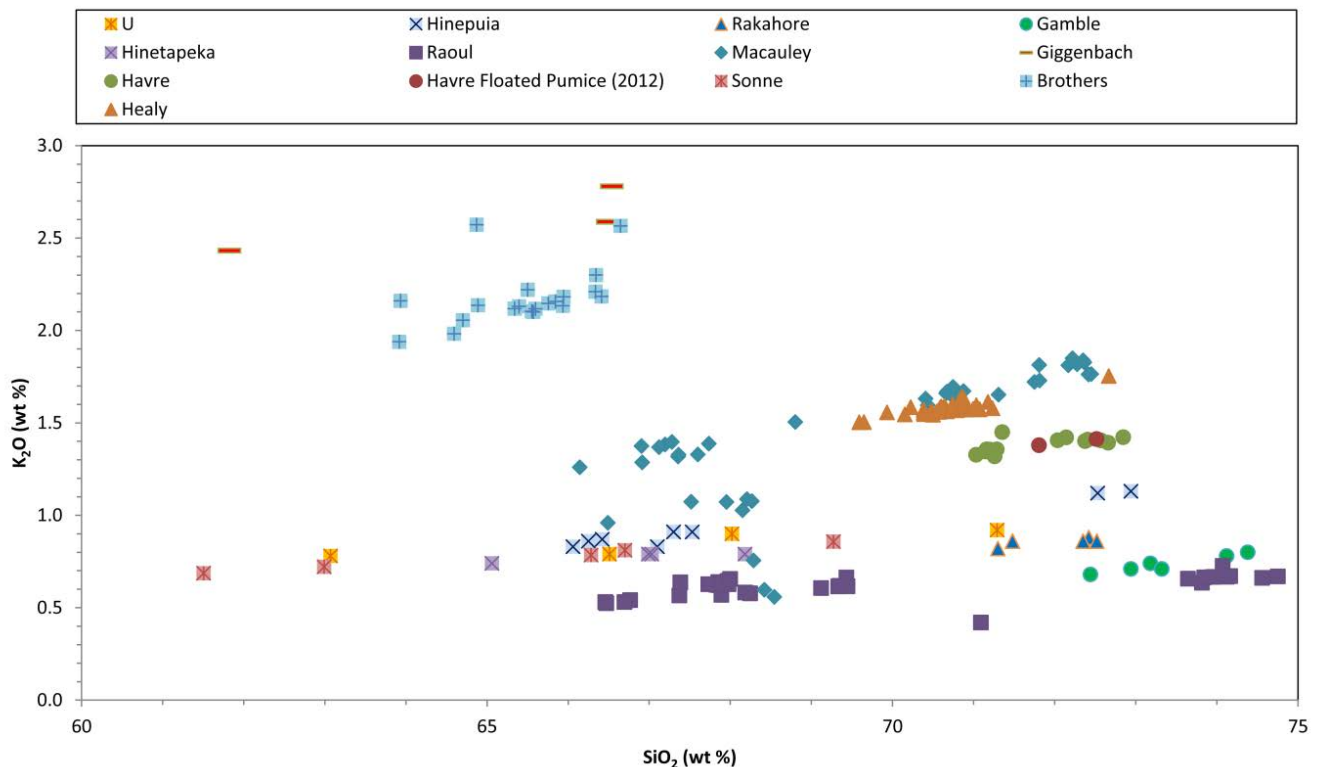


Figure 6.1 K_2O content vs. SiO_2 for volcanic products from volcanoes along the Kermadec arc. Data for volcano U, Hinepuia, Rakahore, Gamble and Hinetapeka from Graham *et al.* (2008), data for Raoul, Macauley and Healy from Barker *et al.* (2013) and data from Giggenbach, Sonne and Brothers from Haase *et al.* (2006). Unpublished data from Havre were provided by Richard Wysoczanski (NIWA).

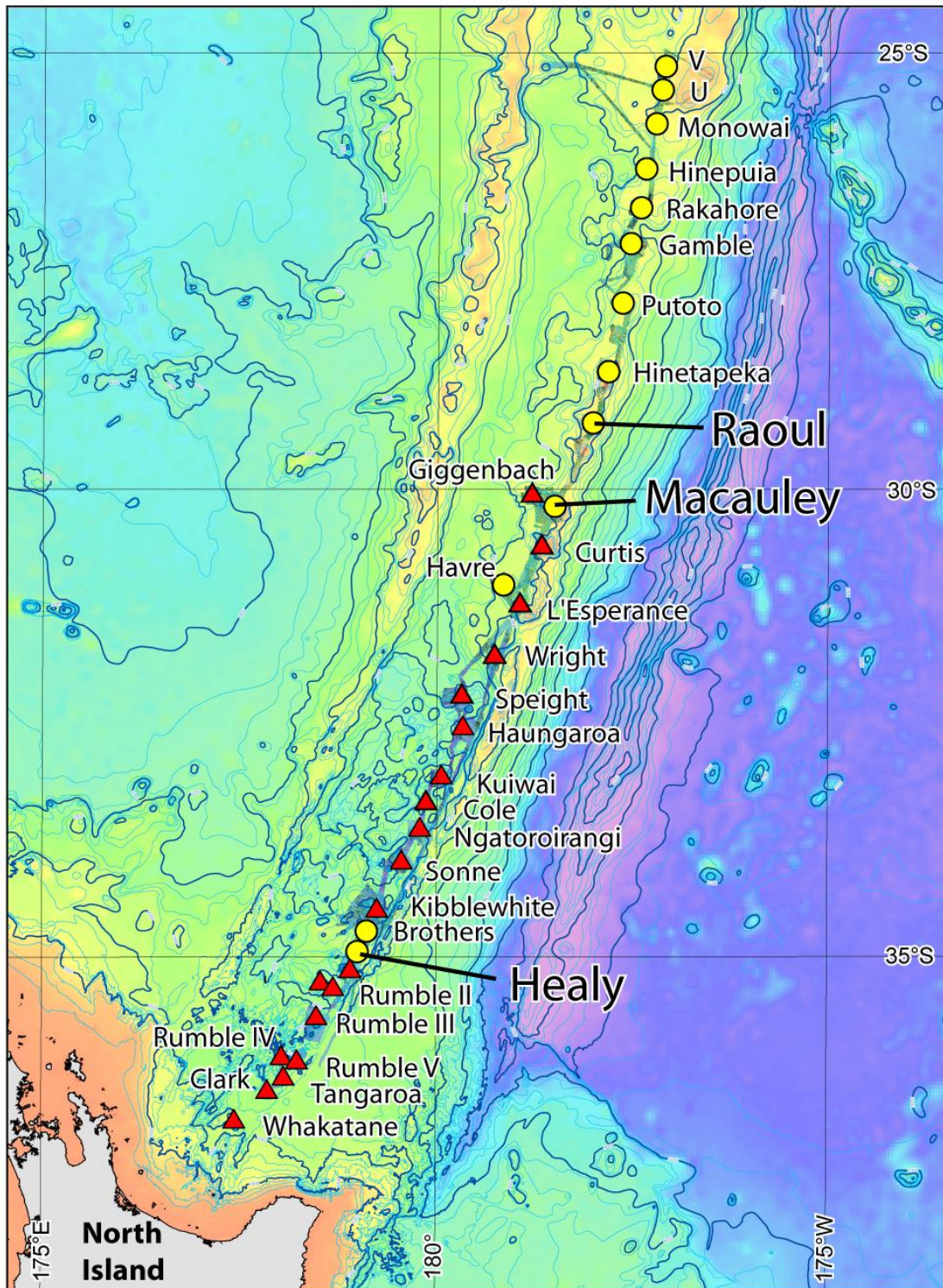


Figure 6.2 Location of submarine and subaerial volcanoes along the Kermadec arc (red triangles are basaltic – andesitic volcanoes, and yellow circles are silicic caldera volcanoes). Raoul, Macauley and Healy volcanoes were the main focus of the TAN0706 research voyage. Image courtesy of NIWA.

Correlation to published data from subaerial formations has also been attempted. As the tephra are more evolved, however, than most of the subaerial material this can only act as a second order method to confirm the source volcano.

Geochemical fields for selected volcanoes (locations shown in Figure 6.2) along the arc were generated, as follows.

1. Giggenbach and Brothers volcanoes are high-K.
2. Macauley and Healy volcanoes are medium-K.
3. Havre forms a distinct third field that has slightly lower-K than the Macauley and Healy field
4. The northern volcanoes, U, Hinepuia and Hinetapeka form a field (here referred to as the Northern field) with K contents between Macauley and Raoul.
5. Raoul and Gamble volcanoes are low-K.
6. Raoul SW is low-K and forms a distinct, slightly more evolved field relative to Raoul

When considering tephra compositions that plot broadly in the Macauley/Healy field, the tephra are assumed to be sourced from Macauley Volcano, due to its close proximity to the core sites and the distance to Healy Volcano. This is supported by the geochemistry which is more similar to Macauley than to Healy. In similar fashion, the Raoul/Gamble field tephra are assumed to be sourced from Raoul, either from Denham or Raoul calderas (unless specifically stated). No samples had compositions to suggest that they could have been sourced from any of Healy, Gamble, Giggenbach or Brothers volcanoes.

The geochemical compositional fields shown by the tephra samples allow for correlation to the volcanic source of the tephra layers (Figure 6.3). Tephra that were not easily distinguished into a geochemical field or crossed over multiple fields were examined in more detail and plotted against geochemical data from onshore deposits. The geochemical trend of these tephra was compared to the onshore deposits, and where possible a source volcano was assigned. Where a specific source was unable to be assigned the tephra the field name is undetermined. A complete list of all tephra examined in this study, along with the assigned volcanic source and age is presented in Table 6.1.

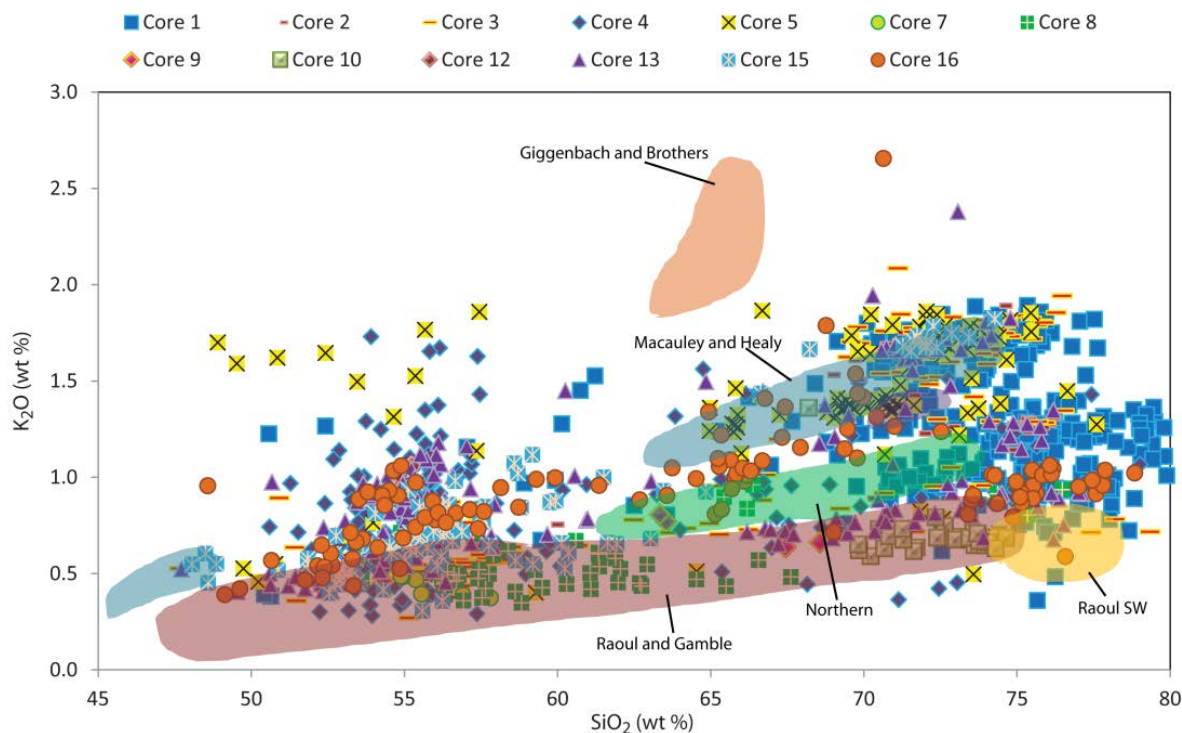


Figure 6.3 Compositions of tephra layers in this study compared to published data on volcanic materials from the region. The orange field represents the spread of data from Brothers and Giggenbach, blue represents Macauley and Healy, purple represents Havre, green represents volcano U, Hinepuia and Hinetapeka (referred to as the Northern field), red represents Raoul and Gamble and the yellow field represents the spread of data from Raoul SW. Data for volcano U, Hinepuia, Rakahore, Gamble and Hinetapeka from Graham *et al.* (2008), data for Raoul, Raoul SW, Macauley and Healy from Barker *et al.* (2013) and data from Giggenbach, Sonne and Brothers from Haase *et al.* (2002). Unpublished data from Havre were provided by Richard Wysoczanski (NIWA).

6.1.2 Volcanic source of tephra layers

The stratigraphically younger medium-K samples from Core 1 plot within the Macauley field with a few glass shards plotting in the Havre field (Figure 6.4). There are three exceptions to this. Tephra 1-87 and 1-97 show both medium-K and low-K compositions, with low-K shards having lower concentrations than stratigraphically older tephra in the core. Tephra C1 114-115 plots only in the low-K field. Tephra 1-87 is predominantly medium-K with only four shards of a low-K composition. This tephra is correlated with the Sandy Bay Tephra (SBT), with the four low-K shards most likely inherited. The SBT will be discussed in more detail later in the chapter. Tephra 1-97 and C1 114-115 lay within the Raoul field.

Tephra C1 158-159 and C1 163-164 plot in the Northern field with a slight overlap with the Raoul field. However the geochemical trend of the samples follows that of the Northern volcanoes, and these samples are interpreted to be sourced from this region. Tephra C1 177-178 has two shard populations. The lower silica shards plot in the Macauley field, whereas the more evolved shards form a near vertical trend between the Macauley and Raoul fields (Figure 6.4). The evolved shards are most likely inherited, although they could also reflect magma mixing in the source chamber. As such the sample is listed as being sourced from Macauley.

Table 6.1 Complete list of all tephras examined in this study, along with the assigned volcanic source and age. Ages calculated using sedimentation rates are in italics, the SBT is in bold, and ages determined from our age model are in regular font.

Tephra	Volcanic Source	Age (ka)	Tephra	Volcanic Source	Age (ka)
C1 39-40	Macauley	<i>2.6</i>	C4 24-25	Raoul	2.8
1-40	Macauley	<i>2.6</i>	C4 40-41	Macauley	5.9
C1 44-45	Macauley	<i>2.9</i>	C4 62-63	Raoul	15.7
C1 75-76	Macauley	<i>5.6</i>	4-.84	Raoul	22.6
C1 80-81	Macauley	<i>6</i>	4-120	Northern	35.4
1-.87	Macauley	6.3	C4 126-127	Macauley	38.0
1-.97	Raoul	<i>6.4</i>	4-129	Macauley	38.0
C1 114-115	Raoul	<i>7.4</i>	C4 144.5-145.5	Undetermined	44.0
C1 158-159	Northern	<i>8.9</i>	C4 151-152	Macauley	43.4
C1 163-164	Northern	<i>9</i>	4-153	Macauley	44.4
C1 177-178	Macauley	<i>9.4</i>	C4158-159	Macauley	46.9
C1 261.5-262.5	Undetermined	<i>10.9</i>	4-161	Macauley	48.8
C1 269-270	Undetermined	<i>10.9</i>	C4 174.5-175.5	Macauley	55.0
C1 287-288	Undetermined	<i>11.2</i>	5-.6	Havre	<i>0.8</i>
C1 288.5-289.5	Undetermined	<i>11.2</i>	C5 30.5-31	Macauley	<i>4.1</i>
C1 291.5-292.5	Undetermined	<i>11.2</i>	C5 41-42	Macauley	5.5
C1 296-297	Undetermined	<i>11.2</i>	5-.45	Macauley	<i>6.0</i>
C1 302-303	Undetermined	<i>11.5</i>	5-.47	Macauley	6.3
2-.33	Macauley	6.3	C7 loose top	Northern	
C3 loose	Raoul	<i><1</i>	C8 1-2	Raoul	
C3 8-9	Northern	<i>1.8</i>	7-.6	Raoul	
C3 10.5-11	Northern	<i>2.0</i>	C8 7-7.5	Raoul	
C3 12-12.5	Raoul	<i>2.4</i>	C8 9.5-10.5	Raoul	
3-.15	Raoul	<i>2.8</i>	C8 22 base	Raoul	
C3 24.5-25.5	Macauley	<i>4.3</i>	7 loose base	Raoul	
C3 27.5-28	Macauley	<i>4.5</i>	Core 9 loose	Raoul	
C3 29-29.5	Macauley	<i>4.8</i>	C10 6-7	Raoul	
3-.31	Macauley	<i>5.0</i>	C10 7-8	Raoul	
			C12 loose	Macauley	

Table 6.1 continued

Tephra	Volcanic Source	Age (ka)
13-.9	Raoul	<6.3
C13 11-12	Macauley	<6.3
13-13 top	Macauley	<6.3
C13 13.5-14	Macauley	<6.3
C13 15-16	Macauley	<6.3
C13 17-17.5	Macauley	<6.3
C13 18.5-19	Macauley	<6.3
C13 21-22	Macauley	<6.3
C13 23.5-24	Macauley	<6.3
13-26	Macauley	6.3
13-33	Raoul	14.3
13-51	Raoul	18.1
C15 0-1	Macauley	
C15 3-4	Macauley	
C15 6-7	Macauley	
C15 12-13	Undetermined	
C15 18-19	Macauley	
C15 22-23	Macauley	
15-32	Macauley	
C16 48.5-49	Raoul	25.4
C16 54-55	Raoul	32.8
C16 152-153	Macauley	110.4
C16 158-159	Macauley	110.4
16-187	Macauley	132.0
C16 206-207	Macauley	146.3
C16 214-215	Macauley	154.1
C16 238-239	Macauley	166.4

The older tephra samples (tephras C1 269-270 to C1 296-297) are interpreted to originate from the same event, due to the tephras having identical major and trace element concentrations. These tephras are low-K and plot in the Northern field (Figure 6.4). These volcanoes are capable of producing large, silicic caldera forming eruptions. The prevailing modern wind direction in the region above 2.1 km is W, however, so material was not likely to have been transported towards the core site from a subaerial plume. Material could possibly be transported to the core locations via a pumice raft, similar to the recent Havre pumice raft but with amounts of tephra entrained in the raft (Priestley, 2012). However current direction makes this unlikely and a large amount of pumice would need to be entrained in the raft in order for a tephra layer to be preserved. Another possibility is that these tephras were sourced from Raoul

Volcano and are more evolved, reflecting a magmatic system that is no longer represented in the subaerial deposits on the island. I list the source of these tephtras to be undetermined.

Tephtra 2-33 is medium-K and is sourced from Macauley Volcano. A few shards in the sample display lower-K contents, but these are most likely inherited grains. The two clasts found in the core will be discussed in detail later.

Samples from Core 3 are sourced from 3 different geochemical fields. Tephtras C3 loose top, C3 12-12.5 and 3-15 are all sourced from Raoul. Tephtras C3 8-9 and C3 10.5-11 correlate to the Northern geochemical field, whilst the older tephtras, C3 24.5 - 25.5 to 3-31 are all sourced from Macauley.

Two tephtras in Core 4 closely mirror the geochemical trends of subaerial deposits of Raoul Island; C4 62-63 and 4-84 (15.7 and 22.6 ka respectively) are very similar geochemically to the Hutchison and Moumoukai – Blue Lake formations. The Hutchison Formation is believed to have formed between 50 and 100 ka and the Moumoukai, between 4 and 10 ka (Lloyd and Nathan, 1981). However these ages are inferred from poor resolution K/Ar dating and the tephtras in this core may be more accurate markers of the true ages of these units. Tephtra C4 62-63 correlates well to the Hutchison Formation; the tephtra shows more evolved compositions than the Moumoukai Formation but it does follow the same geochemical trend.

All of the tephtra layers preserved in Core 5 are sourced from Macauley, with the exception of tephtra 5-6. This tephtra has slightly lower-K than the other samples, and plots in the Havre field.

Tephtras from Cores 7 & 8 are very similar to the subaerial deposits on Raoul Island, with the exception of tephtra C7 loose top, which correlates with the Northern field. While the tephtras are more evolved and show a wider range of K contents, they overlap many of the subaerial deposits. However when the trace elements were examined none of the tephtras could be correlated with specific subaerial examples.

Tephtras from Core 10 are only slightly more evolved than the subaerial deposits on Raoul Island, and follow the same geochemical trend. In this case they could correlate to the Fleetwood Formation, Green Lake Formation or Matatirohia Formation. Age data are lacking for core 10, however, so I cannot correlate the core tephtras with any of the subaerial formations with confidence, but that the data are consistent with these tephtras being sourced from Raoul volcano.

All of the tephtras from Core 13, with the three exceptions (13-9, 13-33, 13-51), are inferred to be sourced from Macauley (Figure 6.5). Tephtra 13-9 displays no clear trend, and glass shards from the tephtra plot in both the Raoul and Macauley fields. This is considered to most likely reflect a combination of eruptive events from different sources. Two tephtras are sourced from Raoul Volcano, 13-33 and 13-51. Tephtra 13-33 closely mirrors a few of the younger subaerial deposits on Raoul Island. Stratigraphically however they cannot be correlated, as 13-33 is beneath the SBT which dates it to >6.3 ka, and older than the subaerial silicic deposits on Raoul.

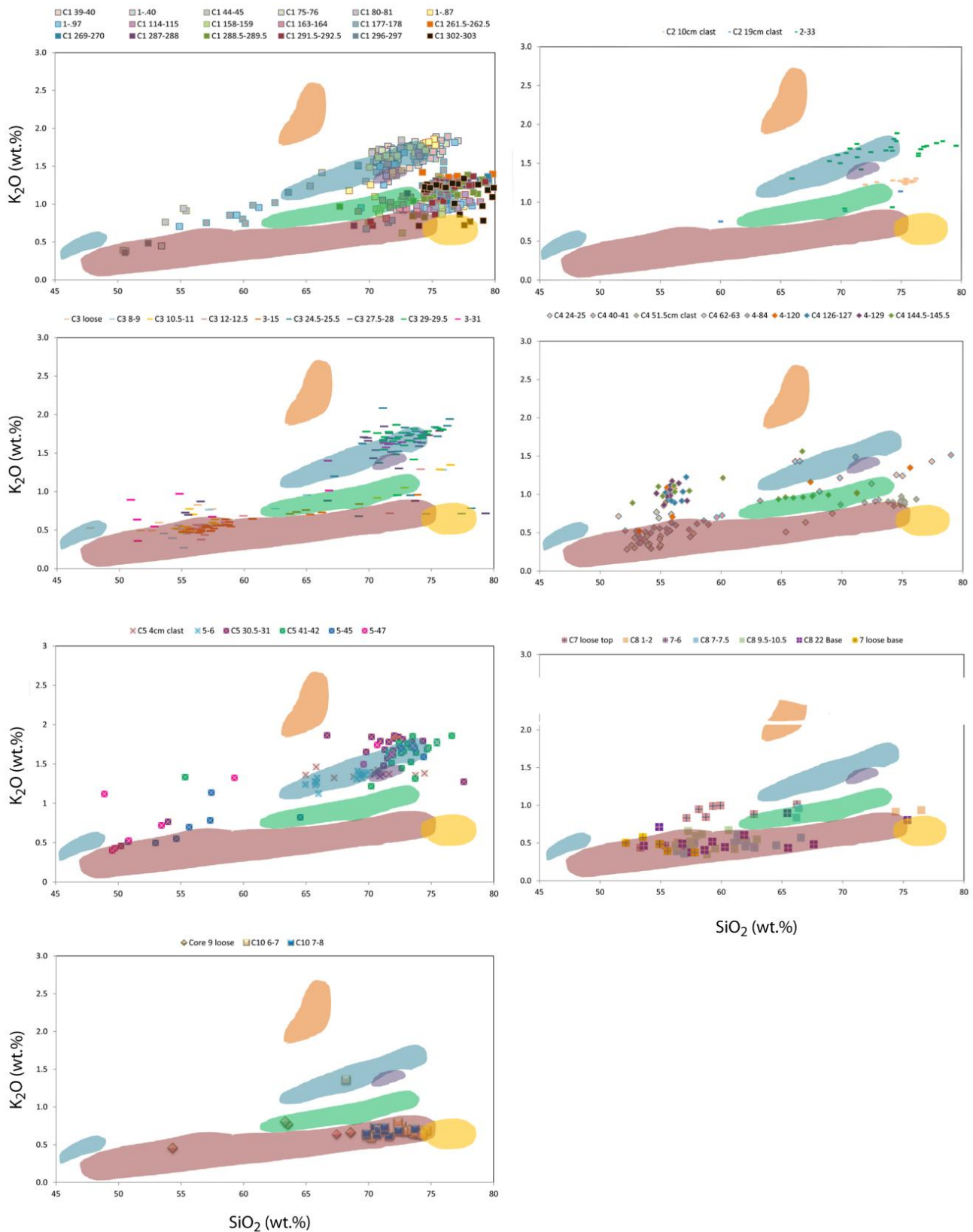


Figure 6.4 Variation diagrams for each core collected from offshore of Raoul Island and examined in the study, compared to published data on volcanic material from the region. The orange field represents data from Brothers and Giggenbach, blue represents Macauley and Healy, purple represents Havre, green represents volcano U, Hinepuia and Hinetapeka (referred to as the Northern field), red represents Raoul and Gamble and the yellow field represents the spread of data from Raoul SW. Data for volcano U, Hinepuia, Rakahore, Gamble and Hinetapeka from Graham *et al.* (2008), data for Raoul, Raoul SW, Macauley and Healy from Barker *et al.* (2013) and data from Giggenbach, Sonne and Brothers from Haase *et al.* (2002). Unpublished data from Havre were provided by Richard Wysoczanski (NIWA). Each symbol represents a single glass shard, and their depth is in cms.

Samples from the banded unit of Core 13 (tephras C13 15-18 to C13 23.5-24) are all heterogeneous and show a wide range of elemental concentrations. The SBT at the base of the unit displays very similar major element geochemical trends to the above banded material, however the trace element concentrations of the SBT are enriched relative to the banded tephtras. The banded tephtra layer will be discussed in section 6.1.4.

All of the tephtras in Core 15 are sourced from Macauley Volcano. Tephtra C15 12-13 is a low silica tephtra and plots across the boundary between the Macauley and Raoul fields. As shown in Figure 4.32, tephtras from 2 to 23 cm depth in Core 15 correlate to the banded tephtra layer, here interpreted to represent the latter eruption stages of the SBT from Macauley Volcano.

Tephtras from Core 16 are sourced from a range of volcanic centres. The youngest tephtras C16 48.5-49 and C16 54-55 are sourced from Raoul Volcano. Tephtra C16 206-207 plots between the Macauley and Northern fields, but fits best with the Northern field. This tephtra is distinct in that as a homogeneous tephtra it somewhat straddles the divide between the bimodal predominant basaltic-andesite and rhyolite compositions of other homogeneous tephtras. It mirrors the geochemical trends of both Hinenuia and Hinetapeka from the Northern field, fitting best with Hinetapeka. Another possible source for this tephtra

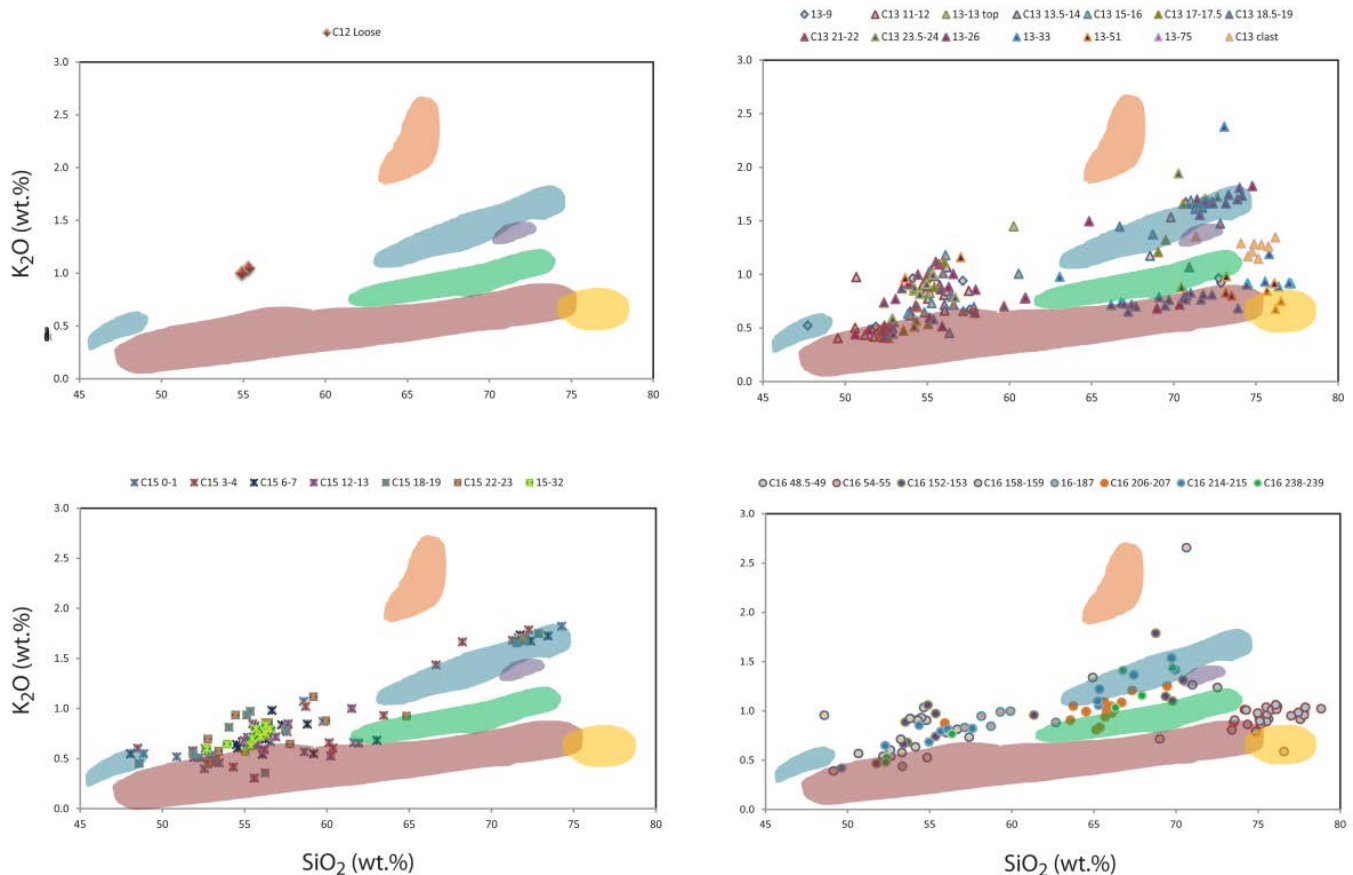


Figure 6.5 Variation diagrams for each core collected from offshore of Macauley Island and examined in the study, compared to published data on volcanic material from the region. The orange field represents spread of data from Brothers and Giggenbach, blue represents Macauley and Healy, purple represents Havre, green represents volcano U, Hinenuia and Hinetapeka (referred to as the Northern field), red represents Raoul and Gamble and the yellow field represents the spread of data from Raoul SW. Data for volcano U, Hinenuia, Rakahore, Gamble and Hinetapeka from Graham *et al.* (2008), data for Raoul, Raoul SW, Macauley and Healy from Barker *et al.* (2013) and data from Giggenbach, Sonne and Brothers from Haase *et al.* (2002). Unpublished data from Havre was provided by Richard Wysoczanski (NIWA). Each symbol represents a single glass shard.

is Havre. The data published for Havre has higher silica content; however the geochemical trend of C16 206-207 aligns perfectly with Havre Volcano. All other tephtras in the core are sourced from Macauley Volcano.

6.1.3 Volcanic source of clasts

Clasts in Core 2 fall within the Northern field, mirroring the trends of Hinetapeka and Hinepuia closely. The glass shards from the C2 10 cm clast are more evolved than the northern samples, whilst the glass shards from the C2 19 cm clast mirror the trend of Hinetapeka samples having slightly higher K contents. It is thus possible that Hinetapeka was the source of this clast.

The clast from Core 4 mirrors in composition the geochemical trend of pumice collected from Raoul SW. The C4 51.5 cm clast and the pumices from Raoul SW (Barker *et al.* 2013) correlate closely in terms of Ca, Al and Mg, but differ in terms of the Ti and total alkali contents (Figure 4.8). This suggests that there was pumice-forming activity at Raoul SW at *ca.* 7.2 ka.

Two samples from Core 5 display an interesting trend; C5 4 cm clast and 5-6 tephra layer are correlatives, and show no increase in K content with increasing Si content. This geochemical trend is identical to that shown by pumice collected from the recent eruption of Havre volcano which lies to the south of the core site (Figure 6.2). The recent pumice raft erupted from Havre has spread out over a large area and generally moved to the northwest, which would take it very near the core site for Core 5 (Richard Wycoczanski, pers. comm.). I propose that the clast in Core 5 was deposited via oceanic transport of a pumice raft; the clast is sub-rounded with slight weathering indicating that it was transported for a distance before deposition occurred. The clast can be correlated to an underlying tephra, 5-6, which possibly represents the fall deposit of a subaerial plume during eruption. The clast was deposited after the tephra layer was deposited, consistent with a pumice raft source. Both the travel time for the raft and the slow settling of the waterlogged pumice would have resulted in the clast being deposited after the main tephra layer. The interpretation is supported by the geochemical and stratigraphic evidence.

C13 clast correlated well with a pumice sample collected from Macauley caldera by Barker *et al.* (2012). C13 clast is slightly more evolved than D33_PC02, which was collected from the E flank of the Macauley edifice, but the two are near identical in elements K, Ti, Al and Ca. The clast in core 13 may represent a slightly more evolved composition from the same eruption as D33_PC02.

Clast	Volcanic Source	Age (ka)
C2 10 cm clast	Northern	<i>2.1</i>
C2 19 cm clast	Northern	<i>4</i>
C4 51.5 cm clast	Raoul SW	<i>7.5</i>
C5 4 cm clast	Havre	
C13 clast	Macauley	

Table 6.2 Complete list of all clasts examined in this study, along with the assigned volcanic source and age. Ages calculated using sedimentation rates are in italics.

6.1.4 Sandy Bay Tephra

The banded tephra unit in Core 13 warrants special mention, as it proves a unique feature within the cores studied. Multiple samples were collected from this unit, due in part to the unique banding as identified using X-ray imaging (Figure 6.6), to see whether the different bands of tephra had different compositions. As shown in Chapter 4, the tephtras from this banded unit are sourced from the same eruption, part of a 12.5 cm thick tephra deposit. They are all heterogeneous, but show the same range and geochemical trend. This indicates that they were erupted from the same magma chamber in a pulsating eruption style, allowing time for particles to settle out to the ocean floor (forming a distinct band) before the next layer was deposited. This is most likely related to the eruption of the SBT, as tephra 13-26 is at the base of the banded unit. .

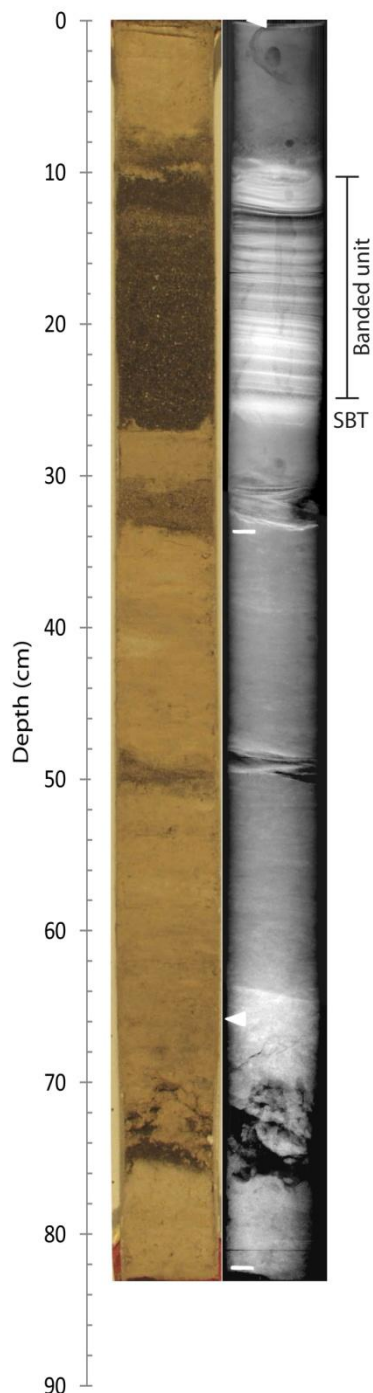


Figure 6.6 Images of the banded tephra unit in TAN0706-13. The X-ray image on the right highlights the banded nature of the deposit, while we can see from the photograph on the left that the unit is continuous and unbioturbated.

Tephra from the banded unit have different trace element compositions to 13-26 when examined, and all have lower silica contents. I propose here that during the initial stages of the SBT more evolved material from near the top of the magma chamber was erupted, producing the pyroclastic deposits recorded in the subaerial units (Smith *et al.*, 2003b). As the eruption continued it progressively tapped down to less evolved magma in the chamber which was entrained into the eruption column, and deposited as the material represented in the banded tephra unit. The lack of bioturbation in the banded unit supports the formation of the tephra within a short amount of time. The thick tephra unit in Core 15, from 2 to 23 cm depth correlates to the banded tephra unit in Core 13 and is therefore also a record of the latter stage of the SBT eruption.

Silicic lithic blocks are also recorded in the pyroclastic onshore deposits (Smith *et al.*, 2003b). Tephra C16 206-207 is a homogeneous tephra which is distinctive (Figure 4.26) in that it is a dacite and does not plot well within any of the defined geochemical fields (Figure 6.5). However, it does plot very well with the existing published data from the silicic lithic clast from the SBT (Figure 6.7). Here I interpret the silicic lithic clasts and tephra C16 206-207 to be correlatives, indicating that the silicic lithic clasts were erupted at *ca.* 146 ka.

Data published on pumice clasts collected from Macauley caldera show three geochemical trends, one medium-K, one low-K, and the other intermediate-K (Barker *et al.*, 2013). The medium-K pumice clast (Macauley D25) is sourced from Macauley, and the low-K clast (Macauley D33_04) is interpreted in this study to be sourced from Raoul, as it falls within the Raoul geochemical field. The source of the intermediate-K pumice (Macauley D33_02) was unclear, as it did not plot in any of the geochemical fields. In light of the identification of silicic volcanism at Macauley as far back as *ca.* 146 ka as discussed above, C13 clast and pumice Macauley D33_02 were plotted against known values of the silicic lithic clasts (Figure 6.8). We can see that they are all geochemically related, as they form a distinct trend, so the pumice clast was likely formed in one of these eruptions. These findings support the conclusions of Barker *et al.* (2012) who stated that the eruptive history of Macauley is much more complex than initially thought and that material preserved onshore records only a part of the eruptive history of the volcanic centre.

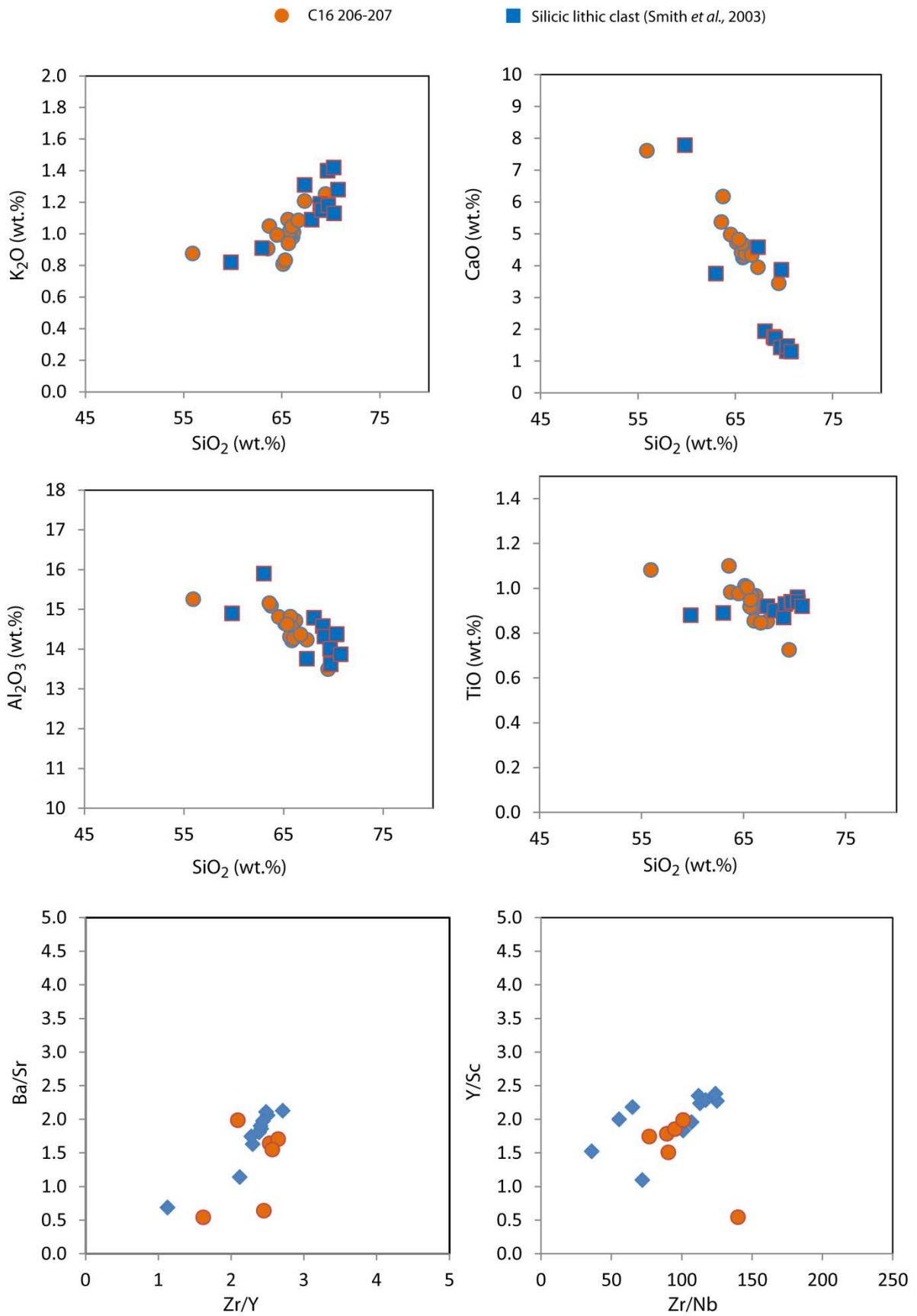


Figure 6.7 Variation diagrams of major oxides and trace elements showing comparisons between tephra layers and silicic lithic blocks erupted as part of the SBT (Smith *et al.*, 2003b). Each point represents a single glass shard, and their depth is in cms.

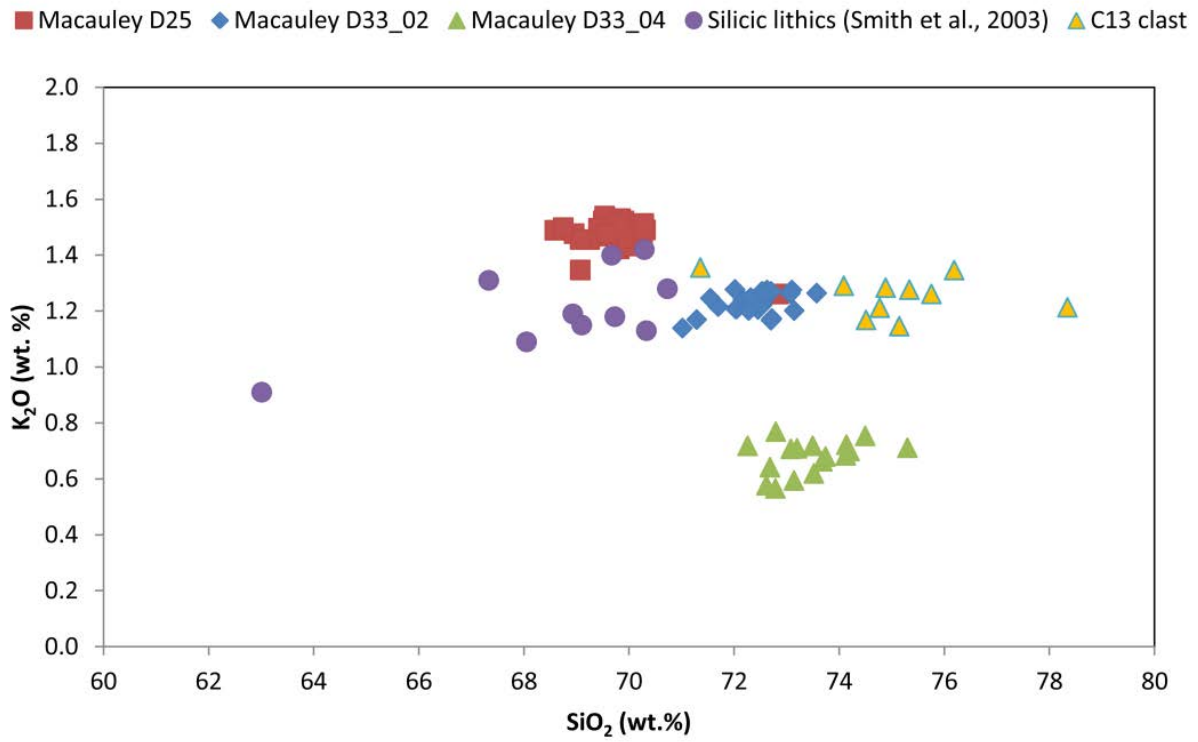


Figure 6.8 Compositions of submarine pumice clasts collected around Macauley (Barker *et al.*, 2013) compared to the silicic lithic clasts found in the Sandy Bay Tephra (Smith *et al.*, 2003b), along with the C13 clast.

6.2 Modes of emplacement and preservation of the tephra layers

Subduction zone volcanoes generate large amounts of volcanoclastic materials due to the explosive nature of the volatile rich silicic magmas, especially those associated with caldera formation. Here I briefly discuss the various possible methods of emplacement that are relevant to the cores described in this thesis.

6.2.1 Primary emplacement processes

6.2.1.1 Subaqueous eruptions

Submarine plumes may be produced by deep to shallow submarine volcanoes. There are three main types of submarine eruption (Kano, 2003; Rotella *et al.*, 2013) that could contribute material to the samples:

1. Explosive magmatic eruption – driven by magma vesiculation, forms an eruption column composed of pumice and volcanic gas which has a similar structure to a subaerial plinian eruption (Cashman and Fiske, 1991). Materials are deposited to the seafloor in turbulent density currents, forming normally graded deposits.
2. Phreatomagmatic eruption – relatively small scale eruption resulting from water interacting directly with magma. Materials are deposited mostly via dilute volcanoclastic flows
3. Tangaroan eruption (Rotella *et al.*, 2013) – effusive eruptive style based upon pumice recovered from the seafloor around Macauley Island. Foamy magma erupts without fragmenting, and rises towards the surface as blebs while still internally vesiculating. The blebs can be transported by currents before becoming waterlogged and/or fragmenting to form clasts.

The most likely eruptive type to provide material present in the sediment cores is a magmatic eruption. This produces larger amount of material which may be transported greater distances. An explosive submarine eruption of silicic composition forms a submarine eruption column, ejecting gas and hot pumice into the water column (Allen and Stewart, 2003; Kano, 2003; Carey and Schneider, 2011). Where eruptions have a high magma flux, buoyant mixtures of pumice, ash and hot water rise to the surface, spreading out to form a mushroom-shaped mixture of water and particles and small subaerial plumes may be produced (Stix, 1991; Carey and Schneider, 2011). A pumice raft is often produced which may float vast distances and for a year or more (Bryan *et al.*, 2004). Material is often entrained in the raft and is transported great distances before falling out and settling to the sea-floor. Deposition of the entrained material is dependent upon local conditions, as wave action and storm condition would disperse the raft and enhance the loss of entrained detritus. This would make the deposition of a discrete tephra layer unlikely. Deposition from a pumice raft is, therefore, dependent upon weather conditions as well as the volume of material initially erupted and entrained in the raft.

As mentioned in the above section, Havre has produced a similar eruption in the recent past (Figure 6.9), with deposits in Core 5 inferred to record both the settling of the ash-laden plume (tephra 5-6) and pumice clasts (C5 4 cm clast) to the seafloor.

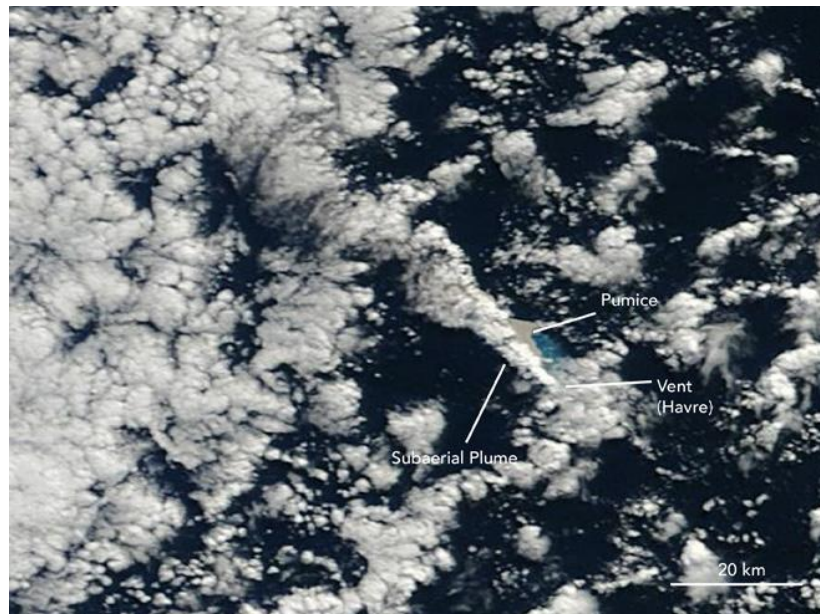


Figure 6.9 Satellite image showing products of the July 2012 eruption of Havre Volcano (image collected July 18, 2012). Note the subaerial plume and pumice raft. The discoloured water near the pumice raft indicates the presence of a plume rich in gas and ash (as discussed in the text). Image from NASA Earth Observatory

6.2.1.2 Subaerial eruptions

Large subaerial explosive eruptions generate buoyant eruption plumes that inject large amounts of tephra into the atmosphere. Winds then distribute the material over large areas. If distributed over water, the tephra eventually falls and settles out through the ocean to produce a distinct isochronous fine-grained deposit that can be correlated over large areas (Carey and Schneider, 2011). The dispersal of tephra erupted in subaerial plumes is controlled by the eruption column height, the wind speed and direction and the volume of material erupted (Sparks *et al.* 1992). Material delivered to the water column from above can either settle via passive fallout (following Stoke's Law, as outlined in Chapter 1) or it can form vertical gravity currents which rapidly transport material to the sea floor (Carey, 1997). Depending on the distance from source, these deposits can be several to tens of centimetres thick and display a sharp base with a bioturbated top. They are also typically normally graded, with crystals and coarser material concentrating at the base of the unit (Sparks and Ledbetter, 1979). The thickness of the tephra layers is a function of the volume of erupted material, height of the eruptive column and the prevailing wind strength and direction (Fisher and Schmincke, 1984).

Pyroclastic flows are also a feature of subaerial eruptions, where partial collapse of a subaerial plume occurs and the pyroclastic flow decouples from the plume and continues to spread laterally along the sea floor. Pyroclastic flows can also be generated directly from submarine eruption plumes. The resulting

deposits contain volcanic material such as crystals, tephra and pumice as well as entrained marine materials such as sediments and foraminifera (Carey and Sigurdsson, 1980; Fisher and Schmincke, 1984). Subaerially generated pyroclastic flows that enter water often generate turbidity currents.

Material in Core 10 provides evidence of submarine pyroclastic flows. A 10 cm section of the core is normally graded, with medium lapilli at the base, grading upwards to fine sand. This differs from the lapilli unit below, as much of the material is covered in olive, muddy sand which is here interpreted to have been entrained into a density current, coating the lapilli in marine sediment before deposition occurred.

6.2.2 Secondary emplacement processes

6.2.2.1 Volcaniclastic turbidites

Sediment gravity flows are the main mechanism for the transport of volcaniclastic material of the ocean floor (Carey and Schneider, 2011). There are many possible causes for volcaniclastic turbidity currents, and all of the primary volcanic processes outlined above can provide material for turbidity currents during or after eruptions. In order to form turbidity currents, rapid accumulation of volcaniclastic debris, a sloping surface, mixing between the sediment and water, and a trigger mechanism is needed to generate initial movement (Carey and Schneider, 2011).

The 28 cm thick, tephra-rich unit in Core 1 (from 269 to 297 cm depth) is interpreted to have formed by a turbidity current, which transported volcaniclastic material to the core site. This would explain the thickness and sediment-rich nature of the unit.

Core 10 shows evidence of having been deposited by a submarine pyroclastic flow as it has normal grading from medium lapilli at the base of the unit to medium ash at the top of the unit (from 11.5-20.5 cm depth). Material near the base of the unit contains distinguishable minerals (quartz and mafic crystals), and blebs of scoria and dacitic material.

6.2.2.2 Settling and winnowing of tephra

Glass shards and other material in the tephra may be sorted during settling in the water column. Larger shards and denser (more mafic) material may settle more quickly than smaller and lighter (silicic) material resulting in grading of the shards. If there is compositional difference between large and small shards this will result in compositional grading of the tephra unit. Another process that can affect tephra composition is winnowing during transport in a turbulent flow. While these processes may affect the composition of tephra samples it is difficult, to identify samples that have been affected. In any case it would not affect any interpretation of a tephra layer representing a single event.

6.2.3 Preservation of tephra layers in the marine environment

Bioturbation has long been recognised as a process effecting the preservation of tephra layers. Marine organisms are capable of dissipating tephra layers with initial thicknesses <1 cm with their ability to mix ash through sediment tens of centimetres thick (Sigurdsson and Carey, 1981; Fisher and Schmincke, 1984; Pillans and Wright, 1992). Bioturbation is present throughout the cores examined in this thesis, mainly associated with sedimentary facies A, C, G and H (see descriptions in Chapter 5). Many of the bioturbated sections contain visible sand size grains that appear to be volcanic ash, potentially thin deposits from eruptions that have been completely obscured and mixed into the surrounding sediment. The top contacts of some of the tephra units show evidence of bioturbation where, after cessation of deposition, marine organisms have disturbed the upper limits of the units. Without bioturbation it is likely that more, thin tephra layers would be preserved.

Another process affecting the preservation of tephra layers is the sedimentation rate. As outlined in Chapter 5, many of the cores have slow sedimentation rates, especially cores 13 and 16 which have sedimentation rates of 11 and 12 mm/kyr respectively. This will result in bioturbation of many of the tephra layers and may also result in tephra layers from multiple eruptions forming what appears to be one unit but which may have contrasting geochemical trends. A few tephra layers in the cores possibly display this feature, particularly tephra C4 144.5-145.5 (Figure 4.27). Tephra samples which do have two distinct geochemical trends within one sample are interpreted to represent multiple eruptive events the deposits of which have subsequently been mixed due to insufficient sediment to separate the individual eruptive deposits.

Sediment reworking can also occur as a result of bottom currents in the area, which are locally intensified around bathymetry (Wright *et al.*, 2001). The cores were collected from >2200 m water depth, so the effects of sediment reworking as a result of currents will be minimal as outlined in Chapter 2.

Secondary remobilisation of volcanoclastic material can also cause mixing of tephra layers, yielding a heterogeneous signature. In some cases slumping can result in repeated sections in marine cores, as reported in the ODP Site 1123 core (Allan *et al.*, 2008). The only evidence of this process recorded in the cores is near the base of Core 13, where it appears either slumping or a turbidity current has emplaced material. The tephra sampled from this unit, 13-75, was difficult to analyse, as much of the deposit was crystal rich, with small amounts of fragmented tephra present, along with foraminifera entrained in the sample (Figure 6.10).

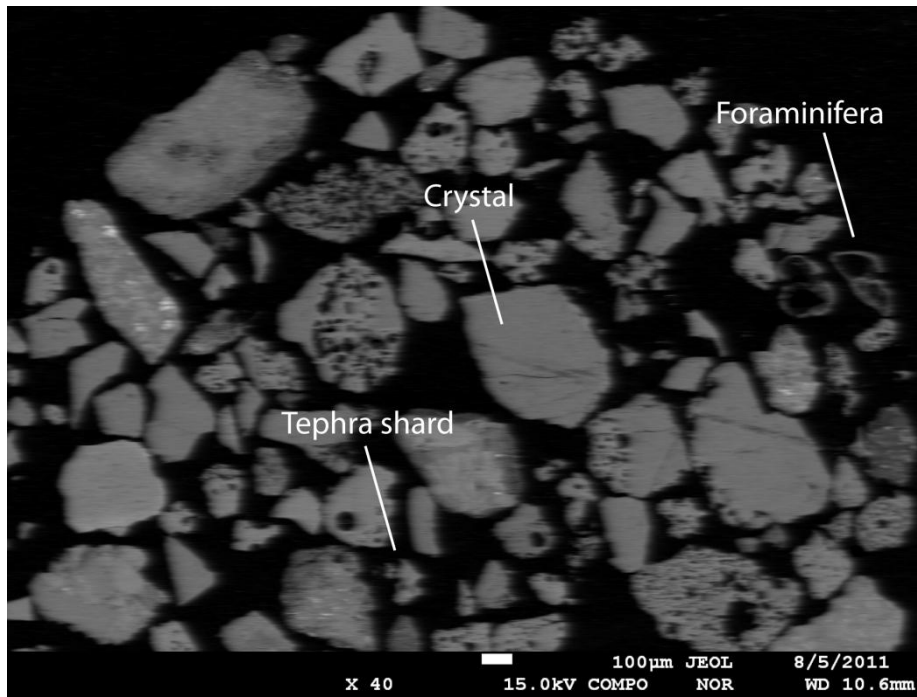


Figure 6.10 SEM Image of sample 13-75 showing the mixed nature of the deposit.

6.3 Homogeneous vs. heterogeneous tephras and implications for magma genesis

6.3.1 Homogeneous tephras

A total of 40 homogeneous samples were analysed in this study. Unless otherwise stated, each of these is interpreted to represent a single eruptive event. Samples may display homogeneity due to either geochemical or depositional processes. As shown in Figure 4.26, the homogeneous tephras range in composition from basaltic-andesitic to rhyolitic, with the majority being of rhyolitic, representing the evolved components of magma chambers.

Geochemically similar magma chambers may deposit tephras that are thought to be from the same event. One of the benefits of trace elements data is that we can see geochemical changes at finer scales than with major elements. These small scale changes can help separate geochemically similar tephras, allowing precise identification of single eruptive events.

6.3.2 Heterogeneous tephras

Out of a total of 89 tephra samples analysed, a total of 32 were heterogeneous in compositional range ($>8\%$ SiO_2 2σ variation). In some samples one or two shards differed from the composition of the rest of the sample, in others there was a broad range of compositional values (see Figures 4.5-4.15).

Heterogeneous tephras include samples with shards of highly variable composition that appear to be genetically unrelated. These samples were likely subjected to secondary processes, such as those outlined

in section 6.2.2 above. Other samples show shards with a wide range in composition but that appear to be related by fractionation and/or mixing processes.

6.3.3 Bimodal tephtras

There are a total of 11 bimodal tephtras preserved in the cores, defined as having two distinct populations within the same sample. The majority of these show basaltic-andesitic and rhyolitic compositions (Figure 4.28). This bimodality could be caused by the sample containing glass shards from two events, as mentioned above, or from magmatic processes. It is most likely that these bimodal samples represent either incomplete magma mingling or magma mixing between a fractionated evolved magma and a basaltic intrusion (as documented for Raoul by Barker *et al.*, 2013). The majority of the bimodal samples show some evidence of geochemical relation between the two populations, indicating that the mafic and silicic members are genetically related.

6.3.4 Kermadec arc magmatic processes and the generation of silicic magmas

Fractional crystallisation is one method proposed to generate silicic magmas in arc settings (Leat *et al.*, 2003; Saunders *et al.*, 2010; Barker *et al.*, 2013). Smith *et al.* (2003a) propose that crustal anatexis is the process whereby much of the magmas in the Kermadec arc were generated. This is contradicted by recent work of Saunders *et al.* (2010) and Barker *et al.* (2013) which argues that fractional crystallisation is the dominant process in the generation of silicic magmas in the Kermadec arc (for a full discussion see Barker *et al.* (2013)). As shown in Figures 4.5-4.15 fractionation trends are evident in many of the tephtra layers, and these indicate that fractional crystallisation is indeed the dominant process in the generation of silicic magmas in the region. This is supported by preliminary interpretation of plots with reference to the model of Brophy (2008), which suggests that as silica increases, La should also increase (Figure 6.11). However, this will not be expanded on here as it is beyond the scope of this study.

Fractionation of magmas may result in eruption of geochemically diverse and related tephtras in the same eruptive event. Many tephtras in this study show a range in silica content, including curvilinear trends rather than linear trends expected for magma mixing. Heterogeneous tephtras that are clearly geochemically related and interpreted to be sourced from a fractionated magma source are considered to represent a single discrete event, and have been added to the final number of distinct eruptions recorded in the sediment cores. Much of the basaltic, basaltic-andesitic material erupted shows wide compositional ranges, and provides evidence for compositionally heterogeneous evolved melts. These melts could be formed by a number of processes, the most likely of which is either magma injection into a partially evolved magma chamber or magma injection into an evolved chamber resulting in magma mixing triggering an eruption which preferentially erupts the more buoyant basaltic material.

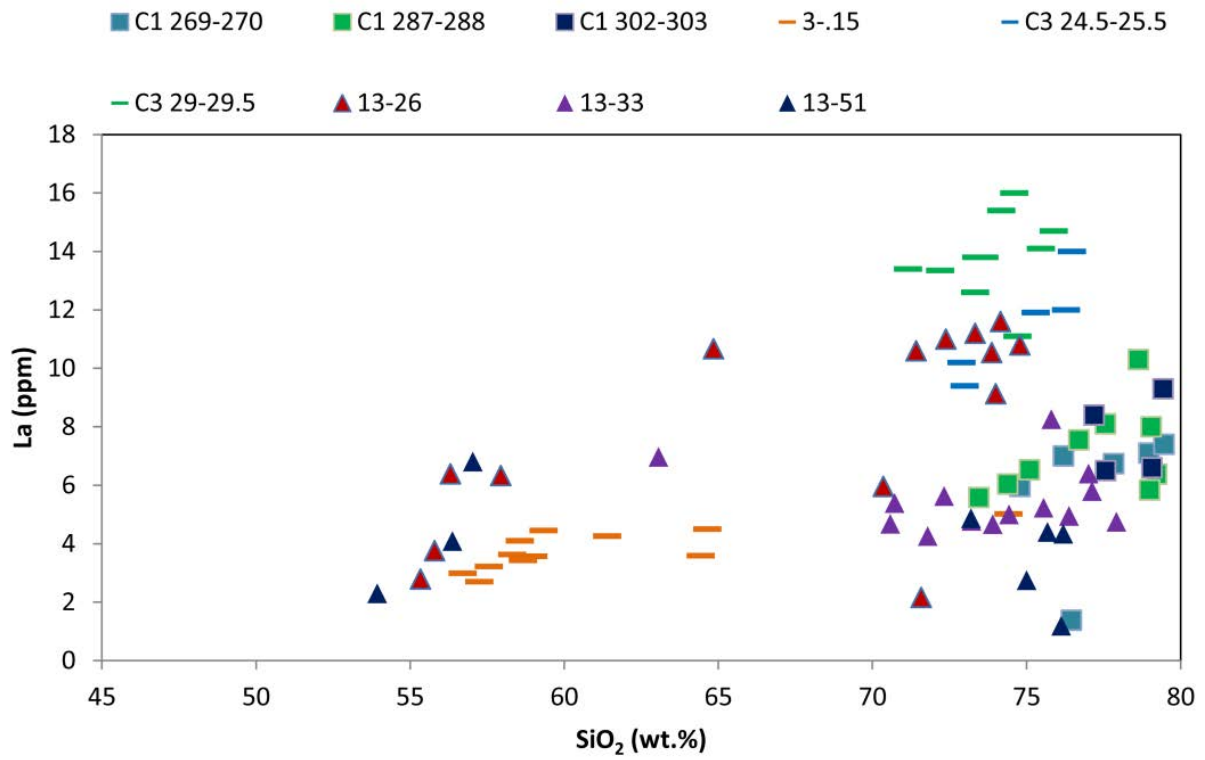


Figure 6.11 Preliminary plots of SiO₂ (wt.%) vs La (ppm) for representative samples, showing clear fractionation trends (following from Brophy, 2008)

6.4 A tephrochronological model for Raoul and Macauley marine cores

An integrated model for the tephrochronology of the Raoul and Macauley cores analysed here is presented as Figure 6.12. Development of a tephrochronology depends upon age dating of the cores so that we are able to date the tephra layers present. It is important to note that once we extend past 50 ka, ^{14}C dating cannot be relied upon and the ages are based on the oxygen isotope model. As shown in Figure 6.12, the carbon ages published by Shane and Wright (2011) do not correlate with our model ages. Whilst the younger ages in Cores 3, 13 and 16 and the two older carbon ages in Core 1 are most likely accurate, we propose here that their carbon dates >13 ka have been affected by sedimentary processes (such as biological reworking of older material or redistribution), as they do not correlate with our age models and yield distinctly older ages than indicated by oxygen isotope analysis, especially evidenced by the reasonable isotope chronology of Core 16.

The 6.0 ka date obtained for Core 1 is here interpreted to be affected by sedimentary processes, as the SBT is present directly above this layer, and from reliable ^{14}C dates from onshore material we know this to be 6.3 ka. In light of discrepancies between our age model and the other carbon ages published by Shane and Wright (2011) we favour the 6.3 ka age for the eruption, rather than the revised age of *ca.* 5.7 ka (Shane and Wright, 2011).

The sedimentation rate ages for Core 1 were calculated in three sections, using the known age of the SBT, as well as the two older carbon dates published to calculate the ages of tephras in Core 1. Ages in Core 2 were calculated using the known age of the SBT at the base of the core. Ages for Core 3 were determined using the ^{14}C age of Shane and Wright (2011) to calculate the sedimentation rate. Ages presented in Figure 6.12 for cores 4, 13 and 16 are calculated using the age model developed in this study. The younger carbon ages from these cores were not used in the development of the age models, but do correlate well with our age model dates.

The final tephrochronology for the marine cores examined in this study indicates that the oldest tephra preserved is *ca.* 166 ka (Figure 6.13). This tephra is also the oldest record of silicic volcanism in the Kermadec arc. The tephra records preserve evidence of fluctuations in magma generation, with periods of quiescence in the generation of both mafic and silicic materials. The cores show that until *ca.* 18 ka basaltic-andesitic materials were abundant, as is recorded in the sediment cores and also onshore Raoul and Macauley Islands. Since that time silicic volcanism has become more prevalent (Figure 6.12).

Other correlations proposed by Shane and Wright (2011) have in this study been discounted. The correlation between 16-71 and 13-51 is dubious, as the age difference between the two based upon the age models is *ca.* 15 ka, however, as mentioned in Chapter 5, this may be within the error of the Core 13 age model. The correlation between 4-161 and 16-187 is in this study discounted, due to the stratigraphic

age difference between the two of *ca.* 83 ka. While they may be similar geochemically, they are not correlatives.

This leaves the only correlative in the cores as the SBT, which is found across five different cores from offshore of Raoul and Macauley islands.

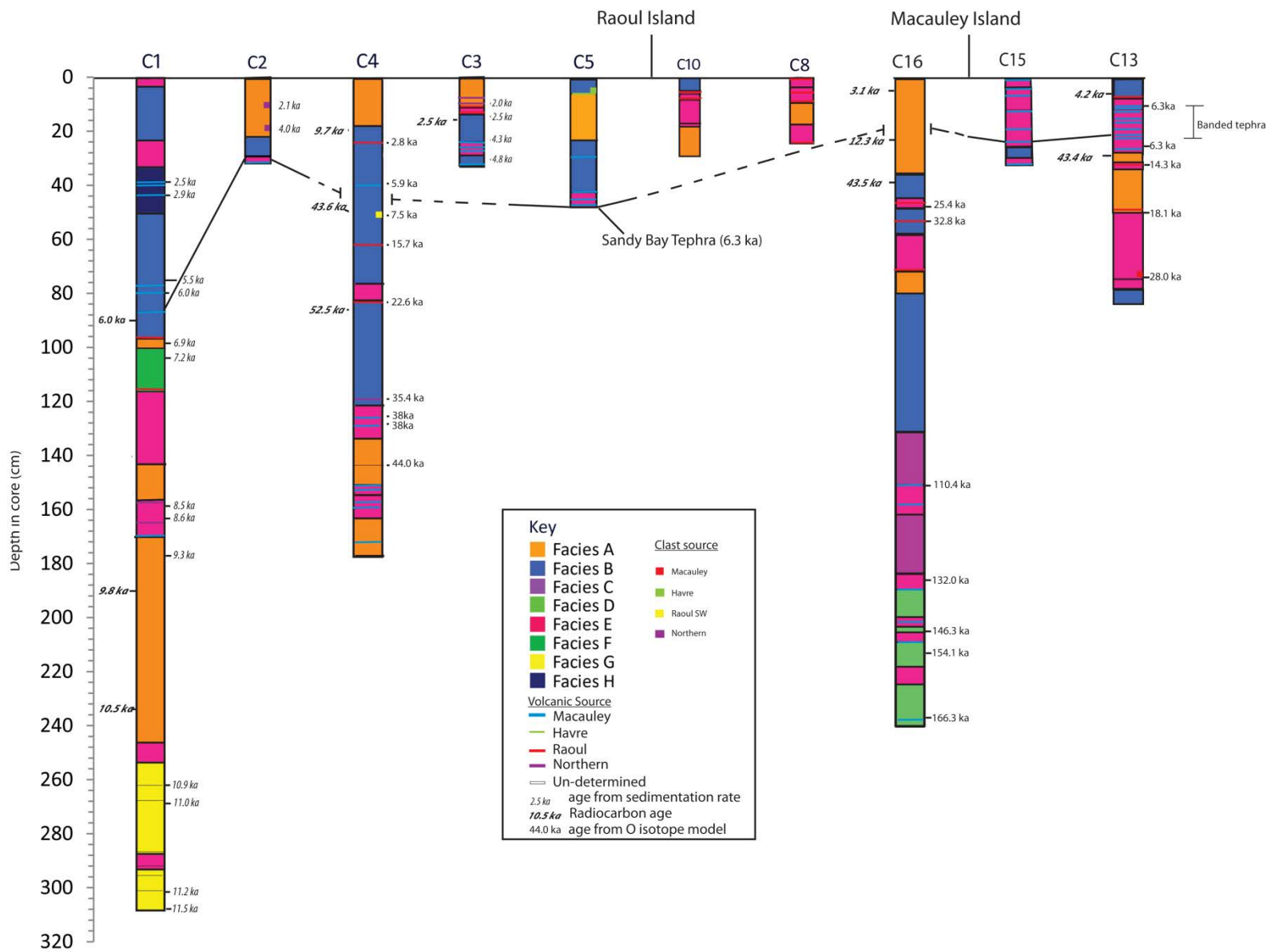


Figure 6.12 Tephrochronology for the cores analysed in this study. Where possible the volcanic source of tephra layers has been assigned, presented as a coloured line. For tephra which were part of a generalised field but a specific source was unable to be identified the tephra has been presented as a white line. A solid line between cores indicates a correlation, and a dashed line infers the relative position of the correlative if it was present. Radiocarbon ages published by Shane and Wright (2011) are to the left of the cores; while ages calculated in this study (either by oxygen isotope analysis or sedimentation rate calculations) are presented on the right. Note that the age calculation for core 3 is based upon radiocarbon ages.

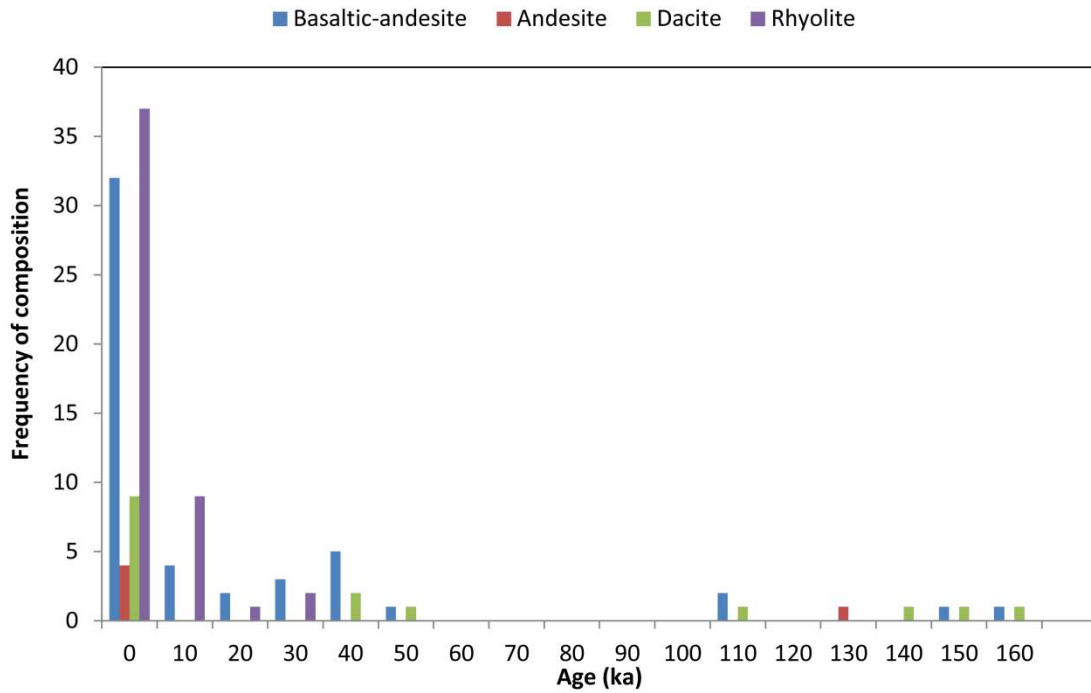


Figure 6.13 Erupted compositions of materials preserved in the cores over the past *ca.* 170 ka. Periods of quiescence are evident as is the increase in silicic volcanism in the past *ca.* 18 ka. Compositions represent populations within each sample (i.e. if a sample is bimodal, both populations are included) (see Appendix C)

6.5 Frequency and magnitude of Kermadec arc eruptions

The cores, while providing a much higher resolution record of volcanism in the region, do not preserve a record of every eruption over the past 170 ka. It must also be noted that there is not a 1:1 correspondence between onshore exposures and preservation in cores. With the exception of the SBT, no tephra layer has been correlated to an onshore deposit with absolute certainty. This again highlights that the cores represent a minimum eruptive frequency.

A total of 43 eruptions are recorded in the cores, with another nine tephra layers potentially representing individual eruptions (lower graph in Figure 6.14). Based on evidence in the cores, the past 10 kyr has been the most volcanically active time period over the past 170 ka, with 25 distinct eruption signatures recorded. There was a period of quiescence around 20 kyr, roughly coincident with the Last Glacial Maximum. There is another period of quiescence between 50-109 ka, and again from 120-130 ka. It is important to note however that prior to 50 ka, there is only one core with a record from this period, so it is not surprising to see a drop in the number of tephtras. Based upon the age models, only four samples were collected from around that time, and they are all heterogeneous. Overall, there is *ca.* 1 eruption of significant enough size to be recorded in the cores every 4 ka. If the record from the past 10 ka is considered, there was an average of 2.5 volcanic eruptions every 1 ka of significant enough size to be preserved. I propose that this is a more realistic estimate of the true eruption rate.

Looking at individual volcanoes, Macauley Volcano produces an eruption of significant size to be preserved in the cores with a frequency of *ca.* 3 eruptions/ 2 kyr while Raoul Volcano has an eruptive frequency of *ca.* 2 eruptions/ 3 kyr, yielding an average eruptive frequency for the two volcanoes at 1/ kyr (using eruptive frequency in the past 10 ka). If all of the volcanoes along the length of the arc show similar eruptive frequencies, the arc produces *ca.* 40 large eruptions/ ka.

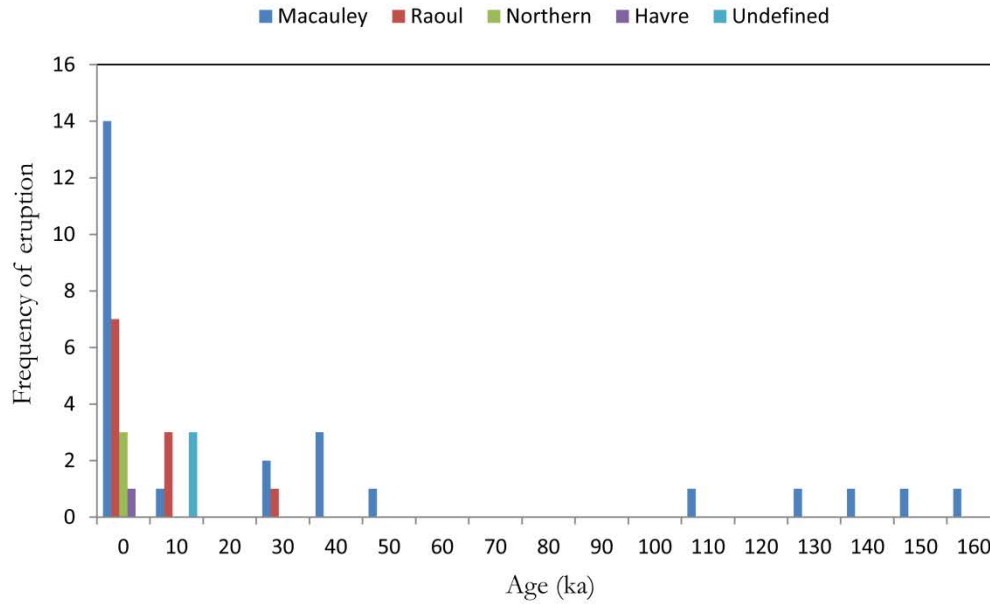
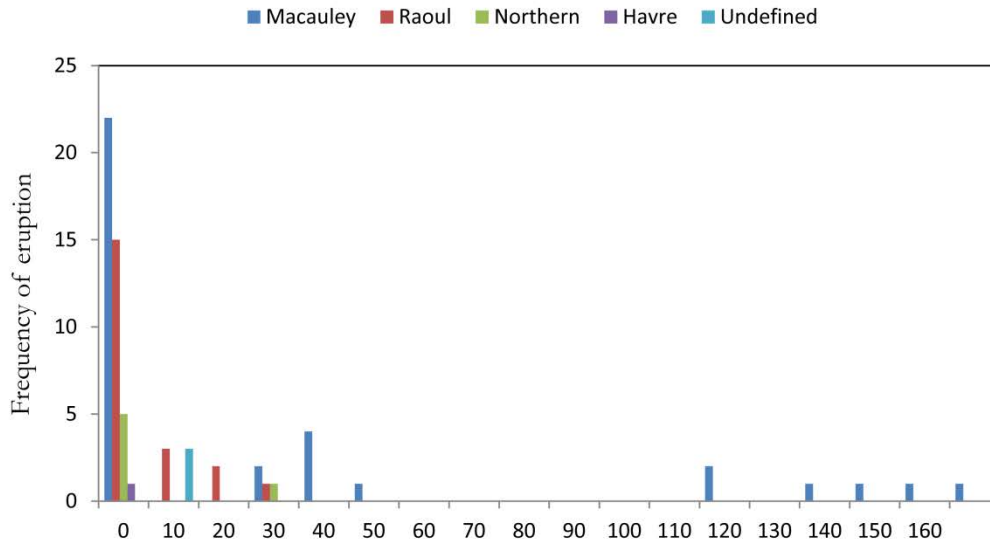


Figure 6.14 Eruptive frequencies of the volcanic centres over time. The top graph plots all tephra samples examined in this study, while the lower graph shows the eruptive frequency for the tephra which represent a single eruptive event.

Chapter 7

Conclusions

7.1 Key findings of this study

A combination of stratigraphic and geochemical data obtained from analysis of marine cores collected from off Macauley and Raoul volcanoes in the Kermadec arc lead to the following key conclusions:

- A. The number of total discrete events preserved in the cores is 51, incorporating the findings of Shane and Wright (2011) who identified 27 eruptive events recorded in the cores. My findings indicate that explosive volcanism is more prevalent at Raoul and Macauley volcanoes than previously thought. Most of the eruptive events recorded in the cores are not represented in the onshore deposits. The geochemistry of these tephra layers indicate that silicic volcanism has been a feature of magmatic systems at the two volcanoes for the late Pleistocene and is not limited to the Holocene as indicated by the onshore exposures (e.g., <4 ka on Raoul).
- B. Construction of an age model for the cores based on oxygen isotope analysis and wiggle-matching to published chronologies indicates that the oldest core (C16, offshore from Macauley Island) extends back to *ca.* 170 ka (MIS6). This has allowed the construction of a more detailed volcanic history for the region. From this we are able to see that there appear to be significant periods of volcanic quiescence (*ca.* >50 ka), where no eruptions of a significant enough size to be preserved are erupted.
- C. Fractionation appears to be the predominant method of generating silicic materials in the region, as the majority of the tephra analysed in this study show distinct fractionation trends from the glass chemistry. Contrasting models have been proposed for the generation of silicic magmas in the Kermadec arc, with crustal anatexis being proposed by some (Smith *et al.*, 2003a, b; 2006; 2010) and fractional crystallisation proposed by others (Saunders *et al.*, 2010; Barker *et al.*, 2013). My preliminary results are consistent with fractional crystallisation being the dominant method by which these silicic magmas are generated.
- D. Trace element geochemistry provides a more precise means of not only correlating tephra, but distinguishing tephra that have near identical major element compositions. Collection of these trace elements also allows for identification of processes occurring in the magma chamber to be made, as is outlined in point C above.

7.2 Key questions addressed

Three key questions were listed in Chapter 1, and the work presented in this thesis addresses them as follows.

Key question (A) was: is silicic volcanism in the Kermadec Arc a recent development, or does it pre-date records preserved onshore? As shown in Chapters 4 and 5, it has been established that the record of

silicic volcanism in the arc dates back to at least *ca.* 170 ka (the oldest tephra contains dominantly dacitic shards) indicating that silicic eruptions are simply not a recent development. It is interesting that none of these eruption deposits prior to 6.3 ka (the Sandy Bay Tephra on Macauley: Smith *et al.*, 2003b) or ~4 ka (Matatirohia on Raoul: *Lloyd and Nathan*, 1981) are preserved subaerially on Macauley or Raoul islands, as these volcanoes appear to have produced the majority of silicic tephtras preserved in the cores. Only one silicic eruption, the Sandy Bay Tephra, is recorded on Macauley Island, which is interesting as much of the silicic material preserved in the cores are inferred to be sourced from Macauley volcano (Figure 6.14). The diverse silicic compositions recorded in glassy lithic fragments in the Sandy Bay Tephra (Smith *et al.*, 2003b) and dredged pumices from the edifice flanks (Barker *et al.*, 2013) show that the erupted history of the arc is much more diverse and complex than previously thought.

Key Question (B) was: is there any cyclicality to the eruption of silicic magmas? If yes, what processes can explain this?. From the tephtras in the cores it can be seen that there are fluctuation in the magma supply, with long periods of quiescence (*ca.* >50 ka) followed by periods of high activity. In this study I interpret this to be due to differences in magma supply rates. In the past, basaltic-andesitic volcanism dominated, as recorded in the sediment cores and more especially in the onshore stratigraphic successions. The main bodies of Raoul and Macauley massifs are composed almost entirely of basaltic material. The stratigraphy of the islands indicates that there were rapid shield building periods followed by periods of lesser volcanic activity, and Holocene eruptions would suggest that the periods of rapid shield growth are followed by periods of smaller silicic eruptions which have low preservation potentials. This is best explained by periods of steady and fast magma supply from below which produces voluminous basaltic eruptions which build up the shield volcano. The magma supply then slows, and due to the density trap in the crust the magma ponds and begins to fractionate, forming more silicic magmas (Barker, 2010). These silicic magmas are erupted periodically and generally in smaller volumes. The magma supply then seems to kick-start and the supply again becomes steady and basaltic cone growth begins again.

Key Question (C) was: how frequent are eruptions of a significant enough size to be preserved in the cores?. Based upon the constructed tephrochronology and the age model developed, I calculate that overall, *ca.* 1 eruption every 4 ka is recorded in the cores. If we look at the eruption rate from the past 10 ka we see that *ca.* 2.3 eruptions are recoded every 1 ka. This is more likely to represent the actual eruptive frequency, as only three cores pre-date 15 ka, and only one extends back to 170 ka.

7.3 Future Work

This study opens up many avenues which can be investigated. Many questions remain about the size and eruptive volume of the silicic volcanism in the arc, which require further investigation.

1. The resolution of the age models for Cores 4 and 13 could be improved with higher resolution sampling. This would allow us to improve the oxygen isotope model and more accurately classify the ages of the tephra preserved in the cores.
2. Collection of more sediment cores from the area would allow a more detailed history of volcanism in the arc to be constructed. Longer cores would preserve more eruptive events, and improve upon our understanding of the frequency of eruptions in the region. Collection to the west of the arc is important for the future, as the prevailing wind direction in the region preferentially disperses volcanic material in that direction, increasing the preservation potential of the tephra layers. Collection of sediment cores to the east of the arc could also yield tephra layers erupted during periods of ENSO, providing a more detailed tephrochronology of arc volcanism.
3. These sediment cores could provide useful data for glacial/interglacial paleoceanographic changes in the mid-latitudes of the Southwest Pacific. Few studies have been conducted on paleoceanographic changes occurring in this region, which lies in a key location to record changes in the DWBC (Wright *et al.*, 1995; Whitworth *et al.*, 1999) and Tasman Front (Carter *et al.*, 2008), as well as changes in the prevailing wind directions. Sediment cores also yield other useful information on grain size, floral and faunal assemblages, and carbonate components, which can tell us much about the nature of the water column and regional water conditions, including changes in sea surface temperatures, stratification, mixing and productivity during glacial/interglacial cycles. The scope of this study cannot investigate all of these variables, but could be an important avenue for future work.
4. Major and trace element data collected in this study indicate that fractional crystallisation is the dominant process in forming silicic tephra in the Kermadec Arc (Saunders *et al.*, 2010; Barker *et al.*, 2013). The dataset could be expanded on and interpreted in greater detail, focusing on modelling of the data using the Brophy (2008) model to classify the fractionation parameters.
5. Trace elements of glass shards examined in this study could be used to conduct a detailed study on the magmatic processes occurring in the magma chamber shortly before eruption. Barker (2010) found that many minerals were not in equilibrium with the melt, indicating magma mixing occurring shortly before eruption. Trace element data analysed in this study could be used to investigate this further, particularly on the tephra mineral assemblages.

References

- Allen, S.R., Stewart, A.L. (2003). Products of explosive subaqueous felsic eruptions based on examples from the Hellenic Island Arc, Greece. In: White, J.D.L., Smellie, J.L. & Clague, D.A. (eds.) *Explosive Subaqueous Volcanism*. American Geophysical Union Geophysical Monograph 140, 285-298.
- Allan, A.S.R., Baker, J.A., Carter, L., Wysoczanski, R.J. (2008). Reconstructing the Quaternary evolution of the world's most active silicic volcanic system: insights from an ~1.65 Ma deep ocean tephra record sourced from Taupo Volcanic Zone, New Zealand. *Quaternary Science Reviews* 27, 2341-2360.
- Arculus, R.J. (2003). Use and abuse of the terms calcalkaline and calcalkalic. *Journal of Petrology* 44, 929-935.
- Ballance, P.F., Ablaev, A.G., Pushchin, I.K., Pletnev, S.P., Biryulina, M.G., Itaya, T., Follas, H.A., Gibson, G.W. (1999). Morphology and history of the Kermadec trench-arc-backarc basin-remnant arc system at 30⁰ to 32⁰: geophysical profile, microfossil and K-Ar data. *Marine Geology* 159, 35-62.
- Barker, S.J. (2010). *The petrology and genesis of silicic magmas in the Kermadec arc*. M.Sc. thesis, Victoria University of Wellington, 1-396.
- Barker, S.J., Rotella, M.D., Wilson, C.J.N., Wright, I.C., Wysoczanski, R.J. (2012). Contrasting pyroclast density spectra from subaerial and submarine volcanism in the Kermadec Arc: implications for eruptive processes and dredge sampling. *Bulletin of Volcanology* 74, 1425-1443.
- Barker, S.J., Wilson, C.J.N., Millet, M-A., Baker, J.A., Rotella, M.D., Wright, I.C., Wysoczanski, R.J. (2013). Petrology and genesis of silicic magmas in the intra-oceanic Kermadec Arc. *Journal of Petrology* in press: doi:10.1093/petrology/egs071.
- Blott, S.J. (2010). *GradiStat Version 8.0: a grain size distribution and statistics package for the analysis of unconsolidated sediments by sieving or laser granulometer*. Crowthorne, UK: Kenneth Pye & Associates Ltd.
- Boggs, S. (1987). *Principles of sedimentology and stratigraphy*. Columbus: Merrill Publishing Company.
- Bostock, H.C., Hayward, B.W., Neil, H.L., Currie, K.I., Dunbar, G.B. (2011). Deep-water carbonate concentrations in the southwest Pacific. *Deep-sea Research* 58, 72-85
- Bryan, S.E., Cook, A., Evans, J.P., Colls, P.W., Wells, M.G., Lawrence, M.G., Jell, J.S., Greig, A., Leslie, R. (2004). Pumice rafting and faunal dispersion during 2001-2002 in the Southwest Pacific: record of a dactylic submarine explosive eruption from Tonga. *Earth and Planetary Science Letters* 227, 135-154.
- Bowles, F.A., Jack, R.N., Carmichael, I.S.E. (1973). Investigation of deep-sea volcanic ash layers from Equatorial Pacific cores. *Geological Society of America Bulletin* 84, 2371-2388.
- Brophy, J.G. (2008). A study of rare earth element (REE)-SiO₂ variations in felsic liquids generated by basalt fractionation and amphibole melting: a potential test for discriminating between the two different processes. *Contributions to Mineralogy and Petrology* 156, 337-357.
- Brothers, R.N. (1970). Petrochemical affinities of volcanic rocks from the Tonga-Kermadec Island Arc, Southwest Pacific. *Bulletin Volcanologique* 34, 308-329.
- Brothers, R.N. and Martin, K.R. (1970). The Geology of Macauley Island, Kermadec Group, Southwest Pacific. *Bulletin Volcanologique* 34, 330-346.
- Brothers, R.N. and Searle, E.J. (1970). The geology of Raoul Island, Kermadec Group, Southwest Pacific. *Bulletin Volcanologique* 34, 7-37.

- Busby, C. (2005). Possible distinguishing characteristics of very deepwater explosive and effusive silicic volcanism. *Geology* 33, 845-848.
- Calderoni, G., Turi, B. (1998). Major constraints on the use of radiocarbon dating for tephrochronology. *Quaternary International* 47, 153-159.
- Campbell, M.E., Rowland, J.V., Wright, I.C., Smith, I.E.M. (2007). Oblique rifting along the central and southern Kermadec Arc from (30°-36°S), SW Pacific. *Geochemistry, Geophysics, Geosystems* 8 Q01007.
- Cane, M.A. (1983). Oceanographic events during El Nino. *Science* 222, 1189-1195.
- Carey, S. (1997). Influence of convective sedimentation on the formation of widespread tephra fall layers in the deep sea. *Geology* 25, 839-842.
- Carey, S.N., Schneider, J.-L. (2011). Volcaniclastic processes and deposits in the deep-sea, In: Huneke, H., Mulder, T. (eds): *Deep-Sea Sediments*. Developments in Sedimentology, 63. Elsevier, Amsterdam, 457-515.
- Carey, S.N., Sigurdsson, H. (1980). The Roseau ash: deep-sea tephra deposits from a major eruption in Dominica, Lesser Antilles. *Journal of Volcanology and Geothermal Research* 7, 67-86.
- Carey, S. and Sparks, R.S.J. (1986). Quantative models of the fallout and dispersal of tephra from volcanic eruption columns. *Bulletin of Volcanology* 48, 109-125.
- Carter, L., McCave, I.N. (1994). Development of sediment drifts approaching an active plate margin under the SW Pacific Deep Western Boundary Current. *Paleoceanography* 9, 1061-1085.
- Carter, L., Mitchell, J. (1987). Late Quaternary sediment pathways through the deep ocean, east of New Zealand. *Paleoceanography* 2, 409-422.
- Carter, L., Carter, R.M., McCave, I.N., Gamble, J. (1996). Regional sediment recycling in the abyssal Southwest Pacific Ocean. *Geology* 24, 735-738.
- Carter, L., Shane, P.A., Alloway, B.A.V., Hall, I.R., Harris, S. (2003). Demise of one volcanic zone and the birth of another - a 12 Ma deep ocean record of major rhyolitic eruptions from New Zealand. *Geology* 31, 493-496.
- Carter, L., Manighetti, B., Ganssen, G., Northcote, L. (2008). Southwest Pacific modulation of abrupt climate change during the Antarctic Cold Reversal - Younger Dryas. *Palaeogeography, Palaeoclimatology, Palaeoecology* 260, 284-298.
- Cashman, K.V., Fiske, R.S. (1991). Fallout of pyroclastic debris from submarine volcanic eruptions. *Science* 253, 275-280.
- DeMets, C., Gordon, R.G., Argus, D.F., Stein, S. (1990). Current plate motions. *Geophysical Journal International* 101, 425-478.
- Douglas, R., Woodruff, F. (1981). Deep-sea benthic foraminifera. In: Emiliani, C. (ed.) *The Oceanic Lithosphere*. New York: John Wiley & Sons, 1233-1327.
- Dunn, D.A. (1980). Revised techniques for quantitative calcium carbonate analysis using the 'Karbonat-Bombe', and comparisons to other methods. *Journal of Sedimentary Petrology* 50, 631-637.
- Emiliani, C. (1955). Pleistocene temperatures. *Journal of Geology* 63, 538-578.

- Ewart, A., Brothers, R.N., Mateen, A. (1977). An outline of the geology and geochemistry, and the possible petrogenetic evolution of the volcanic rocks of the Tonga-Kermadec-New Zealand Island Arc. *Journal of Volcanology and Geothermal Research* 2, 205-250.
- Ewart, A., Collerson, K.D., Regelous, M., Wendt, J.I., Nui, Y. (1998). Geochemical evolution within the Tonga-Kermadec-Lau Arc-Back-arc systems: the role of varying mantle wedge composition in space and time. *Journal of Petrology* 39, 331-368.
- Fisher, R.V. (1965). Settling velocity of glass shards. *Deep-sea Research* 12, 345-353.
- Fisher, R.V., Schmincke, H.-U. (1984). *Pyroclastic Rocks*. Berlin: Springer-Verlag.
- Folk, R.L., Ward, W.C. (1957) Brazos River bar: a study in the significance of grain size parameters. *Journal of Sedimentary Petrology*, 27, 3-26.
- Froggatt, P.C. (1983). Toward a comprehensive Upper Quaternary tephra and ignimbrite stratigraphy in New Zealand using electron microprobe analysis of glass shards. *Quaternary Research* 19, 188-200.
- Gamble, J. A., Woodhead, J., Wright, I., Smith, I. (1996). Basalt and sediment geochemistry and magma petrogenesis in a transect from oceanic island arc to rifted continental margin arc: the Kermadec-Hikurangi margin, SW Pacific. *Journal of Petrology* 37, 1523-1546.
- Ganssen, G.M., Kroon, D. (2000). The isotopic signature of planktonic foraminifera from NE Atlantic surface sediments: implications for the reconstruction of past oceanic conditions. *Journal of the Geological Society, London* 157, 693-699.
- Gill, J.B. (1981). *Orogenic Andesites and Plate Tectonics*. Berlin: Springer-Verlag.
- Gomez, B., Carter, L., Orpin, A., Cobb, K., Page, M., Trustrum, N., Palmer, A. (2011). ENSO/SAM interactions during the middle and late Holocene. *The Holocene* 22, 23-30.
- Graham, I.J., Reyes, A.G., Wright, I.C., Peckett, K.M., Smith, I.E.M, Arculus, R.J. (2008). Structure and petrology of newly discovered volcanic centers in the northern Kermadec-southern Tofua arc, South Pacific Ocean. *Journal of Geophysical Research* 113, B08S02.
- Haase, K.M., Stroncik, N., Garbe-Schonberg, D., Stoffers, P. (2006). Formation of island arc dacite magmas by extreme crystal fractionation: An example from Brothers Seamount, Kermadec island arc (SW Pacific). *Journal of Volcanology and Geothermal Research* 152, 316-330.
- Hall, I.R., McCave, I.N., Shackleton, N.J., Weedon, G.P., Harris, S.E. (2001). Intensified deep Pacific inflow and ventilation in Pleistocene glacial times. *Nature* 412, 809-812.
- Hayward, B.W., Carter, R., Grenfell, H.R., Hayward, J.J. (2001). Depth distribution of Recent deep-sea benthic foraminifera east of New Zealand, and their potential for improving paleobathymetric assessments of Neogene microfaunas. *New Zealand Journal of Geology and Geophysics* 44, 555-587.
- Hayward, B.W., Grenfell, H.R., Sabaa, A.T., Neill, H.L., Buzas, M.A. (2010). Recent New Zealand deep-water benthic foraminifera: Taxonomy, ecologic distribution, biogeography, and use in paleoenvironmental assessment. *GNS Science Monograph* 26.
- Healy, J., Lloyd, E.F., Banwell, C.J., Adams, R.D. (1965). Volcanic eruption on Raoul Island, November 1964. *Nature* 206, 743-745.

- Hembelen, C., Spindler, M., Anderson, O.R. (1989). *Modern planktonic foraminifera*. Springer, New York.
- Irvine, T.N., Baragar, W.R.A. (1971). A guide to the chemical classification of the common volcanic rocks. *Canadian Journal of Earth Sciences* 8, 523-548.
- Jacob, D.E. (2006). High sensitivity analysis of trace element-poor geological reference glasses by Laser Ablation-Inductively Coupled Mass Spectrometry (LA ICP-MS). *Geostandards and Geoanalytical Research* 30, 221-235.
- Jansen, E. (1989). The use of stable oxygen and carbon isotope stratigraphy as a dating tool. *Quaternary International* 1, 151-166.
- Jarosewich, E., Nelen, J.A., Norberg, J.A. (1980). Reference samples for electron microprobe analysis. *Geostandards Newsletter* 4, 43-47.
- Jochum, K.P., Stoll, B., Herwig, K., Willbold, M., Hofmann, A.W., et al. (2006). MPI-DING reference glasses for in situ microanalysis: New reference values for element concentrations and isotope ratios. *Geochemistry, Geophysics, Geosystems* 7, Q02008.
- Jochum, K.P., Weis, U., Stoll, B., Kuzmin, D., Yang, Q., et al. (2011). Determination of reference values for NIST SRM 610-618 glasses following ISO guidelines. *Geostandards and Geoanalytical Research* 35, 397-429.
- Kano, K. (2003). Subaqueous pumice eruptions and their products: a review. In: White, J.D.L., Smellie, J.L., Clague, D.A. (eds.) *Explosive Subaqueous Volcanism*. American Geophysical Union Geophysical Monograph 140, 213-243.
- Karoly, D.J. (1989). Southern Hemisphere circulation features associated with El Nino-Southern Oscillation events. *Journal of Climate* 2, 1239-1252.
- Kennett, J.P. and Huddleston, P. (1972). Late Pleistocene paleoclimatology, foraminiferal biostratigraphy and tephrochronology, western Gulf of Mexico. *Quaternary Research* 2, 38-69.
- Latter, J.H., Lloyd, E.F., Smith, I.E.M. & Nathan, S. (1992). *Volcanic Hazards in the Kermadec Islands, and at Submarine Volcanoes between Southern Tonga and New Zealand*: Ministry of Civil Defence.
- Latter, J.H., Lloyd, E.F., Smith, I.E.M., Nathan, S. (2012). Kermadec Island Geology. In: GNS Science (ed.) *New Zealand Volcanoes*. <http://www.gns.cri.nz/Home/Learning/Science-Topics/Volcanoes/New-Zealand-Volcanoes/Volcano-Geology-and-Hazards/Kermadec-Islands-Geology>
- Le Maitre, R.W., Bateman, P., Dudek, A., Keller, J., Lameyre Le Bas, M.J., Sabine, P.A., Schmid, R., Sorenson, H., Streckeisen, A., Woolley, A.R., Zanettin, B. (1989). *A Classification of Igneous Rocks and Glossary of Terms*. Oxford, UK: Blackwell.
- Leat, P.T., Larter, R.D. (2003). Intra-oceanic subduction systems: introduction. *Geological Society of London, Special Publications* 219, 1-17.
- Leat, P.T., Smellie, J.L., Millar, I.L., Larter, R.D. (2003). Magmatism in the South Sandwich arc. *Geological Society of London, Special Publications*, 285-313.

- Ledbetter, M.T., Sparks, R.S.J. (1979). Duration of large-magnitude explosive eruptions deduced from graded bedding in deep-sea ash layers. *Geology* 7, 240-244.
- Lisiecki, L.E., Raymo, M.E. (2005). A Pliocene-Pleistocene stack of 57 globally distributed benthic $\delta^{18}O$ records, *Paleoceanography*, 20, PA1003.
- Lloyd, E.F., Nathan, S. (1981). Geology and tephrochronology of Raoul Island, Kermadec Group, New Zealand. *New Zealand Geological Survey Bulletin* 105.
- Lloyd, E.F., Nathan, S., Smith, I.E.M., Stewart, R.B. (1996). Volcanic history of Macauley Island, Kermadec Ridge, New Zealand. *New Zealand Journal of Geology and Geophysics* 39, 295-308.
- Lowe, D.J. (2011). Tephrochronology and its application: a review. *Quaternary Geochronology* 6, 107-153.
- Lowe, D.J., de Lange, W.P. (2001). Volcano-meteorological tsunamis, the ca. AD 200 Taupo eruption (New Zealand) and the possibility of a global tsunami. *The Holocene* 10, 401-407.
- Lowe, D.J., Shane, P.A.R., Alloway, B.V., Newnham, R.M. (2008). Fingerprints and age models for widespread New Zealand tephra marker beds erupted since 30,000 years ago: a framework for NZ-INTIMATE. *Quaternary Science Reviews* 27, 95-126.
- Luhr, J.F., Navarro-Ochoa, C., Savov, I.P. (2010). Tephrochronology, petrology, and geochemistry of late-Holocene pyroclastic deposits from Volcan de Colima, Mexico. *Journal of Volcanology and Geothermal Research* 197, 1-32.
- Manville, V., Wilson, C.J.N. (2004). Vertical density currents: a review of their potential role in the deposition and interpretation of deep-sea ash layers. *Journal of the Geological Society of London* 161, 947-958.
- Maunder, W.J. (1971). The climate of New Zealand - physical and dynamic features. In: Gentili, J. (ed.) *Climates of Australia and New Zealand*. Amsterdam: Elsevier Publishing Company, 231-226.
- Miyashiro, A. (1974). Volcanic rock series in island arcs and active continental margins. *American Journal of Science* 274, 321-355.
- McCave, I.N., Carter, L., Hall, I.R. (2008) Glacial-interglacial changes in water mass structure and flow in the SW Pacific Ocean. *Quaternary Science Reviews* 27 1886-1908
- Muller, G., Gastner, M. (1971). The 'Karbonat-Bombe', a simple device for the determination of carbonate content in sediments, soils and other materials. *Neues Jahrbuch für Mineralogie* 10, 466-469.
- Ninkovitch, D. (1968). Pleistocene volcanic eruptions in New Zealand recorded in deep-sea sediments. *Earth and Planetary Science Letters* 4, 89-102.
- NIWA (2007). NIWA Voyage Report TAN0706 Tangaroa (May 2007) Kermadec Island Volcanoes. National Institute of Water and Atmospheric Research, Wellington, New Zealand, 34pp.
- Oberhuber, J.M., Herzog, M., Graf, H-F., Schwanke, K. (1998). Volcanic plume simulation on large scales. *Journal of Volcanology and Geothermal Research* 87, 29-53.
- Paillard, D., Labeyrie, L., Yiou, P. (1996). Macintosh program performs time-series analysis, *Eos Trans. AGU*, 77, 379.

- Patene, M., Guichard, F., Labeyrie, J., Gillot, P.Y., Duplessy, J.C. (1986). Tyrrhenian Sea tephrochronology of the oxygen isotope record for the past 60,000 years. *Marine Geology* 72, 259-285.
- Paton, C., Hellstrom, J., Paul, B., Woodhead, J., Hergt, J. (2011). Iolite: Freeware for the visualisation and processing of mass spectrometric data. *Journal of Analytical Atomic Spectrometry* 26, 2508-2518.
- Pearce, N.J.G., Westgate, J.A., Perkins, W.T. (1996). Developments in the analysis of glass shards by Laser Ablation ICP-MS: quantitative and single internal standard-multi-element methods. *Quaternary International* 34-36, 213-227.
- Pearce, N.J.G., Westgate, J.A., Perkins, W.T., Preece, S.J. (2004). The application of ICP-MS methods to tephrochronological problems. *Applied Geochemistry* 19, 289-322.
- Pillans, B., Wright, I. (1992). Late Quaternary tephrostratigraphy from the southern Havre Trough - Bay of Plenty, northeast New Zealand. *New Zealand Journal of Geology and Geophysics* 35, 129-143.
- Priestly, R. (2012). Fire & Water. *New Zealand Geographic*. Auckland, New Zealand: Kowhai Media Ltd, 92-103.
- Rasmussen, E., Carpenter, T.H. (1982). Variations on tropical sea surface temperature and surface wind fields associated with the Southern Oscillation/El Nino. *Monthly Weather Review* 110, 354-384.
- Rasmussen, E.M., Wallace, J.M. (1983). Meteorological aspects of the El Nino/Southern Oscillation. *Science* 222, 1195-1202.
- Reid, S.J., Penney, A.C. (1982). Upper-level wind frequencies and mean speeds for New Zealand and Pacific Island stations. *New Zealand Meteorological Service Miscellaneous Publication* 174, 1-98.
- Rotella, M.D., Wilson, C.J.N., Barker, S.J., Wright, I.C. (2013). Highly vesicular pumice generated by buoyant detachment of magma in subaqueous volcanism. *Nature Geoscience*, in press, doi:10.1038/ngeo1709
- Salinger, M. J., Basher, .E., Fitzharris, B.B., Jay, J.E., Jones, P.D., MacVeigh, J.P., Schmidley-Leleu, I. (1995). Climate trends in the South-West Pacific. *International Journal of Climatology* 15, 285-302.
- Salinger, M. J., Renwick, J.A. and Mullan, A.B. (2001). Interdecadal Pacific Oscillation and South Pacific climate. *International Journal of Climatology* 21, 1705-172.
- Saunders, K.E., Baker, J.A. & Wysoczanski, R.J. (2010). Microanalysis of large volume silicic magma in continental and oceanic arcs: melt inclusions in Taupo Volcanic Zone and Kermadec Arc rocks, South West Pacific. *Journal of Volcanology and Geothermal Research* 190, 203-218.
- Schulmeister, J., Goodwin, I., Renwick, J., Harle, K., Armand, L., McGlone, M.S., Cook, E., Dodson, J., Hesse, P.P., Mayewski, P., Curran, M. (2004). The Southern Hemisphere westerlies in the Australasian sector over the last glacial cycle: a synthesis. *Quaternary International* 118-119, 23-53.
- Shackleton, N.J., Opdyke, N.D. (1973). Oxygen isotope and paleomagnetic stratigraphy of Equatorial Pacific core V28-238: Oxygen isotope temperatures and ice volumes on a 10⁵ and 10⁶ year scale. *Quaternary Research* 3, 33-55.
- Shane, P. (2000). Tephrochronology: a New Zealand case study. *Earth-Science Reviews* 49, 223-259.

- Shane, P., Wright, I.C. (2011). Late Quaternary tephra layers around Raoul and Macauley Islands, Kermadec Arc: implications for volcanic sources, explosive volcanism and tephrochronology. *Journal of Quaternary Science* 36, 422-432.
- Shaw, D.M., Watkins, N.D., Huang, T.C. (1974). Atmospherically transported volcanic glass in deep-sea sediments: theoretical considerations. *Journal of Geophysical Research* 79, 3087-3094.
- Sigurdsson, H. Carey, S.N. (1981). Marine Tephrochronology and Quaternary explosive volcanism in the Lesser Antilles Arc. In: Self, S., Sparks, R.S.J. (eds.) *Tephra Studies*. Dordrecht: D. Reidel Publishing Company.
- Smith, I.E.M., Price, R.C. (2006). The Tonga-Kermadec Arc and the Havre-Lau back-arc system: Their role in the development of tectonic and magmatic models for the western Pacific. *Journal of Volcanology and Geothermal Research* 156, 315-331.
- Smith, I.E.M., Brothers, R.N., Muiruri, F.G. and Browne, P.r.L. (1988). The geochemistry of rock and water samples from Curtis Island volcano, Kermadec group, southwest Pacific. *Journal of Volcanology and Geothermal Research* 34, 233-240
- Smith, I.E.M., Worthington, T., Stewart, R.B., Price, R.C., Gamble, J.A. (2003a). Felsic volcanism in the Kermadec arc, SW Pacific: crustal recycling in an oceanic setting. *Geological Society of London, Special Publications* 219, 99-118.
- Smith, I.E.M., Stewart, R.B., Price, R.C. (2003b). The petrology of a large intraoceanic silicic eruption: the Sandy Bay Tephra, Kermadec Arc, Southwest Pacific. *Journal of Volcanology and Geothermal Research* 124, 173-194.
- Smith, I.E.M., Worthington, T.J., Price, R.C., Stewart, R.B., Maas, R. (2006). Petrogenesis of dacite in an oceanic subduction environment: Raoul Island, Kermadec arc. *Journal of Volcanology and Geothermal Research* 156, 252-265.
- Smith, I.E.M., Price, R.C., Stewart, R.B., Worthington, T.J. (2009). An assessment of the mantle and slab components in the magmas of an oceanic arc volcano: Raoul Volcano, Kermadec arc. *Journal of Volcanology and Geothermal Research* 184, 437-450.
- Smith, I.E.M., Stewart, R.B., Price, R.C., Worthington, T.J. (2010). Are arc-type rocks the products of magma crystallisation? Observations from a simple oceanic arc volcano: Raoul Island, Kermadec Arc, SW Pacific. *Journal of Volcanology and Geothermal Research* 190, 219-234.
- Sparks, R.S.J., Bursik, M.I., Ablay, G.J., Thomas, R.M.E., Carey, S.N. (1992). Sedimentation of tephra by volcanic plumes. Part 2: controls on thickness and grain-size variations of tephra fall deposits. *Bulletin of Volcanology* 54, 685-695.
- Sparks, R.S.J., Bursik, M.I., Carey, S.N., Gilbert, J.E., Glaze, L.S., Sigurdsson, H. & Woods, A.W. (1997). *Volcanic Plumes*, Hoboken, N.J.: John Wiley.
- Spero, H.J., Lea, D.W. (1996). Experimental determination of stable isotope variability in Globigerina bulloides: implications for paleoceanographic reconstructions. *Marine Micropaleontology* 28, 231-246.

- Stix, J. (1991). Subaqueous, intermediate to silicic-composition explosive volcanism: a review. *Earth-Science Reviews* 31, 21-53.
- Sturman, A., Tapper, D. (2006). *The weather and climate of Australia and New Zealand*. Oxford, UK: Oxford University Press.
- Sun, S.S., McDonough, W.F. (1989). Chemical and isotopic systematics of oceanic basalts: implications for mantle composition and process. *Geological Society of London, Special Publications* 42, 313–345.
- Tamura, Y., Tatsumi, Y. (2002). Remelting of an andesitic crust as a possible origin of rhyolitic magma in oceanic arcs: an example from the Izu-Bonin arc. *Journal of Petrology* 43, 1029-1047.
- Tamura, Y., Wysoczanski, R. (2006). Silicic volcanism and crustal evolution in oceanic arcs: Introduction. *Journal of Volcanology and Geothermal Research* 156, v-vii.
- Thiede, J., Nees, S., Schulz, H., De Deckker, P. (1997). Oceanic surface conditions recorded on the seafloor of the Southwest Pacific Ocean through the distribution of foraminifers and biogenic silica. *Palaeogeography, Palaeoclimatology, Palaeoecology* 131, 207-239.
- Tilburg, C.T., Hurlburt, H.E., O'Brien, J.J., Shriver, J.F. (2001). The dynamics of the East Australian Current system: the Tasman Front, the East Auckland Current, and the East Cape Current. *Journal of Physical Oceanography* 31, 2918-2943.
- Toggweiler, J. R., Russell, J.L., Carson, S.R. (2006). Midlatitude westerlies, atmospheric CO₂ and climate change during the glacials. *Paleoceanography* 21, PA2005.
- Turner, S., Hawkesworth, C., Rogers, N., Bartlett, J., Worthington, T.J., Hergt, J., Pearce, J., Smith, I.E.M. (1997). ²³⁸U - ²³⁰Th disequilibria, magma petrogenesis, and flux rates beneath the depleted Tonga-Kermadec island arc. *Geochimica et Cosmochimica Acta* 61, 4855-4884.
- Udden, J.A. (1914). Mechanical composition of clastic sediments. *Bulletin of the Geological Society of America* 25, 655-744.
- Ummenhofer, C.C., England, M.H. (2007). Interannual extremes in New Zealand precipitation linked to modes of Southern Hemisphere climate variability. *Journal of Climate* 20, 5418-5440.
- Urey, H.C. (1947) The thermodynamic properties of isotopic substances. *Journal of the Chemical Society* [May 1947], 562-581.
- Wallace, L.M., Ellis, S., Mann, P. (2009). Collisional model for rapid fore-arc block rotations, arc curvature, and episodic back-arc rifting in subduction zones. *Geochemistry, Geophysics, Geosystems* 10, Q05001.
- Warren, B.A., Whitworth III, T., Moore, M.I., Nowlin Jnr, W.D. (1994). Slight northwestward inflow into the deep South Fiji Basin. *Deep-sea Research* 41, 953-956.
- Weaver, P.P.E., Carter, L., Neil, H. (1998). Response of surface water masses and circulation to late Quaternary climate change east of New Zealand. *Paleoceanography* 13, 70-83.
- Wentworth, C.K. (1922). A scale of grade and class terms for clastic sediments. *Journal of Geology* 30, 377-392.

- Westgate, J.A., Briggs, N.D. (1980). Dating methods of Pleistocene deposits and their problems: V. Tephrochronology and fission-track dating. *Geoscience Canada* 7, 3-10.
- Westgate, J.A., Perkins, W.T., Fuge, R., Pearce, N.J.G., Wintle, A.G. (1994). Trace-element analysis of volcanic glass shards by laser ablation inductively coupled mass spectrometry: application to tephrochronological studies *Applied Geochemistry* 9, 323-335.
- Whitworth, T., Warren, B.A., Nowlin, W.D., Pillsbury, R.D., Moore, M.I. (1999). On the deep western-boundary current in the Southwest Pacific Basin. *Progress in Oceanography* 43, 1-54.
- Wilson, C.J.N., Houghton, B.F., McWilliams, M.O., Lanphere, M.A., Weaver, S.D., Briggs, R.M. (1995). Volcanic and structural evolution of Taupo Volcanic Zone, New Zealand: a review. *Journal of Volcanology and Geothermal Research* 68, 1-28.
- Wilson, L., Walker, G.P.L. (1987). Explosive volcanic eruptions: VI. Ejecta dispersal in plinian eruptions: the control of eruption conditions and atmospheric properties. *Geophysical Journal of the Royal Astronomical Society* 89, 657-679.
- Wilson, M. (1989). *Igneous Petrogenesis A Global Tectonic Approach*. Dordrecht, Netherlands: Kluwer Academic Publishers.
- Woods, A.W. (1993). Moist convection and the injection of volcanic ash into the atmosphere. *Journal of Geophysical Research* 98, 17627-17636.
- Worthington, T.J., Gregory, M.R., Bondarenko, V. (1999). The Denham Caldera on Raoul Volcano: dacite volcanism in the Tonga-Kermadec arc. *Journal of Volcanology and Geothermal Research* 90, 29-48.
- Wright, I.C. (1993). Pre-spread rifting and heterogeneous volcanism in the southern Havre Trough back-arc basin. *Marine Geology* 113, 179-200.
- Wright, I.C. (1994). Nature and tectonic setting of the southern Kermadec submarine arc volcanoes: An overview. *Marine Geology* 118, 217-236.
- Wright, I.C. (1996). Volcaniclastic processes on modern submarine arc stratovolcanoes: sidescan and photographic evidence from the Rumble IV and V volcanoes, southern Kermadec Arc (SW Pacific). *Marine Geology* 136, 21-39.
- Wright, I.C. (2001). In situ modification of modern submarine hyaloclastic/pyroclastic deposits by ocean currents: an example from the Southern Kermadec arc (SW Pacific). *Marine Geology* 172, 287-307.
- Wright, I.C., McGlone, M.S., Nelson, C.S., Pillans, B.J. (1995). An integrated latest Quaternary (Stage 3 to present) paleoclimatic and paleoceanographic record from offshore northern New Zealand. *Quaternary Research* 44, 283-293.
- Wright, I.C., Worthington, T.J., Gamble, J.A. (2006). New Multibeam mapping and geochemistry of the 30°-35° S sector, and overview of southern Kermadec arc volcanism. *Journal of Volcanology and Geothermal Research* 149, 263-296.
- Wyszczanski, R.J., Todd, E., Wright, I.C., Leybourne, M.I., Hergt, J. M., Adam, C., Mackay, K. (2010). Backarc rifting, constructional volcanism and nascent disorganised spreading in the southern Havre Trough backarc rifts (SW Pacific). *Journal of Volcanology and Geothermal Research* 190, 39-57.